

# **Geometric and Mechanical Modelling of Textiles**

Martin Sherburn

Thesis submitted to The University of Nottingham  
for the degree of Doctor of Philosophy

July 2007

# Contents

<b>Abstract</b>	<b>vii</b>
<b>Acknowledgements</b>	<b>viii</b>
<b>Glossary</b>	<b>ix</b>
<b>Nomenclature</b>	<b>xi</b>
<b>1 Introduction</b>	<b>1</b>
1.1 Textile reinforced composites . . . . .	1
1.2 Types of textile architecture . . . . .	2
1.3 Thesis overview . . . . .	3
<b>2 Geometric modelling of textiles</b>	<b>5</b>
2.1 Introduction . . . . .	5
2.2 Literature survey . . . . .	6
2.2.1 Yarn path and cross-section models . . . . .	6
2.2.2 Textile geometrical modelling software . . . . .	8
2.3 Yarn path representation . . . . .	11
2.3.1 Cubic Bézier splines . . . . .	12
2.3.2 Natural cubic splines . . . . .	13
2.3.3 Periodic cubic splines . . . . .	14
2.4 Yarn cross-section . . . . .	16
2.4.1 Ellipse . . . . .	16
2.4.2 Power ellipse . . . . .	16

## CONTENTS

2.4.3	Lenticular . . . . .	16
2.5	Yarn surface . . . . .	18
2.5.1	Constant cross-section . . . . .	19
2.5.2	Interpolated cross-sections . . . . .	19
2.6	Yarn repeats . . . . .	21
2.7	Domain . . . . .	21
2.8	Surface mesh . . . . .	22
2.9	Volume mesh . . . . .	24
2.9.1	Cross-section meshing . . . . .	24
2.9.2	Linking . . . . .	26
2.10	Fibre volume fraction . . . . .	26
2.11	Intersections . . . . .	28
2.11.1	Point inside yarn . . . . .	28
2.11.2	Yarn intersections . . . . .	30
2.12	Implementation . . . . .	31
2.12.1	Modules . . . . .	31
2.12.2	Core . . . . .	33
2.13	Conclusions . . . . .	35
<b>3</b>	<b>Textile geometry model case validations</b>	<b>36</b>
3.1	Introduction . . . . .	36
3.2	Literature survey . . . . .	37
3.3	Experimental techniques . . . . .	38
3.3.1	Fabric thickness . . . . .	38
3.3.2	Microscopy . . . . .	39
3.3.3	Microtomography . . . . .	40
3.3.4	Measuring parameters . . . . .	40
3.3.5	Image analysis . . . . .	41
3.4	Case study: Chomarat 150TB . . . . .	44
3.4.1	Validation . . . . .	47

## CONTENTS

3.5	Case study: Chomarat 800S4-F1 . . . . .	53
3.5.1	Validation . . . . .	57
3.6	Case study: Unilever woven polyester standard . . . . .	60
3.6.1	Validation . . . . .	62
3.7	Case study: Unilever standard cotton sheeting . . . . .	64
3.7.1	Validation . . . . .	66
3.8	Conclusions . . . . .	66
<b>4</b>	<b>Mechanical modelling of tows</b>	<b>68</b>
4.1	Introduction . . . . .	68
4.2	Literature survey . . . . .	69
4.2.1	Compression of random fibre assemblies . . . . .	69
4.2.2	Compression of orientated fibre assemblies . . . . .	70
4.2.3	Effect of inter-fibre slipping . . . . .	74
4.2.4	Compression modelling of oriented fibre assemblies via energy method . . . . .	76
4.2.5	Deformation behaviour of wavy aligned fibres . . . . .	77
4.2.6	Deformation of unidirectional helically crimped fibre assemblies	79
4.2.7	Application to finite element analysis software . . . . .	79
4.2.8	Computer simulation . . . . .	80
4.2.9	Conclusions . . . . .	81
4.3	Model theory . . . . .	81
4.3.1	Beam theory . . . . .	82
4.3.2	Contact forces . . . . .	83
4.3.3	Contact locations . . . . .	85
4.3.4	Friction . . . . .	90
4.3.5	Strain Energy . . . . .	92
4.3.6	Convergence . . . . .	93
4.4	Compaction of a single tow . . . . .	93
4.4.1	Periodic boundary conditions . . . . .	93

## CONTENTS

4.4.2	Modelling compaction . . . . .	96
4.4.3	Forces from energy . . . . .	96
4.4.4	Compaction test case . . . . .	97
4.4.5	Glass fibre tow . . . . .	104
4.4.6	Conclusions from compaction examples . . . . .	113
4.5	Shearing of polyester plain weave . . . . .	113
4.5.1	Frictional energy minimisation . . . . .	115
4.5.2	Incremental loading . . . . .	116
4.5.3	Boundary conditions . . . . .	116
4.5.4	Forces from energy . . . . .	117
4.5.5	Results . . . . .	119
4.5.6	Conclusions . . . . .	129
<b>5</b>	<b>Mechanical modelling of fabric unit cells</b>	<b>130</b>
5.1	Introduction . . . . .	130
5.2	Literature survey . . . . .	131
5.2.1	Finite element analysis of fabric unit cells . . . . .	131
5.2.2	Experimental methods . . . . .	132
5.3	Experimental techniques . . . . .	134
5.4	Finite element method . . . . .	135
5.4.1	Element definition . . . . .	136
5.4.2	Material model . . . . .	140
5.4.3	Time integration and damping . . . . .	149
5.4.4	Incremental loading . . . . .	152
5.4.5	Contact algorithm . . . . .	153
5.4.6	Periodicity . . . . .	161
5.5	Fabric meshes . . . . .	165
5.5.1	Fibre direction . . . . .	166
5.6	Fabric compression . . . . .	166
5.6.1	Chomarat 150TB . . . . .	166

## CONTENTS

5.6.2	Chomarat 800S4-F1 . . . . .	170
5.7	Fabric tension . . . . .	171
5.7.1	Chomarat 150TB . . . . .	172
5.7.2	Chomarat 800S4-F1 . . . . .	174
5.8	Fabric shear . . . . .	175
5.8.1	Chomarat 150TB . . . . .	175
5.8.2	Chomarat 800S4-F1 . . . . .	176
5.9	Conclusions . . . . .	178
<b>6</b>	<b>Discussion and conclusions</b>	<b>180</b>
6.1	Introduction . . . . .	180
6.2	Discussion . . . . .	180
6.2.1	Geometric modelling . . . . .	180
6.2.2	Mechanical modelling . . . . .	181
6.3	Conclusions . . . . .	182
6.4	Recommendations for further work . . . . .	183
	<b>References</b>	<b>186</b>
	<b>Appendices</b>	
<b>A</b>	<b>Area calculation</b>	<b>199</b>
<b>B</b>	<b>Volume calculation</b>	<b>201</b>
<b>C</b>	<b>Repeat limits</b>	<b>203</b>
<b>D</b>	<b>Sample python scripts</b>	<b>205</b>
<b>E</b>	<b>Graphical user interface screenshots</b>	<b>216</b>
<b>F</b>	<b>Beam theory</b>	<b>219</b>
<b>G</b>	<b>Test case tow compaction graphs</b>	<b>222</b>

CONTENTS

<b>H Glass tow compaction graphs</b>	<b>224</b>
<b>I Finite element code validation</b>	<b>227</b>
<b>J Quadtree</b>	<b>244</b>
<b>K Predicted fabric compaction graphs</b>	<b>253</b>

# Abstract

The quality of a composite material produced using a textile reinforcement depends largely on the way the textile deforms during processing. To ensure the production of high quality parts and minimise costs in designing such parts it is necessary to develop methods to predict the deformations of textiles.

This thesis employs a multi scale modelling approach in predicting mechanical properties of textile fabrics. The three scales involved are the microscopic, mesoscopic and macroscopic. This thesis concentrates on the micro and mesoscopic scales leading to results applicable to the macroscopic scale.

At the microscopic scale fibres are modelled as individual entities and the interactions between these entities are modelled. In compaction of yarns, the contact between fibres and bending resulting from these contacts governs the force response. A numerical model is developed to simulate this behaviour and results are validated against experimental studies found in the literature. The numerical model is extended to the mesoscopic scale where the shear of a plain woven fabric consisting of low filament count yarns is modelled.

At the mesoscopic scale a large part of the work consists of characterising the geometry of textile fabrics. New and existing algorithms are combined together to form a consistent modelling approach. This work was performed in conjunction with the development of a software package named TexGen where these algorithms are implemented. The geometric models created by TexGen are then used to predict mechanical properties of textile unit cells using a finite element method which takes yarn properties as an input. Validation is performed for a series of woven fabrics subjected to compression and in-plane shear.



# Acknowledgements

I would like to thank my academic supervisors Professor Andrew Long and Dr Arthur Jones for their excellent support and advice during the course of my studies. Special thanks go to Dr François Robitaille for offering me the chance to study for a PhD and getting me started in the right direction.

The financial support of the Engineering and Physical Sciences Research Council (EPSRC) is greatly appreciated. Thanks are due to Roger Smith, Paul Johns and Geoff Tomlinson for their technical support and Professor Tom Hyde, head of the School of Mechanical, Materials and Manufacturing Engineering, for the use of the School facilities.

I would also like to thank my friends and colleagues for their kindness and keeping me entertained during my time at Nottingham: Sophie Cozien-Cazuc, Chee Chiew Wong, Jing Yang, Jon Crookston, Joram Wiggers, Wout Ruijter, Dhiren Modi, Phil Harrison, Somsunan Runglawan (a.k.a Kay) and countless others. My family for their support during my studies.

Finally, I dedicate this thesis to my loving wife Didi for taking care of me and putting up with my coding addiction.

# Glossary

Anisotropic	Exhibiting different properties in response to stresses applied along different axes.
Areal density	The weight of fibre per unit area of fabric.
Biaxial load	A loading condition in which a tensile load is applied to a fabric in two different directions.
Binder	A thermoplastic agent applied to yarns to bond the fibres together in a reinforcement.
CAD	Computer-aided design.
Composite	Material composed of two or more constituent materials that remain separate and distinct on a microscopic level while forming a single component.
Crimp	The waviness of a fibre or yarn.
E Glass	A borosilicate glass; the type most commonly used in glass fibre composites.
Elastic deformation	A deformation which is recovered upon removal of load.
Fabric	A material constructed of interlaced yarns, usually planar.
FE	Finite element: A numerical method of solving differential equations.
Fibre	A class of material whose length is far greater than its effective diameter.
Glass fibre	A fibre composed of glass created by drawing glass to a small diameter and extreme length.
KES-f	Kawabata Evaluation System for fabrics.
Matrix	A material used to hold the reinforcement in place forming a composite part.
Plastic deformation	A deformation which remains after removal of load.
Poisson's ratio	A measure of the ratio of change in cross-sectional area to change in length when a material is stretched.

## GLOSSARY

Preform	A preshaped fibrous reinforcement formed to the desired shape before processing.
Prepreg	A ready-to-mould material in a rolled-sheet form impregnated with resin.
Reinforcement	A material forming part of a composite which improves the overall strength and stiffness.
Resin	A viscous liquid capable of hardening used as the matrix material in a composite.
Tow	A large untwisted bundle of continuous filaments.
Transversely isotropic	An anisotropic material which has a plane of symmetry where the stress response is isotropic in that plane.
Unidirectional	Refers to fibres that are oriented in the same direction.
Warp	The yarns running lengthwise in a woven fabric.
Weft	The transverse yarns in a woven fabric.
Yarn	An assembly of continuous fibres, natural or manufactured.

# Nomenclature

## Roman letters

$\vec{a}$	Acceleration	mm/s <sup>2</sup>
$A$	Area	mm <sup>2</sup>
$a$	Position of force application	mm
$A.F.$	Area of fibre	mm <sup>2</sup>
$A.Y.$	Area of yarn	mm <sup>2</sup>
$A_f$	Area fraction	
<b>B</b>	Bezier curve	
<b>C</b>	Cross-section	
$C$	Continuity	
$c$	Damping coefficient	
$c_c$	Critical damping coefficient	
$D$	Pressure	MPa
$d$	Distance	mm
$E$	Young's modulus	MPa
<b>F</b>	Deformation gradient	
$\vec{F}$	(Frictional) force	N
$F$	Force	N
$G$	Shear modulus	MPa

## NOMENCLATURE

$h$	Yarn height (thickness)	mm
$I$	Second moment of area	mm <sup>4</sup>
$K$	Contact coefficient	
$k$	Biaxial tension ration	
$L$	Length	mm
$M$	Moment	N.mm
$m$	Mass	g
$\vec{N}$	Normal (force)	N
$n_d$	Number of fibre length divisions	
$n_i$	Number of strain convergence iterations	
$n_s$	Number of steps	
$o$	Offset	mm
<b>P</b>	Point	
$P(u, v)$	Parametric surface	
$P$	Resultant force	N
$p$	Particle	
$\vec{Q}$	Degree of compaction	
$\vec{R}$	Repeat vector	mm
$r$	Radius	mm
$R^2$	Coefficient of correlation	
<b>S</b>	Spline	
$s$	Yarn spacing (between centre-lines)	mm
$T$	Fabric thickness	mm
$t_d$	Intersection convergence tolerance	
$t_U$	Strain convergence tolerance	

## NOMENCLATURE

$U$	Strain energy	mJ
$\vec{V}$	Velocity	mm/s
$V$	Volume	mm <sup>3</sup>
$v$	Deflection	mm
$V.F.$	Volume of fibre	mm <sup>3</sup>
$V.Y.$	Volume of yarn	mm <sup>3</sup>
$V_{f,y}$	Fibre to yarn volume fraction	
$W$	Work done	mJ
$w$	Yarn width	mm
$x$	Distance along beam	mm
$z$	Distance between yarn centrelines at crossovers	mm

### Greek letters

$\beta$	Ratio of arc length to height	
$\gamma$	Engineering shear strain	
$\kappa$	Curvature	m <sup>-1</sup>
$\mu$	Coefficient of friction	
$\rho$	Density	g/cm <sup>3</sup>
$\rho_A$	Areal density	g/m <sup>2</sup>
$\sigma$	Stress	MPa
$\theta$	Angle	degrees
$\varepsilon$	Strain	

### Kawabata Evaluation System parameters

$2HG$	Hysteresis of shear force at 0.5° of shear angle	gf/cm
$2HG5$	Hysteresis of shear force at 5° of shear angle	gf/cm
$G$	Shear stiffness	gf/cm.degree

## NOMENCLATURE

*MIU* Coefficient of friction

*MMD* Mean deviation of MIU

$T_0$  Thickness at 0.5 gf/cm<sup>2</sup> mm

$T_m$  Thickness at 50 gf/cm<sup>2</sup> mm

*WC* Compressional energy gf.cm/cm<sup>2</sup>

### Subscripts

*c* Centre or Cell

*e* Estimated

*f* Fibre

*L* Longitudinal

*N* Normalised

*rms* Root mean square

*T* Transverse

*t* Total

*x* X axis (warp)

*y* Y axis (weft) or Yarn

*z* Z axis (through thickness)

### Convention

$\vec{A}$  Vector

**A** Point or Tensor

$\vec{A}_i$  Component of a vector

**A<sub>i</sub>** Component of a point

**A<sub>ij</sub>** Component of a tensor

*A* a scalar

# Introduction

## 1.1 Textile reinforced composites

Composite materials (or composites for short) are engineering materials made from two or more constituent materials that remain separate and distinct on a microscopic level while forming a single component. There are two categories of constituent materials: matrix and reinforcement. The matrix material surrounds and supports the reinforcement materials by maintaining their relative positions. Reinforcements impart their special mechanical and physical properties to enhance the matrix properties. A synergy produces material properties unavailable from the individual constituent materials.

Textile reinforced composites are a subclass of composites where the reinforcement is a textile material comprised of a network of natural or artificial fibres, typically arranged as tows or yarns. They are widely used in the aerospace industry due to their high stiffness and strength to weight ratio. Reducing weight while meeting the structural requirements is of paramount importance in order to minimise fuel consumption in aircraft. The need to minimise fuel consumption is twofold: it reduces operating costs and environmental impact. This is merely one example of the use of textile reinforced composites in industry albeit, arguably the most important. Although textile composites do not exhibit as high strengths as their unidirectional prepreg counterpart they are cheaper to produce and less susceptible to growth of damage.

The work presented in this thesis stems from interest in textile reinforced composites; however, the results are applicable to other areas of research involving textiles such as clothing, geotextiles, body armour, thermal protection, chemical protection, smart textiles, etc.



## 1.2 Types of textile architecture

The main categories of textile architecture relevant to composite materials are woven, braided, weft-knit and non-crimp (Figure 1.1).

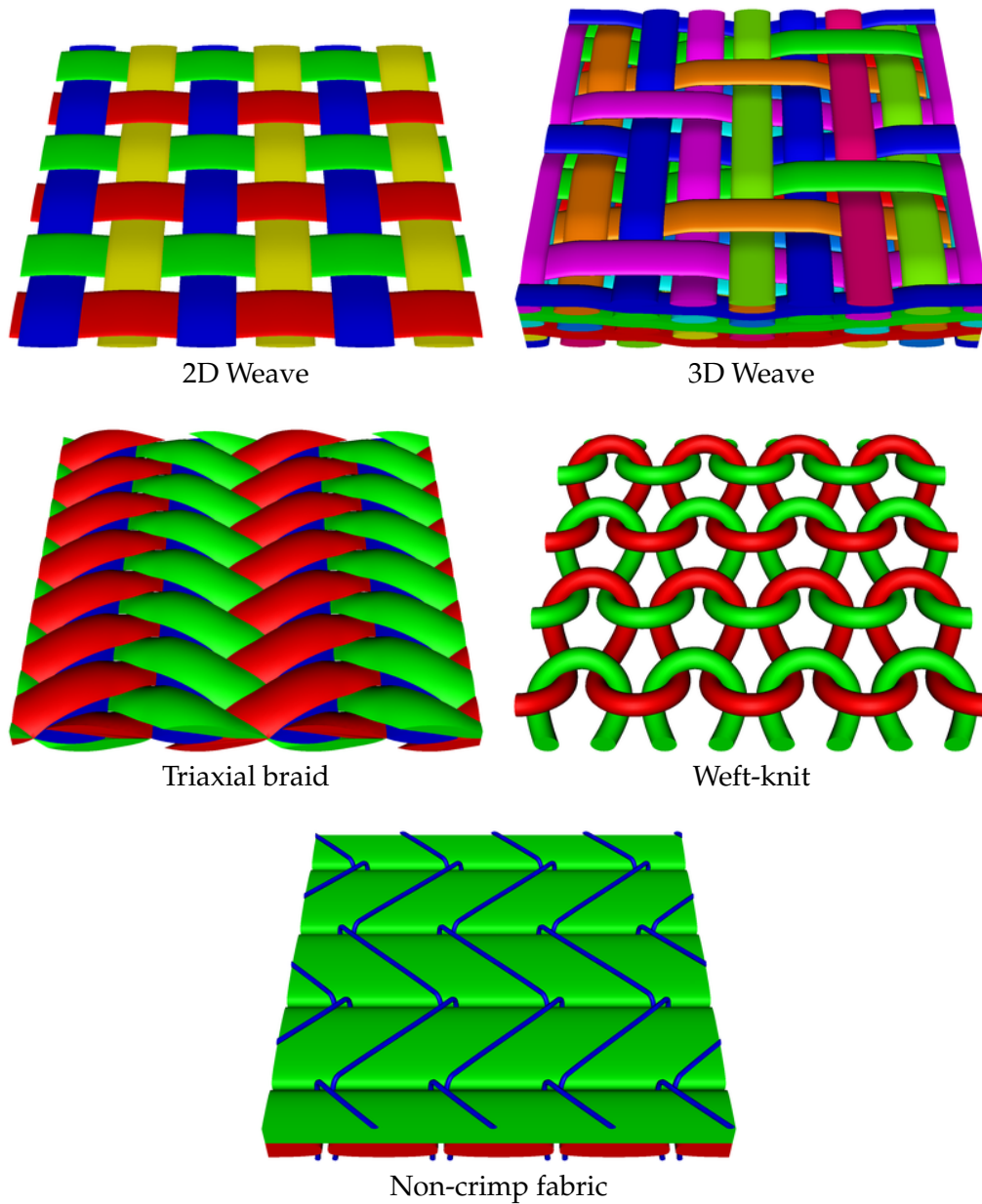


**Figure 1.1:** Images of textile architectures (generated by TexGen; see Chapter 2)

Woven fabrics consist of usually two orthogonal series of yarns, referred to as warp and weft yarns, interlaced to form a self-supporting textile structure. There are a number of possible interlacing patterns, the simplest of which is the plain weave where each warp yarn interlaces with each weft yarn. More complex interlacing patterns can be categorised as twill, satin, crowfoot, rib, basket, herringbone, crepe, etc. Multilayer

woven fabrics, also known as 3D weaves, are composed of several layers of warp and weft yarns woven together. The number of possible interlacing patterns is virtually infinite, however they are broadly categorised as orthogonal, through-thickness angle interlock and angle interlock (also known as layer-to-layer).

Braided fabrics are created by interweaving three or more yarns in a diagonally overlapping pattern. Two types of braided fabrics are widely available, biaxial braids and triaxial braids. The former contains two sets of aligned yarns whereas the latter contains three sets of aligned yarns. Similarly to woven fabrics, multilayered braided fabrics are also possible and are referred to as 3D braided fabrics.

Weft-knitted fabrics consist of only one set of weft yarns. Here the yarns are interlaced with adjacent yarns to construct a self-supporting structure. The different interlacing patterns can be categorised as jersey, rib, interlock, lacoste, pique, etc.

Non-crimp fabrics (NCF) consist of several layers of unidirectional straight yarns that are held together by stitching or knitting of a lightweight thread. Chemical agents may also be used to bond the yarns together. The term warp-knitted refers to the method of stitching the reinforcement yarns together, and resulting reinforcements are often also referred to as 'multiaxial warp-knits'.

Modelling the geometry of textiles is important because a geometric model is necessary as an input to many computational models:

- Modelling the mechanical properties of fabrics for determining forming behaviour, clothing comfort, etc.
- Predicting the permeability of fabrics for processing of composites.
- Modelling the mechanical properties of composite parts and their damage behaviour for use in engineering applications.

In this thesis a generic geometrical modelling approach is presented which encapsulates all of the above mentioned fabrics. Attempts at developing generic methods to predict mechanical properties applicable to all these fabrics have also been made. However, validating the methods for all types of fabrics would be too time consuming, hence validation is limited to a series of 2D woven fabrics.

### 1.3 Thesis overview

Chapter 2 describes the algorithms developed to model the geometry of textile structures which form the basis of the TexGen software. The models represent the smallest

repeatable unit cell of fabric at the mesoscopic scale. Yarns are represented as solid volumes encompassing the fibres from which they are composed. There are many applications for these types of models, one of which is explored in Chapter 5.

Chapter 3 presents a series of four geometrical models created using TexGen. Two of these are textile composite reinforcement fabrics provided by Chomarat and the other two are clothing fabrics provided by Unilever. The geometries of the fabrics are characterised using various experimental methods including optical microscopy, scanning electron microscopy, microtomography and Kawabata Evaluation System for fabrics (KES-f). These models form the basis of the work set out in Chapter 5.

Chapter 4 discusses a novel numerical approach for predicting the compaction behaviour of tows and the shear behaviour low filament count woven fabrics. The approach consists of modelling the bending of individual fibres within a tow following the Euler-Bernoulli beam equations. The results for compaction are validated against experimental compaction tests from the literature on E-glass tows. The results for shear of the polyester fabric are validated against KES-f data obtained from the University of Manchester.

Chapter 5 contains a study on the use of finite element analysis to predict mechanical properties of dry textiles. This is accomplished using the geometrical models presented in Chapter 3 with the tow mechanical properties discussed in Chapter 4, simulated by an explicit FE code developed by the author. The results are validated for shear, axial loading and compaction, against KES-f results and other experimental data obtained at larger deformations.

Chapter 6 contains the overall discussion and conclusions of the work and recommendations for further work.

# Geometric modelling of textiles

## 2.1 Introduction

TexGen is a software package written by the author for the purpose of modelling the 3D geometry of textiles at the level of the unit cell [119]. TexGen is designed to be flexible and multi-functional aiming to be able to accurately model as many types of textiles as possible (e.g. woven, knitted, knotted, non-woven, etc...) with as many techniques as possible (e.g. finite element method, finite difference method, finite volume method, multigrid method, visualisation) for applications such as solid mechanics, fluid dynamics, thermodynamics and electromagnetism. The functionality within TexGen goes far beyond its usage in this thesis. In this chapter the modelling strategy will be developed with little reference to specific fabrics. In Chapter 3 TexGen will be used to model specific fabrics.

Textiles are built up from a number of yarns brought together to form a self supporting structure. The textile unit cell modelled by TexGen is described as being the smallest unit of textile that, when tiled, will recreate the full scale textile. The width of a unit cell will typically range from several millimetres to several centimetres. The fibres within a yarn are not modelled individually, instead yarns are represented as solid volumes representing the approximate bounds of the fibres contained within them. There are several reasons for this, first of all it is much easier to represent the yarn as a solid volume and secondly this kind of representation is much more useful for computational analysis of textile properties (primarily due to processor speed and memory limitations). Cybulska et al. [27] have accurately modelled yarns including their fibres, however the model was used for visualisation only. TexGen models the textile in its final state whilst the manufacturing process to obtain this final state is not modelled. Using this methodology two things are needed to model a yarn: the first is the path of the yarn

through the textile and the second is the cross-section shape, which is not necessarily constant.

## 2.2 Literature survey

### 2.2.1 Yarn path and cross-section models

Peirce [95] made an early attempt at describing the yarn path of a plain woven fabric by a combination of straight lines and circular arcs. The yarn cross-section is assumed to be circular and the yarn path followed a circular arc at crossovers where the radius of curvature is equal to the diameter of the yarn. Thus the yarns are perfectly in contact at crossovers and the yarn path in between crossovers is described by a straight line. A limitation of this model is that the bending rigidity of the yarn is completely ignored. Peirce later considered a model where the yarn is modelled as an elastica and point contact occurs at the crossover between yarns. He also considered using an elliptical yarn cross-section to more accurately represent yarn flattening induced during the weaving process which improved the accuracy of the geometrical model.

Kemp [60] proposed a racetrack section as an alternative to the elliptical section to represent yarn flattening. This section consists of a rectangle with two circular arcs attached on either side. The advantage of this section over the elliptical section is that it is easier to calculate the yarn path such that contact is maintained at crossovers. However this geometry does not represent the true flattened yarn shape very well in most cases.

Hearle and Shanahan [50] proposed a lenticular cross-sectional geometry which represents the geometry of a yarn more accurately. This is represented as the intersection of two circles of equal radii offset by a given distance. Note that a circular geometry is a special case of the lenticular geometry where the offset between the two circles is zero. For many woven fabrics this geometry provides a very good fit to the true yarn geometry.

Searles et al. [115] proposed a more general approach by defining the yarn cross-section shape using splines. Micrographs of an 8 harness woven fabric were obtained and after image processing splines were fit to the yarns. More specifically two natural cubic splines were used to represent the upper and lower halves of the yarn. Two splines were used instead of one supposedly to break first order continuity at the edges of the yarns, which was found to provide a better fit. Although this approach is more general than the idealised shapes and capable of representing real yarn geometry more accu-

rately it also requires a much larger number of parameters to define it only obtainable by image analysis.

Adanur and Liao [1] define a fabric geometrical model using the so-called CAGD (computer aided geometric design) technique. The technique is similar to that described in this chapter. A series of different geometric fabric models were created including woven, braided and knitted fabrics. However all of the geometric models contained a constant elliptical cross-sectional shape. These restrictions are removed in the current work.

Hofstee and van Keulen [54] describe a yarn cross-sectional geometry which varies along the length of the yarn. The cross-section is defined by yarn width and height, in addition to the midplane height and yarn height which are given as a function of position across the width of the yarn. Thus the upper and lower cross-sectional edges of the yarn are essentially each defined by an equation of the form  $y(x)$  where  $y$  is the through-thickness axis and  $x$  is the axis perpendicular to both  $y$  and the yarn direction. This method of defining the yarn cross-section is not suitable for cases where the yarn direction deviates significantly from the fabric midplane. The position of individual fibres within a yarn is related to the yarn cross-section definition. Geometrical models were created for a plain woven fabric in different states including undeformed, stretched and sheared.

Wang and Sun [138] have developed a novel numerical method to predict fabric geometry using so-called digital elements. The technique essentially consists of representing yarns as a series of truss or rod elements along the centreline of the yarn. In order to create a very fast method to predict geometry a large number of simplifications are made. Bending rigidity of the yarns is neglected and as such the model only works well when tension is applied to the yarns. To prevent intersections between the yarns a minimum distance between their nodes is enforced. For this contact algorithm to be valid the length of the truss elements must be much smaller than the radius of the yarn. Using such a simple contact algorithm implies that the yarn cross-section is circular. In order to address this issue Zhou et al. [143] extended the method by representing each yarn by multiple chains of truss elements. In theory each chain represents an individual fibre, however in practise the number of fibres in a yarn is too great to simulate using this technique. Sihn et al. [122] developed algorithms to create a bounding volume encompassing the chains in order to represent the yarns as solid continuum elements for use in finite element analysis. The merits of this technique are that it is completely general and could be used to represent any type of fabric. However the accuracy of the model has not been verified and it is questionable as to whether 19-50 chains is suffi-

cient to represent a yarn with several hundreds or thousands of fibres as claimed by the authors. If the model is found to be inaccurate there is little flexibility in adjusting parameters to provide a closer fit to experimental results.

## 2.2.2 Textile geometrical modelling software

In this section a brief review of the software packages used to model the geometry of textile fabrics is described.

### TexGen

TexGen originates from the work of Robitaille et al. [104, 105, 106, 107]. The authors identified a need for generating unit cell geometric models to be used for prediction of fabric permeability and composite mechanical properties. The requirements were to represent all types of textile reinforcements in the same way without imposing limitations on the methods used for subsequent property prediction. In this way, the prediction of properties should be entirely distinct from the geometric modelling. This was achieved by specifying yarn paths with a series of vectors representing the centrelines of the yarns. Vectors provide a relatively easy way to describe arbitrary yarn paths capable of representing any interlacing pattern. The actual yarn centreline was smoothed to provide a curve with first order continuity, accomplished by joining the vector end points with circular arcs. The surface of the yarn was then defined by sweeping a simple two dimensional shape such as an ellipse or lenticular cross-section along the length of the yarn. The implementation of these concepts was performed by Souter [104] and resulted in TexGen version 1.

The present author re-implemented these concepts starting in 2003 as a learning exercise which resulted in TexGen version 2 [117, 119]. After considerable development and feature additions, the geometrical models produced by this software were used as the basis for numerous publications [8, 24, 56, 81, 82, 108, 114, 120, 140].

Although TexGen version 2 is feature rich and bug free to the extent that it has been tested, the code became difficult to maintain due to a lack of a clear design. Hence the code was re-written resulting in TexGen version 3 [118]. In this new version the concept of vectors defining the yarn path has been revised. To avoid retention of redundant information, the yarn path is defined by a series of control points (see Section 2.3). The smoothing of the yarn path by circular arcs has been removed due to inability to satisfactorily deal with arbitrary control points and instead has been replaced with Bezier and Cubic interpolations. TexGen v3 is a direct implementation of the geomet-

rical modelling concepts described in this chapter.

### **WiseTex**

Lomov and Verpoest [75–79, 137] have developed a software package named WiseTex capable of modelling the geometry of 2D and 3D woven fabrics, UD preforms, 2D braids with and without inlays and multi-axial multi-ply warp-knit stitched preforms. The geometry is calculated based on various analytical models incorporating physical properties of the yarns. Fibre, yarn and fabric properties can all be defined in WiseTex including fibre diameter, density, coefficient of friction, Young’s modulus, Poisson’s ratio, yarn width, yarn height, yarn shape, yarn spacing, fabric thickness, etc. In addition to geometry calculation, various analytical models involving these physical properties have been implemented to calculate tensile, shear and compressional behaviour of the fabrics.

Several software packages that interact with WiseTex have also been developed. LamTex is used for modelling laminated textile composites. FETex is used to export geometry from WiseTex to ANSYS in the form of a script file. The model can then be used to perform any type finite element analysis. MeshTex is used for creating meshes from WiseTex geometrical models and analysed with SACOM FE package [142]. TexComp is used to predict stiffness properties of a textile composite using analytical methods. FlowTex and Celper are used for textile permeability calculations and VRTex is used for visualising WiseTex geometry in VRML format.

The main advantages of TexGen over WiseTex are:

- Less restrictions are placed on the geometry of the fabrics that can be modelled. Yarn paths can be created arbitrarily and variable cross-sections can be assigned to the yarn in a number of different ways.
- The software is free and open source licensed under the GNU General Public License (GPL).
- The software is cross platform, tested on Windows and Linux.
- A powerful Python scripting interface has been implemented.
- It is possible to export geometry directly to IGES and STEP file formats.

Conversely the main advantages of WiseTex over TexGen are:

- Geometry calculation is based on physical properties of fabrics using analytical models.



- Graphical user interface for creating a wider range of different fabric types.
- Built-in analytical models for fabric mechanics predictions.
- Built-in analytical models for composite material stiffness predictions.
- Ability to model gaps created through tows during stitching.

### **TechText CAD**

TexEng Software Ltd have developed two products named TechText CAD and Weave Engineer [48, 49]. TechText CAD is software aimed at transferring academic work on the structural mechanics of textiles into a CAD package that is easy to use and directed at industrial needs. It is able to model geometry of fabrics similarly to TexGen and WiseTex, however it is limited to 2D woven fabrics and weft knitted fabrics at the time of writing. Similarly to WiseTex the yarn paths are calculated based on analytical models, and the software has the ability to predict fabric mechanical properties for woven fabrics based on an energy method using yarn mechanical properties [110, 111]. TechText CAD also contains many basic features such as conversion tool for converting between units and databases for storing fibre, yarn and fabric data. However the software appears to be at an earlier stage of development compared to TexGen and WiseTex.

The Weave Engineer software is dedicated to the design and manufacture of advanced textile structures. It does not contain any features for predicting mechanical properties of fabrics, however it can be used to design 3D woven textile structures, with both solid and hollow architectures and non-crimp composite reinforcement.

### **ScotWeave**

ScotCad Textiles Ltd have been providing CAD software for weaving since 1982 aimed primarily at industrial users. Most of the products work together to model woven fabrics at the macroscopic scale where yarns can be given various colours to create sophisticated visual effects for use in furniture, car interiors, etc. These products contain a number of features valuable to weave designers but of limited use to researchers: yarn costing data, scanning feature, image edit tools, library of over 700 weaves, float checking, auto-drape, fabric finishing, import/export weave data, output instructions directly to the looms, etc.

A relatively new product named the ScotWeave Technical Weaver is aimed specifically at modelling technical textiles at the mesoscopic scale and bears more similarity with

the other software packages presented above than ScotCad's other products. Yarn cross-sectional shape and weave pattern can be specified to create a 3D geometrical model. As of the time of writing it does not contain any algorithms for calculating mechanical properties and is limited to modelling orthogonal woven fabrics.

### 2.3 Yarn path representation

The path of a yarn can be considered as a one dimensional line representing the yarn's centreline in three dimensional space. Thus the yarn path can be defined as position in 3D space as a function of distance along the yarn. Since TexGen aims at modelling the geometry at the level of the unit cell, the yarn is assumed to be repeatable and only modelled at its smallest repeatable length. The same approach is taken in WiseTex and TechText CAD. The most flexible and generic way to describe such a yarn path is to specify a number of discrete positions along the yarn length, known as master nodes, and interpolate [62, 113] between these points. Generally, to obtain an accurate yarn path for woven fabrics it is sufficient to specify one or two master nodes per crossover (see Chapter 3) as long as the interpolation function is suitable.

The interpolation function must have at least continuity  $C^1$ , that is to say that there are no gaps in the yarn path and the yarn path's tangent varies smoothly. A common solution to this problem is the use of splines [2, 6]. A spline is a function defined piecewise by polynomials. In interpolation problems, spline interpolation is often preferred to polynomial interpolation because it yields similar results, even when using low degree polynomials, while avoiding Runge's phenomenon [113] for higher degrees.

In its most general form a polynomial spline  $\mathbf{S} : [a, b] \rightarrow \mathbb{R}$  consists of polynomial pieces  $\mathbf{S}_i : [t_i, t_{i+1}] \rightarrow \mathbb{R}$ , where

$$a = t_0 < t_1 < \dots < t_{k-2} < t_{k-1} = b \quad (2.1)$$

That is,

$$\mathbf{S}(t) = \begin{cases} \mathbf{S}_0(t) & \text{if } t_0 \leq t < t_1 \\ \mathbf{S}_1(t) & \text{if } t_1 \leq t < t_2 \\ \vdots & \\ \mathbf{S}_{k-2}(t) & \text{if } t_{k-2} \leq t \leq t_{k-1} \end{cases} \quad (2.2)$$

The given  $k$  values  $t_i$  are called knots. Several types of splines have been explored: cubic Bézier splines, natural cubic splines and periodic cubic splines. As their names suggest they are all polynomials of degree 3; the latter two have continuity  $C^2$  while

the first generally does not. In Chapter 3 the most appropriate type of spline will be explored for a variety of textiles.

### 2.3.1 Cubic Bézier splines

In this case, a spline is formed from cubic Bézier curves which are themselves defined by four points  $\mathbf{P}_1$ ,  $\mathbf{P}_2$ ,  $\mathbf{P}_3$  and  $\mathbf{P}_4$  in 3D space. The curve starts at  $\mathbf{P}_1$  going toward  $\mathbf{P}_2$  and arrives at  $\mathbf{P}_4$  coming from the direction of  $\mathbf{P}_3$ . The tangent of the curve at  $\mathbf{P}_1$  is parallel to the vector from  $\mathbf{P}_1$  to  $\mathbf{P}_2$ , similarly the tangent of the curve at  $\mathbf{P}_4$  is parallel to the vector from  $\mathbf{P}_3$  to  $\mathbf{P}_4$ . The distance between  $\mathbf{P}_1$  and  $\mathbf{P}_2$  determines how far the curve moves into direction  $\mathbf{P}_3$  before turning toward  $\mathbf{P}_4$ . The parametric equation for a single Bézier curve  $\mathbf{B}$  is defined as:

$$\mathbf{B}(t) = \mathbf{P}_1(1-t)^3 + 3\mathbf{P}_2t(1-t)^2 + 3\mathbf{P}_3t^2(1-t) + \mathbf{P}_4t^3 \quad 0 \leq t \leq 1 \quad (2.3)$$

A typical Bézier curve is shown in Figure 2.1.

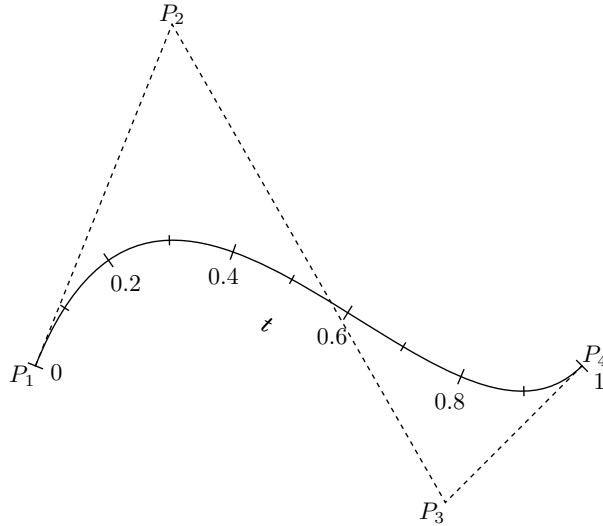


Figure 2.1: Cubic Bézier curve

In order to preserve continuity  $C^0$ , points  $\mathbf{P}_{1i}$  and  $\mathbf{P}_{4i}$  are defined for spline piece  $\mathbf{S}_i$  as follows:

$$\mathbf{P}_{1i} = \mathbf{S}_i(t_i) \quad 0 \leq i \leq k-2 \quad (2.4)$$

$$\mathbf{P}_{4i} = \mathbf{S}_i(t_{i+1}) \quad 0 \leq i \leq k-2 \quad (2.5)$$

There is some flexibility on how points  $\mathbf{P}_{2i}$  and  $\mathbf{P}_{3i}$  are chosen. In order to preserve continuity  $C^1$  one must ensure that the tangents between spline pieces match up. That is:

$$\mathbf{S}'_i(t_{i+1}) = \mathbf{S}'_{i+1}(t_{i+1}) \quad 0 \leq i \leq k-3 \quad (2.6)$$

What this means in practice is that the points  $\mathbf{P}_{3i}$ ,  $\mathbf{P}_{4i}$ ,  $\mathbf{P}_{1i+1}$  and  $\mathbf{P}_{2i+1}$  must be collinear (Note:  $\mathbf{P}_{4i} = \mathbf{P}_{1i+1}$ ). However, the distance between the points and their orientation is not prescribed. This means that the cubic Bézier spline is not fully defined simply by its knots, and in order to fill in the missing parameters the following assumptions are made:

$$\frac{\mathbf{S}'(t_i)}{\|\mathbf{S}'(t_i)\|} = \frac{\mathbf{S}(t_{i+1}) - \mathbf{S}(t_{i-1})}{\|\mathbf{S}(t_{i+1}) - \mathbf{S}(t_{i-1})\|} \quad 1 \leq i \leq k-2 \quad (2.7)$$

$$\|\mathbf{P}_{2i} - \mathbf{P}_{1i}\| = \|\mathbf{P}_{4i} - \mathbf{P}_{3i}\| = \frac{\|\mathbf{P}_{4i} - \mathbf{P}_{1i}\|}{3} \quad (2.8)$$

The tangents at  $t = a$  and  $t = b$  are still not defined. There are two possibilities here. If the yarn is periodic, which it will be in most cases, the additional assumptions can be made:

$$\frac{\mathbf{S}'(a)}{\|\mathbf{S}'(a)\|} = \frac{\mathbf{S}'(b)}{\|\mathbf{S}'(b)\|} = \frac{\mathbf{S}(t_1) - \mathbf{S}(t_0) + \mathbf{S}(t_{k-1}) - \mathbf{S}(t_{k-2})}{\|\mathbf{S}(t_1) - \mathbf{S}(t_0) + \mathbf{S}(t_{k-1}) - \mathbf{S}(t_{k-2})\|} \quad (2.9)$$

otherwise if the yarn is not periodic the following assumptions are made:

$$\frac{\mathbf{S}'(a)}{\|\mathbf{S}'(a)\|} = \frac{\mathbf{S}(t_1) - \mathbf{S}(t_0)}{\|\mathbf{S}(t_1) - \mathbf{S}(t_0)\|} \quad (2.10)$$

$$\frac{\mathbf{S}'(b)}{\|\mathbf{S}'(b)\|} = \frac{\mathbf{S}(t_{k-1}) - \mathbf{S}(t_{k-2})}{\|\mathbf{S}(t_{k-1}) - \mathbf{S}(t_{k-2})\|} \quad (2.11)$$

These assumptions provide a curve of smooth appearance which will be adequate in most cases. However for cases where it is not adequate these parameters may be changed to suit the particular needs of the yarn being modelled. For example it may be desirable to specify a certain tangent at a given knot.

### 2.3.2 Natural cubic splines

In this case no extra points need to be defined in order to specify the yarn path. The same continuity conditions  $C^0$  and  $C^1$  apply as for the Bézier curves:

$$\mathbf{S}_i(t_{i+1}) = \mathbf{S}_{i+1}(t_{i+1}) \quad 0 \leq i \leq k-3 \quad (2.12)$$

$$\mathbf{S}'_i(t_{i+1}) = \mathbf{S}'_{i+1}(t_{i+1}) \quad 0 \leq i \leq k-3 \quad (2.13)$$

In addition, a further continuity condition  $C^2$  applies

$$\mathbf{S}''_i(t_{i+1}) = \mathbf{S}''_{i+1}(t_{i+1}) \quad 0 \leq i \leq k-3 \quad (2.14)$$

The boundary conditions at  $t = a$  and  $t = b$  are as follows:

$$\mathbf{S}''(a) = \mathbf{S}''(b) = 0 \quad (2.15)$$

The derivatives of the spline at the knots can be calculated by solving the following tridiagonal system of equations:

$$\begin{bmatrix} 2 & 1 & & & & \\ 1 & 4 & 1 & & & \\ & 1 & 4 & 1 & & \\ & & \ddots & \ddots & \ddots & \\ & & & 1 & 4 & 1 \\ & & & & 1 & 4 & 1 \\ & & & & & 1 & 2 \end{bmatrix} \begin{bmatrix} \mathbf{S}'(t_0) \\ \mathbf{S}'(t_1) \\ \mathbf{S}'(t_2) \\ \vdots \\ \mathbf{S}'(t_{k-3}) \\ \mathbf{S}'(t_{k-2}) \\ \mathbf{S}'(t_{k-1}) \end{bmatrix} = \begin{bmatrix} 3(\mathbf{S}(t_1) - \mathbf{S}(t_0)) \\ 3(\mathbf{S}(t_2) - \mathbf{S}(t_0)) \\ 3(\mathbf{S}(t_3) - \mathbf{S}(t_1)) \\ \vdots \\ 3(\mathbf{S}(t_{k-2}) - \mathbf{S}(t_{k-4})) \\ 3(\mathbf{S}(t_{k-1}) - \mathbf{S}(t_{k-3})) \\ 3(\mathbf{S}(t_{k-1}) - \mathbf{S}(t_{k-2})) \end{bmatrix} \quad (2.16)$$

Once the derivatives are known, the coefficients of the spline pieces can easily be determined. For each cubic spline piece there are 4 equations with 4 unknown coefficients  $a_i$ ,  $b_i$ ,  $c_i$  and  $d_i$ :

$$\mathbf{S}_i(t_i) = a_i + b_i t_i + c_i t_i^2 + d_i t_i^3 \quad (2.17)$$

$$\mathbf{S}_i(t_{i+1}) = a_i + b_i t_{i+1} + c_i t_{i+1}^2 + d_i t_{i+1}^3 \quad (2.18)$$

$$\mathbf{S}'_i(t_i) = b_i + 2c_i t_i + 3d_i t_i^2 \quad (2.19)$$

$$\mathbf{S}'_i(t_{i+1}) = b_i + 2c_i t_{i+1} + 3d_i t_{i+1}^2 \quad (2.20)$$

The natural cubic spline has a very important variational interpretation as it is the function that minimizes the following function:

$$J(\mathbf{S}) = \int_a^b \|\mathbf{S}''(t)\|^2 dt \quad (2.21)$$

The function  $J$  contains an approximation of the total curvature of  $\mathbf{S}(t)$ . The natural cubic spline is thus an approximation of the spline with minimal curvature. Since the total energy of an elastic strip is proportional to the curvature, the spline is the approximate configuration of minimal energy of an elastic strip constrained to  $k$  points.

### 2.3.3 Periodic cubic splines

This type of spline is similar to the natural cubic spline but with different boundary conditions. Equation 2.15 is replaced by the following periodic boundary conditions:

$$\mathbf{S}'(a) = \mathbf{S}'(b) \quad (2.22)$$

$$\mathbf{S}''(a) = \mathbf{S}''(b) \quad (2.23)$$

The system of Equations 2.16 becomes:

$$\begin{bmatrix} 4 & 1 & & & & & & 1 \\ 1 & 4 & 1 & & & & & \\ & 1 & 4 & 1 & & & & \\ & & & \ddots & \ddots & \ddots & & \\ & & & & & 1 & 4 & 1 \\ 1 & & & & & 1 & 4 & \end{bmatrix} \begin{bmatrix} \mathbf{S}'(t_0) \\ \mathbf{S}'(t_1) \\ \mathbf{S}'(t_2) \\ \vdots \\ \mathbf{S}'(t_{k-3}) \\ \mathbf{S}'(t_{k-2}) \end{bmatrix} = \begin{bmatrix} 3(\mathbf{S}(t_1) - \mathbf{S}(t_0) + \mathbf{S}(t_{k-1}) - \mathbf{S}(t_{k-2})) \\ 3(\mathbf{S}(t_2) - \mathbf{S}(t_0)) \\ 3(\mathbf{S}(t_3) - \mathbf{S}(t_1)) \\ \vdots \\ 3(\mathbf{S}(t_{k-2}) - \mathbf{S}(t_{k-4})) \\ 3(\mathbf{S}(t_{k-1}) - \mathbf{S}(t_{k-3})) \end{bmatrix} \tag{2.24}$$

Note that the number of equations in this system is one less than for the natural cubic spline, as here  $\mathbf{S}'(t_{k-1})$  is equal to  $\mathbf{S}'(t_0)$ . This type of spline is very useful for modelling yarn paths of a unit cell. Since the path is only a small section of the full yarn, it needs to be periodic. This type of spline ensures continuity  $C^2$  across repeated unit cells (see Section 2.6).

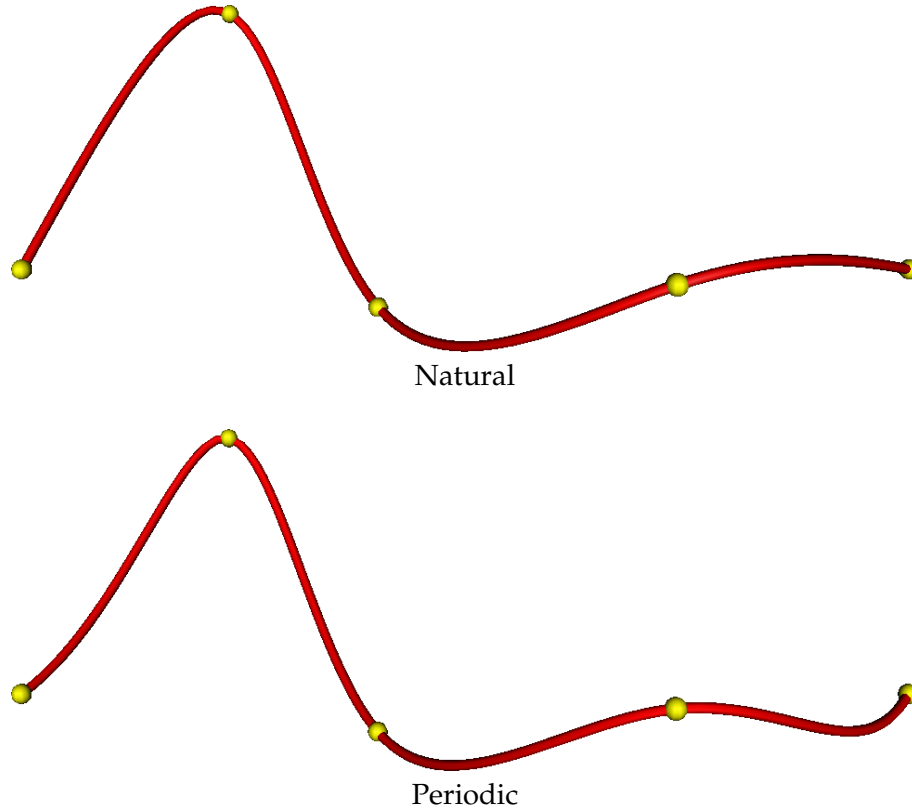


**Figure 2.2:** Natural and periodic cubic splines

A comparison between a natural cubic spline and a periodic cubic spline with the same knots is shown in Figure 2.2.

## 2.4 Yarn cross-section

The cross-section is defined as the 2D shape of the yarn when cut by a plane perpendicular to the yarn path tangent. Since yarns are treated as solid volumes the cross-section is approximated to be the smallest region that encompasses all of the fibres within the yarn (it will generally be convex). The outline of the cross-sections can be defined using parametric equations in 2 dimensions. Various shapes have been explored including the ellipse proposed by Peirce [95], power ellipse [140] and a modified lenticular shape proposed by Hearle and Shanahan [50]. The accuracy of these cross-sections for real textiles will be explored in Chapter 3.

### 2.4.1 Ellipse

The elliptical cross-section is one of the simplest approximations, with given width  $w$  and height  $h$  the equation is defined as follows:

$$\mathbf{C}(t)_x = \frac{w}{2} \cos(2\pi t) \quad 0 \leq t \leq 1 \quad (2.25)$$

$$\mathbf{C}(t)_y = \frac{h}{2} \sin(2\pi t) \quad 0 \leq t \leq 1 \quad (2.26)$$

### 2.4.2 Power ellipse

The power ellipse is a slight modification to the elliptical cross-section where the  $y$  coordinate is assigned a power  $n$  to make the section resemble a rectangle with rounded edges when  $n < 1$  or a shape similar to a lenticular cross-section when  $n > 1$  [140]. However, it is in fact a specialisation of the Superellipse discovered by Gabriel Lamé [38]. It is defined as follows:

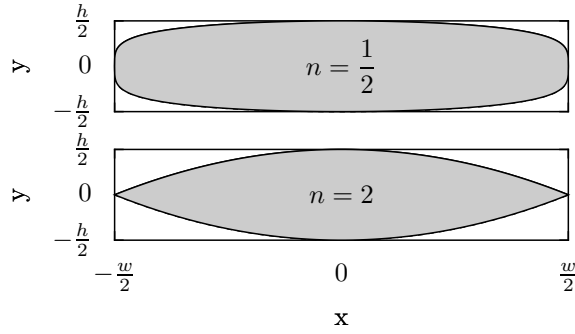
$$\mathbf{C}(t)_x = \frac{w}{2} \cos(2\pi t) \quad 0 \leq t \leq 1 \quad (2.27)$$

$$\mathbf{C}(t)_y = \begin{cases} \frac{h}{2} (\sin(2\pi t))^n & \text{if } 0 \leq t \leq 0.5 \\ -\frac{h}{2} (-\sin(2\pi t))^n & \text{if } 0.5 \leq t \leq 1 \end{cases} \quad (2.28)$$

Two typical power elliptical cross-section are shown in Figure 2.3.

### 2.4.3 Lenticular

The lenticular cross-section is the intersection of two circles of radii  $r_1$  and  $r_2$  each offset vertically by distances  $o_1$  and  $o_2$  respectively. The parameters  $r_1$ ,  $r_2$ ,  $o_1$  and  $o_2$  can be


**Figure 2.3:** Power elliptical cross-sections

calculated from the desired width  $w$ , height  $h$  and distortion distance  $d$  of the lenticular section:

$$r_1 = \frac{w^2 + (h - 2d)^2}{4(h - 2d)} \quad (2.29)$$

$$r_2 = \frac{w^2 + (h + 2d)^2}{4(h + 2d)} \quad (2.30)$$

$$o_1 = -r_1 + \frac{h}{2} \quad (2.31)$$

$$o_2 = r_2 - \frac{h}{2} \quad (2.32)$$

The section is defined as follows:

$$\mathbf{C}(t)_x = \begin{cases} r_1 \sin \theta & \text{if } 0 \leq t \leq 0.5 \\ r_2 \sin \theta & \text{if } 0.5 \leq t \leq 1 \end{cases} \quad (2.33)$$

$$\mathbf{C}(t)_y = \begin{cases} r_1 \cos \theta + o_1 & \text{if } 0 \leq t \leq 0.5 \\ -r_2 \cos \theta + o_2 & \text{if } 0.5 \leq t \leq 1 \end{cases} \quad (2.34)$$

where:

$$\theta = \begin{cases} (1 - 4t) \sin^{-1} \left( \frac{w}{2r_1} \right) & \text{if } 0 \leq t \leq 0.5 \\ (-3 + 4t) \sin^{-1} \left( \frac{w}{2r_2} \right) & \text{if } 0.5 \leq t \leq 1 \end{cases} \quad (2.35)$$

Two typical lenticular cross-sections are shown in Figure 2.4. Note that if the distortion parameter is zero, the radii of the two circles are the same and the offsets are equal and opposite.



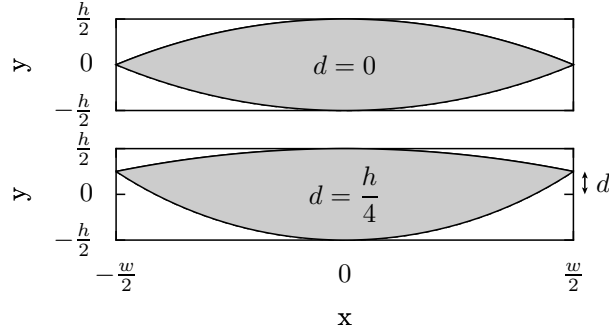


Figure 2.4: Lenticular cross-sections

## 2.5 Yarn surface

Having defined the yarn path and cross-section, the two need to be brought together. In general the cross-section may vary along the length of the yarn because the yarn is easily deformed even under very low loads. In a weaving process for example, the yarns will be compacted at crossover points. Thus the cross-section should be defined as a function of distance along the yarn. The boundaries of the yarn can be defined as a parametric surface  $\mathbf{P}(u, v)$  from yarn path  $\mathbf{S}$  and cross-section  $\mathbf{C}$ :

$$\mathbf{P}(u, v) = \mathbf{S}(u) + (\mathbf{C}(u, v)_x \vec{\mathbf{X}}'(u) + \mathbf{C}(u, v)_y \vec{\mathbf{Y}}'(u)) \quad a \leq u \leq b \quad 0 \leq v \leq 1 \quad (2.36)$$

where  $\vec{\mathbf{X}}'$  and  $\vec{\mathbf{Y}}'$  are the local coordinate axes of the yarn path defined as follows:

$$\vec{\mathbf{X}}'(u) = \frac{\mathbf{S}'(u) \times \vec{\mathbf{U}}}{\|\mathbf{S}'(u) \times \vec{\mathbf{U}}\|} \quad (2.37)$$

$$\vec{\mathbf{Y}}'(u) = \frac{\vec{\mathbf{X}}'(u) \times \mathbf{S}'(u)}{\|\vec{\mathbf{X}}'(u) \times \mathbf{S}'(u)\|} \quad (2.38)$$

where  $\vec{\mathbf{U}}$  is the so-called up vector which will be defined as  $(0, 0, 1)$  assuming the textile lies in the  $X/Y$  plane. This up vector is necessary to orient the cross-section in the plane perpendicular to the yarn path's tangent. The local  $\vec{\mathbf{Y}}'$  is obtained by projecting  $\vec{\mathbf{U}}$  to the plane defined by the normal  $\mathbf{S}'$  (Figure 2.5). Unfortunately this method of defining a constant up vector is flawed. When  $\mathbf{S}'$  is parallel to  $\vec{\mathbf{U}}$ , the term  $\|\mathbf{S}'(u) \times \vec{\mathbf{U}}\|$  in Equation 2.37 becomes zero, i.e. where the tangent of the yarn path is vertical the parametric surface cannot be evaluated. Whilst for most textiles this will not be an issue, some 3D woven fabrics may contain vertical yarns. The solution is to specify an alternate  $\vec{\mathbf{U}}$  vector for the offending yarns either as a constant vector or one which varies along the length of the yarn, ensuring  $\vec{\mathbf{U}}$  is never parallel with  $\mathbf{S}'$ .

In Equation 2.36 the cross-section  $\mathbf{C}$  is defined as a function of two variables  $u$  and  $v$  where  $u$  relates to the distance along the yarn and  $v$  relates to the position around the

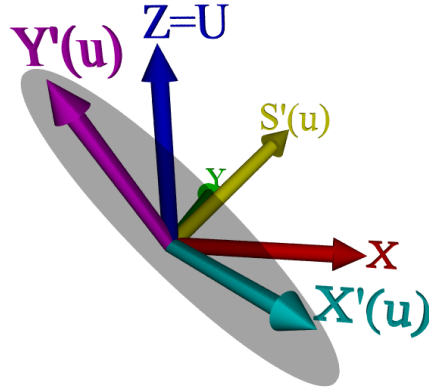


Figure 2.5: Illustration of how  $X'$  and  $Y'$  are calculated

cross-section. Several options have been considered for variation of the cross-section as a function of distance along the yarn. The most accurate and convenient methods for specific fabrics will be discussed in Chapter 3.

### 2.5.1 Constant cross-section

Here the cross-section is assumed constant along the length of the yarn. Models can be created very quickly with this method. In some cases this assumption may hold true, with the changes in shape so small that they are insignificant. These issues will be discussed in Chapter 3.

### 2.5.2 Interpolated cross-sections

In this case, cross-sections are specified at discrete positions along the length of the yarn. Cross-sections are then interpolated between these specified points. Suppose two cross-sections  $\mathbf{A}(t)$  and  $\mathbf{B}(t)$  are defined which are to be interpolated. The interpolated cross-section  $\mathbf{C}(t)$  is defined as:

$$\mathbf{C}(t, \mu) = \mathbf{A}(t) + (\mathbf{B}(t) - \mathbf{A}(t))\mu \quad 0 \leq t \leq 1 \quad 0 \leq \mu \leq 1 \quad (2.39)$$

where  $\mu$  varies from 0 to 1 linearly with distance between cross-sections  $\mathbf{A}(t)$  and  $\mathbf{B}(t)$ . This linear interpolation is the simplest approach to allow a smooth transition with continuity  $C^0$  between two different cross-sectional shapes. Note that it is necessary for the cross-sections  $\mathbf{A}(t)$  and  $\mathbf{B}(t)$  to be defined in a similar manner, i.e. points  $\mathbf{A}(t)$  and  $\mathbf{B}(t)$  should describe similar positions on the cross-section for all values of  $t$ . All the parametric equations described in Section 2.4 begin on the positive  $x$  axis at  $t = 0$  going counter-clockwise as  $t$  increases. Figure 2.6 displays the interpolation between

an elliptical cross-section shown in blue (width  $w$  and height  $h_e$ ) and a lenticular cross-section shown in red (width  $w$  and height  $h_l$ ). The heights of the two sections are different to better illustrate the interpolation.

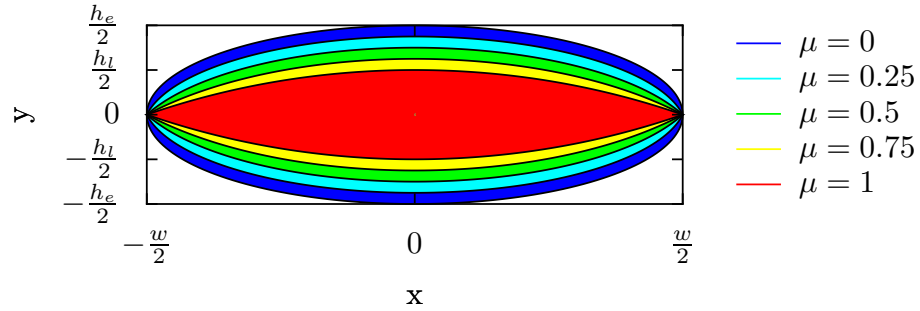


**Figure 2.6:** Interpolation between elliptical and lenticular cross-sections

The linear interpolation approach can be modified slightly in order to provide interpolation with continuity  $C^1$ . Instead of varying the interpolation parameter  $\mu$  linearly with distance  $x$ , it can be ramped with a cubic equation such that at  $x = 0$ :

$$\mu = 0 \quad (2.40)$$

$$\frac{d\mu}{dx} = 0 \quad (2.41)$$

and at  $x = d$ , where  $d$  is the distance between the nodes:

$$\mu = 1 \quad (2.42)$$

$$\frac{d\mu}{dx} = 0 \quad (2.43)$$

Which results in the following equation:

$$\mu = \frac{3x^2}{d^2} - \frac{2x^3}{d^3} \quad (2.44)$$

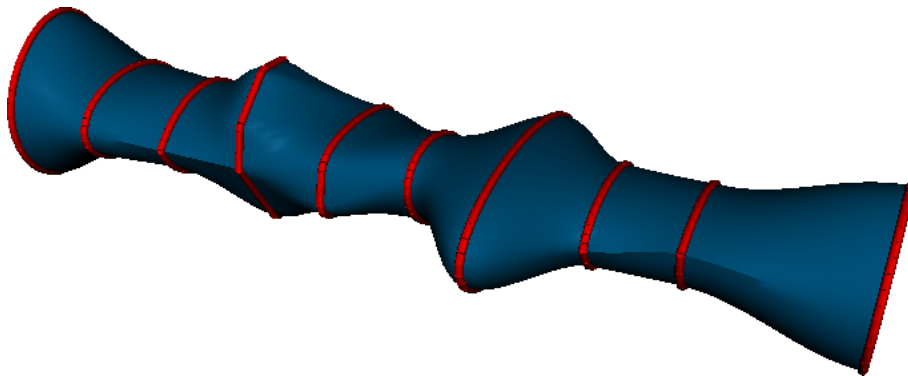


**Figure 2.7:** Cross-section interpolation

Figure 2.7 illustrates an imaginary straight yarn with a number of cross-sections assigned along the length to illustrate the interpolation.

## 2.6 Yarn repeats

Normally only the smallest repeatable section of a yarn is specified in TexGen in order to avoid duplication of data. It is thus necessary to specify how the yarn repeats itself and this is done with vectors. Generally each yarn section in a textile will have 2 repeat vectors but this is not always the case. The smallest repeatable length of a yarn  $\mathbf{P}$  is defined in Equation 2.36. The yarn for the entire textile can be described as follows given  $n$  repeat vectors  $\vec{\mathbf{R}}_i$ :

$$\mathbf{P} + C_0\vec{\mathbf{R}}_0 + C_1\vec{\mathbf{R}}_1 + \cdots + C_{n-1}\vec{\mathbf{R}}_{n-1} \quad -\infty \leq C_i \leq \infty \quad (2.45)$$

where the coefficients  $C_i \rightarrow \mathbb{Z}$  are integers. Figure 2.8 illustrates this with two repeat vectors. Note that the repeats apply to the yarns themselves rather than the unit cell. However, in most cases the repeat vectors for all the yarns will be identical.

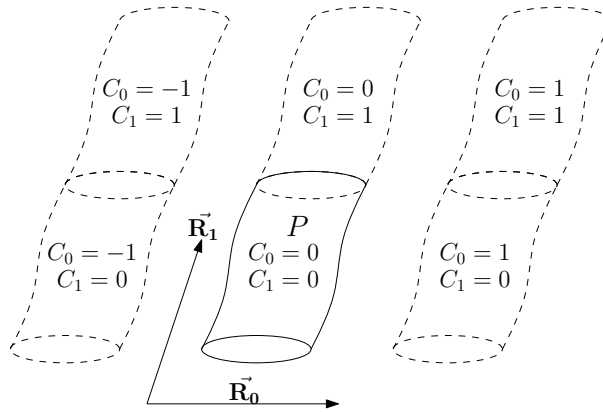


Figure 2.8: Yarn repeated with two repeat vectors

## 2.7 Domain

In TexGen only the smallest repeatable section of yarns is described, but combined with the repeat vectors the size of the textile is infinite. Thus for most applications it is necessary to restrict the model to a finite region of space called the domain. In most cases the domain will correspond to the unit cell of the textile but the distinction between the two is made for added flexibility. For example, it may be desirable to create a domain that encompasses two unit cells and compare FE results against a single unit cell to verify that periodic boundary conditions have been implemented correctly.

The domain is specified by planes where the space on the negative side of the plane is considered to be outside of the domain. Each plane is defined as:

$$Ax + By + Cz + D = 0 \quad (2.46)$$

The vector  $(A, B, C)$  represents the unit normal to the plane, and  $D$  represents the distance from the plane to the origin. In order to specify an axis aligned bounding box with minimum of  $(x_1, y_1, z_1)$  and maximum of  $(x_2, y_2, z_2)$ , six planes  $P$  need to be defined as shown in Table 2.1. Using this definition of planes, it is clear that a simple axis aligned bounding box is easily represented while leaving the flexibility to approximate any convex shape.

**Table 2.1:** Planes defining axis aligned bounding box domain

	A	B	C	D
$P_0$	1	0	0	$x_1$
$P_1$	-1	0	0	$-x_2$
$P_2$	0	1	0	$y_1$
$P_3$	0	-1	0	$-y_2$
$P_4$	0	0	1	$z_1$
$P_5$	0	0	-1	$-z_2$

## 2.8 Surface mesh

The easiest and most efficient way to render a three dimensional body is to represent its surface with polygons and then render the polygons. The work of actually rendering polygons to a two dimensional screen can be achieved using mature hardware accelerated graphics libraries such as OpenGL [9] or Direct3D [131]. Thus the only concern for rendering is to obtain a polygonal representation of the surface which will be referred to as a surface mesh. Aside from being used to render yarns, the surface mesh can be used for other numerical purposes such as calculating the volume (Appendix B), or for boundary element analysis.

In order to create a surface mesh, the parametric surface of the yarn defined in Equation 2.36 must be sampled (Figure 2.9). For convenience the limits  $a$  and  $b$  are defined as 0 and 1 respectively. Taking  $k$  and  $n$  samples at regular intervals of  $\frac{1}{k-1}$  and  $\frac{1}{n}$  respectively such that:

$$u_i = \frac{i}{k-1} \quad 0 \leq i \leq k-1 \quad (2.47)$$

$$v_j = \frac{j}{n} \quad 0 \leq j \leq n-1 \quad (2.48)$$

Since the point at  $v = 1$  is always the same as the point at  $v = 0$  it is not necessary to sample at  $v = 1$ . This is the reason the denominator of Equation 2.48 is  $n$  rather than  $n-1$ .

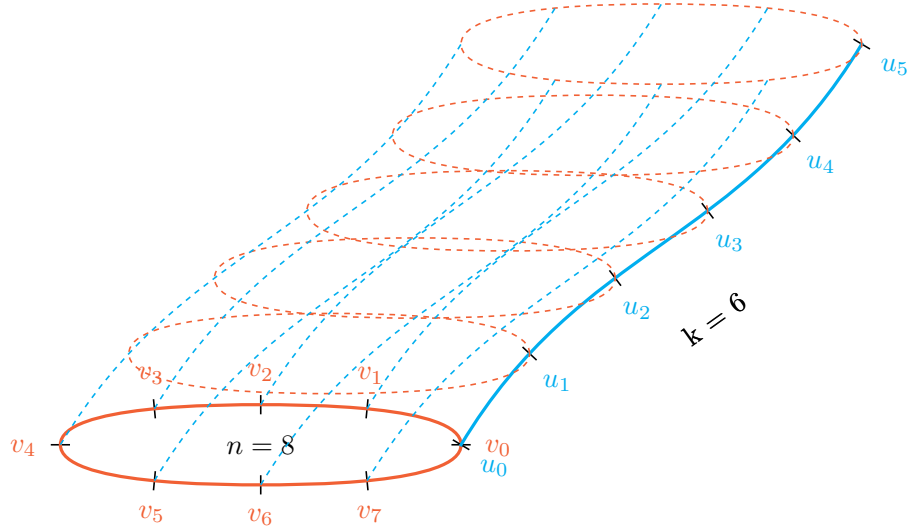


Figure 2.9: Sampled parametric surface

Quadrilateral elements with four corners  $\mathbf{Q}_i$  representing the surface can be created as follows:

$$\mathbf{Q}_1 = \mathbf{P}(u_i, v_j) \quad (2.49)$$

$$\mathbf{Q}_2 = \mathbf{P}(u_{i+1}, v_j) \quad (2.50)$$

$$\mathbf{Q}_3 = \mathbf{P}(u_{i+1}, v_{j+1}) \quad (2.51)$$

$$\mathbf{Q}_4 = \mathbf{P}(u_i, v_{j+1}) \quad (2.52)$$

The density of the mesh is controlled by the number of sample points  $k$  and  $n$ . Generally it is desirable for elements to have all edges of similar length. Thus it is only really necessary to have one parameter which controls the density of the mesh rather than two. The parameter  $k$  can be determined from  $n$  such that the elements are of high quality. In order to do this, the average element edge length  $\bar{L}$  is calculated from  $n$  with the following equation:

$$\bar{L} = \frac{1}{n} \int_0^1 \sum_{j=0}^{n-1} \|\mathbf{P}(u, v_{j+1}) - \mathbf{P}(u, v_j)\| du \quad (2.53)$$

The value of  $k$  can then be calculated from:

$$k = \left\lceil \frac{1}{\bar{L}} \int_0^1 \|\mathbf{S}'(t)\| dt \right\rceil + 1 \quad (2.54)$$

where the square brackets  $\lceil \cdot \rceil$  represent the nearest integer function [39].

## 2.9 Volume mesh

For finite element analysis, a surface mesh defining the boundaries of the volume is not sufficient. A volume mesh constructed from 3D continuum elements is necessary. Many volume meshing algorithms exist for completely arbitrary geometries as well as semi-arbitrary geometries. In the case of a yarn, the volume is relatively easy to mesh. The meshing can be separated into two steps. The first is to mesh the cross-sections in two dimensions ensuring that the cross-section meshes are compatible. It is then simply necessary to link adjacent cross-section meshes together to form 3D elements.

### 2.9.1 Cross-section meshing

A simple rectangular mesh generator has been implemented to create cross-section meshes in a regular grid. Figure 2.10 shows an elliptical cross-section meshed using this technique. Note that the four corners of the grid contain triangular elements rather than quadrilateral elements. This is to avoid having highly distorted elements which are undesirable in numerical simulations.

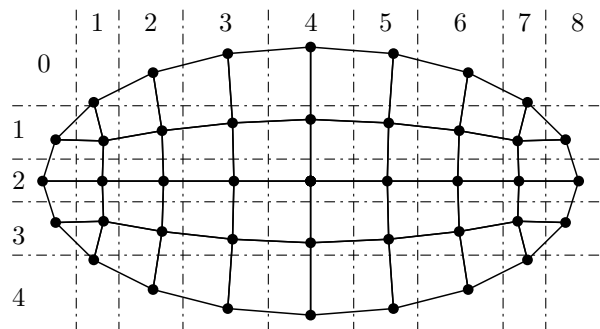


**Figure 2.10:** Cross-section meshed with rectangular mesh generating technique

Given  $n$  equi-spaced points on the boundary of the cross-section a rectangular grid is fit to the geometry. The elements are split into  $c$  columns and  $r$  rows. The nodes defining the corners of the elements can also be split into  $c + 1$  columns and  $r + 1$  rows.  $n$ ,  $c$  and  $r$  are related by the following equation:

$$n = 2(c + r) - 4 \quad (2.55)$$

In order for this meshing technique to succeed  $n$  must be an even number and the number of rows  $r$  should also be even. The second condition is not strictly necessary, however since TexGen always defines cross-sections starting by a point lying on the positive x axis, ignoring this condition would result in an asymmetric mesh about the x and y axes.

Node positions  $\mathbf{P}_{ij}$  are arranged in a grid where subscript  $i$  refers to nodes in the  $i$ th row and subscript  $j$  refers to nodes in the  $j$ th column. The positions of the nodes on the boundary are known whereas positions for the interior nodes must be calculated. In order to do this, two new sets of points are defined,  $\mathbf{A}_{ij}$  and  $\mathbf{B}_{ij}$ . Points  $\mathbf{A}_{ij}$  are the linear interpolation of points on the left of the grid  $\mathbf{P}_{i0}$  and points on the right of the grid  $\mathbf{P}_{ic}$ . Similarly points  $\mathbf{B}_{ij}$  are the linear interpolation of points on the top of the grid  $\mathbf{P}_{0j}$  and points on the bottom of the grid  $\mathbf{P}_{ic}$ . They are defined as:

$$\mathbf{A}_{ij} = \mathbf{P}_{i0} + \frac{j}{c}(\mathbf{P}_{ic} - \mathbf{P}_{i0}) \quad (2.56)$$

$$\mathbf{B}_{ij} = \mathbf{P}_{0j} + \frac{i}{r}(\mathbf{P}_{rj} - \mathbf{P}_{0j}) \quad (2.57)$$

The internal node positions  $\mathbf{P}_{ij}$  are then calculated as the weighted average of these two sets of points. The weights  $w_{Aij}$  and  $w_{Bij}$  are calculated as a function of distance  $d_{Aij}$  and  $d_{Bij}$ . Here  $d_{Aij}$  represents the shortest of distances from point  $\mathbf{A}_{ij}$  to  $\mathbf{P}_{i0}$  and  $\mathbf{A}_{ij}$  to  $\mathbf{P}_{ic}$ , and  $d_{Bij}$  represents the shortest of distances from point  $\mathbf{B}_{ij}$  to  $\mathbf{P}_{0j}$  and  $\mathbf{B}_{ij}$  to  $\mathbf{P}_{rj}$ :

$$d_{Aij} = \|\mathbf{P}_{i0} - \mathbf{P}_{ic}\| \left( \frac{1}{2} - \left| \frac{i}{r} - \frac{1}{2} \right| \right) \quad (2.58)$$

$$d_{Bij} = \|\mathbf{P}_{0j} - \mathbf{P}_{rj}\| \left( \frac{1}{2} - \left| \frac{j}{c} - \frac{1}{2} \right| \right) \quad (2.59)$$

$$w_{Aij} = \frac{d_{Bij}}{d_{Aij} + d_{Bij}} \quad (2.60)$$

$$w_{Bij} = \frac{d_{Aij}}{d_{Aij} + d_{Bij}} \quad (2.61)$$

$$\mathbf{P}_{ij} = w_{Aij}\mathbf{A}_{ij} + w_{Bij}\mathbf{B}_{ij} \quad (2.62)$$

Figure 2.11 shows this meshing technique applied to an elliptical cross-section with different values of  $n$ ,  $r$  and  $c$ . It can be seen from the figure that the quality of the mesh depends on these parameters. In order to avoid distorted elements, the ratio of number of columns  $r$  to rows  $c$  should be similar to the ratio of cross-section width  $w$  to height  $h$ :

$$\frac{c}{r} \approx \frac{w}{h} \quad (2.63)$$

It is not possible for the ratios to be exactly equal in all cases because  $r$  and  $c$  are integers whereas  $w$  and  $h$  need not be. The value of  $c$  can be calculated using the nearest integer function:

$$c = \left[ \frac{rw}{h} \right] \quad (2.64)$$

With Equations 2.55 and 2.64, the values of  $r$  and  $c$  can be determined from  $n$  alone. The number of cross-section points  $n$  then controls the density of the mesh.



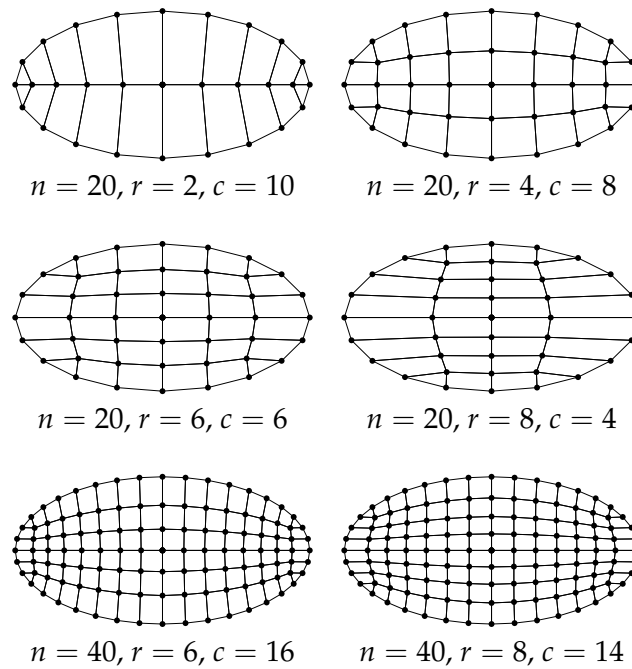


**Figure 2.11:** Cross-section meshed varying  $n, r$  and  $c$

## 2.9.2 Linking

A number of equi-spaced meshed cross-sections are created along the length of the yarn path. Consecutive cross-sections are linked together to form 3D volume elements. In order to link two cross-sections together, the meshes must be compatible, i.e. each element from one cross-section must map to an element on the other cross-section. In this way, pairs of triangles can be linked together to form 6 noded wedge elements and pairs of quadrilaterals can be linked together to form 8 noded hexahedral elements. If constant cross-sections are used compatibility is not an issue, however if the cross-section varies along the length of the yarn it can be difficult to obtain compatible meshes for the whole length of the yarn. Meshes generated by conventional meshing techniques are generally not compatible. The rectangular mesh generator was designed to generate compatible meshes regardless of the geometry given as long as parameters  $r, c$  and  $n$  are the same for each cross-section along the length of the yarn.

## 2.10 Fibre volume fraction

As an approximation the yarn has been modelled as a solid volume, however this volume is of course not entirely occupied by fibres. The proportion of fibres is defined as the fibre volume fraction of the yarn.

In order to calculate the fibre volume fraction the yarn boundaries must first be de-

fined so that a volume for the yarns can be calculated (see Appendix B). However these boundaries are somewhat arbitrary; in Section 2.4 they have been described as the smallest region encompassing all the fibres. How they are defined for specific yarns is open to interpretation, cotton yarns for example have many stray fibres that can generally be ignored. Fibre volume fraction should therefore be associated with a specific approximated yarn geometry.

The total volume of fibres within a yarn or textile,  $V.F.$ , can be calculated by experimentally measuring the weight of the yarn or fabric  $m$ . Assuming the fibres all have the same density  $\rho$  the volume is:

$$V.F. = \frac{m}{\rho} \quad (2.65)$$

A measure of fibre volume fraction  $V_{f,y}$  can then be calculated:

$$V_{f,y} = \frac{V.F.}{V.Y.} \quad (2.66)$$

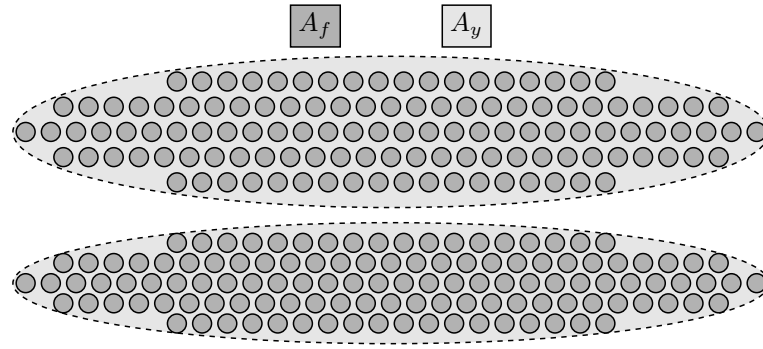


**Figure 2.12:** Schematic of fibres contained in a yarn with different degree of compaction

This gives a constant fibre volume fraction for an entire yarn or fabric. This is suitable for cases where the cross-sectional area along the length of a yarn does not vary significantly. However for cases with varying cross-sectional area a more useful quantity would be the ratio of fibre area  $A.F.$  to yarn area  $A.Y.$  in a cross-section. Assuming that individual fibres are incompressible as a yarn is compressed (Figure 2.12), the area of fibres at any cross-section along the length of a yarn will remain constant. See Chapter 4 for a discussion on the assumptions made here. The fibre area fraction  $A_f$  can be calculated with the following equation:

$$A_f = \frac{A.F.}{A.Y.} \quad (2.67)$$

Given the linear density  $\zeta$  of a yarn and the density of its constituent fibres  $\rho$  the area of fibres  $A.F.$  is calculated as:

$$A.F = \frac{\zeta}{\rho} \quad (2.68)$$

And hence the fibre area fraction  $A_f$  can be expressed as:

$$A_f = \frac{\zeta}{A.Y.\rho} \quad (2.69)$$

Note that the yarn cross-sectional area  $A.Y.$  may vary along the length of a yarn. Appendix A contains a derivation of yarn cross-sectional area  $A.Y.$ .

Alternatively  $A.F.$  can be related to the total volume of fibre in a yarn  $V.F.$  and its length  $L$  with the following equation:

$$A.F. = \frac{V.F.}{L} \quad (2.70)$$

## 2.11 Intersections

### 2.11.1 Point inside yarn

There are various occasions when it is useful to obtain information about a certain point contained within the unit cell. For example in finite element analysis, once a mesh has been created it is often necessary to assign material properties to elements, which are anisotropic for textiles or textiles composites. Material properties often also depend on the fibre volume fraction within the yarn which may vary from position to position. In order to obtain this information it is first necessary to find out if and where the point intersects the yarn. An algorithm to accomplish this has been developed and is described in this section.

The intersection of a point  $\mathbf{P}$  and a yarn is evaluated in two stages. The first stage is to find a plane which contains the point  $\mathbf{P}$  and a point  $\mathbf{S}(t)$  on the centreline of the yarn and whose normal is parallel to  $\mathbf{S}'(t)$  ( $\mathbf{S}(t)$  is defined in Equation 2.2). In mathematical terms this means solving the following equation for  $t$ :

$$\mathbf{S}'(t) \cdot (\mathbf{P} - \mathbf{S}(t)) = 0 \quad (2.71)$$

There may be an infinite number of solutions to this equation. It is not possible to solve this equation analytically for cases where the yarn path  $\mathbf{S}(t)$  is a complicated function. Instead a numerical technique is adopted to search for the solution in an iterative manner. The minimum signed distance  $d(t)$  from the plane defined at  $t$  to the point  $\mathbf{P}$  can be calculated as:

$$d(t) = \frac{\mathbf{S}'(t)}{\|\mathbf{S}'(t)\|} \cdot (\mathbf{P} - \mathbf{S}(t)) \quad (2.72)$$

If two values of  $t$  denoted by  $t_a$  and  $t_b$  are chosen, it is possible to estimate if a solution lies between those two points. At least one solution exists between  $t_a$  and  $t_b$  if  $d(t_a)$  is

positive and  $d(t_b)$  is negative. The opposite is not necessarily true, as solutions may exist where the distance between the point  $\mathbf{P}$  and the yarn centreline  $\mathbf{S}(t)$  exceeds the radius of curvature  $\frac{1}{\kappa(t)}$  (where  $\kappa(t)$  is the curvature at  $t$ ). However these solutions are not important because if the cross-section exceeds this radius of curvature the yarn will be self intersecting and hence invalid. Further solutions may exist in extreme cases where the tangent  $\mathbf{S}'(t)$  varies significantly between  $t_a$  and  $t_b$ . In practise this is unlikely to occur if  $t_a$  and  $t_b$  are chosen between adjacent master nodes as is the case in the TexGen implementation.

Once a solution is known to lie between  $t_a$  and  $t_b$ , an initial guess  $t_0$  at the solution  $t_s$  can be obtained with the following equation:

$$t_0 = t_a + (t_b - t_a) \frac{d(t_a)}{d(t_a) - d(t_b)} \quad (2.73)$$

At each following iteration a closer estimate at the solution can be obtained with the following equation:

$$t_{i+1} = \mathbf{S}'(t_i) \cdot (\mathbf{P} - \mathbf{S}(t_i)) \quad (2.74)$$

The process continues until  $d(t_i)$  becomes less than a certain tolerance. Typically a converged solution can be found in 6 or 7 iterations to within a tolerance of  $10^{-6}$ . Figure 2.13 illustrates the search for a point  $\mathbf{P}$ .

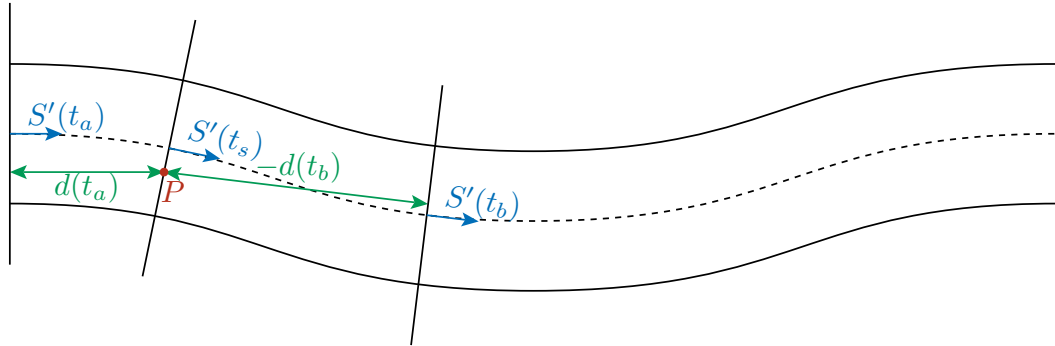


Figure 2.13: Point inside yarn

Once a solution  $t_s$  is found, the coordinates of  $P$  are transformed to the 2D cross-section coordinate system. The local coordinates  $x'$  and  $y'$  of  $\mathbf{P}$  are calculated as follows:

$$x' = (\mathbf{P} - \mathbf{S}(t_s)) \cdot \vec{\mathbf{X}}'(t_s) \quad (2.75)$$

$$y' = (\mathbf{P} - \mathbf{S}(t_s)) \cdot \vec{\mathbf{Y}}'(t_s) \quad (2.76)$$

Vectors  $\vec{\mathbf{X}}'(t_s)$  and  $\vec{\mathbf{Y}}'(t_s)$  are defined in Equations 2.37 and 2.38. The second stage consists of checking that  $x'$  and  $y'$  lie within the cross-section  $\mathbf{C}$  defined at  $t_s$ . This step can easily be accomplished analytically for certain types of sections. For a more general

approach, the section can be approximated by a closed polygon. Various standard numerical techniques exist for determining if a point lies within a 2D polygon [126]. If the point lies within the cross-section then the search ends and various information can be extracted from the procedure. It is known that the point lies within the yarn and the tangent of the yarn at that point is known, defined by  $\mathbf{S}'(t_s)$ , and the local cross-section coordinates  $x'$  and  $y'$  of the point are also known.

In order to also include repeated yarns in the search (see Section 2.6), the procedure could be carried out on yarns translated by the vectors  $\vec{\mathbf{V}}_j$ :

$$\vec{\mathbf{V}}_j = C_0\vec{\mathbf{R}}_0 + C_1\vec{\mathbf{R}}_1 + \cdots + C_{n-1}\vec{\mathbf{R}}_{n-1} \quad -\infty \leq C_i \leq \infty \quad (2.77)$$

where the coefficients  $C_i \rightarrow \mathbb{Z}$  are integers and  $\vec{\mathbf{R}}_i$  are repeat vectors. However a more efficient method is to simply translate the point  $P$  by the vectors  $-\vec{\mathbf{V}}_j$ . Since the limits for  $C_i$  are infinite, the number of vectors  $\vec{\mathbf{V}}_j$  is also infinite. It is necessary to reduce the number of vectors  $\vec{\mathbf{V}}_j$  to a finite number before the procedure can be carried out numerically. This done by calculating limits for the coefficients  $C_i$ :

$$a_i \leq C_i \leq b_i \quad (2.78)$$

where  $a_i$  and  $b_i$  are referred to as the repeat limits. The values of  $a_i$  and  $b_i$  are calculated such that if  $C_i$  is outside this range point  $\mathbf{P}$  is guaranteed not to intersect with the yarn. This is described in Appendix C.

### 2.11.2 Yarn intersections

It is useful to have a method to determine if two yarns intersect. These situations should be avoided as they are not physically possible and also cause problems with meshing. At the time of writing TexGen implements this by determining a list of sampled surface points  $\mathbf{P}_i$  for each yarn (Section 2.8) and checking if any of the points lie within any of the other yarns (Section 2.11.1). If they do then the yarns intersect, however if the number of sampled points is not large enough then the method may fail to find all intersections. A more robust method is to find intersections between the surfaces meshes [90]. If any of the surface elements intersect with each other then the yarns intersect. This method will only fail if a yarn is completely contained within another. However this method also relies on the accuracy of the surface mesh which is only an approximation of the surface, and, if too coarse, could also lead to missing yarn intersections.

## 2.12 Implementation

TexGen has been implemented in C++ in an object-oriented manner with a cross platform design (currently tested on Windows and Linux). The code has been split into several modules which will be detailed in the following section.

### 2.12.1 Modules

- Core
- Renderer
- Export
- Python interface
- GUI

The core module contains everything that has been discussed in this chapter and constitutes the largest part of the software. The core module depends on three third party libraries. The first is **Triangle** [121] which is used for meshing 2D cross-sections. The second is **HXA7241 Octree Component C++** [3] which is used for optimising various operations. The third is **TinyXML** [130] which is used for reading and writing XML files. All three libraries are small and free to use without restriction. Additionally TexGen relies heavily on the C++ Standard library.

The renderer module contains the code necessary to visualise the textile models in 3D. This module depends on the third party library **VTK** [86] (Visualisation Toolkit). VTK is an open source, cross-platform, freely available software system for 3D computer graphics, image processing and visualization. The TexGen Core module is able to function without the use of this library.

The export module contains code to export geometric models to file formats widely used by other computer-aided design (CAD) systems. These formats include IGES and STEP. IGES stands for Initial Graphics Exchange Specification and defines a neutral data format that allows the digital exchange of information among CAD systems. STEP stands for Standard for the Exchange of Product model data and was intended to be a replacement for IGES. TexGen relies on the third party library **OpenCASCADE** [112] for writing the IGES and STEP files.

The Python interface actually consists of two wrapper modules, each module providing a Python interface to the corresponding core and renderer modules described

above. **Python** [135] is a dynamic object-oriented programming language that offers strong support for integration with other languages. The two modules are compiled as dynamically linked libraries which can be imported from Python scripts at run time. The Python scripts can be used to create, visualise and export TexGen textile models. Python scripting is a viable interfacing method for the developer and advanced user. The Python interface modules are generated automatically by **SWIG** [7] (Simplified Wrapper and Interface Generator). Essentially SWIG parses the C++ header files and generates a Python module that wraps all the specified classes and functions. Appendix D contains a sample Python script making use of the TexGen Python interface.

The GUI module contains the code for the graphical user interface. This essentially allows the user to interact with TexGen in a user friendly graphical environment. This module depends on the third party library **wxWidgets** [123]. wxWidgets (formerly known as wxWindows) is an open source, cross-platform widget toolkit; that is, a library of basic elements for building a graphical user interface. This module also depends on the three TexGen modules: Core, Renderer and Python interface. Strictly speaking the GUI does not need to depend on the Python interface. However, important GUI commands are sent through the Python interface rather than directly to the core and renderer module. This enables the commands to be recorded in the form of a Python script for later modification and/or playback. The GUI module also includes some Python interfacing code in order for the scripts to perform GUI specific operations such as creating and deleting render windows. Appendix E contains screenshots of the graphical user interface.

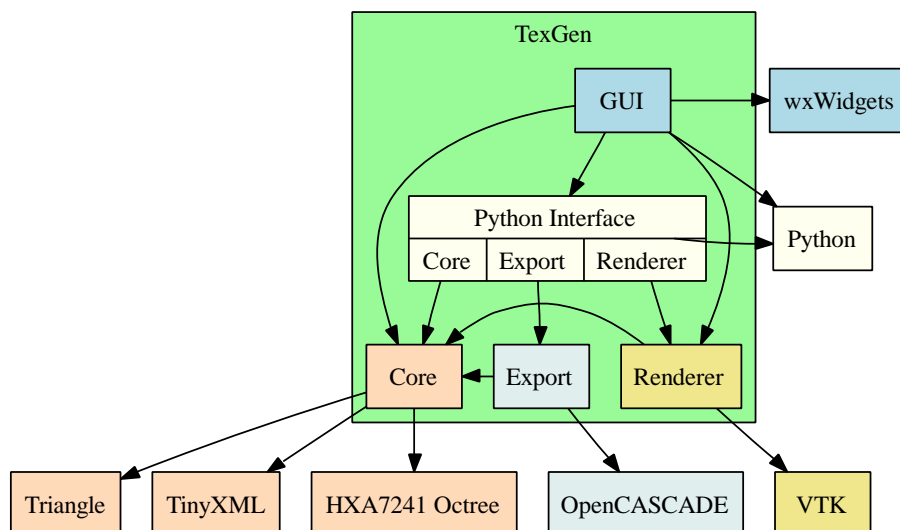


Figure 2.14: TexGen modules

Figure 2.14 illustrates the dependencies of the various internal and external modules. The advantage of separating code into different modules is that only the required modules need be compiled. For example, a user may want to create a batch of different textile models and output them to a certain file format for stochastic analysis. In this case the GUI and Renderer modules are not necessary, also removing the need for the external wxWidgets and VTK libraries. Downloading, configuring and installing external modules ensuring that compatible versions are used can be very time consuming, especially considering that these external libraries often also depend on further third party libraries. For windows users this is less of a concern since only the developers will need to compile the code; end users will simply use the binary files. However on Unix based systems users are accustomed to compiling all applications from source.

Compilation issues are not the only reason for using such a modular design. If one of the third party libraries becomes obsolete or unusable due to licensing restrictions, only the module that depends on it needs to be re-written. It also makes the code easier to maintain and debug.

### 2.12.2 Core

The details of how the GUI, Renderer and Python interface work will not be discussed in this chapter. However it is worth providing slightly more detail about the Core module. Figure 2.15 illustrates the main classes that constitute the Core module in the form of a UML (Unified Modelling Language) Class Diagram. The methods and attributes are omitted due to space restrictions.

The singleton class **C<sub>TexGen</sub>** contains a database of textiles and domains created as well as an instance of **C<sub>Logger</sub>**. The virtual base class **C<sub>Logger</sub>** receives all the log, warning and error messages that may be issued by any of the other classes. The **C<sub>LoggerScreen</sub>** implementation simply displays the messages on screen via standard output. The **C<sub>LoggerGUI</sub>** implementation displays the messages to the log window in the GUI. This class is in fact part of the GUI module but is shown in the diagram to illustrate at least two different implementations.

**C<sub>Domain</sub>** and more specifically **C<sub>DomainPlanes</sub>** is an implementation of a domain bounded by planes as described in Section 2.7. **C<sub>Textile</sub>** is an assembly of yarns which is further specialised by **C<sub>TextileWeave</sub>**, **C<sub>TextileWeave2D</sub>** and **C<sub>TextileWeave3D</sub>**. The specialised classes allow for automated creation of textile geometries with less input variables. More specialisations are likely to be included in the future (e.g. for weft knits, warp knits, braids, etc).



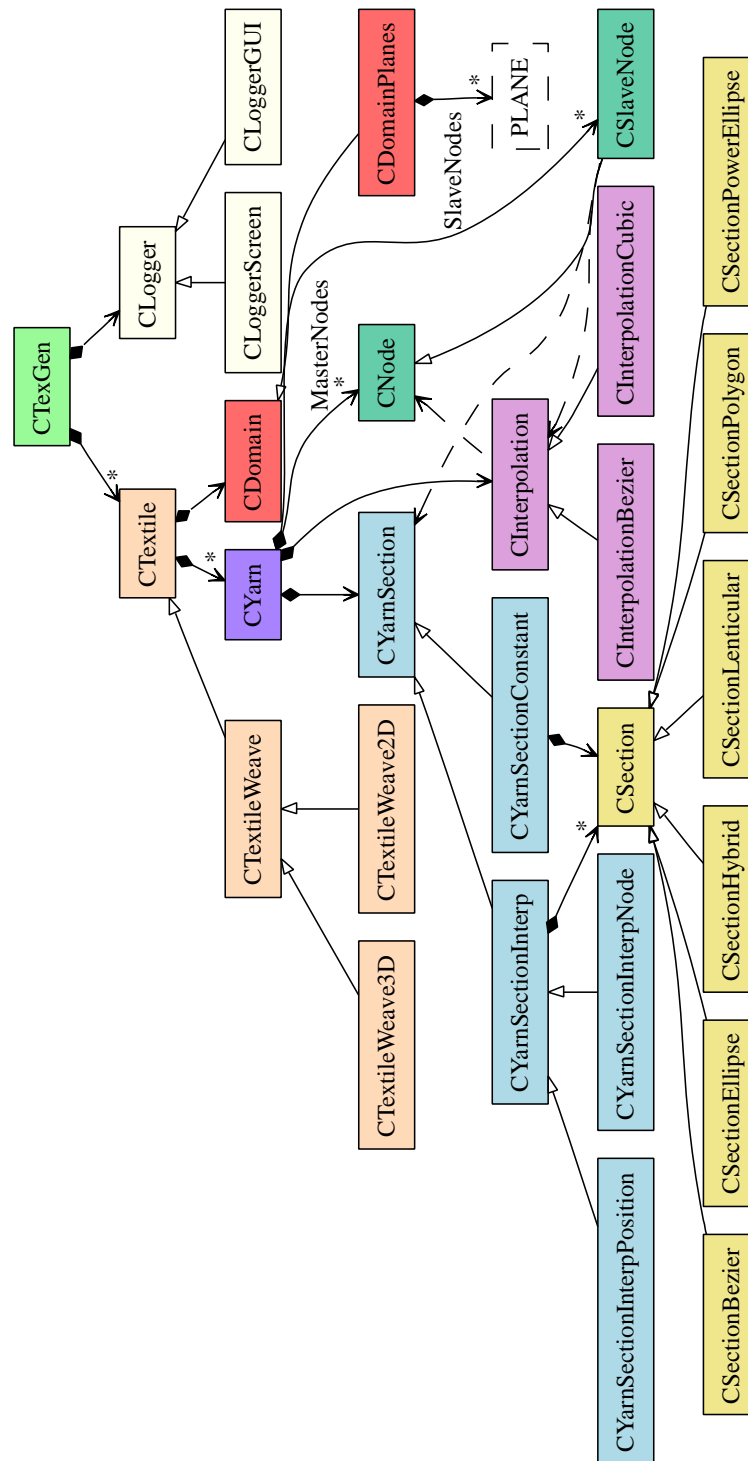


Figure 2.15: UML Class Diagram for the Core module

**CYarn** represents a yarn which is composed of a number of master nodes, an interpolation function (**CInterpolation**), and a section definition (**CYarnSection**). The master nodes correspond to the control points for the interpolation algorithm. The slave nodes are created by the interpolation function depending on the position of the master nodes. The slave nodes are then assigned sections by **CYarnSection**.

The virtual base class **CInterpolation** represents a general interpolation function. Two implementations of it are **CInterpolationCubic** and **CInterpolationBezier** as described in Section 2.3.

The virtual base class **CYarnSection** represents a general yarn section definition. The simplest implementation of this is **CYarnSectionConstant** which contains a single **CSection** applied along the yarn length. A further virtual base class **CYarnSectionInterp** represents a section that is interpolated either between nodes (**CYarnSectionInterpNode**) or at some arbitrary position (**CYarnSectionInterpPosition**). These classes are the implementation of algorithms discussed in Section 2.5.

The virtual base class **CSection** represents a general section. Several implementations of it exist as described in Section 2.4.

The procedure for creating a textile mesh as discussed in Section 2.8 is demonstrated in pseudo code:

```

for each Yarn in Textile
  get SlaveNodes from CInterpolation given MasterNodes
  for each SlaveNode
    get Section from CYarnSection given SlaveNode
    assign Section to SlaveNode
  create YarnMesh from SlaveNodes
  add YarnMesh to TextileMesh

```

## 2.13 Conclusions

In this chapter the geometric modelling methodology and implementation have been discussed. These are the foundations necessary for creating geometric models of textile structures. In the following chapter real examples will be used to demonstrate the validity of these concepts, with the aim of developing a general methodology for generating accurate textile models.

# Textile geometry model case validations

## 3.1 Introduction

In this chapter, geometric models for various 2D woven fabrics will be created with TexGen. From a geometric perspective some aspects of the models can be generalised to all 2D woven fabrics whilst other aspects are specific to the fabric being modelled. A moderately realistic model can be created with only a few input parameters, however accuracy can be improved with additional input. Ideally it should be possible to predict the geometry of any fabric without knowing the yarn path and cross-sectional shape given information about the yarn mechanics and the manufacturing process. However, this goes beyond the intended scope of this chapter. The objective of this chapter is to set out a modelling methodology able to create models quickly based on geometry alone with sufficient accuracy to be used in predicting various fabric properties. In this thesis the focus is on fabric mechanics (see Chapter 5), however the models are also suitable for fluid dynamics [140], thermodynamics [52, 53], etc. A list of all the fabrics modelled in this section are shown in Table 3.1 along with the minimum input parameters. The method with which these parameters are obtained is detailed further in this chapter.

**Table 3.1:** Summary of fabric measurements

	$s_x$	$s_y$	$T$	$w_x$	$w_y$	$\rho_A$	$A_c$	$V.Y.$	$\rho_f$
150TB	1.666	2	0.3	0.83	0.83	150	13.3	1.38	2.62
800S4-F1	3.16	3.16	1.0	3.16	3.16	780	159	116	2.62
Polyester	0.23	0.19	0.1	0.19	0.17	69	0.175	0.0108	1.39
Cotton	0.36	0.33	0.3	0.3	0.26	160	0.475	0.0855	1.54
	mm	mm	mm	mm	mm	g/m <sup>2</sup>	mm <sup>2</sup>	mm <sup>3</sup>	g/cm <sup>3</sup>

## 3.2 Literature survey

In this section the previous work reported on measuring fabric geometric parameters is discussed. Various techniques have been used including optical scanning, optical microscopy, confocal microscopy, optical coherence tomography and x-ray microtomography.

Dunkers et al. [34, 35] compared three imaging techniques including optical coherence tomography, confocal microscopy and x-ray microtomography ( $\mu$ CT) for characterising impact damage on glass reinforced composite structures. It was found that optical coherence tomography exhibited more detail and a higher depth of penetration than confocal microscopy. But x-ray microtomography performed the best at clearly imaging the reinforcement microstructure of the entire sample and was not limited in depth. Although  $\mu$ CT was not able to satisfactorily characterise the damage, this is of no concern in the context of this chapter.

Chang et al. [17] characterized the effect forming on the geometry of fabrics. Micrographs were obtained for undeformed fabrics and fabrics undergoing various deformations induced by picture frame, bias extension and biaxial tests. In a subsequent paper Chang et al. [18] obtained micrographs of fabric draped over a helmet component and then vacuum consolidated. The outline of yarn cross-sections were identified by eye and defined by picking points using image processing software. An ellipse was then fitted to the outline to identify the centre of the yarn. Various parameters were extracted from the micrographs including yarn thickness, yarn spacing, yarn width, crimp amplitude, crimp angle and unit cell length. These parameters were then compared between undeformed and deformed cases. It was found that the deformed geometry depends on the test method applied.

Desplentere et al. [29, 30] characterised the geometry of 4 fabrics using a combination of optical microscopy and microtomography. The yarn spacing and yarn width were measured from images of the fabric obtained from an optical scanner. Cross-section

images of the fabric were obtained by casting the fabric in epoxy resin in its relaxed state and cutting samples to be viewed under an optical microscope. A different set of measurements including yarn spacing, yarn width and fabric thickness were obtained from the cross-sectional images. A third set of measurements were obtained by scanning the fabric cast in epoxy resin with a microtomography machine. For each of these sets of measurements the variability of each parameter was observed. Using the average of these data sets models were generated using the WiseTex software. However no attempt was made to compare the geometry generated by WiseTex with the microscopy or microtomography data.

Potluri et al. [99] used optical microscopy to measure geometric parameters from a series of glass woven composite preforms. A series of high resolution images were stitched together to provide easier measurement of geometric parameters. Yarn spacing, tow widths, crimp values and tow thicknesses were measured for all fabrics. The maximum angle between the yarn direction and the horizontal plane was measured for the plain woven fabric. These parameters were used as input to their energy based fabric mechanical model [110, 111].

### **3.3 Experimental techniques**

This section describes the methods used to obtain and compare fabric geometric data.

#### **3.3.1 Fabric thickness**

Fabric thickness measurement can be problematic due to the high level of fabric compressibility. The thickness obtained is highly sensitive to the amount of pressure applied during measurement. This chapter aims to model dry, undeformed fabrics hence the undeformed fabric thickness is required. This is defined as the distance between the closest two planes which encompass the fabric without intersecting with it. However some fabrics may contain stray fibres which artificially increase this thickness. Some common sense is needed for determining which fibres to ignore. In practical terms it is necessary to place the fabric between two flat plates and apply a small pressure to ensure the plates are touching the surface of the fabric.

For the Chomarat fabrics, the manufacturers provide a fabric thickness measurement obtained as described in British Standard Method (BS ISO 4603:1993). The method consists of placing the fabric between two plates of 20 mm diameter and applying a force between 3 and 8 N. This is equivalent to a pressure of between 10 and 25 kPa (100

and  $260 \text{ gf/cm}^2$ ). This is a substantial force capable of compressing the material to a large degree. In order to obtain the undeformed thickness a much smaller force should be applied.

The Kawabata evaluation system for fabrics (KES-f) [59] is a very sensitive system able to precisely measure the thickness of fabrics as a function of pressure. This system also operates on the principle of applying a small force to a fabric between two plates. Two thickness values are specified by the KES-f system,  $T_0$  and  $T_m$  which represent the fabric thickness at minimum pressure ( $0.5 \text{ gf/cm}^2$  or  $0.05 \text{ kPa}$ ) and maximum pressure ( $50 \text{ gf/cm}^2$  or  $5 \text{ kPa}$ ) respectively. This is a very useful system but is also very expensive and not widely available. However some KES-f compaction tests were performed at Heriot Watt University for the present study.

An alternative is to obtain cross-sectional images of the fabric and measure the thickness of the fabric from these. This has the advantage that no force needs to be applied to the fabric during measurement. However it is possible that the sample may be disturbed during the mounting and/or casting process.

### 3.3.2 Microscopy

Microscopy is used to obtain cross-sectional images of a fabric cut along a particular plane. In order to restrict the movement of the fibres during the cutting phase the fabric is first cast in Reichhold Polylyte 32032-00 resin. After allowing the resin to cure the composite structure can be cut along a desired plane. The surface is then polished on a Struers Dap-7, Pedemin-S polishing machine to obtain a smooth flat surface. A Zeiss Axiolab microscope is used to take highly magnified images of the structure. In order to obtain an image covering a large area it is necessary to take a large number of small images and assemble them together. This is accomplished automatically with a mobile stage controlled by an ITK Multicontrol 2000. The images are assembled together by a Python script making use of the Python Imaging Library [85].

The images of the cotton and polyester fabrics were provided by Unilever [74]. The fabrics were cast in resin and sectioned in a similar manner as described above. Images of the cotton and polyester sections were obtained with a scanning electron microscope (SEM). Additional images were taken of polyester fabric sections through an optical microscope.

### 3.3.3 Microtomography

This is the most advanced form of validation used in the present study. While microscopy is used to obtain 2D images, microtomography is used to obtain 3D volumetric data of a fabric. Microtomography, also known as MicroCT or  $\mu$ CT, is a microscopic form of X-ray computed tomography and uses x-rays to create cross-sections of a 3D object that can later be used to recreate a virtual model without destroying or disrupting the original object. In microtomography the pixel sizes of the cross-sections are in the micrometer range. It is important to note that the virtual model in this context is only suitable for viewing purposes and image analysis. It is the 3D analogue of a 2D image, with the virtual model made up of a 3D array of voxels (3D pixels). The geometric models created by TexGen have more detailed information such as the yarn path and cross-sectional shapes. The data obtained from  $\mu$ CT is an aid to creating accurate geometric models rather than a replacement for such models.

The machine used was a SCANCO Medical  $\mu$ CT 40. The fabric samples were placed in a 2 cm diameter tube held in place by a foam structure invisible to x-rays. Due to the small size of the samples, tape was placed at the cut edges to keep the fabric from falling apart. The tape is also fairly transparent to x-rays.

The polygonisation of voxel data from the  $\mu$ CT machine is obtained using an implementation of the marching cubes algorithm [83] programmed by the present author. The images are not perfect, due to a certain amount of noise present during the scanning process and also limitations on resolution (18  $\mu$ m in this case). Although visually impressive, it is difficult to use reconstructed 3D images directly for validation purposes. However 2D slices of the  $\mu$ CT data can be extracted along any plane as a post-processing step.

### 3.3.4 Measuring parameters

Yarn spacing, width, height and fabric thickness are measured from cross-sectional images of the fabric obtained from both microscopy and  $\mu$ CT using GIMP [61] (GNU Image Manipulation Program). Yarn spacing was measured as the distance from the edge of one yarn to the corresponding edge of an adjacent yarn. Yarn width and height were measured as the maximum distance between yarn edges along the major and minor axes respectively. Fabric thickness was measured as the maximum through fabric distance between the opposite edges of two crossing yarns. The height of the yarn was assumed to be equal to half the fabric thickness and only one of these two measurements was taken. In the case of the  $\mu$ CT images where the resolution is lower and the

boundary between two crossing yarns is difficult to identify, the fabric thickness measurement was taken. In the case of the microscopy images where the image resolution is higher and the yarn boundaries are clearly identifiable the yarn thickness measurement was taken.

Direct spacing measurements of the fabric were also performed with a ruler. In order to minimise the effect of fabric variability and measurement inaccuracies, the number of yarns was counted over a length of approximately 5 cm. The spacing measurement was then calculated as measurement length divided by number of yarns.

### 3.3.5 Image analysis

Cross-sectional images of the fabric obtained from microscopy were compared against cross-sections of the TexGen model to validate yarn path and cross-sectional shape. An image analysis technique with some manual intervention was used to identify various coordinates. Two steps were performed, determining the path of the transverse yarn and location of the longitudinal yarns.

The first step in the image analysis is to determine the path of the transverse yarn, which is done by manually selecting pixel coordinates that lie on the centre of the yarn at the crossovers and either edge of the image. The transverse yarn is given a height measured in pixels. Then using either a bezier or periodic cubic interpolation function, the path of the yarn with given height is drawn.

The second step is to determine the position and rotation of the longitudinal yarns. This is accomplished using an algorithm which overlays predefined cross-sections over the image at all possible locations. At each location the average intensity of the pixels located within the cross-section is computed and used as a measure of fit. The process is shown graphically in Figure 3.1. The image resolution has been reduced for illustration purposes. The red outline is the closest approximation of an elliptical cross-section fit to the boundaries of the pixels. The numbers represent the intensity of each pixel and the number at the centre of the cross-section represents the average intensity of all the pixels contained within the cross-section (i.e. fit factor). A tolerance is applied to the fit factor to discard locations which clearly do not correspond to longitudinal yarns. Then remaining cross-sections which overlap are compared together, removing the one with the lowest fit factor. Figure 3.2 displays two overlapping cross-sections offset horizontally by 1 pixel from each other. Cross-section B has a lower fit factor (46.8) than cross-section A (47.6), hence cross-section B is discarded. After repeating this process for all overlapping cross-sections only the best fit cross-section remains.



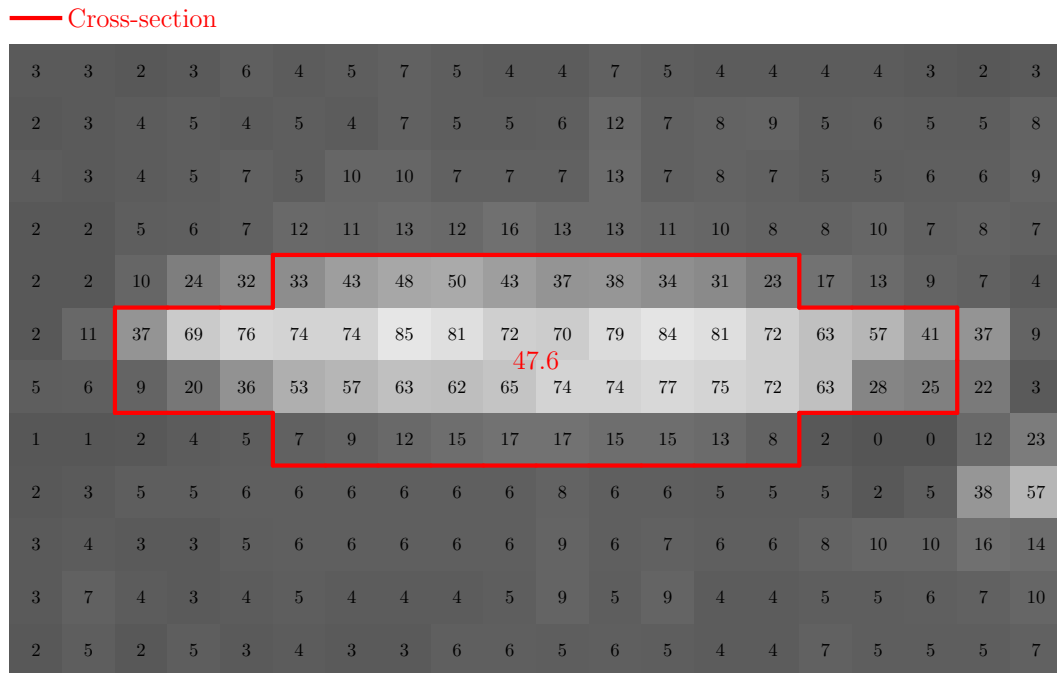


Figure 3.1: Pixel intensities averaged over predefined cross-section

Figure 3.3 illustrates the result of a high resolution cross-section image analysed with this technique. Note that this method is only applicable to images where the pixel intensity of yarns is significantly greater than that of the regions around it (i.e.  $\mu$ CT images and not microscopy images).

In order to create the predefined cross-section an assumption about its shape, size and rotation must be made. The width and height of the sections are measured from the image beforehand and an assumed shape is used. Generally an elliptical cross-section shape is adequate for the purpose of determining the centre and rotation of the yarn. A range of rotations at given intervals are tried by the algorithm to obtain the rotation which best fits the section image. This algorithm is not suitable for comparisons between cross-sections with different areas because the fit factor is biased towards lower area.

### Path comparison

A method to quantify how closely two yarn paths match up is presented in this section. Given two yarn centrelines  $\mathbf{S}_a$  and  $\mathbf{S}_b$ , it is useful to be able to quantify how closely these two paths agree. The root mean square  $d_{rms}$  of the distance  $d$  between the two paths is a good measure of fit and is calculated as follows.

A series of  $n$  equi-spaced point samples  $\mathbf{P}_{ai}$  are created along the length of the yarn

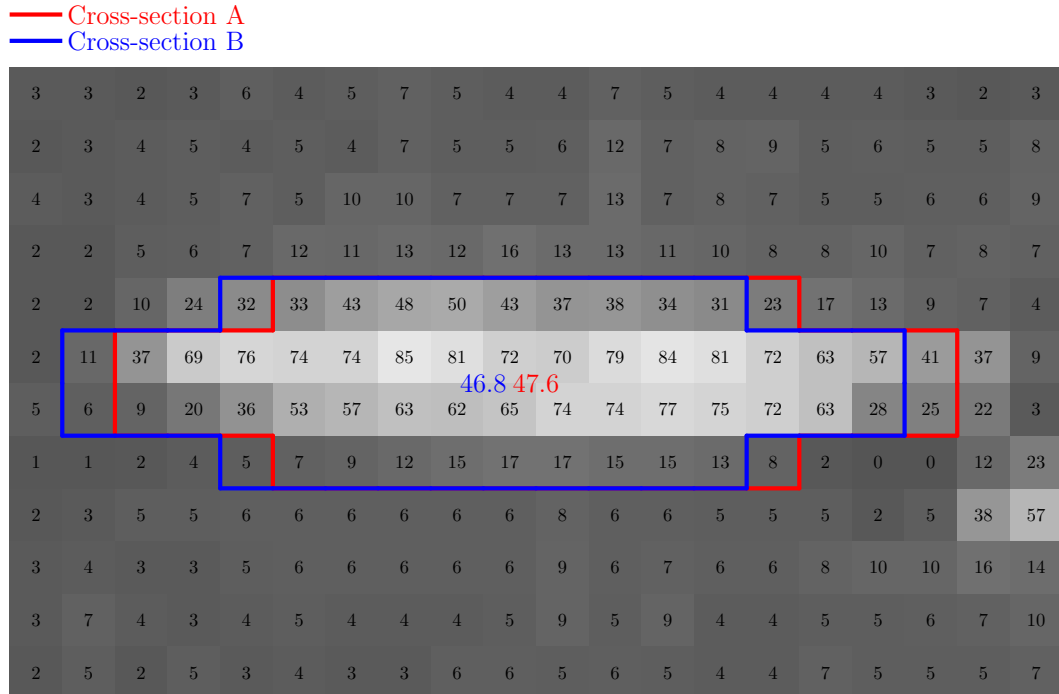


Figure 3.2: Comparison of pixel intensities averaged over two predefined cross-section



Figure 3.3: Image analysis example

centreline  $\mathbf{S}_a$ . A second series of  $n$  points  $\mathbf{P}_{b_i}$  are calculated such that all points lie on the yarn centreline  $\mathbf{S}_b$  and the distances  $d_i$  between each pair of points  $\mathbf{P}_{a_i}$  and  $\mathbf{P}_{b_i}$  are minimised. The algorithm to find the closest point on a yarn centreline to an arbitrary point is described in Section 2.11.1. If the two paths do not deviate significantly then  $\mathbf{S}_a$  and  $\mathbf{S}_b$  can be interchanged without affecting the values of  $d_i$ .

The distance  $d_i$  between each pair of points is defined as:

$$d_i = \|\mathbf{P}_{a_i} - \mathbf{P}_{b_i}\| \quad (3.1)$$

The root mean square  $d_{rms}$  can be expressed as:

$$d_{rms} = \sqrt{\frac{1}{n} \sum_{i=1}^n d_i^2} \quad (3.2)$$

The same approach can be taken to compare experimental data with an analytical yarn path. The only difference is the way in which the points  $\mathbf{P}_{a_i}$  are obtained. The points can be identified by manually selecting equi-spaced pixel coordinates lying on the centreline of a yarn from cross-section images. Before calculating the distances  $d_i$  the coordinates of  $\mathbf{P}_{a_i}$  and  $\mathbf{P}_{b_i}$  must be in the same coordinate space. This is achieved either by transforming the pixel coordinate system to the yarn centreline  $\mathbf{S}_b$  coordinate system or vice versa. An alternative approach is to construct the yarn centreline  $\mathbf{S}_a$  directly in pixel coordinate space (this is the approach taken for convenience). When calculating the root mean square value in pixel coordinate space, it is given in pixels and thus must be converted back to the appropriate units (i.e. metres or millimetres).

### Fibre volume fraction measurement

A simple method to determine the fibre volume fraction within a fabric from cross-sectional images is presented in this section. Given a grayscale cross-sectional image of a fabric an estimate of the fibre volume fraction can be obtained. The fibres in the image will generally have a higher brightness than the matrix region. Thus the ratio of pixels with a brightness greater than a threshold value to the total number of pixels gives an estimate of fibre volume fraction. In order for this technique to be reliable the contrast between the fibres and resin must be good. Without good contrast the choice of a suitable threshold is subjective.

## 3.4 Case study: Chomarat 150TB

Chomarat 150TB is a glass fibre plain woven fabric (Figure 3.4). This open plain weave fabric proves to be a good initial study, posing relatively little challenge in terms of

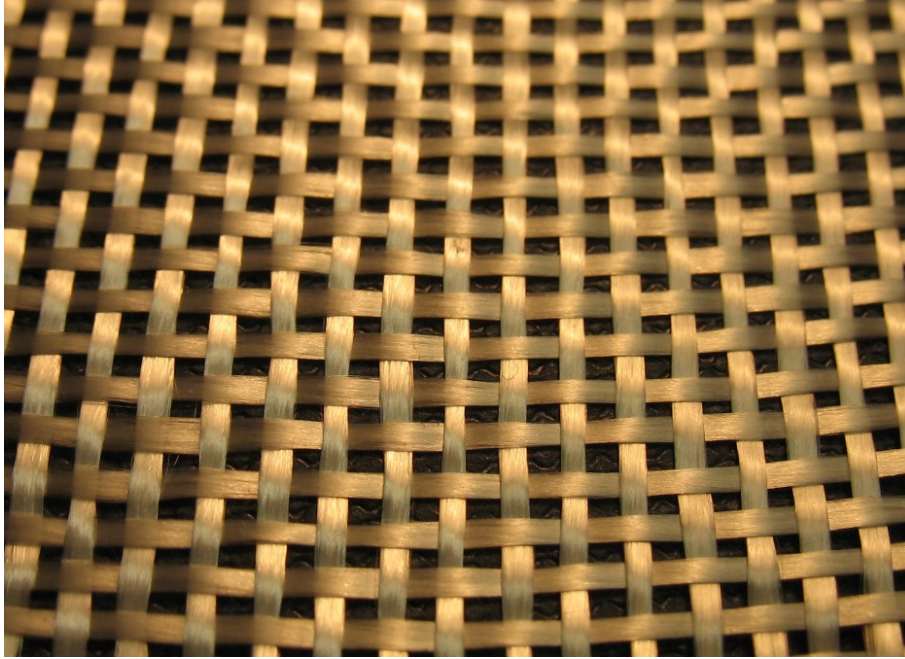


Figure 3.4: Chomarat 150 TB

geometric modelling.

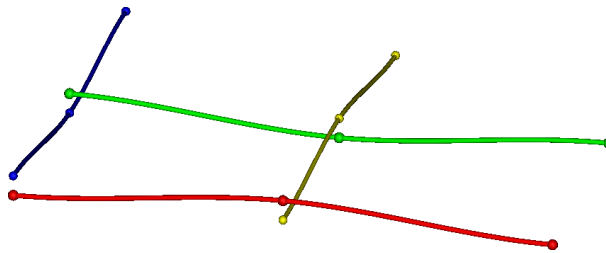


Figure 3.5: Illustration of discrete points for defining the yarn paths

To start with, the paths of the yarns are described by specifying discrete points along it and interpolating as described in Section 2.3. The simplest way to do this is by specifying points at the crossovers only as shown in Figure 3.5. Two measurements from the fabric are needed for this step, the yarn spacing  $s$  and vertical distance  $z$  between yarn centrelines at crossovers. In this case the yarn spacing between warp and weft yarns are different and are denoted as  $s_x$  and  $s_y$  respectively. The height of a yarn  $h$ , thickness of a fabric  $T$  and vertical distance  $z$  are all assumed to be related in the following manner:

$$z = h = \frac{T}{2} \quad (3.3)$$

From cross-sectional images all three of these quantities are measurable, however when using a mechanical measuring device such as the KES-f only the value  $T$  is measurable. For comparison purposes the value measured will be converted to fabric thickness  $T$

henceforth. The thickness measurements<sup>1</sup> using the techniques available are shown in Table 3.2 and the yarn spacing measurements<sup>2</sup> are shown in Table 3.3.

**Table 3.2:** Chomarat 150TB thickness measurements

Method	Mean (mm)	Pressure (gf/cm <sup>2</sup> )	STD (mm)	Samples
KES-f	0.301	0.5	0.00404	3
$\mu$ CT	0.297	0	0.0127	10
Microscopy	0.248	0	0.0171	10
KES-f	0.205	50	0.00361	3
Manufacturer	0.18	100 - 260	N/A	10

**Table 3.3:** Chomarat 150TB yarn spacing measurements

Method	Mean $s_x$ (mm)	Mean $s_y$ (mm)	STD (mm)	Samples
Ruler	1.666	2	0	3
$\mu$ CT	1.686	1.97	0.087	10
Microscope	1.602	1.93	0.074	10

The thickness measurements tend to vary significantly depending on the method used. This is thought to be due to the high sensitivity to pressure. Sensitivity of mechanical properties to fabric thickness will be explored in Chapter 5. The spacing measurements are more consistent between the different methods used.

Secondly the yarn cross-sections must be defined. The cross-section will be defined initially as constant throughout the whole unit cell. The measurements for the width<sup>3</sup>  $w$  of the yarn are shown in Table 3.4. An elliptical cross-section is assumed at this stage (validated later).

**Table 3.4:** Chomarat 150TB yarn width measurements

Method	Mean (mm)	STD (mm)	Samples
$\mu$ CT	0.819	0.064	10
Microscope	0.841	0.063	10

Finally the interpolation function must be specified. Two options are considered, periodic cubic interpolation and Bézier interpolation. Two models have been created to compare the two different interpolations as shown in Figure 3.6. Upon visual inspection the models generated by using the two different interpolation functions appear to

<sup>1</sup>The average of the KES-f and  $\mu$ CT values rounded to 2 decimal places is used to generate the model

<sup>2</sup>The values measured by ruler are used to generate the model

<sup>3</sup>The average of the  $\mu$ CT and Microscope values rounded to 2 decimal places is used to generate the model

be identical. The root mean square  $d_{rms}$  of the distances between the two curves is insignificant at  $4.683 \times 10^{-6}$  mm with 100 sample points. Hence the choice of interpolation function between the two proposed is not important for this fabric (Bézier interpolation is used for convenience).

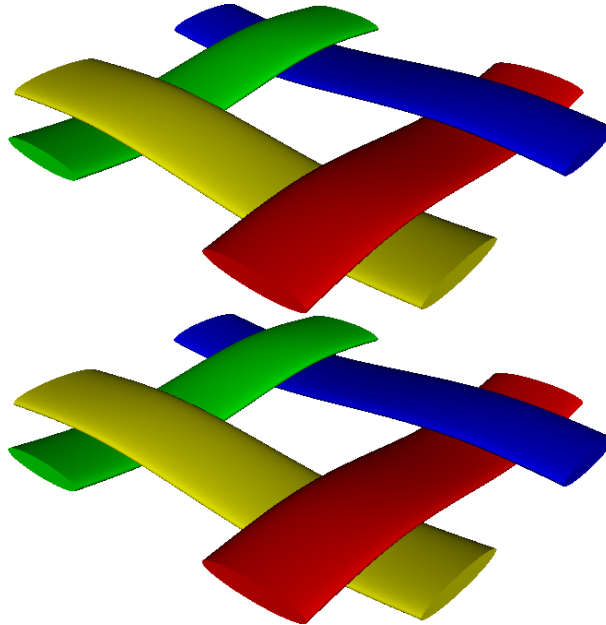


**Figure 3.6:** Chomarat 150TB with Bézier interpolation (top) and with periodic cubic interpolation (bottom)

Due to the variable nature of the fabrics it is necessary to create a series of geometric models incorporating the variability to accurately represent the fabric. Rather than displaying images and calculations for each possible model, a base model is created with rounded values for convenience (see Table 3.1). In Chapter 5 variations on the base model will be analysed to assess the effect of these parameters on fabric mechanical properties.

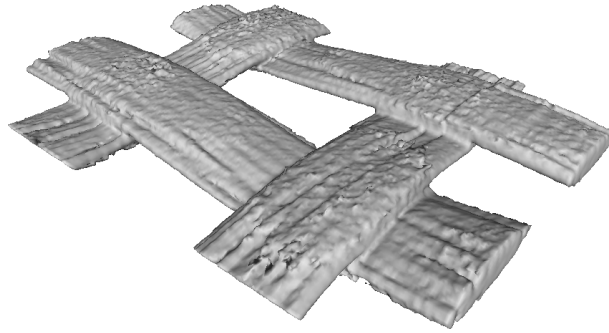
Having created a base geometric model of the textile, it is necessary to validate the assumptions made such as yarn path and cross-sectional shape.

### 3.4.1 Validation

#### $\mu$ CT analysis

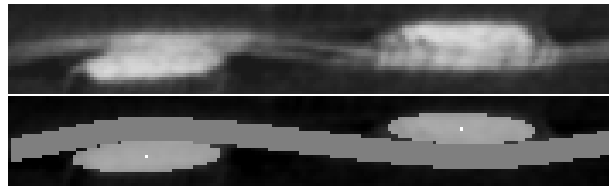
Using  $\mu$ CT, a reconstructed image of the Chomarat 150 TB fabric was created (Figure 3.7).

Figure 3.8 shows a single slice of the  $\mu$ CT data before and after image analysis. The analysis (as described in Section 3.3.5) was done with an assumed elliptical shape, with



**Figure 3.7:** Chomarat 150TB  $\mu$ CT reconstruction

rotations ranging from -0.1 to 0.1 radians in 20 intervals.



**Figure 3.8:** Chomarat 150TB  $\mu$ CT slice, original (top) analysed (bottom)

From image analysis the yarn path fits the interpolated path constrained at the cross-overs alone very well. The root mean square  $d_{rms}$  of the distances between points chosen along the yarn centreline and the analytical spline is  $6.20 \times 10^{-3}$  mm (Note the value is the same for both Bézier and Natural cubic spline).

The high resolution images of the fabric cross-sections obtained from microscopy are ideal for determining yarn cross-section shape. Unfortunately the cross-section fitting algorithm described in Section 3.3 is not suitable for microscopy images, thus the fit must be done manually. One such image is shown in Figure 3.9 with a lenticular section fitted to it. As can be seen by the image, the lenticular section is more suitable than an elliptical section. Although the cross-section fit may be improved by using a polygon or a spline, both require many more parameters. The lenticular section described in Section 2.4.3 only requires 3 parameters to define it: width, height and distortion. Due to the variable nature of the cross-sectional shape, it is necessary to take measurements from several sections and average the parameters. This task is simplified by choosing a simple shape such as the lenticular cross-section.

The lenticular shape parameters can be obtained by measuring 4 points  $P_1$ ,  $P_2$ ,  $P_3$  and  $P_4$  on the yarn cross-section as shown in Figure 3.9. A fifth point  $P_5$  is defined as the intersection between the line segments created between points  $P_1$ - $P_2$  and  $P_3$ - $P_4$ . The

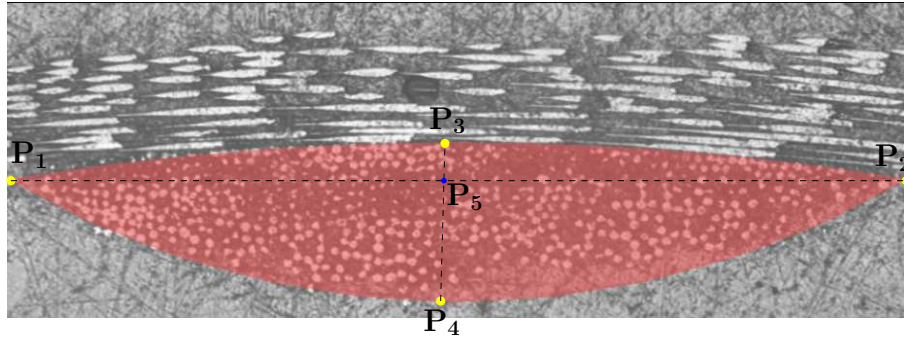


Figure 3.9: Chomarat 150TB yarn cross-section shape at crossover

width  $w$ , height  $h$  and distortion  $d$  can then be calculated as follows:

$$w = \|\mathbf{P}_2 - \mathbf{P}_1\| \quad (3.4)$$

$$h = \|\mathbf{P}_4 - \mathbf{P}_3\| \quad (3.5)$$

$$d = \|\mathbf{P}_5 - \mathbf{P}_3\| - \frac{h}{2} \quad (3.6)$$

However, only the width and height of the section are strictly necessary. The distortion parameter  $d$  can be calculated such that points  $\mathbf{P}_1$  and  $\mathbf{P}_2$  are in contact with the crossing yarn (this is the approach used). Since the section is not symmetric about the x axis it is necessary to invert it from one crossover to the next along the length of the yarn. This is done as described in Section 2.5.2. Figure 3.10 illustrates the comparison of a TexGen generated cross-section and a micrograph cross-section half way between two crossovers. The full TexGen model is shown in Figure 3.11.

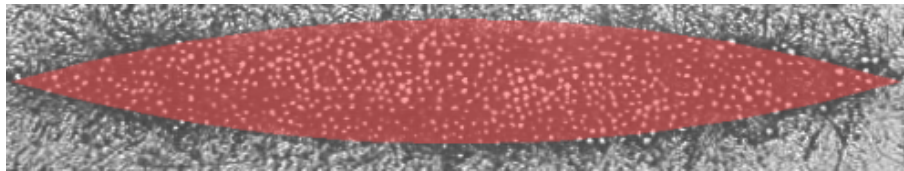


Figure 3.10: Chomarat 150TB yarn cross-section shape between crossovers

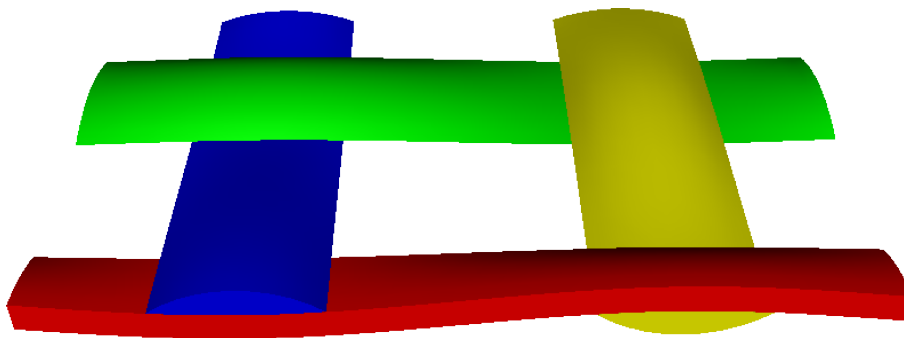


Figure 3.11: Chomarat 150TB refined model



**Table 3.5:** Chomarat 150TB distortion measurements

Method	Mean (mm)	STD (mm)	Samples
Microscope	0.0284	0.00528	5

For completeness Table 3.5 shows the average distortion parameter obtained from a series of cross-section measurements.

### Volume fraction

It is necessary to ensure that the yarn volumes in the geometric model do not intersect. This validation can be done without any further knowledge of the textile (see Section 2.11.2). In the model created above, there are no intersections between the yarn volumes. This is due in part to the fact that the ratio of yarn width to yarn spacing is large.

It is possible to perform some consistency checks between the mass  $m$  and volume  $V_y$  of yarns in a unit cell (see Section 2.10). The areal density  $\rho_A$  of the fabric was obtained from the manufacturer's data sheet, the density  $\rho$  of E-glass fibres was obtained from Reinhard et al. [101] and the yarn volumes and unit cell area are calculated from the geometric model.

**Table 3.6:** Chomarat 150TB properties

Fabric properties	
Total areal density $\rho_A$	150 g/m <sup>2</sup>
Warp areal density	82 g/m <sup>2</sup>
Weft areal density	68 g/m <sup>2</sup>
Fibre density $\rho_f$	2.62 g/cm <sup>3</sup>
Geometric model properties	
Unit cell area $A$	13.333 mm <sup>2</sup>
Total yarn volume $V.Y.$	1.384 mm <sup>3</sup>
Warp yarn volume	0.755 mm <sup>3</sup>
Weft yarn volume	0.630 mm <sup>3</sup>
Volume fraction calculations	
Volume of fibres $V.F.$	0.763 mm <sup>3</sup>
Volume fraction $V_{f_y}$	0.552

The total volume of the fibres  $V.F.$  within a unit cell of fabric is calculated with the

following equation:

$$V.F. = \frac{m}{\rho_f} = \frac{\rho_A A}{\rho_f} \quad (3.7)$$

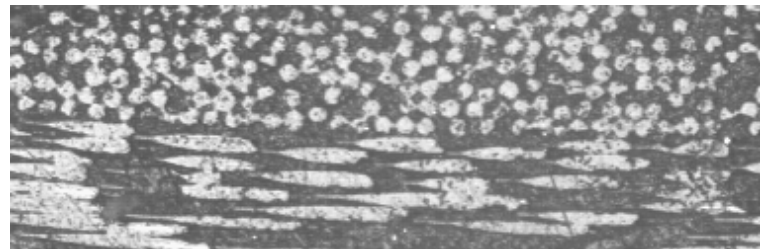
The ratio of fibre volume to yarn volume  $V_{fy}$  is then calculated with:

$$V_{fy} = \frac{V.F.}{V.Y.} \quad (3.8)$$

The results are shown in Table 3.6.

The absolute maximum acceptable volume fraction for circular fibres would be 0.907, assuming the fibres are arranged in a hexagonal array and all fibres are just touching each other. This is a rather idealised case; in actual yarns the fibres are not organised in a regular array. In order to verify the calculation a threshold is applied to a cross-sectional image obtained by optical microscopy such that 55% of the brightest pixels are highlighted (Figure 3.12). The boundaries of the fibres are not clearly visible indicating that the threshold may be too high. The threshold was then manually adjusted until the boundaries of the fibres were clearly visible without losing pixels corresponding to fibres. The best fit was found at approximately 41%. This indicates that there may have been some inaccuracies in the volume fraction calculation. A possible cause for the inaccuracies may be that the volume of the yarns  $V.Y.$  in the model is smaller than in reality. However since the contrast between the fibres and matrix in the micrograph was not sufficient to clearly distinguish between the two, this method should not be considered reliable.

As a further consistency check the ratio of warp/weft yarn masses (1.206) obtained from the manufacturers data should be approximately equal to the ratio of warp/weft yarn volumes (1.198) calculated from the geometric model. There is less than a 0.7% difference between these two ratios.



Original grayscale image



55% white pixels



41% white pixels

**Figure 3.12:** Threshold applied to Chomarar 150TB micrograph

### 3.5 Case study: Chomarat 800S4-F1

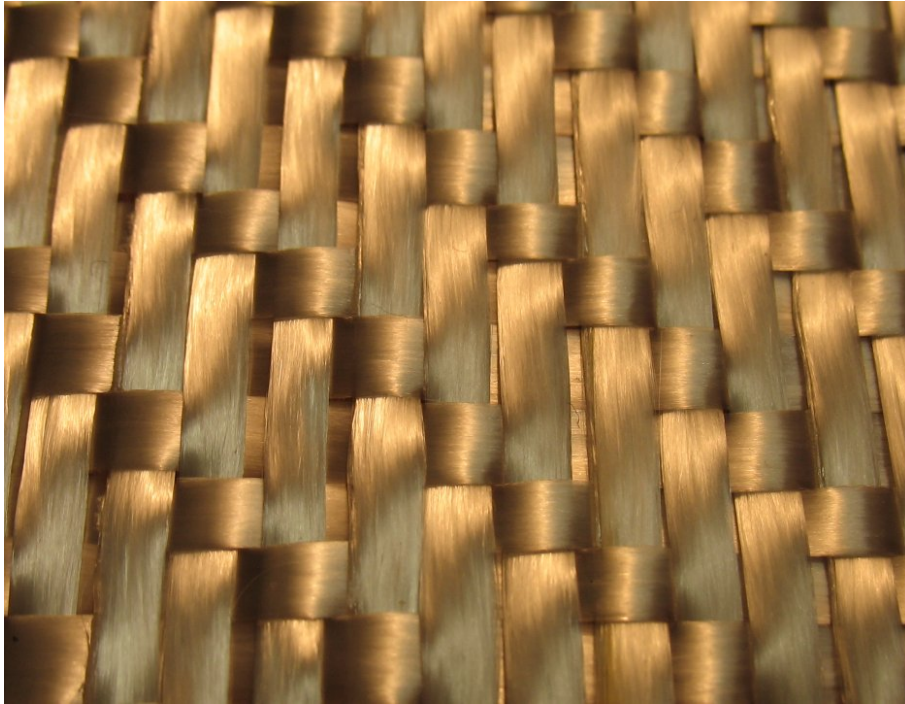


**Figure 3.13:** Chomarat 800S4-F1

Chomarat 800S4-F1 is glass fibre 4 harness satin woven fabric (Figure 3.13).. This fabric is more challenging to model due to its higher tightness.

Fabric thickness measurements<sup>4</sup> are shown in Table 3.7 using the various methods available. Yarn spacing<sup>5</sup> and width<sup>6</sup> measurements are shown in Table 3.8 and Table 3.9 respectively. In this case the spacings between warp and weft yarns are the same, thus only one spacing measurement appears in the table. With these measurements and visual observation of the fabric weave pattern, the yarn path is described by specifying points at crossovers alone. The cross-section is defined as an ellipse all along the yarn as with the initial Chomarat 150TB model and the yarn path is interpolated with a Bézier spline.

Figure 3.14 shows the TexGen model created. Although the model looks similar to the real fabric, after analysis it is clear that there are intersections between the yarn volumes. The measurements taken above cannot be modified since they have been measured from the real fabric. The only parameters which can be changed are the assumed yarn path and section shape.

<sup>4</sup>The average of the KES-f and  $\mu$ CT values rounded to 1 decimal place is used to generate the model

<sup>5</sup>The values measured by ruler rounded to 2 decimal places are used to generate the model

<sup>6</sup>The width of the yarn in the model is the maximum allowable by the interference correction algorithm

**Table 3.7:** Chomarat 800S4-F1 thickness measurements

Method	Mean (mm)	Pressure (gf/cm <sup>2</sup> )	STD (mm)	Samples
KES-f	1.146	0.5	0.210	3
KES-f	0.978	50	0.0762	3
$\mu$ CT	0.904	0	0.0334	10
Microscopy	0.828	0	0.0551	6
Manufacturer	0.75	100 - 260	N/A	10

**Table 3.8:** Chomarat 800S4-F1 yarn spacing measurements

Method	Mean (mm)	STD (mm)	Samples
Ruler	3.158	0.0382	3
$\mu$ CT	3.322	0.354	10
Microscope	3.167	0.245	5

**Table 3.9:** Chomarat 800S4-F1 yarn width measurements

Method	Mean (mm)	STD (mm)	Samples
$\mu$ CT	3.314	0.182	10
Microscope	2.920	0.0857	6

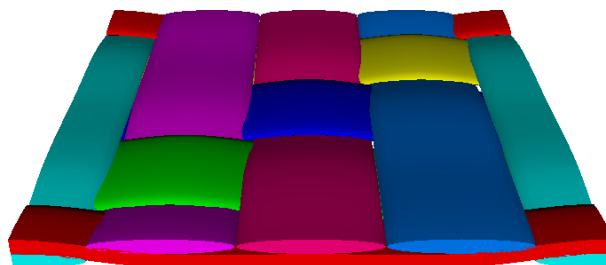


**Figure 3.14:** Basic Chomarat 800S4-F1 TexGen model

First the yarn cross-section shapes will be refined at the crossovers in an attempt to remove intersections. By displaying a cross-section through the textile at the crossovers the intersections are clearer. From Figure 3.15 three types of crossovers can be identified labelled 1, 2 and 3. The first is when the crossing yarn changes position on both sides, the second is when the crossing yarn changes position on only one side and the third case is when the crossing yarn does not change position on either side. Cases 1 and 2 intersect with the crossing yarn, while case 3 does not.



**Figure 3.15:** Cross-section of basic Chomarat 800S4-F1 TexGen model

For case 1, the half of the yarn cross-section that is in contact with the crossing yarn (the lower half in this case) will be modified to follow the yarn path. This is done numerically by obtaining a number of points  $P_i$  lying on the edge of the yarn cross-section. If the line segment from the centre of the yarn  $P_c$  to point  $P_i$  intersects with the transverse yarn then the point is moved. The new position of the point is the intersection of the line with the transverse yarn surface.

For case 2, the section is rotated before the point positions are adjusted in order to minimise cross-section deformation (these rotations can be observed in micrographs and  $\mu$ CT images, as presented in Section 3.5.1). The angle of rotation  $\theta$  is calculated as:

$$\theta = \tan^{-1} \left( \frac{h}{2s} \right) \quad (3.9)$$

The resulting cross-section of the textile is shown in Figure 3.16.



**Figure 3.16:** Cross-section of refined Chomarat 800S4-F1 TexGen model

The full refined TexGen model can be seen in Figure 3.17. The number of intersections has been reduced, but they have not been completely eliminated. The model is transparent such that the intersections can be seen, illustrated as small white spheres. The intersections can be seen more clearly by taking a cross-section diagonally across the fabric where the intersections occur (Figure 3.18).

The remaining intersections occur between crossovers rather than at the crossovers themselves. With some further refinement of the yarn cross-section, these intersections can be removed. First of all it is necessary to ensure that the centreline of the yarn

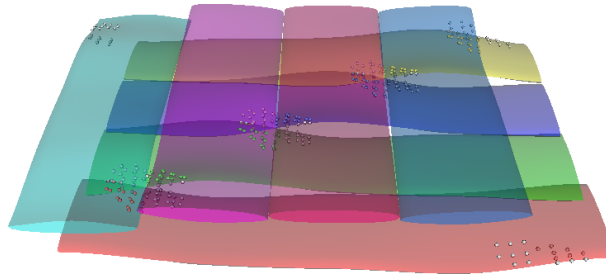


**Figure 3.17:** Refined Chomarat 800S4-F1 TexGen model with intersections shown

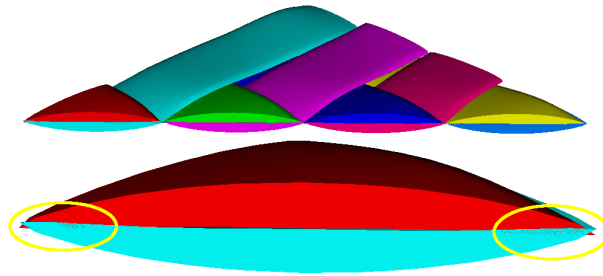


**Figure 3.18:** Diagonal cut of refined Chomarat 800S4-F1 TexGen model

half way between crossovers lies exactly on the mid-plane of the fabric. This can be achieved by adding an additional node at this position, however a more convenient alternative is to create a spline that passes through this point without specifying additional nodes. This is done by using a Bézier spline and specifying that the tangents at all the nodes lie in the horizontal plane. It is not possible to specify the tangents for the cubic periodic spline. Secondly the section shape half way between crossovers must be specified such that it does not intersect with crossing yarns. The section shape is created as the intersection of the two unrotated sections at the master nodes between which it lies (Figure 3.19).

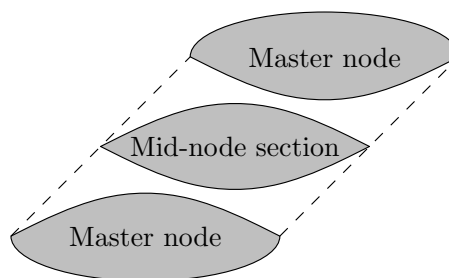


**Figure 3.19:** Section specified between crossovers

With these refinements, an intersection free model can be created and is shown in Figure 3.20.

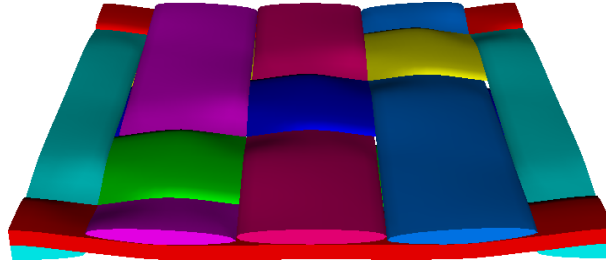


Figure 3.20: Final Chomarat 800S4-F1 TexGen model

### 3.5.1 Validation

#### $\mu$ CT analysis

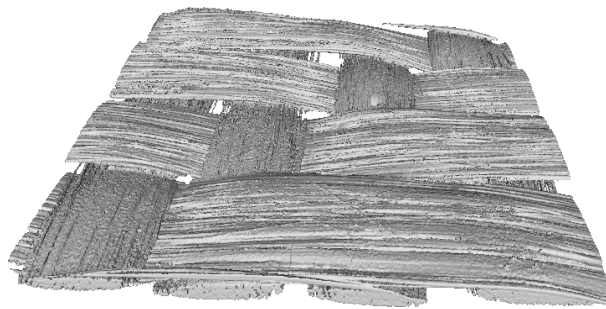


Figure 3.21: Chomarat 800S4-F1  $\mu$ CT reconstruction

Figure 3.21 shows the reconstructed fabric from the  $\mu$ CT data. Firstly, a comparison of the differences between Bézier and periodic cubic splines is shown in Figure 3.22. The figure shows a section taken from the  $\mu$ CT data, with points on the crossing yarn identified manually and interpolated by a Bézier spline and a periodic cubic spline respectively. The root mean square  $d_{rms}$  value between the Bézier spline and the periodic cubic spline is  $11.96 \times 10^{-3}$  mm which is far greater than for the Chomarat 150TB plain weave. This is due to the fact that this fabric is not a plain weave and the tangents at the nodes will be different between the two splines as a result. The root mean square  $d_{rms}$  fit for the Bézier spline is  $9.59 \times 10^{-3}$  mm, whereas the periodic cubic spline has a  $d_{rms}$  of  $17.4 \times 10^{-3}$  mm. Both paths provide a good fit; in this case the Bézier spline is preferred because it gives control over the node tangents which are used to prevent interference in the model.

With image analysis the positions and rotations of the longitudinal yarns were determined for several cross-sections along the centre of the transverse yarns. Three such cross-sections are shown in Figure 3.23. An assumed elliptical shape was used for the algorithm, with rotations ranging from  $\pm 10^\circ$  at 20 intervals.

The rotations of the sections are of special interest since in the TexGen model, rotations



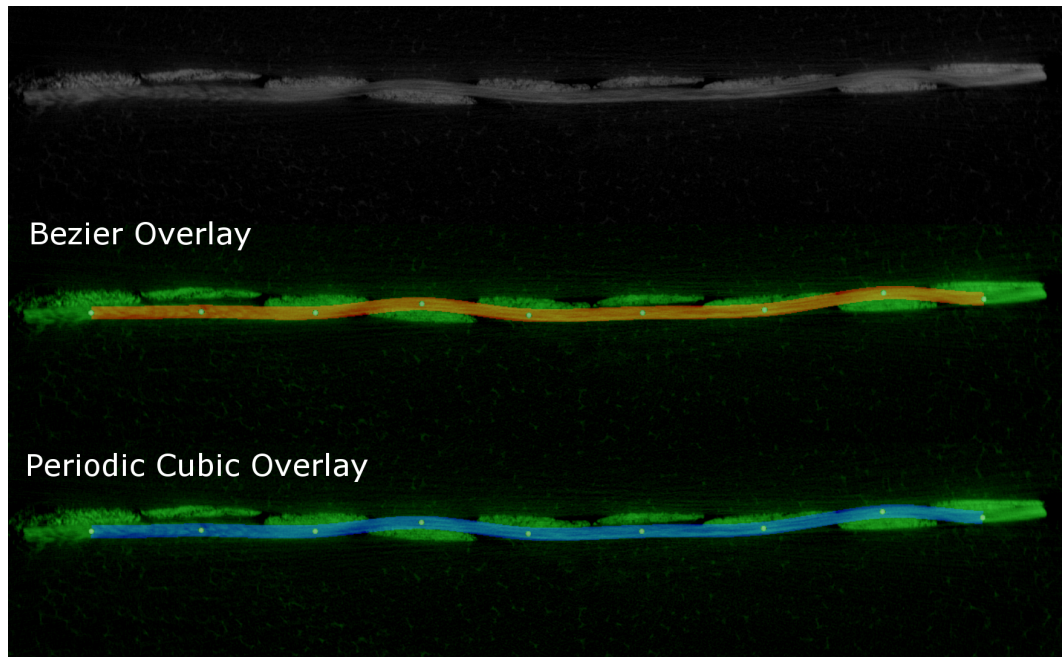


Figure 3.22: Yarn path comparison for 800S4-F1

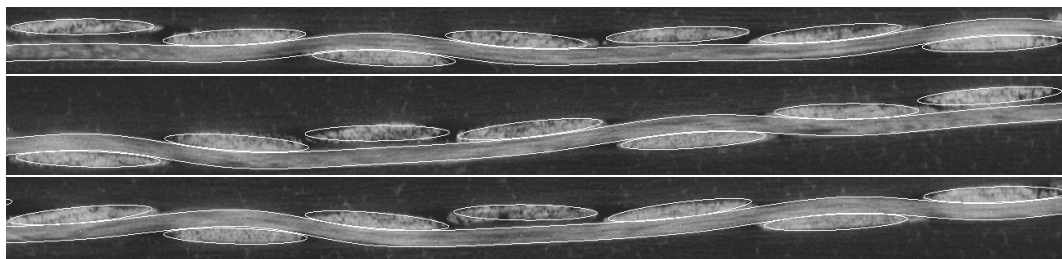
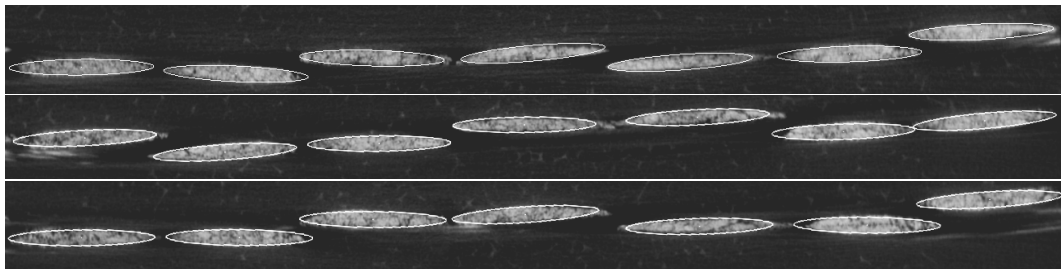


Figure 3.23: Yarn path and cross-section fits for 800S4-F1

have been applied at certain positions. It is possible to verify that this use of rotations is correct by comparing with the  $\mu$ CT cross-section images. The average rotation over 10 cross-sections of type 2 (see Figure 3.15) is 3.87 degrees with a standard deviation of 0.54 degrees. The assumed rotation was 3.04 from Equation 3.9. Agreement is close enough to suggest that the revised model is accurate.

Cross-sections taken between longitudinal yarns (where the longitudinal yarns cannot be seen) are also extracted from the  $\mu$ CT data. Three such cross-sections are shown in Figure 3.24. To compare against the TexGen model, a cross-section is also taken between yarns and shown side by side with a representative  $\mu$ CT cross-section in Figure 3.25. Similarities between the two can be seen, with the rotations of the sections in the same directions. The two lower left cross-sections form a sharp edge where they meet which is not present in the two upper right cross-sections. Again variability exists within the real fabric that is not captured within the TexGen model, but overall the shape agreement is good.



**Figure 3.24:** Cross-section fits for 800S4-F1

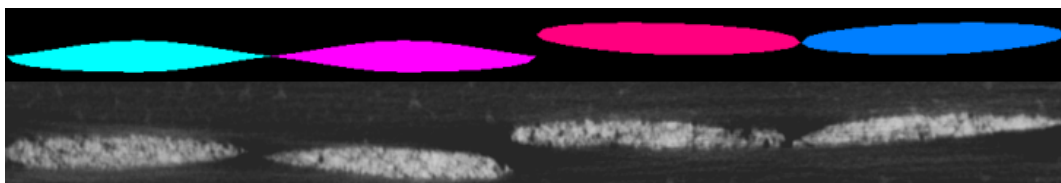


**Figure 3.25:** Cross-section comparison for 800S4-F1

In conclusion, a method to create a geometric model of an interference free tightly packed 2D weave has been generated that is applicable to any 2D weave. The revised algorithms to define yarn rotations and to modify cross-sections (avoiding interference) have been implemented as advanced options in TexGen.

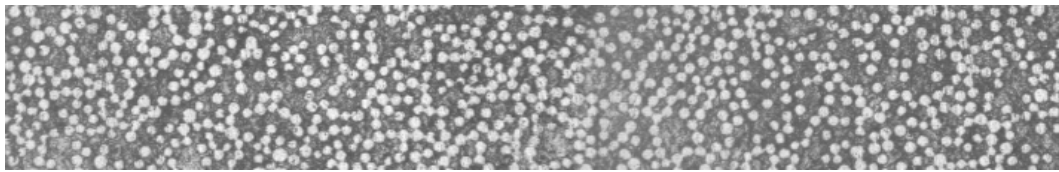
The geometry created for the Chomarat 800S4-F1 has been verified against  $\mu$ CT measurements, showing good agreement.

**Table 3.10:** Chomarat 800S4-F1 properties

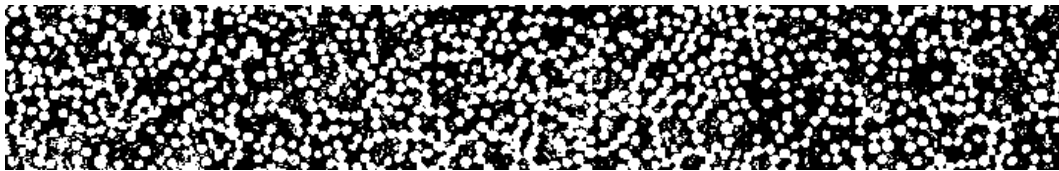
Fabric properties	
Total areal density	780 g/m <sup>2</sup>
Fibre density	2.62 g/cm <sup>3</sup>
Geometric model properties	
Unit cell area	159.7 mm <sup>2</sup>
Total yarn volume	115.6 mm <sup>3</sup>
Volume fraction calculations	
Volume of fibres $V_f$	47.54 mm <sup>3</sup>
Volume fraction $VF$	0.411

### Volume fraction

From the fabric properties and the geometric model properties the volume fraction of the yarns is calculated and shown in Table 3.10. As an additional validation a threshold is applied to a cross-sectional image obtained by optical microscope such that 41% of the brightest pixels are highlighted (Figure 3.26). Individual fibres are clearly visible, providing confidence in the accuracy of the volume fraction calculation.



Original grayscale image



41% white pixels

**Figure 3.26:** Threshold applied to Chomarat 800S4-F1 micrograph

### 3.6 Case study: Unilever woven polyester standard

The polyester fabric, like the Chomarat 150TB, is a plain woven fabric with untwisted yarns (Figure 3.27). The input dimensions which were measured from SEM images of the fabric provided by Unilever are shown in Table 3.11. The model was created using Bézier interpolation and cross-section interference correction as described for the

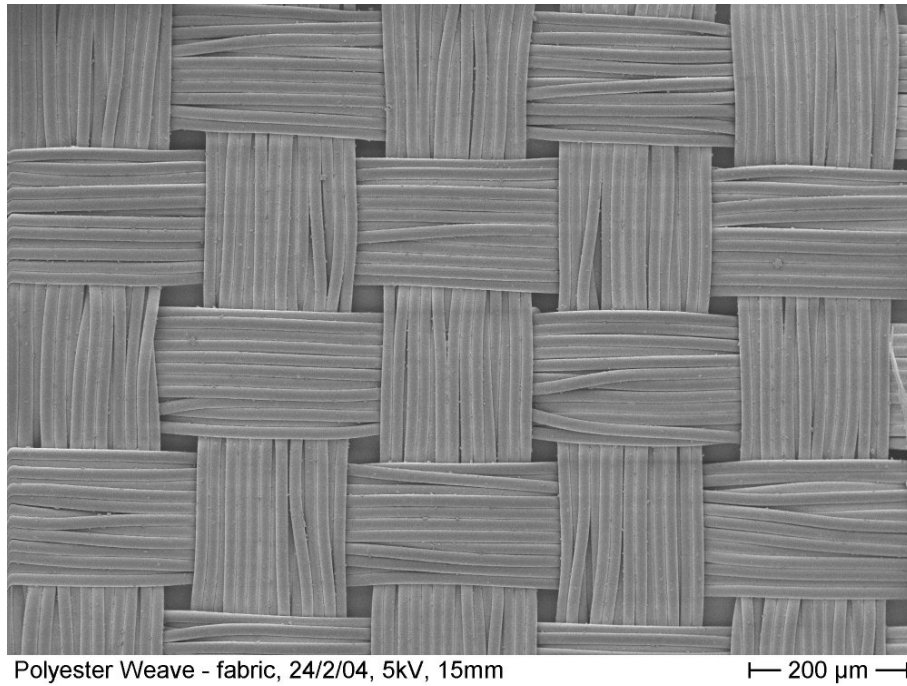


**Figure 3.27:** Polyester fabric

Chomarar 800S4-F1 fabric. The generated model is shown in Figure 3.28.

**Table 3.11:** Polyester yarn measurements

Value	Mean (mm)	STD (mm)	Samples
$s_x$	0.226	0.00474	10
$s_y$	0.190	0.00423	10
$T$	0.0970	0.00645	4
$w_x$	0.192	0.00398	8
$w_y$	0.170	0.00724	8

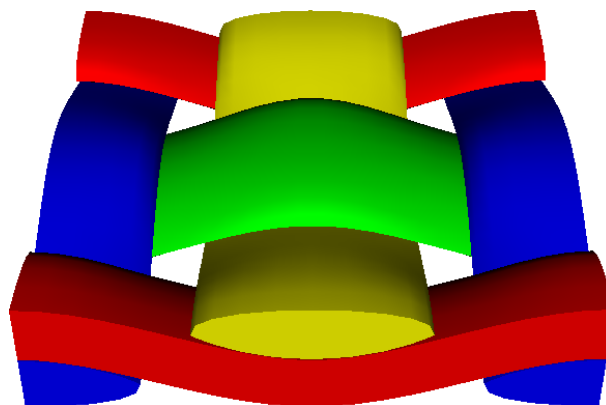


**Figure 3.28:** Polyester TexGen model

A visual comparison between the TexGen model cross-section and the real fabric cross-section is shown in Figure 3.29. The  $d_{rms}$  value between the Bézier and periodic cubic spline is an insignificant  $8.862 \times 10^{-5}$  mm. Hence the type of spline used for this fabric is not important. The  $d_{rms}$  value between points selected on the image and the spline is  $1.86 \times 10^{-3}$  mm which is small in comparison with the fabric thickness of 0.1 mm. The fit between the spline and the real fabric path is good.

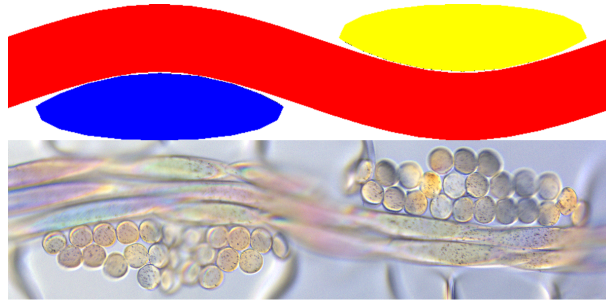


**Figure 3.29:** Polyester section comparison

As can be seen from the cross-section image, the number of fibres contained with a yarn is 24 which is very small compared to the previous examples. It is debatable whether it is reasonable to model the yarns of such a fabric with solid volumes. This may depend on the calculation to be undertaken, hence this discussion will be saved for Chapter 5. In Chapter 4 the fabric will be modelled with each fibre as a separate entity hence the radius of the fibres is important. Table 3.12 shows the fibre radius measurements obtained from the cross-sectional images of the fabric.

**Table 3.12:** Polyester fibre radius measurements

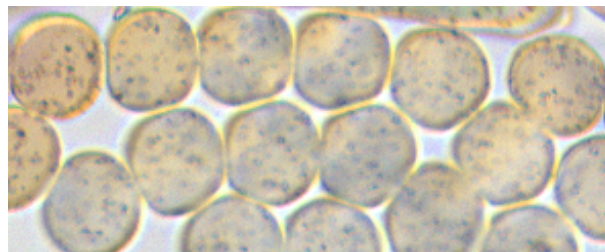
Value	Mean (mm)	STD (mm)	Samples
$r$	0.0183	0.000687	10

### 3.6.1 Validation

From the fabric properties and geometric model properties the volume fraction of the yarns is calculated and shown in Table 3.13. The volume fraction is higher than all the previous fabrics. It can be seen from the cross-sectional Figure 3.29 that the fibres are tightly packed together. This is verified with image analysis (Figure 3.30). In this case the image obtained from the thresholding technique was manually edited with GNU Image Manipulation Program (GIMP [61]) to improve the determination of fibre and resin areas. Since the fibres are so large in comparison with the tow it is difficult to identify a representative area over which to determine the threshold but the technique gives an estimate (84%).

**Table 3.13:** Polyester properties

Fabric properties		
Areal density	69	g/m <sup>2</sup>
Fibre density	1.39	g/cm <sup>3</sup>
Geometric model properties		
Unit cell area	0.1748	mm <sup>2</sup>
Yarn volume	0.0108	mm <sup>3</sup>
Volume fraction calculations		
Volume of fibres $V.F.$	0.008677	mm <sup>3</sup>
Volume fraction $V_{f_y}$	0.80	



Original image



84% black pixels

**Figure 3.30:** Threshold with manual intervention applied to polyester micrograph

### 3.7 Case study: Unilever standard cotton sheeting

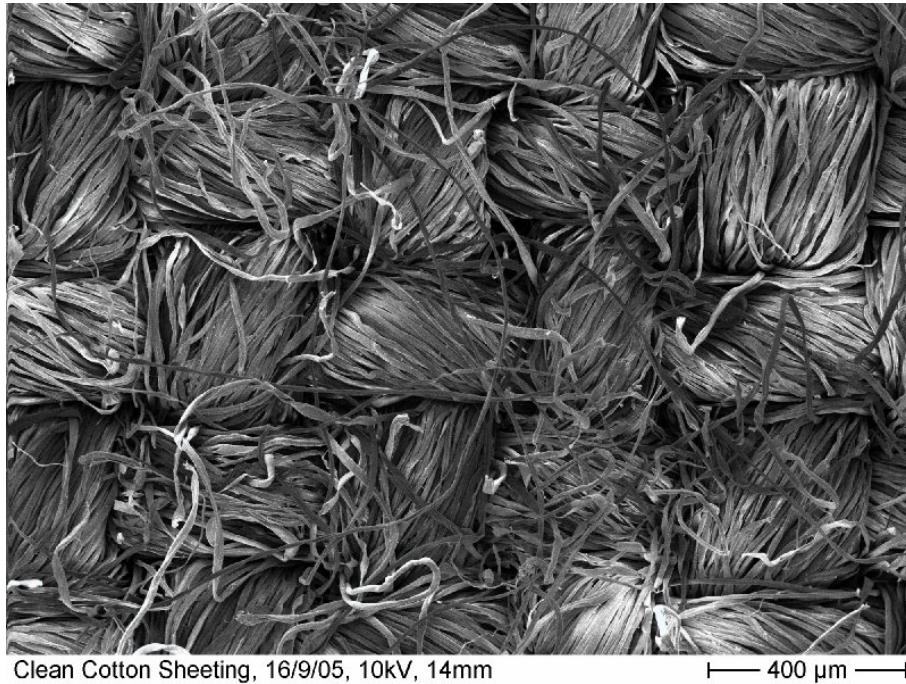


**Figure 3.31:** Cotton fabric

The cotton fabric is also a plain weave (Figure 3.31). Unlike all the other fabrics presented in this chapter the yarns are twisted. However since the yarns are modelled as solid volumes, this has little impact on the geometrical model. The input dimensions are shown in Table 3.14 and the generated model is shown in Figure 3.32. Bézier splines are used for the yarn paths and cross-sections are generated as with the Cho-marat 800S4-F1. The measurements were obtained from scanning electron microscope cross-section images of the fabric.

**Table 3.14:** Cotton yarn measurements

Value	Mean (mm)	STD (mm)	Samples
$s_x$	0.359	0.0285	8
$s_y$	0.327	0.0155	8
$T$	0.287	0.0166	10
$w_x$	0.295	0.0521	8
$w_y$	0.255	0.0169	8

Figure 3.33 shows a comparison of the TexGen model with the cross-section images of the fabric. Unlike all the previous examples, this fabric has twisted yarns which is the reason for the poorly defined cross-sections. This does not affect the TexGen

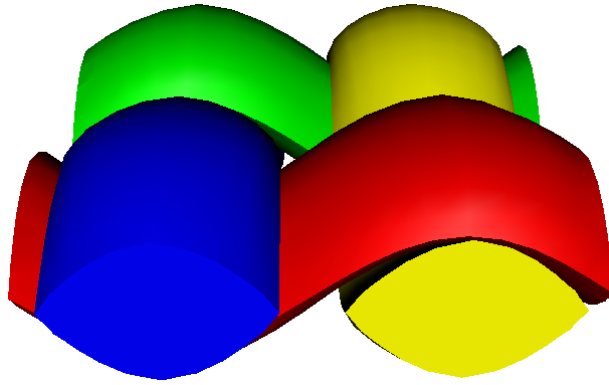


Figure 3.32: Cotton TexGen model

model since the yarns are modelled as solid volumes, however it will influence the mechanical properties of the yarns as discussed in Chapter 5. The  $d_{rms}$  value between the Bézier and periodic cubic spline is  $0.854 \times 10^{-3}$  mm which is larger than for the other plain weaves analysed earlier. This is due to the amount of crimp present in the fabric. The differences between the two splines start to become apparent as the amplitude increases. The  $d_{rms}$  value between points selected on the image and the periodic cubic spline is  $7.914 \times 10^{-3}$  mm. The  $d_{rms}$  value between points selected on the image and the Bézier spline is  $6.967 \times 10^{-3}$  mm. The results are not conclusive but the Bézier spline seems to provide a slightly better fit.

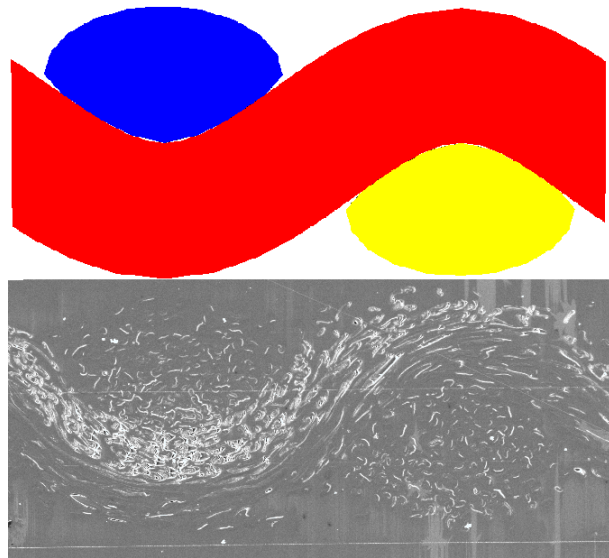


Figure 3.33: Cotton section comparison

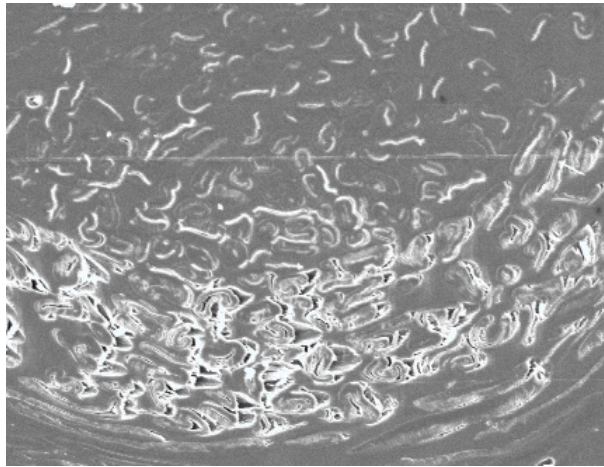


**Table 3.15:** Cotton properties

Fabric properties	
Areal density	160 g/m <sup>2</sup>
Fibre density	1.54 g/cm <sup>3</sup>
Geometric model properties	
Unit cell area	0.4752 mm <sup>2</sup>
Yarn volume	0.0855 mm <sup>3</sup>
Volume fraction calculations	
Volume of fibres $V.F.$	0.0493 mm <sup>3</sup>
Volume fraction $V_{f,y}$	0.577

### 3.7.1 Validation

From the fabric properties and geometric model properties the volume fraction of the yarns is calculated and shown in Table 3.15. Validation of the volume fraction with thresholding was not performed as it was difficult to distinguish between the fibres and matrix from the images (see Figure 3.34).

**Figure 3.34:** Close up of cotton micrograph

## 3.8 Conclusions

The geometrical modelling of a range of 2D woven textiles has been presented in this section including two fabrics typically used as textile composite reinforcements (Chomarar 150TB and 800S4-F1) and two fabrics typically used as clothing fabrics (Unilever polyester and cotton). Cross-sectional images of all the fabrics were obtained using optical microscopy and SEM. 3D data of the Chomarar fabrics were obtained via microto-

mography. Using this data, measurements of yarn width, spacing and fabric thickness were obtained. Fabric thickness was also obtained from KES-f measurements. Using this input, geometrical models of the fabrics were created using the TexGen software described in Chapter 2.

Intersection between yarns was found to be a problem for the Chomarat 800S4-F1, cotton and polyester models. A generic method applicable to 2D woven fabrics was devised to modify the models such to remove these intersections without requiring additional input parameters or modifying the original input parameters.

The resulting models were validated against the microscopy, SEM and  $\mu$ CT data. Validation included a visual comparison between yarn path and cross-sectional shape and numerical calculation of the root mean square difference of the generated and measured yarn path. The yarn path fit was found to be better for fabrics with lower crimp. For the Chomarat 800S4-F1 fabric, yarn rotations were obtained from image analysis and compared against the modelled rotations. Fibre volume fractions within yarns were calculated for all the fabrics and found to lie within acceptable limits. The final geometric models are considered to be highly accurate, however the accuracy of the dimensions of the models depends entirely on the input parameters. A high degree of variability was found between the different measurement techniques, especially for the fabric thickness. This is thought to be due to the susceptibility of fabrics to deformations during manufacture and handling.

The two Chomarat geometric models will be used in Chapter 5 for finite element analysis of their mechanical properties. The dimensions measured for the polyester fabric will be used in Chapter 4 for modelling its shear behaviour using a novel numerical technique. The cotton fabric geometric model has been created to demonstrate the ability to model a wider range of fabrics, and is not carried further in the present study.

# Mechanical modelling of tows

## 4.1 Introduction

In this chapter the mechanical behaviour of yarns and more specifically tows is analysed. This is a challenging task considering that each fibre within a yarn is a separate body. There are various types of yarn. Some yarns have sizing applied to them which keep the fibres bonded together and promote fibre-resin bonding. Some yarns are twisted in order to keep the fibres together. Tows are a subclass of yarns where the fibres are all aligned parallel to the yarn axis (i.e. untwisted yarns). Each type of yarn requires a very different modelling approach. The focus of this chapter is on non-impregnated tows. The literature survey (Section 4.2) shows that the interactions between fibres within a yarn plays a significant role in its mechanical properties.

In Section 4.3 details of a numerical model designed to model these interactions are presented. Fibres are modelled as cylinders which are able to bend according to Euler-Bernoulli beam equations. A small section of tow is modelled containing a number of these fibres all approximately parallel to each other. The fibres are distributed randomly following a pre-defined distribution. Contact forces between the fibres are resolved in an iterative manner to obtain a converged steady state. In Section 4.4 the model is used to simulate the compaction of a tow. Boundary conditions are applied to the tow section calculating deformation energy in the fibres over a series of steps. Hundreds of these small sections of tow are modelled and results are averaged to approximate the behaviour of an entire tow. These results are compared to experimental data from various sources.

In Section 4.5 the model is extended to represent several tows interacting with each other in a simple plain weave arrangement. Due to limitations in CPU power, the number of fibres within a tow must be relatively small. However this model is suitable

for modelling the behaviour of the polyester plain weave presented in Chapter 3. The initial geometry of the plain weave can be predicted with this model and is compared against the TexGen model previously created. The model is also able to predict the friction energy dissipated during shearing of the fabric.

## 4.2 Literature survey

In this section, a survey of the existing publications relevant to modelling of mechanical properties of tows is described. Characterising the mechanical properties of tows is an important step in modelling of textile unit cells. One of the most important properties to obtain is the transverse compaction of tows. As will be shown in Chapter 5, the compaction properties of tows not only affect the compaction properties of textile unit cells but also their tensile and shear properties.

### 4.2.1 Compression of random fibre assemblies

Several studies have developed analytical models for the compaction of fibre assemblies. One of the earliest dates back to 1946 and was by van Wyk [136]. He proposed an analytical model for the compression of randomly oriented wool fibres which in contrast to tows have no preferential fibre direction. More specifically, he determined the pressure applied to an assembly of fibres as a function of their bounding volume. van Wyk simplified the problem by assuming that the only force resisting compression is due to bending of fibres caused by fibre to fibre point contacts. The average distance  $\lambda$  between contact points along the length of a fibre is calculated by taking the total length of fibre  $L$  within the bounding volume  $v$  and dividing by twice the total number of contacts  $n$  within that volume. Two different methods are described for calculating the number of contacts within the volume based on mathematical probabilities of fibres intersecting, each of which provide virtually identical results.

With the average distance between contacts known and assuming that the fibres bend following the Euler-Bernoulli beam equation for a point load applied at the centre of a beam with built-in ends, an equation relating the pressure necessary to compress the fibre assembly is obtained. Integrating gives the total pressure  $P$  for a given compaction:

$$P = \frac{KEm^3}{\rho^3} \left( \frac{I}{v^3} - \frac{I}{v_0^3} \right) \quad (4.1)$$

where  $K$  is a constant to be determined experimentally, and used to fit experimental data. The mass  $m$  represents the total mass of the fibre assembly with fibre density  $\rho$ ,

the volume  $v$  represents the bounding volume of the fibre assembly.  $v_0$  is the initial bounding volume when  $P = 0$ , although in practice this should be chosen as the value that gives the best fit to the experimental results rather than the actual measured initial bounding volume.  $E$  and  $I$  are the Young's modulus and second moment of area of the fibre.

Experimental results for the compression of wool taken from three to four year-old African merino sheep were obtained. The comparisons between the equation and experimental results are good except for low degrees of compression. However this equation applies only to fibres that are oriented completely randomly in 3D space, and is therefore not directly applicable to yarns.

#### 4.2.2 Compression of orientated fibre assemblies

To address the above limitation Komori and Makishima [65] expanded van Wyk's work by deriving an equation to calculate the number of contacts within an assembly of fibres of non-uniform random orientation. A density function is introduced which defines how the fibres are orientated in 3D space by assigning a certain probability to each possible direction. The number of fibre to fibre contacts can then be calculated using this density function. The number of contacts in a fibre assembly is one of the most important factors when trying to derive mechanical properties for it since it is at these contacts that the forces are transmitted through the structure.

The density function is based on polar coordinates, defining fibre orientations as two independent angles. The angle  $\theta$  is defined as the angle between the z axis and the axis of the fibre. The angle  $\varphi$  is defined as the angle between the x axis and the projection of the axis of the fibre on to the x-y plane (see Figure 4.1).

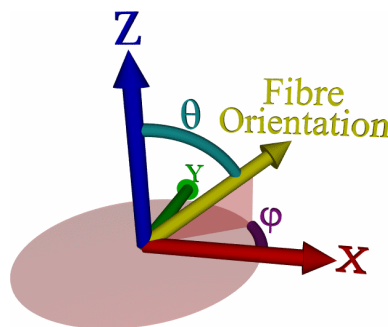
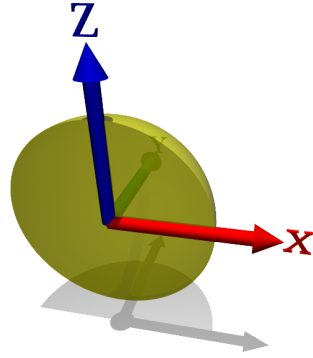


Figure 4.1: Diagram showing definitions of angles  $\theta$  and  $\varphi$

Both angles are confined between the limits of 0 and  $\pi$ , giving the range shown in Figure 4.2. Note that the orientation of a fibre defined by a vector  $\vec{V}$  is identical to the orientation of a fibre defined by the vector  $-\vec{V}$ . Thus the range does not need to span

a full sphere, a hemisphere is sufficient.



**Figure 4.2:** Diagram showing range of angles  $\theta$  and  $\varphi$  when integrating from 0 to  $\pi$

The density function is defined as follows. The probability of finding the orientation of fibre in the infinitesimal range of angles  $\theta$  to  $\theta + d\theta$  and  $\varphi$  to  $\varphi + d\varphi$  is defined as  $\Omega(\theta, \varphi) \sin \theta d\varphi d\theta$ . The  $\sin \theta$  component is to account for the fact that if a number of random values were generated for  $\theta$  and  $\varphi$ , a higher distribution of fibres would be found to be oriented towards the z axis. This definition ensures that a constant value for the density function  $\Omega(\theta, \varphi)$  will give a uniform distribution of fibres. To ensure that the probability of finding a fibre of orientation in the range 0 to  $\pi$  for both angles (i.e. all possible orientations) is 1, the density function must satisfy the following equation:

$$\int_0^\pi \int_0^\pi \Omega(\theta, \varphi) \sin \theta d\varphi d\theta = 1 \quad (4.2)$$

Given two short fibre segments of fixed orientations  $(\theta, \varphi)$  and  $(\theta', \varphi')$  respectively, it is possible to calculate the volume of the region which the centre of the second fibre must enter in order to intersect with the first fibre. The volume of this region depends on the angle between the two fibre axes. The volume is at a maximum when the two axes are perpendicular, and at a minimum when the two axes are parallel. The probability  $p$  that these two short fibre segments of length  $\lambda$  and diameter  $D$  come into contact is the volume of this region divided by the total bounding volume of the fibre assembly  $v$ :

$$p = \frac{2D\lambda^2}{v} \sin \chi \quad (4.3)$$

where the angle  $\chi$  is defined by the following formula:

$$\cos \chi = \cos \theta \cos \theta' + \sin \theta \sin \theta' \cos(\varphi - \varphi') \quad (4.4)$$

The total number of contacts  $n$  within the fibre assembly is defined by the following equation:

$$n = \frac{DL^2}{V} \int_0^\pi \int_0^\pi \left( \int_0^\pi \int_0^\pi \Omega(\theta', \varphi') \sin \chi(\theta, \varphi, \theta', \varphi') \sin \theta' d\varphi' d\theta' \right) \Omega(\theta, \varphi) \sin \theta d\varphi d\theta \quad (4.5)$$

where  $V$  represents the fibre volume fraction of the fibre assembly. The number of contacts obtained using a uniform density function (i.e. where fibres are randomly oriented) is in agreement with that derived by van Wyk. Using a density function which corresponds to a 2D network of fibres, it has been shown that the results correspond to those derived by Kallmes and Corte [57].

These equations can be applied directly to tows if a suitable density function can be obtained by characterising the orientations of fibres within a tow. It may be feasible to derive a density function by analysing data of a yarn obtained via microtomography.

Using the results derived by Komori and Makishima, Lee and Lee [70, 71] studied the compression of fibre assemblies with orientations defined by the density function. The method described can be used to predict the effective Young's modulus and Poisson's ratio of the fibre assembly given the fibre diameter, fibre volume fraction, Young's modulus of the fibres and the density function.

The deflection of a fibre of a specific orientation is calculated using the Euler-Bernoulli Beam Equation for a point load applied at the centre of a beam with pin-jointed ends (note: van Wyk used built-in ends). The force used to calculate this deflection is equal to the average contact force projected to the plane perpendicular to the fibre axis. The average contact force  $C$  applied on each contact in a fibre assembly is determined by dividing the total applied force by the number of contacts in the assembly. Note that the deflection of the fibre will not be in the same direction as the force applied unless the force is perpendicular to the fibre axis.

The deflection of individual fibres is thus given as a function of orientation. The average deflection for all three axes can be determined by integrating the deflection over all fibre orientations multiplied by the density function. However for a fibre assembly which has a symmetric density about the x-y and y-z planes, deflections perpendicular to the compression direction will cancel out leaving an average deflection of 0. Therefore to obtain a measure of Poisson's ratio the absolute average deflection is needed. To obtain this the integration is performed between the limits of 0 and  $\frac{\pi}{2}$  instead of 0 to  $\pi$  (see Figure 4.3). Thus only positive values for deflection in the x, y and z axes are taken into account. The result is then multiplied by 4 to account for the change in limits. This simplification only works when the density function is symmetric about the x-y and y-z planes which in most cases will be the case.

Values for the effective Young's Modulus ( $E_x, E_y, E_z$ ) and Poisson's Ratio ( $\nu_{xy}, \nu_{xz}, \nu_{yx}, \nu_{yz}, \nu_{zx}, \nu_{zy}$ ) can be extracted from the average deflection and total force applied. There are however a large number of assumptions made that affect the validity of the model:

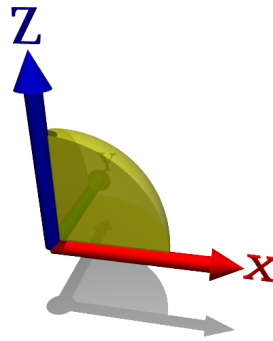


**Figure 4.3:** Diagram showing range of angles  $\theta$  and  $\varphi$  when integrating from 0 to  $\frac{\pi}{2}$

- The contact force between fibres is assumed to be identical for all contacts and in the same direction as the force applied to the fibre assembly. In fact there is likely to be a large variation in contact forces between fibres both in magnitude and direction. Whether this has a significant effect on the results remains to be shown.
- The contacts between fibres are assumed to be uniformly spaced with fixed distance between them. In reality there is likely to be a large variation in distances between contacts. This has been shown to have an insignificant effect on the results by Pan and Carnaby [92].
- The contact force is assumed to be applied half way between adjacent contacts and in the opposite direction of adjacent contacts. In reality contacts could occur anywhere along the length of a fibre and in any direction.
- Deflection of the fibre is calculated such that the fibre is assumed to be straight before loading. This assumption is reasonable, as there should be little fibre deflection before loading especially for tows.
- Fibres in contact are assumed to be rigidly fixed to each other, not allowing any slippage or separation. In reality fibres will slip along each other when the tangential force exceeds the static friction force. Carnaby and Pan [15, 93] have extended the model to include fibre slippage which will be discussed further in Section 4.2.3.
- The fibre density function is assumed to remain constant during the compression stage. In reality fibres will tend to align themselves with the plane perpendicular to the direction of compression. Hence the model is only valid for the initial compression stage.

Experimental results were obtained for uniaxial twisted fibre assemblies and uniform



random fibre assemblies. Although there are large differences between the experimental values of the initial compressive Young's modulus and theoretical values, the plot of experimental values against the cube of fibre volume fraction is linear in agreement with the theory.

Pan and Carnaby [92] extended Lee and Lee's work to include shear moduli predictions using the same assumptions. They determined the average absolute deflection of a contact point caused by a set of shear forces. The shear strains were then obtained by relating the average deflection with the relevant dimensions of the bounding volume of the fibre assembly. Hence shear moduli values could be calculated. The equation was verified by obtaining a value of shear modulus for the uniform random case. This case should be isotropic hence the shear modulus  $G$  should be related to the Young's modulus  $E$  and Poisson's ratio  $\nu$  by the following equation:

$$G = \frac{E}{2(1 + \nu)} \quad (4.6)$$

This was shown to be the case by using the results obtained by Lee and Lee [70, 71]. A similar verification was performed for uniaxially oriented fibres with helical crimp.

The question was raised as to whether the fibres should be modelled as beams with built-in ends or pin-jointed ends. van Wyk originally used built-in ends, while Lee and Lee opted for the pin-jointed ends. Pan and Carnaby decided to revert to built-in ends as they believed this to be more suitable. The argument in favour of built-in ends is that continuity of curvature is ensured at the supported ends, although when compared against experimental results pin-jointed ends give closer agreement. The difference in solution between the two models is that built-in ends increase the stiffness by a factor of 4. The different formulations do not affect the shape of the curve, only the scale and since these models require a fitting parameter to be compared to experiments the different formulations only affect the fitting parameter. Therefore it is the opinion of the present author that the choice of formulation is not important until predictive results can be achieved.

### 4.2.3 Effect of inter-fibre slipping

Carnaby and Pan [15] also considered the effect of fibre slippage in a separate study. The general procedure consists of classifying contacts as slipping or non-slipping. Considering two fibres in contact it is possible to split the contact force into two components, a component normal to the contact surface and a component tangential to the contact surface. If tangential force exceeds the multiplication of the normal force and the coefficient of friction  $\mu$  then slipping will occur.

Grosberg [40], Grosberg and Smith [41] showed that even without external loading, significant contact forces already exist within a fibre assembly. These forces are assumed to act in the direction normal to the contact surface with no tangential component. Hence the frictional force that must be overcome for the fibres to slip relative to each other is increased by this phenomenon. This force is quantified by the withdrawal force per unit length necessary to remove a fibre from the assembly ( $WF_0$ ).

The magnitudes of the tangential and normal components of the contact force  $\vec{C}$  are a function of the angle between the compression direction of the fibre assembly and the normal to the contact surface. If this angle exceeds a certain critical angle, the contact is classified as slipping. Equation 4.7 was derived classifying fibres that are likely to slip based on their orientations  $\theta$  and  $\varphi$  and the compression forces applied to the fibre assembly. The equation is general enough to take into account external loading from several directions but unfortunately an analytical solution for the equation could not be found.

$$\vec{C}_x \sin \theta \cos \varphi + \vec{C}_y \sin \theta \cos \varphi + \vec{C}_z \cos \theta \geq \mu(\vec{C}_x \sqrt{1 - \sin^2 \theta \cos^2 \varphi} + \vec{C}_y \sqrt{1 - \sin^2 \theta \sin^2 \varphi} + \vec{C}_z \sin \theta) + WF_0 \lambda \quad (4.7)$$

However for the case of compression along the  $z$  axis alone, the slip limit is independent of the angle  $\varphi$  and depends only on the angle  $\theta$ . For compression along the  $x$  and  $y$  axes, the slip limit is more complicated and depends on both angles  $\theta$  and  $\varphi$ . However this is only a consequence of the orientation definitions. By transforming the coordinate system, simple slip limits depending on only one angle for compression along the  $x$  and  $y$  axes can be obtained.

In order to obtain a compression modulus taking into account fibre slippage, the proportion of slipping contacts and non-slipping contacts must be known. The total number of contacts can already be determined as demonstrated by Komori and Makishima [65]. Dividing the number of slipping contacts by the total number of contacts gives the required proportion. The number of slipping contacts is determined in the same manner as the total contacts except that the integration limits are chosen to include only slipping contacts.

Slip is incorporated into the results by assuming that only the non-slipping contacts cause deflections in the fibres. It is also this deflection which accounts for the change in volume of the fibre assembly. The element length is the total fibre length divided by the number of non-slipping contacts. Part of the force used to compress the fibre assembly causes the contacts to slip over each other. Young's modulus and Poisson's

ratio are derived in the same manner as by Lee and Lee [70, 71].

The inclusion of the fibre slipping has made it possible to model the hysteresis effect of the fibre assembly. After an external load applied to a fibre assembly is removed, the assembly does not return to its original state. A great deal of irrecoverable energy is lost due to inter-fibre friction. An incremental approach is used to predict the compression and recovery curves. At each successive increment the load applied to the fibre assembly is increased by a small amount until the full forces is reached. Then for the recovery stage, the load is slowly decreased until all load has been removed.

The model has been compared against theoretical and experimental results obtained by Lee and Lee [70, 71] for uniform random fibre assemblies. The effect of including fibre slippage greatly reduces the initial Young's modulus bringing it closer to the experimental results. Unfortunately no comparison was made against experimental results for non-uniform random fibre assemblies.

#### **4.2.4 Compression modelling of oriented fibre assemblies via energy method**

Komori and Itoh [55, 63, 64] proposed a new theory for the compression of fibre assemblies. The theory differs from the previous theories in three ways: the length of the bending element depends on the orientation of the fibre, the law to describe the change in the direction distribution induced by the compression is given in a differential form, and the mechanical relation is derived using an energy method.

Fibre elements are assumed to bend to a circular arc rather than under three point bending. In this study, rather than trying to calculate the deflection due to a certain force acting between fibre contacts a different approach is taken: the deflection of the fibre elements is assumed to be proportional to the compression of the total fibre assembly. The energy required to cause this deflection is calculated such that the change in total energy stored within the fibre assembly can be calculated. The change in energy can be related to the change in stress acting on the fibre assembly, and hence Young's modulus can be determined. Poisson's ratio can equally be determined due to the assumed proportional deflection of fibre elements.

Using the assumption that the deflection of the fibres is proportional to the compaction of the fibre assembly, an equation for the change in density function can be derived with respect to compaction. Updating the density function as the fibre assembly is compacted should improve accuracy.

The results of this model have been compared against the equations from van Wyk [136] for uniformly randomly distributed fibres under hydrostatic compression. There

is agreement between the two methods except for the numerical constants which are different due to the assumed bending shape. Results from this model using other loading conditions and fibre distributions have been derived, however no comparisons to experimental results were performed.

Lee and Carnaby [69, 73] conducted a similar study on uniform random assemblies of fibres using an energy method, however this method was not applied to unidirectional fibre assemblies.

#### 4.2.5 Deformation behaviour of wavy aligned fibres

Gutowski and Cai developed a theory for the deformation behaviour of aligned fibres suitable for production of composite materials [14, 42, 43]. The path of each individual fibre is assumed to follow a sine wave defined by Equation 4.8 with arc length  $l$  and height  $a$  as parameters to be determined.

$$y = \frac{a}{2} \left( 1 - \cos \frac{2\pi x}{l} \right) \quad (4.8)$$

Although this fibre path is arbitrary it was found that results for other reasonable paths follow the same trends but on a different scale. In this case the scale is not important because the model is not able to predict properties without fitting parameters. Hence using different fibre paths will merely change the fitting parameters. However, no justification was given for assuming that fibres do indeed have a periodic waviness that repeats itself at regular intervals. In reality one might expect fibres to deviate from their direction axis in a more random way.

An attempt was made at determining the parameters of arc length and height experimentally for graphite fibres by taking a section of fibres cast in epoxy resin in a plane parallel to the fibre direction and observing them under a microscope. The ratio  $\beta$  of arc length divided by height was found to be of the order of  $10^2$  [43].

In contrast with the previous papers reviewed, the number of contacts between fibres is inferred from the waviness of the fibres rather than calculating it from the distribution of fibre orientations. It is assumed that there is one contact per half arc length of fibre. The approach taken by Komori and Makishima [65] is perhaps more rigorous since they attempted to predict the number of contacts statistically rather than assuming a certain number of contacts.

The arc length is assumed to be proportional to the height, hence as the fibre segment is transversely compressed the arc length decreases which not only increases the stiffness of the fibre segment but also increases the number of assumed contacts. There is no

physical basis for this dubious assumption and the shape given to the compression versus fibre volume fraction curve is largely governed by this assumption.

Nevertheless, in order to obtain a stress-strain relationship for transverse compression of the fibre assembly a single fibre is enclosed within a bounding box. The compressive modulus of the fibre assembly is assumed to be the same as the compressive modulus of the bounding box containing this single fibre (Figure 4.4). The compression direction is always assumed to be in the same plane as the tow waviness with no twisting of the fibre permitted.

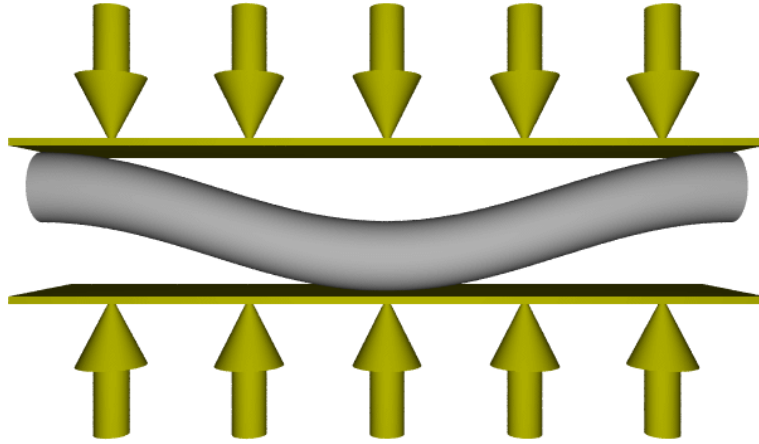


**Figure 4.4:** Compression of a single fibre within a bounding box

Similarly the stress-strain relationship for axial extension of the fibre assembly is obtained from the extension of a single fibre enclosed within a bounding box (Figure 4.5). There is a slight non-linear effect due to the straightening of the fibre.



**Figure 4.5:** Axial extension of a single fibre within a bounding box

The deflections of the fibre in the axial and transverse directions due to the forces applied are obtained by using the unit load energy technique [132]. The equation relating transverse compression stresses  $\sigma_x$  and  $\sigma_y$  with fibre volume fraction is given in Equation 4.9, where  $z$  is parallel to the fibre axis.

$$\sigma_x = \sigma_y = \frac{3\pi E \left(1 - \sqrt{\frac{V_f}{V_0}}\right)}{\beta^4 \left(\sqrt{\frac{V_a}{V_f}} - 1\right)^4} \quad (4.9)$$

Gutowski and Cai assumed the shear modulus in the plane transverse to the fibres to be zero and they did not derive the shear moduli in the other directions. In contrast

McBride [88] assumed the shear modulus in the plane transverse to the fibres to be defined by Equation 4.6. This equation may be used due to the transverse isotropy. The transverse Poisson's ratio is assumed to be constant and should be determined experimentally. Furthermore he assumed that the longitudinal shear modulus is proportional to the transverse shear modulus by a constant of proportionality set to a value of around 2 with no further explanation. Direct measurement of this constant was deemed to be impracticable.

Gutowski and Cai's comparisons against experimental results for compression of carbon fibre tows provide very good agreement when the parameters  $\beta$  and  $V_0$  are adjusted to fit the data, despite the simplicity of the model. It was found that a different set of parameters were needed to fit the model to experimental data obtained for seemingly similar yarns. This could be attributed to the variability within the fibre assembly. McBride's comparisons against experimental results for compression of Kevlar and E-Glass fibres also gave very good agreement for plain strain compression once the model had been fitted to the results. The values of initial volume fraction  $V_0$  were fairly low at 0.24 and 0.35 for the Kevlar and E-Glass yarns respectively and the values of  $\beta$  were of the order of  $10^2$  as observed experimentally by Gutowski et al. [43]. However there are some discrepancies between the model and the experimental results for uniaxial compression which are thought to be partly due to the model and partly due to the experimental technique used.

#### 4.2.6 Deformation of unidirectional helically crimped fibre assemblies

A number of studies have been made on compression of fibre assemblies assuming an initially curved fibre as a bending element rather than a straight fibre [16, 32, 66, 72, 87]. The fibres are assumed to be helical in shape which is a valid assumption for wool fibres. However the main interest of this chapter is in tows where fibres tend to be straight with negligible crimp for which these models are unsuitable.

#### 4.2.7 Application to finite element analysis software

Curiskis and Carnaby [26] performed a study on the extent to which continuum mechanics may be used to model the mechanical properties of assemblies of unidirectional fibres. Assemblies of unidirectional fibres may be regarded as transversely isotropic, which means that the mechanical properties are isotropic in the plane perpendicular to the direction of the assembly of fibres. They concluded that for small strain and linear elastic behaviour the assembly of fibres might best be characterised mechanically as a

degenerate square-symmetric homogeneous continuum. However it is only reasonable to treat it as such if the number of fibres is large enough that the influence of individual fibres on the overall assembly is small.

Djaja et al. [31] have derived a tangent stiffness formulation from previous micromechanical models suitable for use by finite element packages. The models used are the ones derived by Lee and Lee [70] for Young's modulus and Poisson's ratio and Pan and Carnaby [92] for shear modulus. These models do not include fibre slipping, however the method of obtaining the tangent stiffness matrix can be used in conjunction with other models. The values of Young's modulus, shear modulus and Poisson's ratio are combined into a six by six tangent compliance matrix. Most finite element analysis packages required a tangent stiffness matrix rather than a tangent compliance matrix. In order to convert between the two, the matrix needs to be inverted.

Due to the non-linearity of the mechanical properties of fibre assemblies, the tangent stiffness matrix must be updated as the continuum deforms. This can generally be performed with a user-defined subroutine for most commercial finite element analysis packages at each increment of the analysis.

#### **4.2.8 Computer simulation**

All of the previous models reviewed are analytical models. More recently Roberts and Beil [102] developed a computer model based on the theory of elastic rods [84]. Their model consists of randomly placing helix shaped fibres in three-dimensional space which have realistic mechanical properties that are easily measured. The computer simulation then tracks the motions and interactions between fibres including slipping of fibres with frictional contacts as the fibre assembly is compressed. The problem is tackled as a dynamic analysis where conservation of momentum in the model is derived from a force balance on a small segment of fibre. The initial fibre volume fraction in the case shown was 0.8%, which is extremely low compared to the case of a textile tow. The results of the computer simulation show good correlation for the pressure versus compaction when compared against van Wyk's analytical model [136], also showing a reasonable ability to predict the undetermined constant  $K$  in his model. If this model was to be applied to uni-directional assemblies of fibres there may be issues with the large number of contacts due to the much higher fibre volume fractions exhibited.

### 4.2.9 Conclusions

A great deal of research has been performed on analysis the mechanical properties of assemblies of fibres. However, an accurate predictive model for the compaction of unidirectional fibre assemblies suitable for use in modelling mechanical properties of textile preforms remains to be found.

With the continuing advance in computing speeds, such a model may be possible in the form of computer simulation building on existing concepts.

### 4.3 Model theory

The structure of the numerical model proposed in this section is illustrated in the flow chart shown in Figure 4.6. This model has been implemented in C++ which provides good performance for the CPU intensive task. The details are explained in the following subsections.

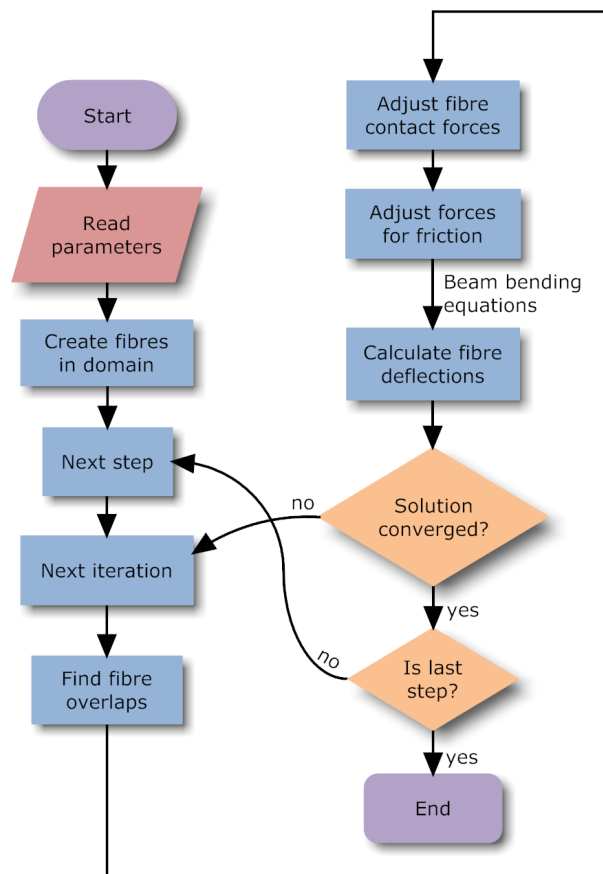


Figure 4.6: Tow model program flowchart



### 4.3.1 Beam theory

The mechanical behaviour of the fibres is modelled using Euler-Bernoulli beam bending theory [139] as used in many of the papers reviewed in Section 4.2. There are a number of assumptions which must be satisfied in order for the theory to be applied. First, the beam must be long and slender, that is to say the length of the beam must be much larger than its cross-sectional diameter. (clearly the case with fibres). Secondly the deformations must remain small (buckling and plasticity are not accounted for); this restricts the applicability of the model for large deformations. The fibre material is assumed to be isotropic, hence non-isotropic fibres such as carbon fibres cannot be modelled directly with this theory. Finally a number of other requirements that are satisfied are:

- The beam cross-section is constant along its axis.
- The beam is loaded in its plane of symmetry.
- Plane sections of the beam remain plane.

The key beam bending equations will be presented here. A more detailed derivation is shown in Appendix F. The moment  $M$  and deflection  $v$  as a function of distance  $x$  along the length of a beam, simply supported at both ends, are obtained by substituting Equations F.21 and F.22 into Equations F.1, F.2, F.9 and F.10:

$$M_1(x) = Px \left(1 - \frac{a}{L}\right) \quad (4.10)$$

$$M_2(x) = Pa \left(1 - \frac{x}{L}\right) \quad (4.11)$$

$$v_1(x) = Px \frac{(L-a)(-a^2 + 2La - x^2)}{6EIL} \quad (4.12)$$

$$v_2(x) = Pa \frac{(L-x)(-a^2 + 2Lx - x^2)}{6EIL} \quad (4.13)$$

where  $P$  is the force applied at distance  $a$  along a beam of length  $L$ .  $E$  and  $I$  are the Young's modulus and second moment of area of the beam respectively. The equations with subscript 1 are valid for the range  $0 \leq x \leq a$  while equations with subscript 2 are valid for the range  $a \leq x \leq l$ .

The above equations can only be used directly for a single force acting at a given position on the fibre. However in reality there will be a number of forces acting on each fibre. Fortunately the equations derived above are valid for multiple forces acting on the fibre by using the method of superposition. This is possible due to the linearity

of the beam bending equations. For fibres subjected to several loads of different types the resulting bending moment, slope and deflection can be found at any location by summing the effects due to each load acting separately. This is illustrated in Figure 4.7.

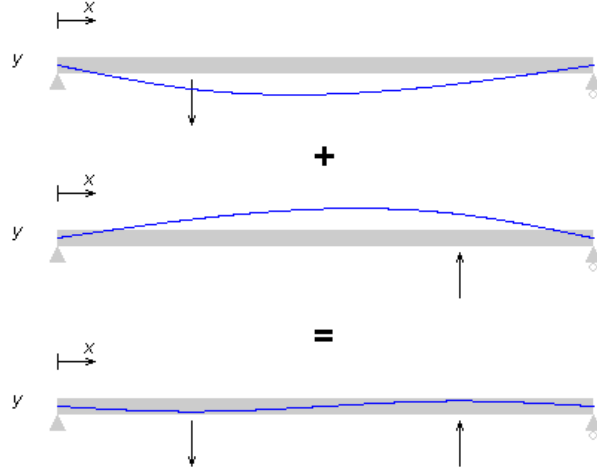


Figure 4.7: Beam superposition

In order to deal with the 3D nature of the problem, it can be split into two 2D problems. Two orthogonal planes are constructed perpendicular to the tow axis, and all forces are resolved in these two planes. The problem is solved in each plane separately with the results combined to obtain 3D deflections, slopes and moments.

### 4.3.2 Contact forces

The behaviour of fibres under given loads has been defined, and it is now necessary to determine the position, direction and magnitude of the forces acting on the fibres. This is addressed numerically and is accomplished through an iterative geometric algorithm. Suppose two fibres  $A$  and  $B$  in space intersect as shown in Figure 4.8. Two points  $\mathbf{A}_c$  and  $\mathbf{B}_c$  are defined as the closest two points lying on the centrelines of the fibres  $A$  and  $B$  respectively. The intersection distance  $d$  is defined as:

$$d = \|\mathbf{B}_c - \mathbf{A}_c\| - (r_A + r_B) \quad (4.14)$$

where  $r_A$  and  $r_B$  are the radii of the fibres  $A$  and  $B$  respectively.

Two equal and opposite forces  $\vec{\mathbf{P}}_A$  and  $\vec{\mathbf{P}}_B$  are applied to each fibre at points  $\mathbf{A}_c$  and  $\mathbf{B}_c$  respectively. The direction  $\vec{\mathbf{P}}_A$  is in line with the vector  $\mathbf{A}_c - \mathbf{B}_c$ , similarly the direction of  $\vec{\mathbf{P}}_B$  is in line with the vector  $\mathbf{B}_c - \mathbf{A}_c$ . The magnitude of the forces  $P$  required to remove the intersection is estimated as a function of  $d$  (typically  $P = cd$  is a suitable

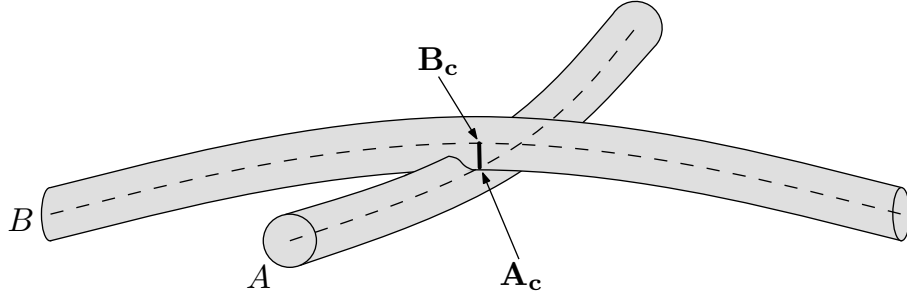


Figure 4.8: Fibres intersecting

function to use, where  $c$  is an arbitrary constant). These two forces will deflect the fibres all along their length (as described in Section 4.3.1). Points  $\mathbf{A}_c$  and  $\mathbf{B}_c$  will be deflected to two new positions denoted by  $\mathbf{A}'_c$  and  $\mathbf{B}'_c$ . The new intersection distance  $d'$  can be calculated as:

$$d' = \|\mathbf{B}'_c - \mathbf{A}'_c\| - (r_A + r_B) \quad (4.15)$$

If  $P$  is too large, the fibres will be pushed too far apart leaving a gap between the fibres in which case  $d' < 0$ . If  $P$  is too small, the fibres will not be pushed far apart enough and  $0 < d' < d$ . In the unlikely event that  $P$  is exactly right the fibres will be just touching and  $d' = 0$ . The rate at which the simulation converges to the stable state solution depends on the function used to calculate  $P$ . Given function  $P = cd$ , a small value of  $c$  will result in a slow convergence rate, higher values of  $c$  will generally result in faster convergence. However if the value of  $c$  is too large the system will become unstable. If the system is stable then  $|d'| < |d|$ .

For the next iteration, two new forces  $\vec{\mathbf{P}}'_A$  and  $\vec{\mathbf{P}}'_B$  need to be estimated in an attempt to reduce the intersection  $d'$  further. As before, the direction of the forces are parallel to the vector  $\mathbf{B}'_c - \mathbf{A}'_c$ . The magnitude  $P'$  is estimated as a function of  $d'$  and  $P$  (typically  $P' = P + cd'$  works well, where  $c$  is an arbitrary constant). The fibres will now have a new deflected shape determined by the forces  $\vec{\mathbf{P}}'_A$  and  $\vec{\mathbf{P}}'_B$ .

The process is repeated until the simulation is deemed to have converged to a stable state. The criterion used to determine what is a stable state will be discussed in Section 4.3.6.

In this simple case with only two fibres present the magnitude of forces  $\vec{\mathbf{P}}'_A$  and  $\vec{\mathbf{P}}'_B$  required to reach a stable state can be calculated directly from the equations described in Section 4.3.1 without need for iterations. However in the complicated case where there are multiple fibres in contact at multiple points, the number of simultaneous equations to solve would be very large. It would be possible to solve the equations, indeed this is how implicit finite element analysis [145] works. However there is a further complication: once the equations have been solved the fibres will have new deflected shapes.

The new state will inevitably contain intersections that were not present initially and also contain contacts that should no longer be present. Equations could be added and removed as necessary and solved again. However this process is unlikely to result in a converged state.

### 4.3.3 Contact locations

In Section 4.3.2 the method to calculate the forces based on given contacts was discussed. In this section, the numerical method used to determine the position of the contacts is discussed. Two types of contacts are considered, first of all point contact and secondly linear contact and its approximation to a series of point contacts.

#### Point contacts

If there are two fibres  $A$  and  $B$  in contact as described previously, the objective is to obtain the closest two points  $\mathbf{A}_c$  and  $\mathbf{B}_c$  that lie on the centrelines of two fibres. If the fibres  $A$  and  $B$  are straight as in Figure 4.9, the solution is straightforward [36]. The end points of fibre  $A$  are  $\mathbf{A}_1$  and  $\mathbf{A}_2$  respectively, similarly the end points of fibre  $B$  are  $\mathbf{B}_1$  and  $\mathbf{B}_2$  respectively. The equations that constrain points  $\mathbf{A}_c$  and  $\mathbf{B}_c$  on the centrelines of the fibres are:

$$\mathbf{A}_c = \mathbf{A}_1 + \mu_A(\mathbf{A}_2 - \mathbf{A}_1) \quad (4.16)$$

$$\mathbf{B}_c = \mathbf{B}_1 + \mu_B(\mathbf{B}_2 - \mathbf{B}_1) \quad (4.17)$$

where  $\mu_A$  and  $\mu_B$  are parameters to be determined.

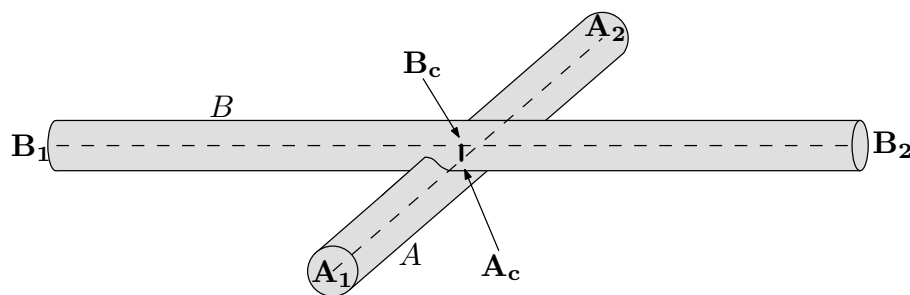


Figure 4.9: Intersection between two lines in 3D

There are two ways to proceed from here, either the distance  $\|\mathbf{B}_c - \mathbf{A}_c\|$  can be minimised, or alternatively the fact that  $\mathbf{A}_c$  and  $\mathbf{B}_c$  will be closest when the vector  $\mathbf{B}_c - \mathbf{A}_c$

is perpendicular to both  $A$  and  $B$  can be exploited:

$$(\mathbf{B}_c - \mathbf{A}_c) \cdot (\mathbf{A}_2 - \mathbf{A}_1) = 0 \quad (4.18)$$

$$(\mathbf{B}_c - \mathbf{A}_c) \cdot (\mathbf{B}_2 - \mathbf{B}_1) = 0 \quad (4.19)$$

Substituting Equations 4.16 and 4.17 into 4.18 and 4.19 leads to:

$$(\mathbf{A}_1 - \mathbf{B}_1) \cdot (\mathbf{A}_2 - \mathbf{A}_1) + \mu_A \|\mathbf{A}_2 - \mathbf{A}_1\|^2 - \mu_B (\mathbf{B}_2 - \mathbf{B}_1) \cdot (\mathbf{A}_2 - \mathbf{A}_1) = 0 \quad (4.20)$$

$$(\mathbf{A}_1 - \mathbf{B}_1) \cdot (\mathbf{B}_2 - \mathbf{B}_1) + \mu_A (\mathbf{B}_2 - \mathbf{B}_1) \cdot (\mathbf{A}_2 - \mathbf{A}_1) - \mu_B \|\mathbf{B}_2 - \mathbf{B}_1\|^2 = 0 \quad (4.21)$$

Solving the set of simultaneous equations results in:

$$\mu_A = \frac{[(\mathbf{A}_1 - \mathbf{B}_1) \cdot (\mathbf{B}_2 - \mathbf{B}_1)] [(\mathbf{B}_2 - \mathbf{B}_1) \cdot (\mathbf{A}_2 - \mathbf{A}_1)]}{\|\mathbf{A}_2 - \mathbf{A}_1\|^2 \|\mathbf{B}_2 - \mathbf{B}_1\|^2 - [(\mathbf{B}_2 - \mathbf{B}_1) \cdot (\mathbf{A}_2 - \mathbf{A}_1)]^2} - \frac{[(\mathbf{A}_1 - \mathbf{B}_1) \cdot (\mathbf{A}_2 - \mathbf{A}_1)] [(\mathbf{B}_2 - \mathbf{B}_1) \cdot (\mathbf{B}_2 - \mathbf{B}_1)]}{\|\mathbf{A}_2 - \mathbf{A}_1\|^2 \|\mathbf{B}_2 - \mathbf{B}_1\|^2 - [(\mathbf{B}_2 - \mathbf{B}_1) \cdot (\mathbf{A}_2 - \mathbf{A}_1)]^2} \quad (4.22)$$

$$\mu_B = \frac{(\mathbf{A}_1 - \mathbf{B}_1) \cdot (\mathbf{B}_2 - \mathbf{B}_1) + \mu_A (\mathbf{B}_2 - \mathbf{B}_1) \cdot (\mathbf{A}_2 - \mathbf{A}_1)}{\|\mathbf{B}_2 - \mathbf{B}_1\|^2} \quad (4.23)$$

Solutions for  $\mu_A$  and  $\mu_B$  can be substituted into 4.16 and 4.17 to obtain the positions of  $\mathbf{A}_c$  and  $\mathbf{B}_c$ .

However, fibres are rarely straight which means that this method cannot be used directly. If the method were to be extended to detect the closest two points between curved fibres following beam bending theory (Section 4.3.1) then Equations 4.18 and 4.19 would need to be replaced by cubic equations. Substituting the cubic equations into the equation for the distance between two points would lead to a sixth order equation. Minimising this means finding the roots of a quintic equation, for which there is no analytical formula [127].

Instead, the shape of the fibre can be approximated by a sequence of straight line segments. Using the equations for finding the closest point between two lines, each line segment of fibre  $A$  can be compared against each line segment of fibre  $B$ . The minimum distance between all the line segments represents the closest distance between the two fibres. The accuracy of such a method depends on the number of segments used to approximate the fibre. However using a very large number of segments will considerably increase the computation time.

### Line contacts

So far it has been assumed that contacts between two fibres occur at a single point. However if two fibres are parallel to each other, when they come into contact there are

an infinite number of pairs of points  $\mathbf{A}_c$  and  $\mathbf{B}_c$  that are all equi-distant. This results in a contact all along the length of the fibres. In fact it can be shown that the denominator of Equation 4.22 is equal to 0 when the fibres are parallel:

$$\|\mathbf{A}_2 - \mathbf{A}_1\|^2 \|\mathbf{B}_2 - \mathbf{B}_1\|^2 - ((\mathbf{B}_2 - \mathbf{B}_1) \cdot (\mathbf{A}_2 - \mathbf{A}_1))^2 = 0 \quad (4.24)$$

$$\|\mathbf{A}_2 - \mathbf{A}_1\|^2 \|\mathbf{B}_2 - \mathbf{B}_1\|^2 - (\|\mathbf{B}_2 - \mathbf{B}_1\| \|\mathbf{A}_2 - \mathbf{A}_1\| \cos \theta)^2 = 0 \quad (4.25)$$

Hence Equations 4.22 and 4.23 cannot be solved. A more common occurrence would be when two fibres partially wrap around each other which would also result in a line contact. An exaggerated case where the fibres are wrapped around each other several times is shown in Figure 4.10.

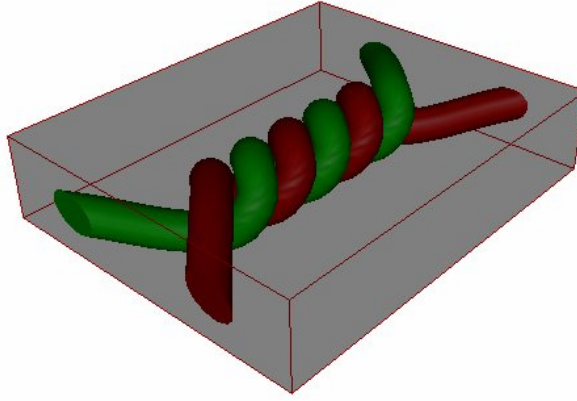


**Figure 4.10:** Fibres wrapping around each other

In a tow all the fibres tend towards being parallel to each other. Thus it is not reasonable to assume that all contacts will be single points when modelling this type of yarn. Contacts between fibres within a tow need to be handled differently from contacts between fibres of crossing yarns.

A new method is proposed to detect contacts between fibres within a tow handling both point and line contacts. For simplicity, the 3D problem can be split up into a large number of 2D problems. Cross-sections along the length of the tow axis are taken at regular intervals as shown in Figure 4.11. At each cross-section the distance between fibre centrelines is calculated using Pythagoras' theorem. If intersection occurs the distance is used to apply forces as described in Section 4.3.2. In this way, a line contact is approximated by a series of individual point contacts as seen in Figure 4.12. As the number of cross-sections  $n$  approaches infinity, line contact is accurately simulated. In practise it is not necessary for  $n$  to be very large to obtain accurate results (see Section 4.5.5).

It should be noted that the magnitude of the individual point forces  $\vec{\mathbf{P}}_i$  will depend on

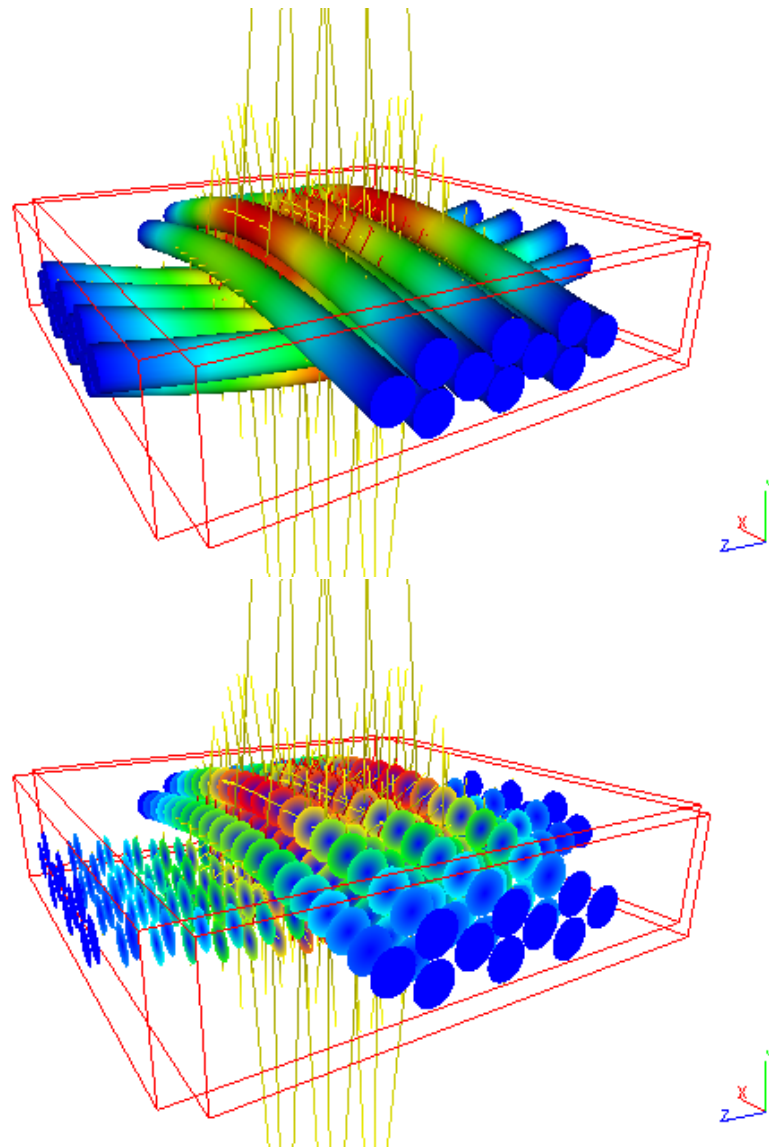
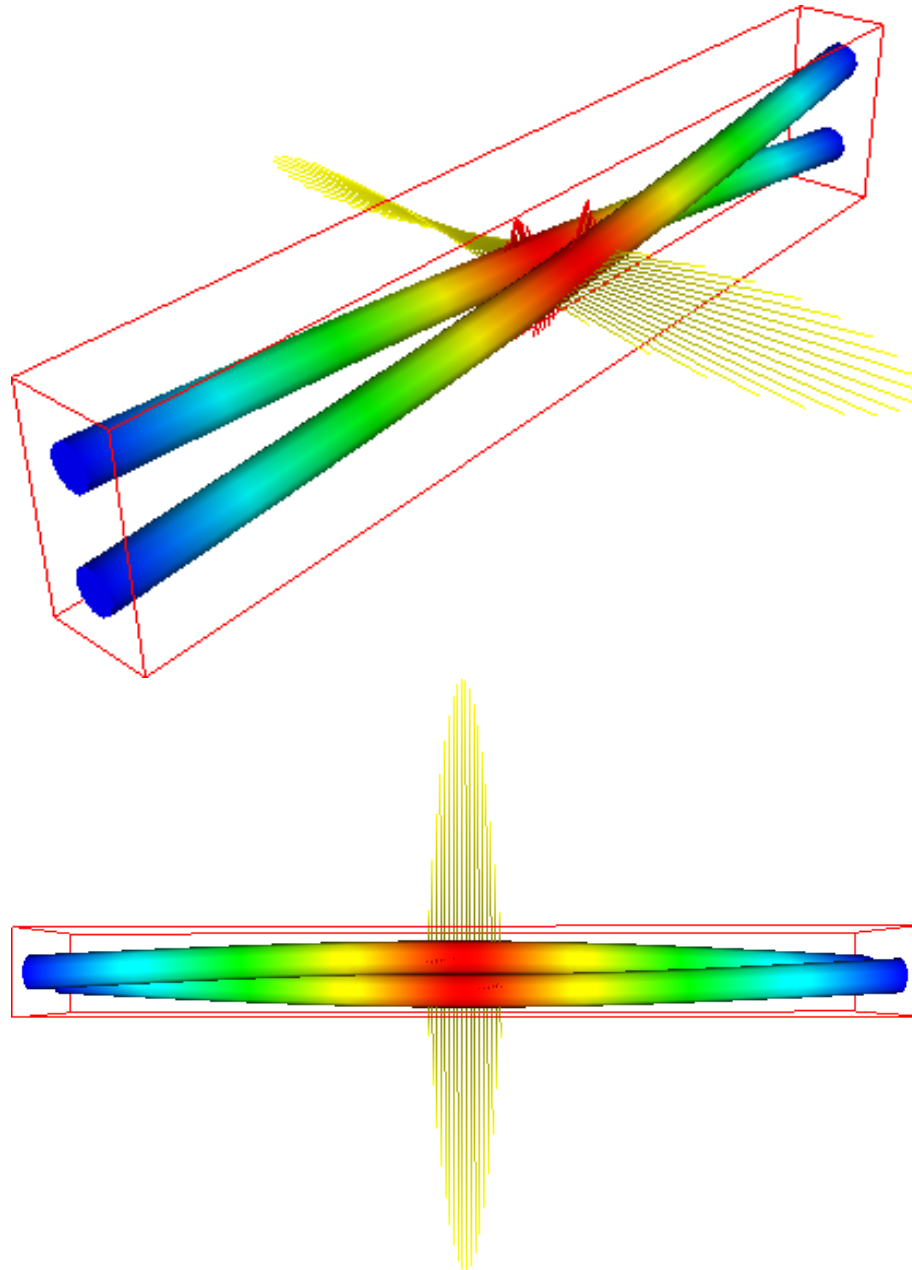


Figure 4.11: (top) Solid fibres (bottom) Cross-sections along fibre length



**Figure 4.12:** Two fibres forming a line contact with forces illustrated in yellow



$n$ . For a line contact, the total force  $\vec{P}_t$  between two fibres should not depend on  $n$ .  $\vec{P}_t$  can be expressed in terms of  $\vec{P}_i$ :

$$\vec{P}_t = \sum_{i=1}^n \vec{P}_i \quad (4.26)$$

The average of the individual point forces  $\bar{P}$  is:

$$\bar{P} = \frac{\sum_{i=1}^n \vec{P}_i}{n} \quad (4.27)$$

hence

$$\bar{P} = \frac{\vec{P}_t}{n} \quad (4.28)$$

It can be seen that if  $n$  decreases and  $\vec{P}_t$  remains constant, the average  $\bar{P}$  must increase. This needs to be taken into account when choosing a function to estimate the force as a function of intersection distance as described in Section 4.3.2.

#### 4.3.4 Friction

Friction between fibres within a yarn is thought to have a significant effect on its mechanical properties. Therefore an attempt has been made to incorporate it into the model. This is made difficult by the nature of friction which opposes the relative motion or tendency of such motion of two surfaces in contact [133]. Unfortunately the relative motion of the fibres is unknown at the time the forces are calculated. Only after the forces are applied can the relative motion of the fibres be known. It would be possible to step back and calculate frictional forces but these changes in forces would in turn affect the relative motion. An iterative process might result in a converged state, however this would be prohibitive in computation time.

Instead the frictional forces are approximated to minimise relative motion as much as possible without stepping back to a previous iteration. This process is illustrated in Figure 4.13 where the cross-sections of two fibres  $A$  and  $B$  running almost parallel to each other are taken at the contact point. Suppose fibres  $A$  and  $B$  are in contact with equal and opposite normal forces  $\vec{N}_A$  and  $\vec{N}_B$  acting on them. There is no frictional force between them so the resultant force  $\vec{P}_A$  is equal to  $\vec{N}_A$ , similarly  $\vec{P}_B$  is equal to  $\vec{N}_B$ . Now suppose fibres  $A$  and  $B$  have moved relative to each other due to some other forces acting somewhere along the fibre after an iteration. The normal forces must always be perpendicular to the contact surface, hence the new normal forces  $\vec{N}'_A$  and  $\vec{N}'_B$  are calculated as the projection of forces  $\vec{N}_A$  and  $\vec{N}_B$  to the surface normal. The frictional forces  $\vec{F}'_A$  and  $\vec{F}'_B$  are added such that the resultant forces  $\vec{P}$  between the two

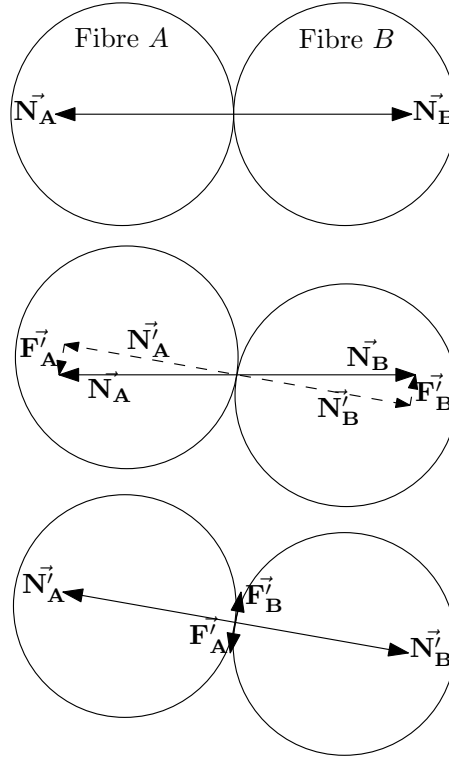


Figure 4.13: Frictional force approximation

fibres remain the same before and after the iteration:

$$\vec{P}'_A = \vec{N}'_A + \vec{F}'_A = \vec{N}_A = \vec{P}_A \quad (4.29)$$

$$\vec{P}'_B = \vec{N}'_B + \vec{F}'_B = \vec{N}_B = \vec{P}_B \quad (4.30)$$

This additional frictional force does not prevent or revert any sliding that has already occurred but will help prevent further sliding and maintain stability. There is of course a limit on the magnitude of the frictional force defined by the classical Coulomb friction equation:

$$F = \mu N \quad (4.31)$$

where  $\mu$  is the coefficient of friction. Thus the following equations must be satisfied:

$$\|\vec{F}'_A\| \leq \mu \|\vec{N}'_A\| \quad (4.32)$$

$$\|\vec{F}'_B\| \leq \mu \|\vec{N}'_B\| \quad (4.33)$$

Figure 4.14 shows the forces between fibres in a cross-section of a tow containing ten fibres for a converged state. The yellow lines represent the normal forces acting on the fibres, the red lines represent the frictional forces acting on the fibres. The colour of the outer rim of the fibre itself represents the magnitude of the moment in the fibre at

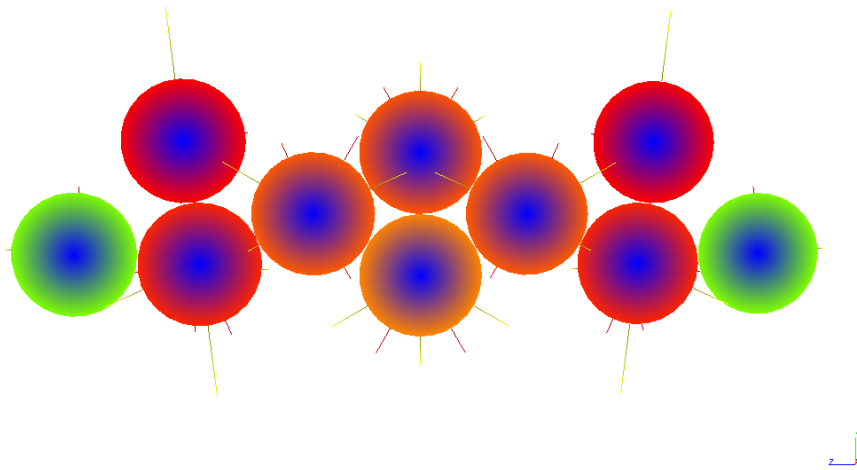


**Figure 4.14:** Forces in a cross-sectional slice

this cross-section. As can be seen from the figure, the fibres are just touching while the contact forces between them vary.

It should be noted that frictional forces are likely to give rise to twisting of fibres, however this effect has been neglected to avoid over complicating the model.

### 4.3.5 Strain Energy

With such a complicated structure as a yarn where the number of forces and possible deformations are large it is convenient to work in terms of energy [19, 68, 141]. Strain energy can be used to determine the deformation of a yarn as a single scalar value.

The strain energy  $U_i$  of an individual fibre of length  $L$  can be calculated with the following equation:

$$U_i = \int_0^L \frac{M^2}{2EI} dx \quad (4.34)$$

The values of  $M$ ,  $E$  and  $I$  are defined in Section 4.3.1. The integration can be done numerically using the Trapezium rule [13] at intervals equal to the cross-section intervals (see Section 4.3.3). The total strain energy  $U$  within a yarn composed of  $n$  fibres is simply calculated by summing the individual fibre strain energies:

$$U = \sum_{i=1}^n U_i \quad (4.35)$$

### 4.3.6 Convergence

In order for the iteration process to complete, a convergence criterion must be defined. An equation must be derived that determines if the simulation is in a stable state. A stable state can be defined as when all the contacting fibres are just touching (i.e.  $d = 0$  for all contacts). In practice this will never happen due rounding errors, so a tolerance  $t_d$  must be used (i.e.  $|d| < t_d$  for all contacts).

Another definition of convergence could be when the total strain energy in the system no longer changes. The system can be considered to have converged when the strain energies of the last  $n_i$  iterations are all within an absolute tolerance  $t_U$  of the current strain energy. If the strain energy remains constant over a number of iterations, it is likely that the solution has converged. There is a possibility that the strain energy in the individual fibres changes while their sum remains constant. However if the value  $n_i$  is high enough the chances of this are remote.

In practice both methods of convergence are implemented with the simulation being terminated when one of the convergence criteria is satisfied.

## 4.4 Compaction of a single tow

Using the model described in this chapter it is possible to estimate the force required to cause compaction of a single tow, however tows can consist of several thousand fibres and the implementation of this model is not able to deal with such a large number of fibres within a reasonable time frame. Instead hundreds of small parts of the tow can be analysed and results averaged to obtain results for an entire yarn. In order to do this periodic boundary conditions are necessary.

### 4.4.1 Periodic boundary conditions

A boundary is defined as an axis aligned box where one of the axes runs parallel to the tow centreline. Suppose the  $x$  and  $y$  axes are in the plane perpendicular to the tow centreline and  $z$  is parallel to it. The box has width  $w$ , height  $h$  and depth  $L$  parallel to axes  $x$ ,  $y$  and  $z$ . Periodic boundary conditions are the boundary conditions that would give the same result as modelling an infinite space where for any particle  $\mathbf{p}$  of material within the domain there are an infinite number of corresponding particles  $\mathbf{p}'_{ijk}$  defined

as:

$$\mathbf{p}'_{ijk_x} = \mathbf{p}_x + iw \tag{4.36}$$

$$\mathbf{p}'_{ijk_y} = \mathbf{p}_y + jh \tag{4.37}$$

$$\mathbf{p}'_{ijk_z} = \mathbf{p}_z + kL \tag{4.38}$$

where  $i, j$  and  $k$  are integers ranging from  $-\infty$  to  $\infty$ .

**Transverse contact periodicity**

Assuming fibres are not perfectly aligned with the tow centreline, it is likely that fibres will cross the planes of the box defined by normals  $x$  and  $y$ . Periodicity implies that if any fibre crosses one of these planes an equivalent fibre should cross the opposite plane at the same position and angle as shown in Figure 4.15.



**Figure 4.15:** Fibre crossing boundary

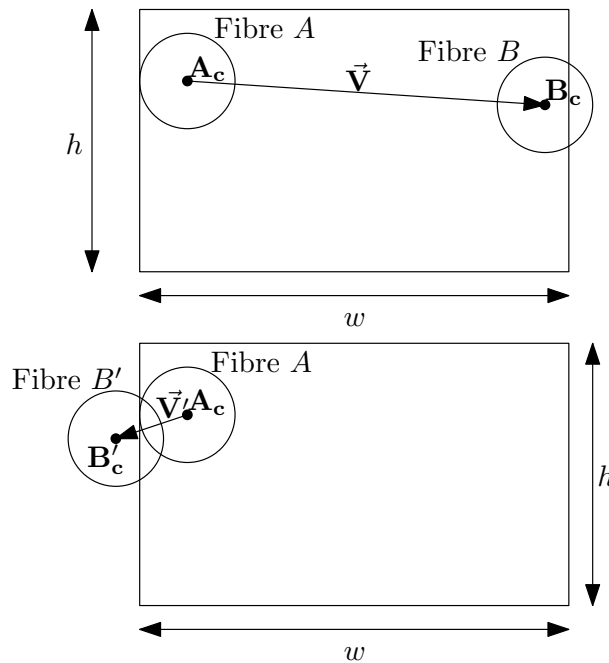


**Figure 4.16:** Contacts across bounds

Although conceptually this seems difficult to implement, in practice it is straightforward. In Figure 4.16 a cross-section of two fibres crossing the boundary on opposite

sides is shown. The length of the vector  $\vec{V}$  from  $\mathbf{A}_c$  to  $\mathbf{B}_c$  represents the distance between the two fibres.

$$\vec{V} = \mathbf{B}_c - \mathbf{A}_c \quad (4.39)$$

The two fibres are clearly not intersecting in their original configuration. However since fibre  $B$  crosses the boundary, another fibre  $B'$  should exist on the opposite boundary. The length of the vector  $\vec{V}'$  represents the distance between the centres of fibres  $A$  and  $B'$ . It can be seen that fibres  $A$  and  $B'$  are intersecting, because the length  $\|\vec{V}'\|$  is less than the sum of the radii  $r_A$  and  $r_B$ . In this case  $\vec{V}'$  is related to  $\vec{V}$  by the following equations:

$$\vec{V}'_x = \vec{V}_x - w \quad (4.40)$$

$$\vec{V}'_y = \vec{V}_y \quad (4.41)$$

More generally, the vector  $\vec{V}'$  is defined as the shortest vector from  $\mathbf{A}_c$  to any  $\mathbf{B}'_{cij}$  (see Equations 4.36 to 4.38)

$$\vec{V}'_x = \mathbf{B}_{cx} + iw - \mathbf{A}_{cx} = \vec{V}_x + iw \quad (4.42)$$

$$\vec{V}'_y = \mathbf{B}_{cy} + jh - \mathbf{A}_{cy} = \vec{V}_y + jh \quad (4.43)$$

The values of the integers  $i$  and  $j$  can be calculated as follows:

$$i = \left[ -\frac{\vec{V}_x}{w} \right] \quad (4.44)$$

$$j = \left[ -\frac{\vec{V}_y}{h} \right] \quad (4.45)$$

where the square brackets  $[\ ]$  represent the nearest integer function. It is worth noting that  $\vec{V}'$  is always contained within the range:

$$-\frac{w}{2} \leq \vec{V}'_x \leq \frac{w}{2} \quad (4.46)$$

$$-\frac{h}{2} \leq \vec{V}'_y \leq \frac{h}{2} \quad (4.47)$$

Contacts are always calculated using the vector  $\vec{V}'$  rather than  $\vec{V}$  since  $\vec{V}'$  represents the closest distance between two fibres with periodic boundary conditions. Forces are applied between fibres  $A$  and  $B'$ . However, any forces applied to  $B'$  are also applied to  $B$  due to the periodicity.

### Longitudinal periodicity

It is fairly straightforward to apply periodicity along the length of the fibres. The periodic boundary conditions for the fibre modelled as a beam are described in Section

4.3.1. However if these equations are used then all the fibres will be perfectly straight and parallel to each other. If this is the case then no bending will occur and since the model is based on bending of fibres alone no compaction resistance will be predicted.

In order to create some contacts the origin and end of the fibre can be offset by an arbitrary distance and either pinned or clamped boundary conditions applied. Both pinning and clamping the ends violate the periodicity of the model. However clamping the ends such that the tangents of the fibre are normal to the boundary at the ends simulates a fibre mirrored at the boundary. This setup is equally as valid as periodic boundary conditions. However this requires the fibres to be initially curved resulting in strain energies being contained within the fibres. The equations set out in Section 4.3.1 may be modified to allow for initially unstrained wavy fibres as future work.

#### 4.4.2 Modelling compaction

The simplest way to model compaction would be to place a plane below and above the specimen and reduce the distance between the two planes until the specimen had been compressed by the desired amount. However since only a small part of a tow is being modelled this method would not be suitable. The compaction can be simulated by applying a linear transformation to the tow. By applying a linear transformation to a particle of material  $\mathbf{p}$  the transformed particle  $\mathbf{p}'$  can be obtained from the following equation:

$$\mathbf{p}'_x = \vec{\mathbf{Q}}_x \mathbf{p}_x \quad (4.48)$$

$$\mathbf{p}'_y = \vec{\mathbf{Q}}_y \mathbf{p}_y \quad (4.49)$$

$$\mathbf{p}'_z = \vec{\mathbf{Q}}_z \mathbf{p}_z \quad (4.50)$$

where  $\vec{\mathbf{Q}}$  represents the degree of compaction. For example to compact the tow to 50% of its original size along the  $y$  axis,  $\vec{\mathbf{Q}}$  would be defined as  $(1, 0.5, 1)$ . The linear transformation is applied to the fixed ends alone, with the shape of the fibres between the ends calculated from the forces acting upon them.

#### 4.4.3 Forces from energy

Mechanical work is defined mathematically as the line integral of a scalar product of force and displacement vectors [116, 134]. In this case the displacement vector is parallel to the force vector hence the equation can be simplified to scalar values. It can be used to calculate the force  $F$  needed to compress the small section of tow contained within the boundary in terms of energy. The work done  $W$  on the small section of tow

by compressing it by a distance  $ds$  can be expressed as:

$$W = \int F ds \quad (4.51)$$

In this model it is assumed that all the work goes into bending the fibres, and any frictional energy dissipated through fibre sliding is neglected. Thus the strain energy  $U$  equals  $W$ :

$$U = \int F ds \quad (4.52)$$

The strain energy  $U$  is known (see Section 4.3.5), therefore the force  $F$  can be calculated in terms of  $U$ :

$$F = \frac{dU}{ds} \quad (4.53)$$

The force is distributed over an area  $A$ , hence the pressure  $D$  is:

$$D = \frac{1}{A} \frac{dU}{ds} \quad (4.54)$$

The differentiation in Equation 4.54 can be approximated numerically. The pressure  $D$  and strain energy  $U$  are both functions of  $s$ , written as  $D(s)$  and  $U(s)$ . Pressure  $D(s)$  can be expressed as:

$$D(s) = \frac{1}{A} \lim_{ds \rightarrow 0} \frac{U(s+ds) - U(s)}{ds} \quad (4.55)$$

In order to obtain a graph of pressure versus compaction, the compaction must be applied in a number of steps. The simulation begins with  $s = 0$  and at each following step,  $s$  is increased by  $ds$ . At each step the strain energy is calculated, and for each pair of steps  $D$  is calculated using Equation 4.55.

The values  $A$  and  $s$  can be related to the boundary in the following way: suppose the section of tow contained within a box of width  $w$ , height  $h$  and depth  $L$  parallel to axes  $x$ ,  $y$  and  $z$  respectively is compressed along the  $y$  axis. The area  $A$  is:

$$A = wL \quad (4.56)$$

and  $s$  can be expressed as:

$$s = h(1 - \vec{Q}_y) \quad (4.57)$$

where the value  $\vec{Q}$  is described in Section 4.4.2. Here it is assumed that the compression occurs only along the  $y$  axis (i.e.  $\vec{Q}_x = \vec{Q}_z = 1$ ).

#### 4.4.4 Compaction test case

In order to check the model has been derived and implemented correctly, it is important to run a simulation where the result is known. A tow where the fibres are arranged as



shown in Figure 4.17 was constructed. This is not a realistic tow, but is one where an analytical solution is easily obtained and which is sufficiently complicated to test the computational model.

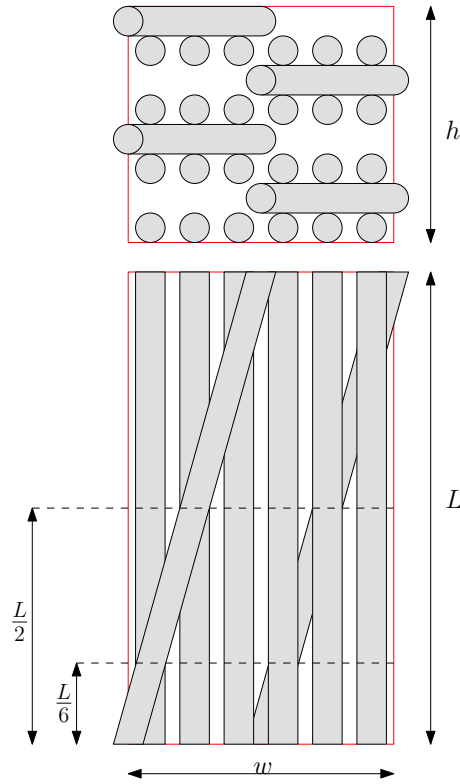


Figure 4.17: Two orthogonal views of the fibre compaction test case

### Analytical solution

Due to symmetry it can be seen that the four slanted fibres do not bend at all. The 24 straight fibres each bend due to a force applied to each one at a single point. This point is at  $\frac{L}{2}$  for 8 of the fibres. For the other 16 fibres the point is at  $\frac{L}{6}$ . These assumptions are only valid for small deflections; once the fibres start to bend the contact points and direction of the forces will change. The ends of the fibres are pinned, so that no deformation or strain energy is present before compaction. From Equation 4.12 or 4.13, the displacement  $v$  at point  $a$  of a fibre pinned at either end caused by a force  $P$  acting at point  $a$  is:

$$v(a) = \frac{P(L-a)a^3}{6EIL} - \frac{Pa(2L^2 - 3La + a^2)}{6EIL}a \quad (4.58)$$

which can be simplified and re-arranged to give  $P$  in terms of  $v$ :

$$P(a) = -\frac{3EILv}{a^2(a-L)^2} \quad (4.59)$$

An arbitrary set of dimensions and properties have been chosen as shown in Table 4.1. Note that a consistent set of units has been chosen to avoid having to convert to SI units.

**Table 4.1:** Fibre compaction test case dimensions

Fibre radius $r$	0.01 mm
Domain width $w$	0.16 mm
Domain height $h$	0.16 mm
Domain length $L$	1 mm
Young's modulus $E$	$80 \times 10^3$ MPa
Second moment of area $I$	$7.85 \times 10^{-9}$ mm <sup>4</sup>

For the fibres which have the force applied at their centre (i.e.  $a = \frac{L}{2}$ ), the force is:

$$P = 30.1 \times 10^{-3} v \quad (4.60)$$

For the fibres which have the force applied at  $a = \frac{L}{6}$ , the force is:

$$P = 97.7 \times 10^{-3} v \quad (4.61)$$

Figure 4.18 illustrates eight layers in which contacts between fibres occur. Compaction

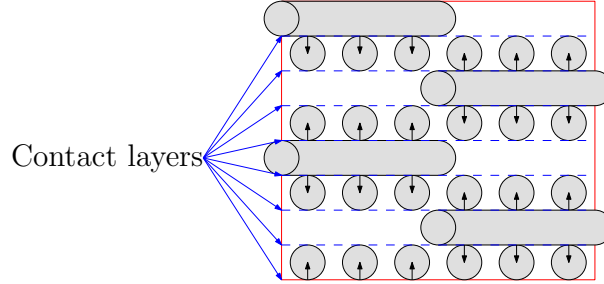


**Figure 4.18:** Fibre contact layers

forces applied to the top surface of the tow are propagated through the tow by these contact layers. In each of these layers there is one fibre with force applied at the axial centre and two fibres with force applied at axial position  $\frac{L}{6}$ . This test case has been designed to contain easily identifiable contact layers, however in a randomly distributed tow these layers do not exist, hence demonstrating the need for an energy based method.

The total force  $F$  acting on one layer would be:

$$F = [(30.1 \times 10^{-3}) + 2(97.7 \times 10^{-3})] v = 225.5 \times 10^{-3} v \quad (4.62)$$

The strain energy within the fibres will also be obtained analytically for comparison with the model. In order to do this the moment  $M$  from Equations 4.10 and 4.11 is

substituted into Equation 4.34 to obtain the strain energy  $U$ :

$$U_i = \frac{1}{2EI} \left( \int_0^a \left( \frac{P(L-a)x}{L} \right)^2 dx + \int_a^L \left( Pa \left( 1 - \frac{x}{L} \right) \right)^2 dx \right) \quad (4.63)$$

$$U_i = \frac{1}{2EI} \left( \left( \frac{P(L-a)}{L} \right)^2 \left[ \frac{x^3}{3} \right]_0^a + (Pa)^2 \left[ x - \frac{x^2}{L} + \frac{x^3}{3L} \right]_a^L \right) \quad (4.64)$$

$$U_i = \frac{P^2 a^2 (L^4 - 2L^2 a + La^2 + (1-L)a^3)}{6EIL^2} \quad (4.65)$$

For the fibres which have the force applied at the centre of the fibre (i.e.  $a = \frac{L}{2}$ ), the strain energy is:

$$U_i = 15.0 \times 10^{-3} v^2 \quad (4.66)$$

For the fibres which have the force applied one sixth of the way along the length (i.e.  $a = \frac{L}{6}$ ), the force is:

$$U_i = 48.9 \times 10^{-3} v^2 \quad (4.67)$$

The total strain energy in the system is thus:

$$U = [8(15.0 \times 10^{-3}) + 16(48.9 \times 10^{-3})] v^2 = 902 \times 10^{-3} v^2 \quad (4.68)$$

In Section 4.4.3 it was shown that the force  $F$  could be related to the strain energy with Equation 4.53. Thus  $F$  can be expressed in terms of  $U$  as:

$$F = \frac{d}{ds} (902 \times 10^{-3} v^2) \quad (4.69)$$

Before it can be evaluated  $s$  needs to be related to  $v$ . Initially when the fibres are just touching the distance between the centrelines is  $2r$  where  $r$  is the radius of the fibres. As the yarn is compacted by compaction  $Q$ , the distance between the centrelines will reduce to  $2rQ_y$ . Rather than the fibres being compressed, one is deflected by distance  $v$  while the other remains undisplaced. The distance  $v$  can be expressed as:

$$v = 2r - 2rQ_y \quad (4.70)$$

It can be seen from Figure 4.17 that the height  $h$  is equal to  $16r$ , hence:

$$v = \frac{h(1 - Q_y)}{8} \quad (4.71)$$

From Equation 4.57 it can be shown that:

$$s = 8v \quad (4.72)$$

which can then be used to evaluate  $F$ :

$$F = \frac{d}{dv} \frac{(902 \times 10^{-3} v^2)}{8} = 225.5 \times 10^{-3} v \quad (4.73)$$

which agrees exactly with Equation 4.62 thus proving that the energy method is valid.

### Computation model solution

A computational model of the same tow has been built and can be seen in Figure 4.19. As well as the dimensions specified in Table 4.1, some additional parameters are needed for the computational model and are specified in Table 4.2.

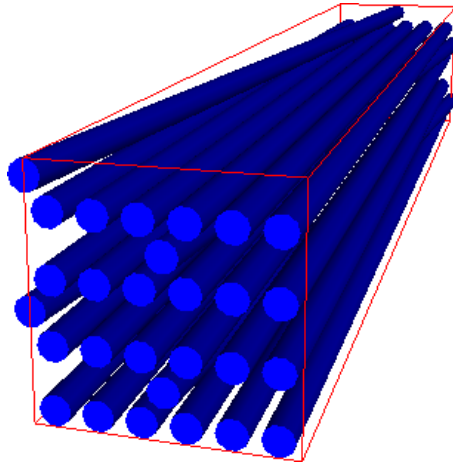


**Figure 4.19:** Computation test case model

**Table 4.2:** Parameters for fibre compaction test case

Coefficient of friction $\mu$	0.3
Final compaction $\vec{Q}$	(1, 0.75, 1)
Number of steps $n_s$	50
Number of fibre length divisions $n_d$	200
Intersection convergence tolerance $t_d$	$10^{-6}$
Strain convergence tolerance $t_U$	0.001
Strain convergence iterations $n_i$	50
Contact coefficient $K$	10

The contact coefficient  $K$  shown in the table is used to control how much force is applied to the fibres when they intersect by a distance  $d$ . In Section 4.3.2, it is suggested that a suitable equation to calculate the magnitude of force between two fibres is:

$$\|\vec{P}'\| = \|\vec{P}\| + cd' \quad (4.74)$$

The value of  $c$  affects the rate of convergence and should be chosen such that the convergence rate is maximised without causing model instabilities. The optimum value of  $c$  depends on the fibre properties such as modulus, radius and length. It is convenient to define  $c$  in terms of a new constant  $K$  that is independent of the dimensions and

properties of the fibres. The magnitude of the force between two fibres becomes:

$$\|\vec{\mathbf{P}}'\| = \|\vec{\mathbf{P}}\| + \vec{\mathbf{P}}_e K \frac{L}{n_d} \quad (4.75)$$

where  $\vec{\mathbf{P}}_e$  is the estimated force necessary to displace two fibres so that they are just touching assuming they are the only two fibres in contact:

$$\|\vec{\mathbf{P}}_e\| = -\frac{3EILd'}{2a^2(a-L)^2} \quad (4.76)$$

This is the same as Equation 4.59 except that  $v$  has been replaced by  $\frac{d'}{2}$ , since the deflection of each fibre will be half the total intersection distance. The term  $\frac{L}{n_d}$ , which is length of the fibres divided by the number of fibre length divisions, represents the distance between two consecutive cross-sections. It is included since shorter distances between cross-sections will result in more contact points, thus the force on each contact force must be less.

After about 20 minutes, 9443 iterations and 50 steps, the simulation successfully completed. Figure 4.20 shows the simulation at step number 25 with forces illustrated in yellow and moments in green. The plot of strain energy  $U$  versus distance  $s$  for the analytical and computation model are shown in Figure 4.21. Similarly the plot of  $F$  versus  $s$  is shown in Figure 4.22. The computational model follows the analytical solution very closely for small compactions. However as the compaction increases, the analytical model becomes invalid. The contact forces no longer remain vertical as the fibres begin to bend, as can be seen in Figure 4.20. As expected, the more accurate computational model shows higher values of  $U$  and  $F$  for higher degrees of compaction.

The curve of the computational solution in Figure 4.22 is slightly jagged. This is due to the approximation created by the fibre length divisions. If a curve of strain energy  $U$  were plotted against contact force location  $a$  (see Section 4.3.1), the curve should have continuity  $C^1$ . However in the computational model the strain energy varies linearly between fibre length divisions hence resulting in a curve with continuity  $C^0$  only. Since the force  $F$  is proportional to  $U'$ , a curve of  $F$  plotted against  $a$  does not have continuity  $C^0$ . The jaggedness of the curve in Figure 4.22 is a result of one or more contact force locations  $a$  crossing a fibre length division. The problem is exacerbated in this case due to the symmetry of the model, as all of the contact force locations move in unison. Appendix G contains graphs showing the effect of varying the number of divisions  $n_d$ . Nevertheless, the high level of agreement for low compaction levels is very encouraging. It shows that the computational model has been correctly implemented and that the iterative technique to obtain a converged solution is valid.

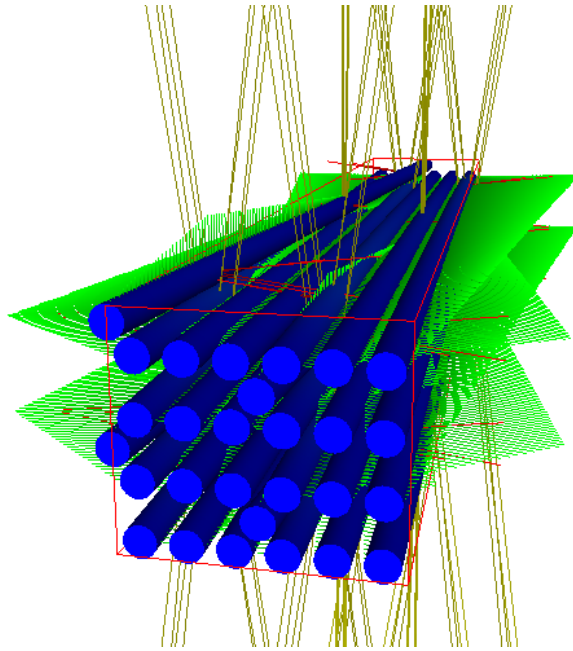


Figure 4.20: Computational test case model at step 25

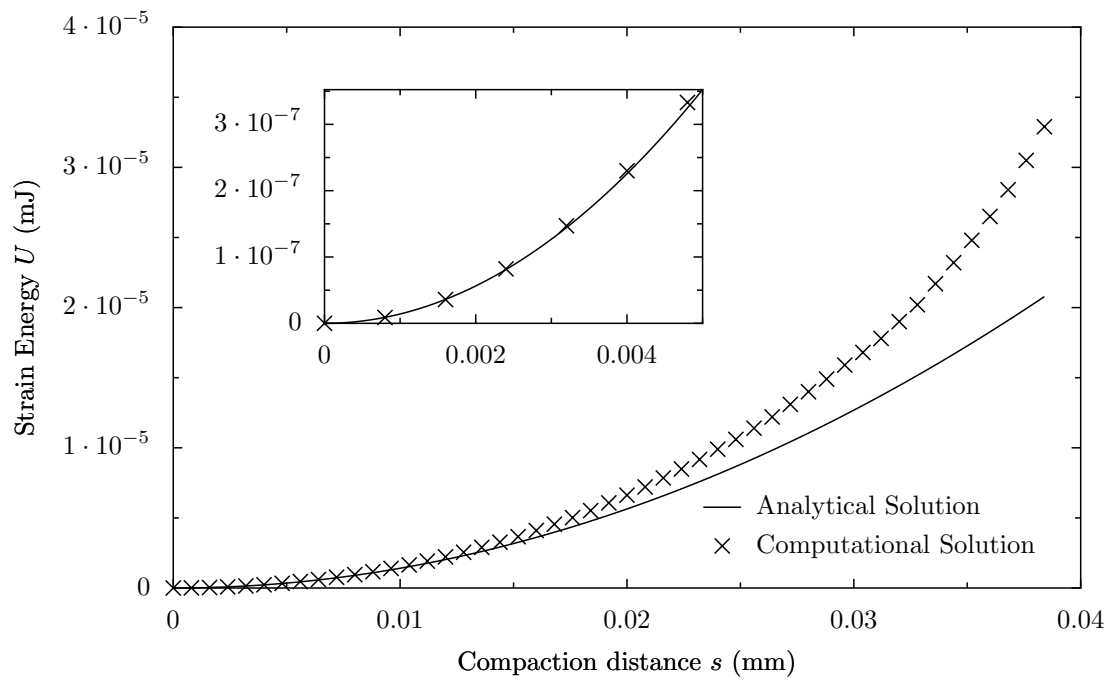


Figure 4.21:  $U$  versus  $s$  for compaction test case

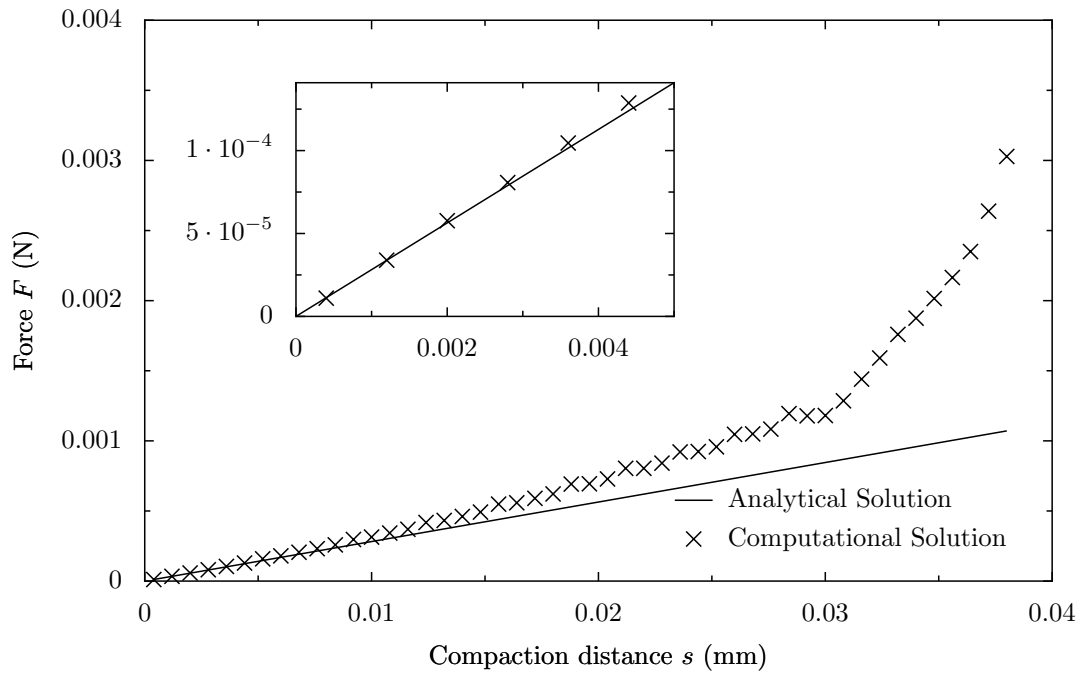


Figure 4.22:  $F$  versus  $s$  for compaction test case

#### 4.4.5 Glass fibre tow

In this section an attempt is made to simulate the compaction of a real glass fibre tow. In order to do this a fibre arrangement must be chosen along with boundary conditions for the fibres, specifically a small section of tow contained within a domain small enough to be modelled without excessive computation and large enough to give meaningful results. Fibres are added one at a time by selecting random positions on one face of the box for the origin of the fibre. The end of the fibre lies on the opposite face of the box such that the angle between the fibre centreline and the face normal is chosen by a standard normal random variable [28] with given standard deviation  $\sigma$  and mean 0. If the fibre is found to intersect with any of the other fibres already present it is discarded. This process continues until the desired fibre volume fraction is reached. If the specified volume fraction is too high this process may never complete in which case the simulation cannot be carried out.

The longitudinal boundary conditions are a problem as discussed in Section 4.4.1. Results for various boundary conditions are compared, none of which are fully satisfactory. Ideally the length of the tow section should not affect the results, however here this is not the case. A base model is created that attempts to represent a glass fibre tow with parameters shown in Table 4.3. Starting from the base case the effect of each parameter on pressure versus fibre volume fraction is determined. First of all a sensitivity study is performed on the model parameters which should not affect the results. For

each set of parameters 800 simulations are run and the average is shown. For the base case, each simulation takes up to 5 minutes to run, taking several days to run 800 simulations on a single computer. To speed the process up the simulations are spread over several processors reducing the run time down significantly depending on the number of processors available.

**Table 4.3:** Parameters for glass fibre compaction (base case)

Fibre radius $r$	0.01mm
Young's modulus $E$	65000 MPa
Coefficient of friction $\mu$	0.3
Angle standard deviation	0.02 rad
Domain size ( $w \times h \times L$ )	0.16 x 0.16 x 1 mm
Final compaction $\vec{Q}$	(1, 0.75, 1)
Number of steps $n_s$	10
Number of fibre length divisions $n_d$	100
Interesection convergence tolerance $t_d$	$10^{-6}$
Strain convergence tolerance $t_U$	0.001
Strain convergence iterations $n_i$	50
Contact coefficient $K$	1

A selection of steps from a single simulation is shown in Figure 4.23 with parameters shown in Table 4.3. The yellow lines represent the normal contact forces between fibres, the red lines represent the frictional forces and the green lines represent the moment of the fibres. This illustrates the complexity of the model. As the simulation gets to the last steps the number of contact forces becomes very large which can cause instabilities. All of the following graphs show pressure versus fibre volume fraction varying one of the parameters shown in Table 4.3.

First of all the reason for averaging results of several simulations is illustrated in Figure 4.24. Each line represents the average of a certain number of simulations. As the number of simulations increases it can be seen that the lines tend to converge. The individual simulations do not give the same results each time but by averaging the results over a representative number of simulations they become repeatable. The error bars represent the standard deviation of 600 simulations. The error bars are very large due to the small scale on which the simulations are run.

Experimental data is available for compaction of fabrics and groups of tows but not for small sections of tow as simulated in the numerical method. Thus the variability found in the simulations is much larger than one would expect from experiments, as



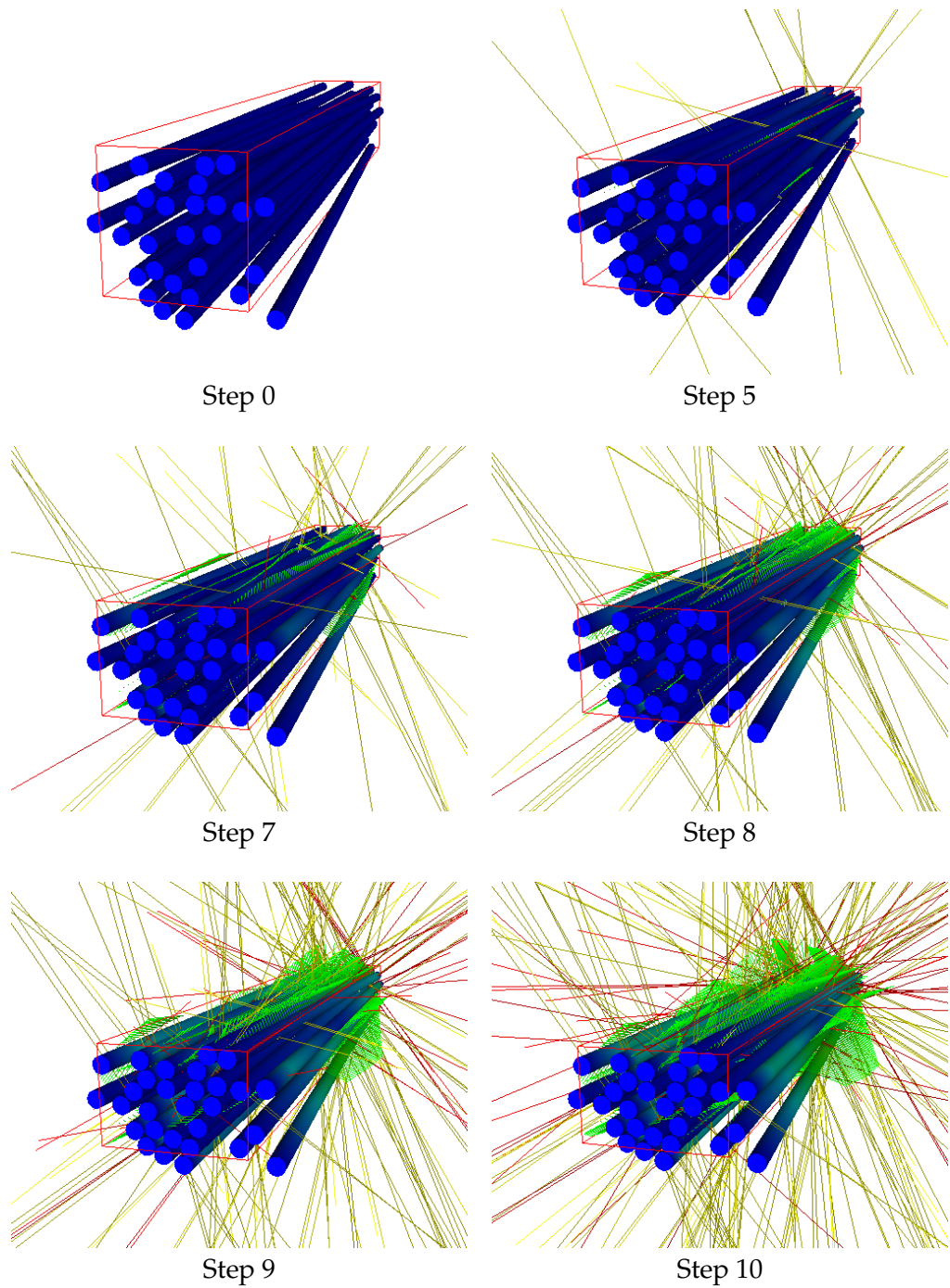


**Figure 4.23:** Visualisation of the simulation of compaction for a portion of glass fibre tow

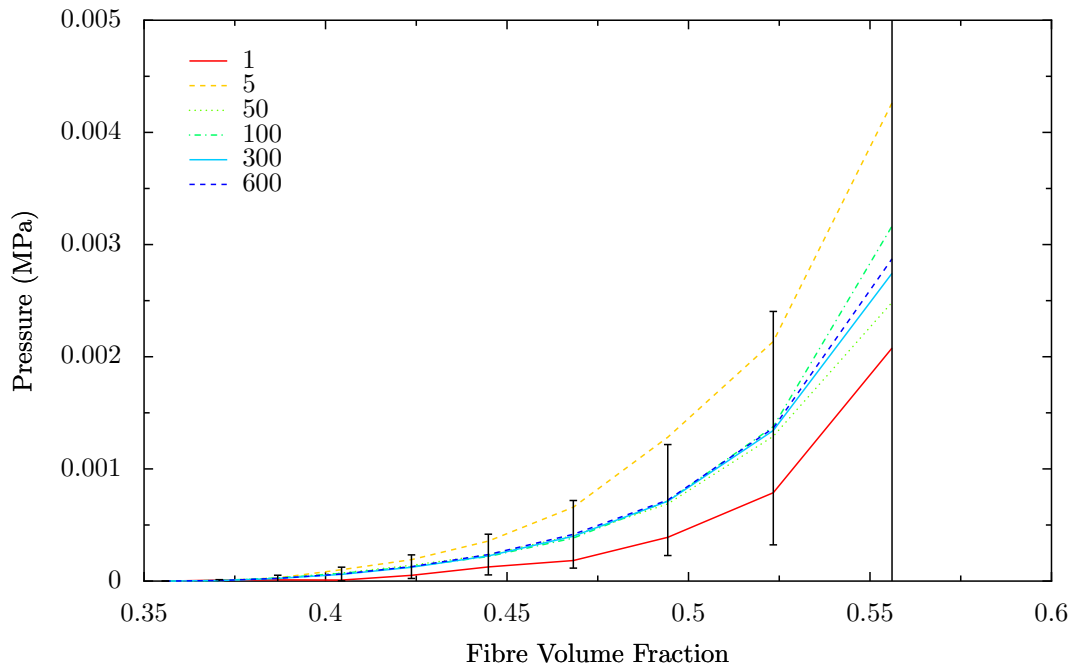


**Figure 4.24:** Pressure versus fibre volume fraction varying number of simulations

the variations will average out at a larger scale.

Appendix H contains graphs showing that the optimum number of fibre length divisions is 100 and that the model is not sensitive to domain height or number of steps.

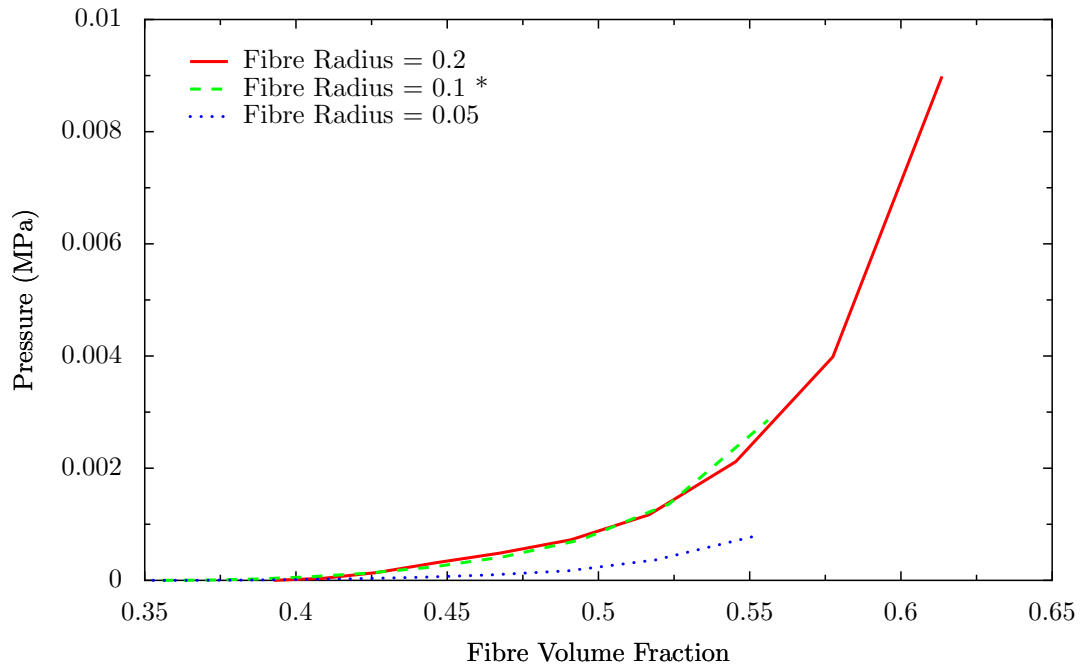


**Figure 4.25:** Pressure versus fibre volume fraction varying fibre radius

Figure 4.25 shows the effect of the fibre radius on pressure. The pressure increases with radius, as is expected since the bending stiffness of each fibre will increase with

radius. Unfortunately by increasing the fibre radius to 0.2mm the initial fibre volume fraction has increased, causing the curve to be shifted to the right making it appear that the radius does not affect pressure between radius 0.1mm and 0.2mm. The increased volume fraction is due to the way the fibres are placed inside the domain. Fibres are added one by one until the volume fraction is greater than or equal to the desired initial fibre volume fraction. As the volume of each individual fibre is large in comparison with the domain size, the initial fibre volume fraction is overshoot by a large amount.

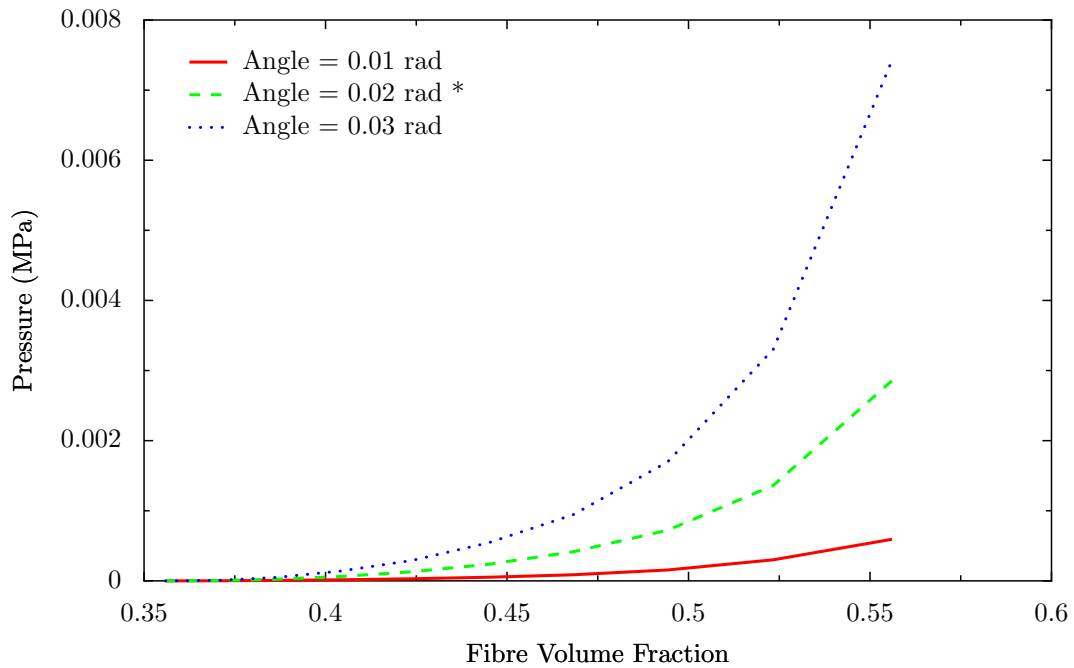


**Figure 4.26:** Pressure versus fibre volume fraction varying fibre angle

Next the effect of varying the angle standard deviation between fibres in a tow is investigated in Figure 4.26. It can be seen that increasing the angle between fibres increases the amount of compression pressure. This is to be expected since the number of contacts between fibres increases as angle increases, leading to an increase in the average bending energy stored in the fibres and thus an increase in pressure.

The effect of friction is shown in Figure 4.27. An increase in friction coefficient shows a slight increase in pressure, most prominently at low values. Note that the frictional energy dissipated during fibre sliding is not taken into account when calculating the pressure due to limitations in the modelling approach. If this were to be taken into account a more significant difference may be observed.

The effect of domain length is shown in Figure 4.28. As can be seen from the graph, the length has a large effect on the pressure. Decreasing the length of the domain causes an increase in pressure. At very small lengths it also affects the shape of the

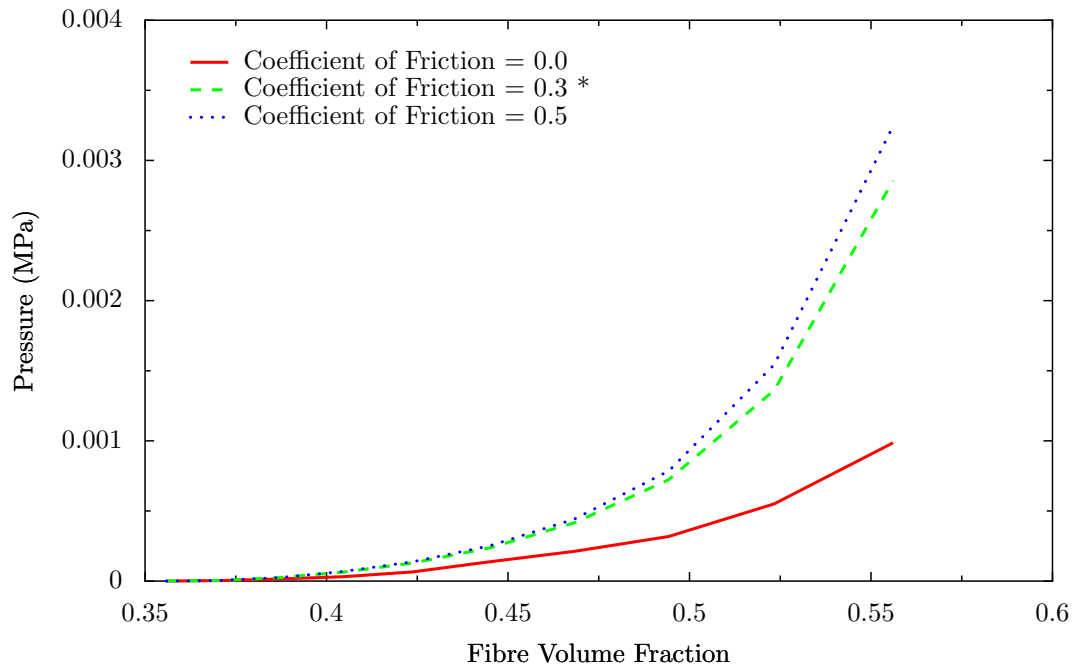


Figure 4.27: Pressure versus fibre volume fraction varying fibre friction

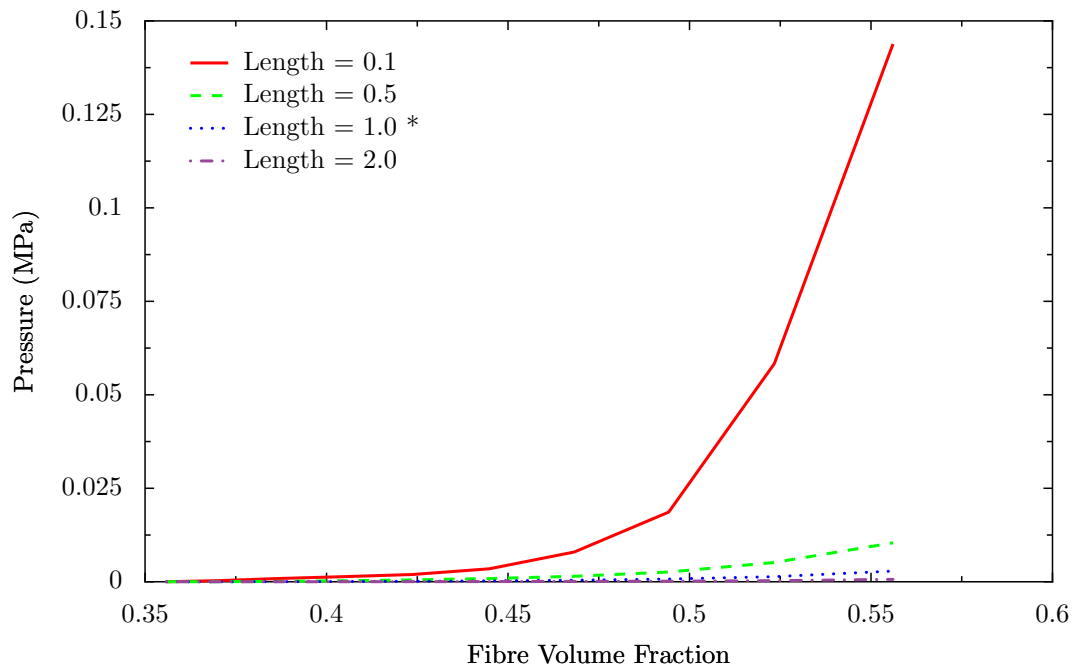
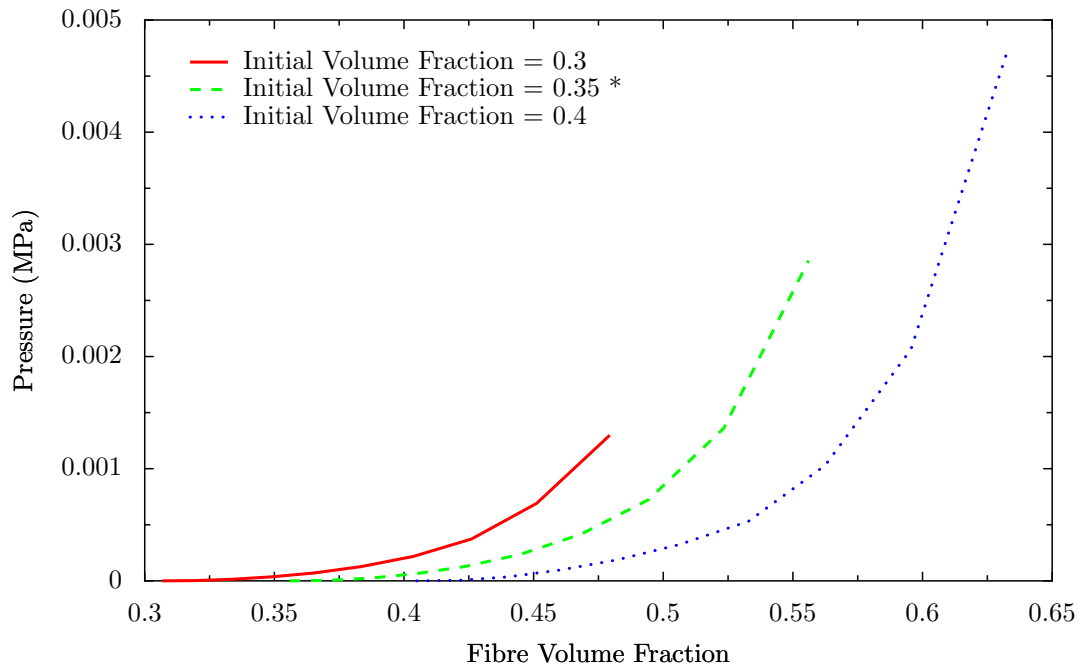


Figure 4.28: Pressure versus fibre volume fraction varying domain length

curve making it more shallow. However the smallest length plotted of 0.1mm is not considered reasonable as it is approaching the radius of the fibres. Ideally the pressure should not vary with the length of domain analysed. Unfortunately this is not the case due to the difficulties in choosing appropriate longitudinal boundary conditions. The boundary conditions chosen were pinned at each end. Decreasing the domain length has the effect of increasing the bending stiffness between the pinned ends thus increasing the compaction pressure.



**Figure 4.29:** Pressure versus fibre volume fraction varying initial fibre volume fraction

The effect of initial fibre volume fraction is shown in Figure 4.29. This represents the fibre volume fraction where no pressure has been applied to the tow and no internal energy exists. By increasing the initial fibre volume fraction, the volume fraction at which a certain pressure is attained is delayed. The overall shape of the curve is not modified, it is simply shifted and scaled. The reason for this is that the initial distribution of fibres is always created in such a manner that no intersections are present. Therefore the compaction pressure at the start of the simulation is always zero no matter what the initial fibre volume fraction is.

From the sensitivity study it can be seen that the shape of the curve remains the same (except for the case of very small domain lengths). It has been shown in the literature that the compaction curve of pressure versus fibre volume fraction can be approximated by a power law requiring only 2 fitting parameters. Alternatively experimental data can also be fitted to the Gutowski model [43] requiring 3 fitting parameters  $V_0$ ,

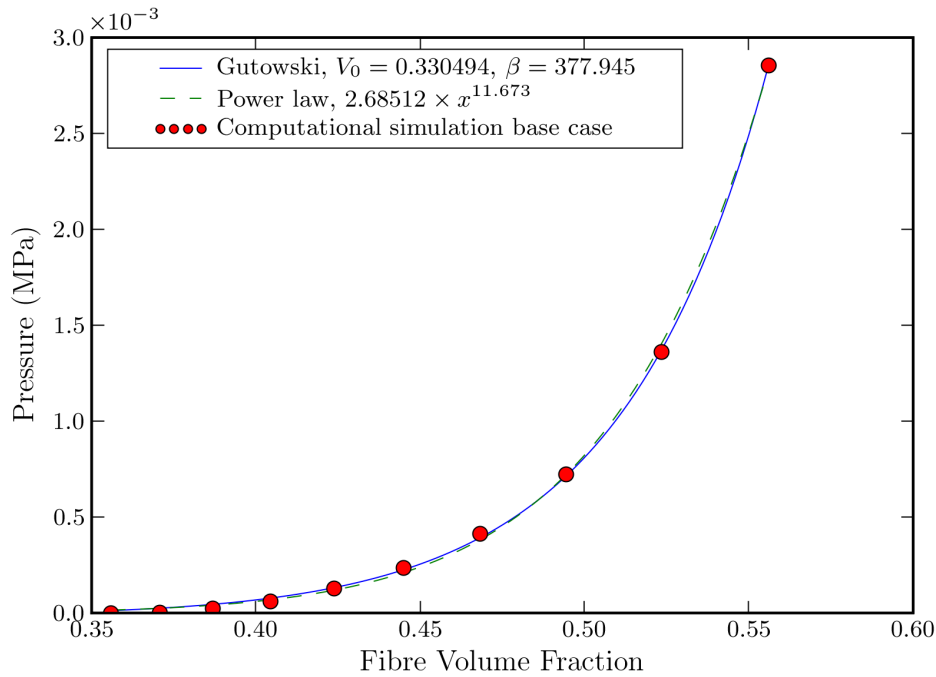


**Figure 4.30:** Pressure versus fibre volume fraction base case fit against analytical curves

$V_a$  and  $\beta$  (Equation 4.9). McBride [88] found that using a maximum volume fraction  $V_a$  of 0.85 gave good fit to the experimental results for both E-Glass and Kevlar tows. This value falls between that of square packed and hexagonally packed arrays. Hence  $V_a = 0.85$  is used here and the fitting parameters are reduced to  $V_0$  and  $\beta$ . The base simulation case fitted to both types of curves is shown in Figure 4.30 using the least squares method. The fit is almost perfect, demonstrating that the simulation produces curves similar to those obtained from experimental testing. Note also that the value of  $V_0$  obtained from the fit is very close to the actual initial fibre volume fraction modelled. The coefficient of correlation  $R^2$  is 0.994 for the Gutowski model and 0.997 for the power law.

McBride [88] performed compaction experiments on a series of aligned yarns. Two methods were explored, the first where yarns were simply placed between two plates and compressed with free edges referred to as transverse uniaxial compression. The second method involved placing plates on the sides of the yarns to prevent them from expanding horizontally, referred to as transverse plane strain compression. Since the model presented in this chapter corresponds better to the plane strain method, results will be compared against this method.

Figure 4.31 shows a comparison of pressure versus volume fraction to McBride's data. Unfortunately the pressure values for the computational simulations are much lower

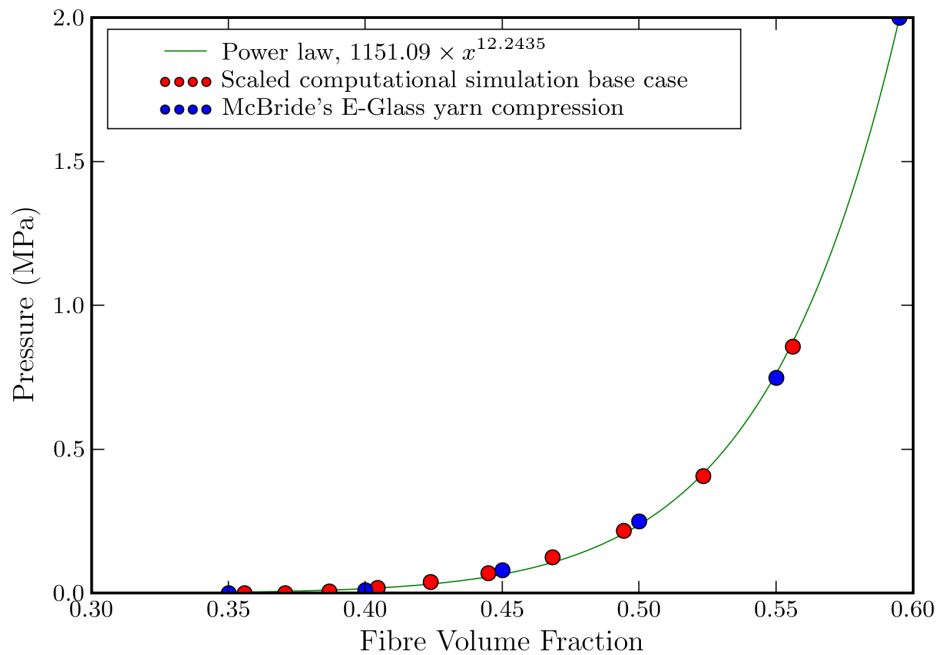


**Figure 4.31:** Pressure versus fibre volume fraction base case comparison showing base case against experimental data

than experimental data, by a factor of about 300. Therefore to be able to make a meaningful comparison the pressures from the computational data has been scaled accordingly. It should be noted that currently no model is able to predict the magnitude of compaction pressure without using a fitting parameter of some form. Unfortunately the model presented here also falls into that category.

The reason for the failure to accurately predict the scale of the pressure is thought to be due to the existence of non-physical parameters which have a significant effect on the results. These include the length of the domain and the unsatisfactory longitudinal boundary conditions. The neglect of frictional energy dissipated in calculating the compaction pressure may also contribute to the under-prediction. Future work on this model should revise the boundary conditions. One solution may be to assume that the fibre path is wavy in its unstrained state. This would enable the use of longitudinal periodic boundary conditions while still enabling contacts within the system. The length of the domain should then be a multiple of the fibre path wavelength to ensure periodicity. With a wavy fibre path the number of contacts is likely to be increased resulting in a larger compaction pressure approaching experimental results. The inclusion of frictional energy should also be considered. However the model does provide insights into how certain physical parameters will affect the compaction behaviour, such as fibre radius, fibre angle and initial fibre volume fraction.

#### 4.4.6 Conclusions from compaction examples

An original computational model able to predict the behaviour of a tow under compression has been developed. The model was implemented in C++ and verified for a simple test case where an analytical solution is known. The model has shown its ability to simulate accurately the test case. The model was then used to predict the compaction pressure of a random distribution of fibres in a small domain similar to that found in a real tow. The results from these simulations show curves identical in shape to those found in experimental testing. By varying parameters in the model, change in compaction behaviour can be predicted. However the model is still unable to predict accurately the scale of the pressure applied without fitting to experimental data.

### 4.5 Shearing of polyester plain weave

Collaborating with Unilever and the University of Manchester, an attempt at characterising the effect of fabric conditioner on the mechanical properties of cotton and polyester fabrics was made. It is thought that the application of fabric conditioner affects the coefficient of friction between yarns and fibres, however it is not clear whether the fabric conditioner is able to penetrate the yarns or if it only affects the surface of the yarns. To account for this the fabric behaviour is modelled with two coefficients of friction; a coefficient of friction between yarns  $\mu_y$  and a coefficient of friction between fibres  $\mu_f$ . In the case where the fabric conditioner penetrates the yarns, the coefficients of friction  $\mu_y$  and  $\mu_f$  will be equal.

The polyester plain weave presented in Chapter 3 contains only 24 fibres per tow. For such a tow it is reasonable to perform a micro scale unit cell analysis using the model presented in this chapter. In order to simulate a unit cell with this model, several tows must be constructed with interactions between them. The interactions between fibres of different tows are implemented as described in Section 4.3.3 by splitting the fibres into small straight line segments. Due to the symmetry of the plain weave, only a quarter of the unit cell needs to be modelled. In this case the shearing behaviour of the fabric is of interest.

In this model fabric shear is represented by a linear shear transformation of the fibre centrelines. The fibres themselves however do not shear, it is assumed that the fibre cross-sections remain perpendicular to the fibre centrelines. For convenience in dealing with contacts, the fibre length divisions follow the linear shear transformation. Hence



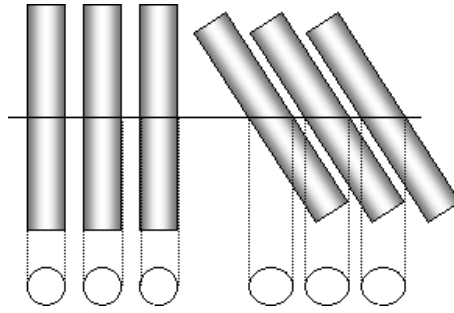


**Figure 4.32:** cross-section after shearing

after shear, the fibre length divisions are no longer perpendicular to the fibre direction and thus the cross-sectional shape of fibres across each division is no longer circular. The change in shape is illustrated in Figure 4.32. The height of the fibre cross-section remains the same, but the width increases as the shear increases. The resulting shape is an ellipse of width  $w$  and height  $h$  defined by the following equation:

$$w = 2r\sqrt{1 + \varepsilon_{xy}^2} \quad (4.77)$$

$$h = 2r \quad (4.78)$$

where  $r$  is the radius of the fibre and  $\varepsilon_{xy}$  is the in plane shear strain of the tow.

The detection of intersections between fibres within a tow is now performed over ellipses rather than circles. However, since the ratio of major axis to minor axis is the same for all ellipses and the major axes of all the ellipses have the same orientation, all the ellipses can be linearly transformed back to circles. The intersection detection can then be performed over the circles yielding the same results as if it were done over ellipses.

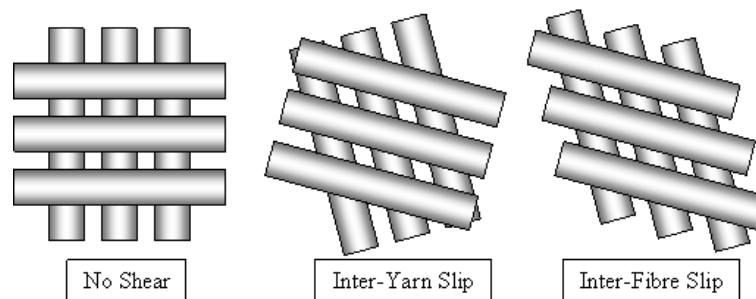


**Figure 4.33:** Shearing modes

Considering the case where there are two tows crossing over each other as illustrated in Figure 4.33, there are two extreme modes of shear. The first case is where the fibres within a tow are adhered together and do not slide past each other, however sliding does occur between the yarns (inter-yarn slip). The second case is where no sliding between the yarns occurs but there is sliding between fibres (inter-fibre slip). The mode

that occurs depends on the relative contact forces between the fibres and the relevant coefficients of friction. Note that the only difference between the inter-yarn slip and inter-fibre slip cases is a translation of the fibres along their axis. Hence the problem can be simplified to the case where each fibre only has one degree of freedom.

An energy minimisation principle is used to determine where inter-yarn slip occurs and where inter-fibre slip occurs. The work done  $W$  when two fibres slide can be expressed as the frictional force  $\mu F$  multiplied by sliding distance  $ds$ :

$$W = \int \mu F ds \quad (4.79)$$

The work done is equivalent to frictional energy dissipated. The total dissipated energy can be calculated by summing each of these individual energy contributions. The objective then becomes minimisation of the total dissipated energy for all possible sliding configurations.

#### 4.5.1 Frictional energy minimisation

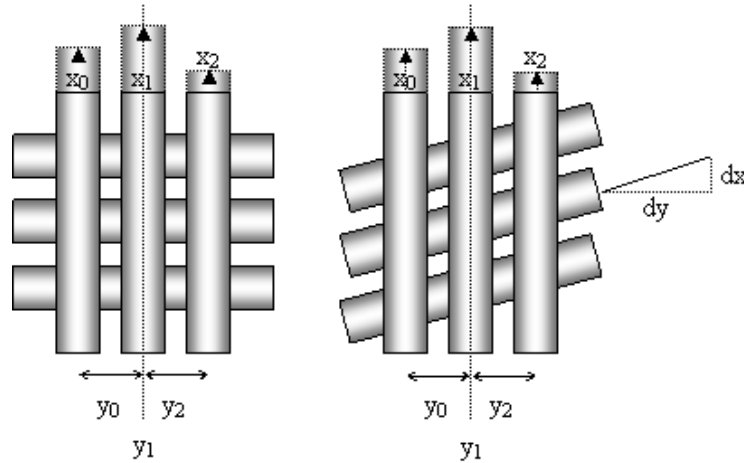


**Figure 4.34:** Fibre degrees of freedom illustrated

In order to minimise the amount of frictional energy dissipated due to fibre sliding, an equation for frictional energy based on sliding must be derived. Each fibre has one degree of freedom allowing it to slide along its axis by a distance denoted by  $x_0, x_1 \dots x_{n-1}$ , where  $n$  is the number of fibres. The in-plane distance of each fibre from the central tow axis is denoted by  $y_0, y_1 \dots y_{n-1}$  (Figure 4.34). The shear strain is denoted by:

$$\varepsilon_{xy} = \frac{dx}{dy} \quad (4.80)$$

The contact force between fibre  $i$  and the crossing yarn is  $F_i$ . Similarly the contact force between fibre  $i$  and fibre  $j$  is defined as  $F_{ij}$ . The dissipated frictional energy due to

crossing yarn contact is:

$$W_i = F_i \mu_y |x_i - \varepsilon_{xy} y_i| \quad (4.81)$$

where  $\mu_y$  represents the coefficient of friction between yarns. The dissipated frictional energy due to fibre-fibre contact within the same yarn is expressed as:

$$W_{ij} = F_{ij} \mu_f |x_i - x_j| \quad (4.82)$$

where  $\mu_f$  represents the coefficient of friction between fibres within the same yarn. The total frictional energy dissipated is denoted by  $W$  and is simply the sum of the frictional energies dissipated by each fibre:

$$W = \sum_{i=1}^n W_i + \sum_{i=1}^n \sum_{j=i+1}^n W_{ij} \quad (4.83)$$

$$= \sum_{i=1}^n F_i \mu_y |x_i - \varepsilon_{xy} y_i| + \sum_{i=1}^n \sum_{j=i+1}^n F_{ij} \mu_f |x_i - x_j| \quad (4.84)$$

The only unknown variables in Equation 4.84 are  $x_0, x_1 \dots x_{n-1}$ , therefore the number of degrees of freedom is equal to the number of fibres. The coefficients of friction are input values that can be varied to establish their effects on total frictional energy dissipated. The forces are obtained from the fibre model, and all forces are summed along the length of the fibre to obtain a single value for each fibre-fibre or fibre-yarn interaction.

#### 4.5.2 Incremental loading

The dissipated frictional energy calculation assumes that the forces between the fibres remain constant during shearing. This is of course not true, as when shearing occurs the fibres tend to become compacted together increasing the contact forces between them and changing the geometric configuration. However over small increments of shear, these changes will be small and therefore if the shearing is simulated over a number of steps a reasonable approximation can be reached. In between the shearing steps, the fibre geometry and forces are recalculated. Since the geometry is not affected by sliding of the fibres, the energy minimisation for a whole set of different coefficients of friction can be performed in the same simulation.

#### 4.5.3 Boundary conditions

Symmetry is used to analyse just a quarter of a unit cell with appropriate boundary conditions. The fibre ends do not have any moment acting on them similarly to the pinned case. However the fibres are permitted to move with some restrictions. The

fibres are initially arranged in a hexagonal pattern with 3 layers, with the middle layer containing 7 fibres while the upper and lower layers contain 6 fibres as shown in Figure 4.35. Note that the exact number of fibres is slightly less than the real case in order to reduce the computational time necessary to run the simulations.

The fibres on the middle layer can move horizontally but cannot move vertically. The fibres on the top and lower layers are paired together and must move in unison mirrored about the central horizontal axis. That is to say that the distance  $a$  between a fibre and the central horizontal axis must be equal to the distance  $a$  of the fibre it is paired to. The horizontal displacements of the two fibres must also be the same.

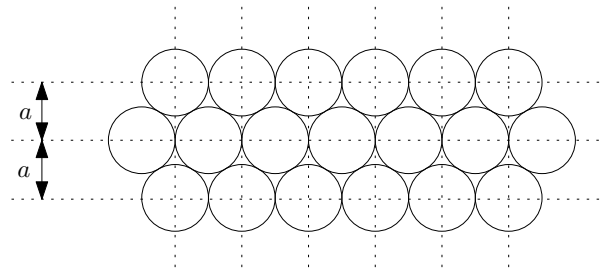


Figure 4.35: Fibre arrangement

#### 4.5.4 Forces from energy

Mechanical work is defined mathematically as the line integral of a scalar product of force and displacement vectors [116, 134]. It can be used to calculate the force  $\vec{F}$  needed to shear the fabric in terms of energy. Figure 4.36 illustrates the boundaries of the fabric with shear force  $\vec{F}$  acting on the sides.

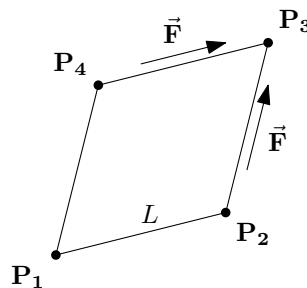


Figure 4.36: Shear force diagram

The work done  $W$  on the fabric by a shear force  $\vec{F}$  can be expressed as:

$$W = \int \vec{F} \cdot d\vec{s} \quad (4.85)$$

where  $\vec{s}$  represents the position vector of the point of application of force  $\vec{F}$ . From Figure 4.36 it can be seen that there are two equal shear forces acting on the fabric, one

on side  $\mathbf{P}_2\text{-}\mathbf{P}_3$  and the other on side  $\mathbf{P}_3\text{-}\mathbf{P}_4$ . Assuming the force is uniformly distributed over the side, the position vector  $\vec{\mathbf{s}}$  for the right side can be expressed as:

$$\vec{\mathbf{s}} = \int_0^1 \mathbf{P}_2 + u(\mathbf{P}_3 - \mathbf{P}_2) du \quad (4.86)$$

$$= \frac{\mathbf{P}_2 + \mathbf{P}_3}{2} \quad (4.87)$$

The points  $\mathbf{P}_1, \mathbf{P}_2, \mathbf{P}_3$  and  $\mathbf{P}_4$  can be expressed in terms of shear strain  $\varepsilon_{xy}$ :

$$\mathbf{P}_{1x} = \mathbf{P}_{1y} = 0 \quad (4.88)$$

$$\mathbf{P}_{2x} = \mathbf{P}_{4y} = L \frac{1}{\sqrt{1 + \varepsilon_{xy}^2}} \quad (4.89)$$

$$\mathbf{P}_{2y} = \mathbf{P}_{4x} = L \frac{\varepsilon_{xy}}{\sqrt{1 + \varepsilon_{xy}^2}} \quad (4.90)$$

$$\mathbf{P}_{3x} = \mathbf{P}_{3y} = L \frac{1 + \varepsilon_{xy}}{\sqrt{1 + \varepsilon_{xy}^2}} \quad (4.91)$$

And  $\vec{\mathbf{s}}$  becomes:

$$\vec{\mathbf{s}}_x = L \frac{2 + \varepsilon_{xy}}{2\sqrt{1 + \varepsilon_{xy}^2}} \quad (4.92)$$

$$\vec{\mathbf{s}}_y = L \frac{1 + 2\varepsilon_{xy}}{2\sqrt{1 + \varepsilon_{xy}^2}} \quad (4.93)$$

It is now possible to differentiate  $\vec{\mathbf{s}}$  in terms of shear strain  $\varepsilon_{xy}$ :

$$\frac{d\vec{\mathbf{s}}_x}{d\varepsilon_{xy_x}} = L \frac{1 - 2\varepsilon_{xy}}{2(1 + \varepsilon_{xy}^2)^{\frac{3}{2}}} \quad (4.94)$$

$$\frac{d\vec{\mathbf{s}}_y}{d\varepsilon_{xy_y}} = L \frac{2 - \varepsilon_{xy}}{2(1 + \varepsilon_{xy}^2)^{\frac{3}{2}}} \quad (4.95)$$

The direction  $\vec{\mathbf{T}}$  of the force vector  $\vec{\mathbf{F}}$  is known, but the magnitude  $F$  is not. Splitting the magnitude and direction,  $\vec{\mathbf{F}}$  can be expressed as:

$$\vec{\mathbf{F}} = F\vec{\mathbf{T}} \quad (4.96)$$

The direction  $\vec{\mathbf{T}}$  can be expressed in terms of shear strain  $\varepsilon_{xy}$ :

$$\vec{\mathbf{T}}_x = \frac{\varepsilon_{xy}}{\sqrt{1 + \varepsilon_{xy}^2}} \quad (4.97)$$

$$\vec{\mathbf{T}}_y = \frac{1}{\sqrt{1 + \varepsilon_{xy}^2}} \quad (4.98)$$

Equation 4.85 can now be expressed as:

$$W = \int F \left( \vec{T} \cdot \frac{d\vec{s}}{d\varepsilon_{xy}} \right) d\varepsilon_{xy} \quad (4.99)$$

which becomes:

$$W = \int F \left( L \frac{1 - \varepsilon_{xy}^2}{(1 + \varepsilon_{xy}^2)^2} \right) d\varepsilon_{xy} \quad (4.100)$$

Note this expression accounts only for the work done by the shear force on side  $\mathbf{P}_2, \mathbf{P}_3$ . The same expression can be derived for the shear force on side  $\mathbf{P}_3, \mathbf{P}_4$  due to symmetry.

Equation 4.100 can be re-arranged to give the magnitude of the shear force  $F$  in terms of  $W$ :

$$F = \frac{dW}{d\varepsilon_{xy}} \frac{(1 + \varepsilon_{xy}^2)^2}{L(1 - \varepsilon_{xy}^2)} \quad (4.101)$$

Assuming the work done by both shear forces is the same, the work done  $W$  on the fabric by a single shear force can be equated to the change in energy in the system before and after shearing divided by 2:

$$W = \frac{(U - U_0) + G}{2} \quad (4.102)$$

where  $U$  is the strain energy within the fibres,  $U_0$  is the strain energy within the fibres before shearing and  $G$  is the frictional energy dissipated during fibre sliding.

The differentiation in Equation 4.101 can be approximated numerically. The force  $F$  and work done  $W$  are both functions of  $\varepsilon_{xy}$ , written as  $F(\varepsilon_{xy})$  and  $W(\varepsilon_{xy})$ . Force  $F(\varepsilon_{xy})$  can be expressed as:

$$F(\varepsilon_{xy}) = \lim_{d\varepsilon_{xy} \rightarrow 0} \frac{W(\varepsilon_{xy} + d\varepsilon_{xy}) - W(\varepsilon_{xy})}{d\varepsilon_{xy}} \frac{(1 + \varepsilon_{xy}^2)^2}{L(1 - \varepsilon_{xy}^2)} \quad (4.103)$$

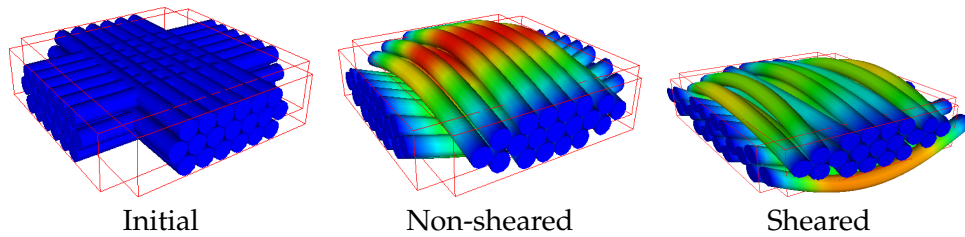
#### 4.5.5 Results

The properties used for the model are shown in Table 4.4. The tow is modelled as 3 layers of fibres arranged in a hexagonal pattern as shown in Figure 4.37. In the initial state all the fibres are perfectly straight with clear intersections between the two tows. A number of iterations are computed before the shear deformation begins in order to resolve the fibre intersections, this corresponds to the non-sheared configuration in the figure. The sheared configuration is after a number of shear steps have been performed. The colour represents the moment of the fibre.

A number of cases were run varying the number of fibre length divisions to find the optimal number of divisions (see Section 4.3.3). A graph of strain energy within the

**Table 4.4:** Parameters for polyester fabric shear

Fibre radius $r$	0.009 mm
Number of fibres	19
Young's modulus $E$	13200 MPa
Domain size	0.44 mm x 0.44 mm
Shear strain increment	0.01
Number of steps $n_s$	21
Number of fibre length divisions $n_d$	20
Intersection convergence tolerance $t_d$	$10^{-6}$
Strain convergence tolerance $t_U$	$10^{-5}$
Strain convergence iterations $n_i$	50
Contact coefficient $K$	1

**Figure 4.37:** Fabric shear model including individual fibres

system versus shear strain is shown in Figure 4.38. The strain energy is larger for lower numbers of divisions which is to be expected due to the nature of the inter-yarn contact algorithm. It was concluded that 20 divisions is sufficient for accurate results in this case.

The effect of changing the coefficient of friction between yarns  $\mu_y$  and coefficient of friction between fibres  $\mu_f$  was simulated. Figure 4.39 shows  $\mu_y$  and  $\mu_f$  plotted along the x and y axes, and frictional energy dissipated is plotted along the z axis for a shear strain of 0.2. It can be seen that when the ratio of  $\mu_y$  to  $\mu_f$  is below a certain value,  $\mu_f$  does not affect the frictional energy dissipated because all of the sliding occurs between the yarns. Likewise when the ratio of  $\mu_y$  to  $\mu_f$  is above a certain value,  $\mu_y$  does not affect the frictional energy dissipated because all of the sliding occurs between the fibres within a tow. From the graph it can be seen that the critical ratio is approximately 0.3.

Figures 4.40 and 4.41 show the effect of varying  $\mu_y$ ,  $\mu_f$  and shear strain on the frictional energy dissipated. It can be seen that increases in shear strain always increase frictional energy dissipated. Increasing coefficient of friction  $\mu_y$  increases frictional energy dissipated until the critical ratio is reached at which point further increases no longer have

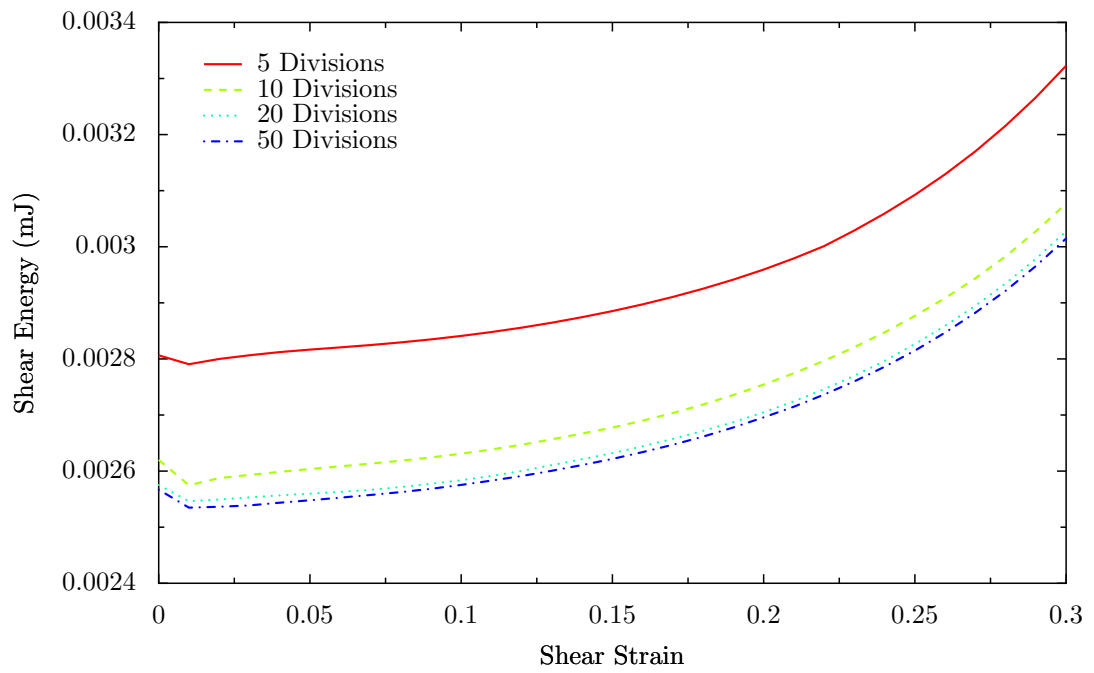


Figure 4.38: Strain Energy vs. Shear Strain for various number of divisions

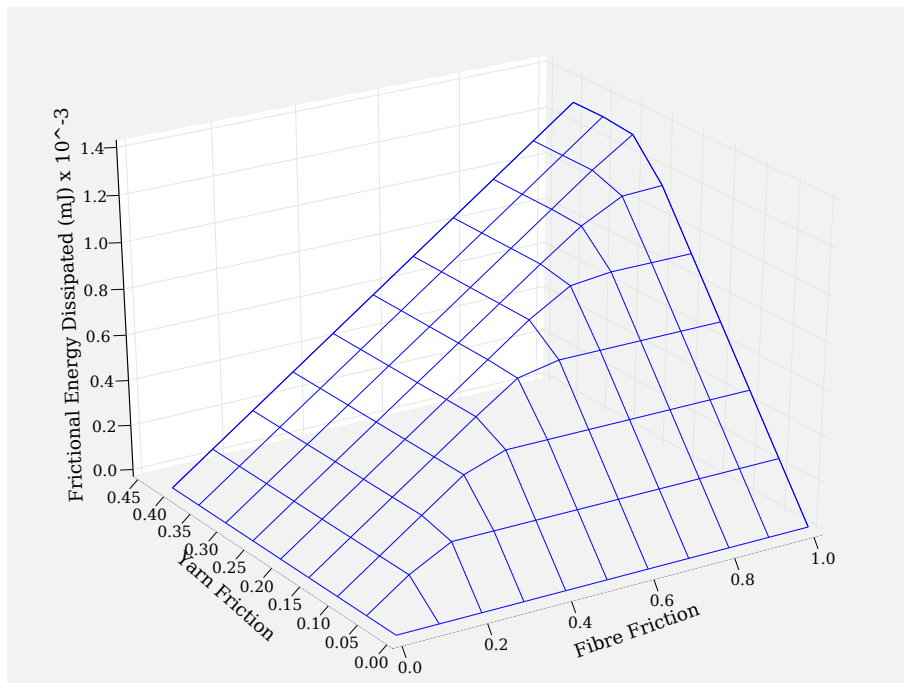


Figure 4.39: Effect of  $\mu_f$  &  $\mu_y$  on frictional energy dissipated at shear strain of 0.2



any effect.

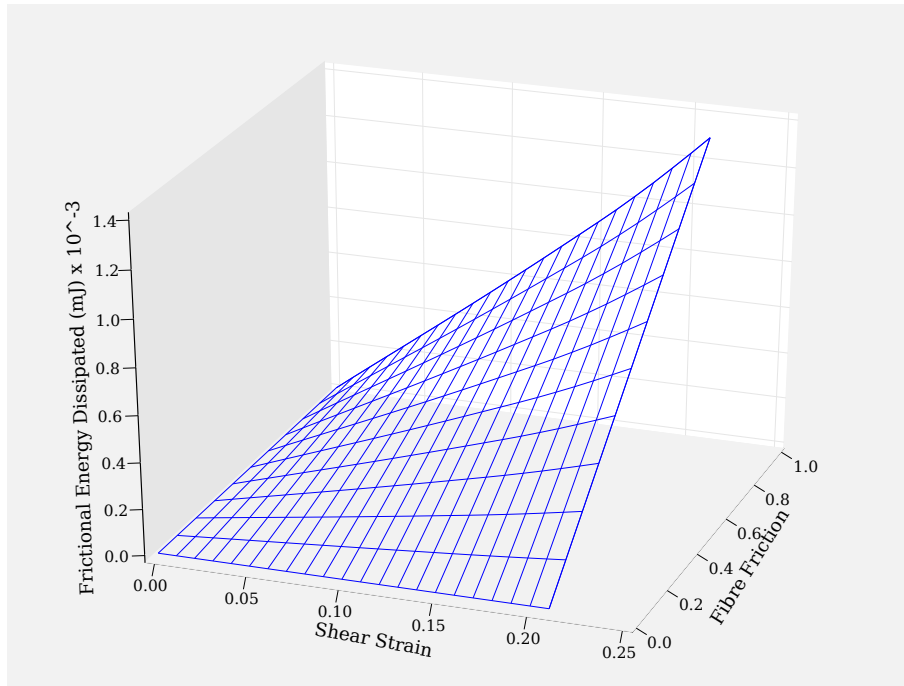


Figure 4.40: Effect of  $\mu_f$  and shear strain on frictional energy dissipated at  $\mu_y = 0.4$

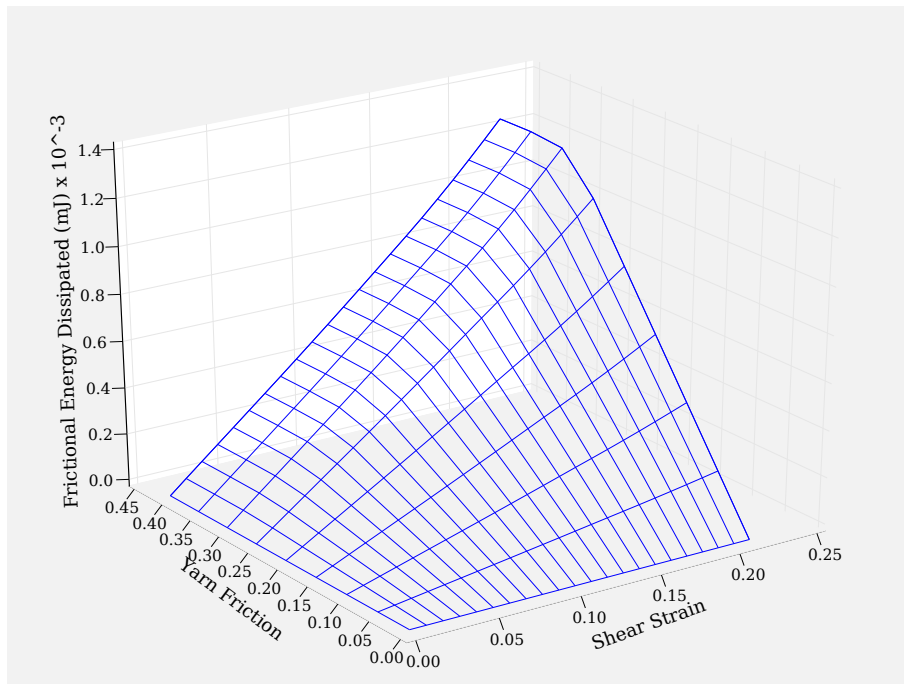
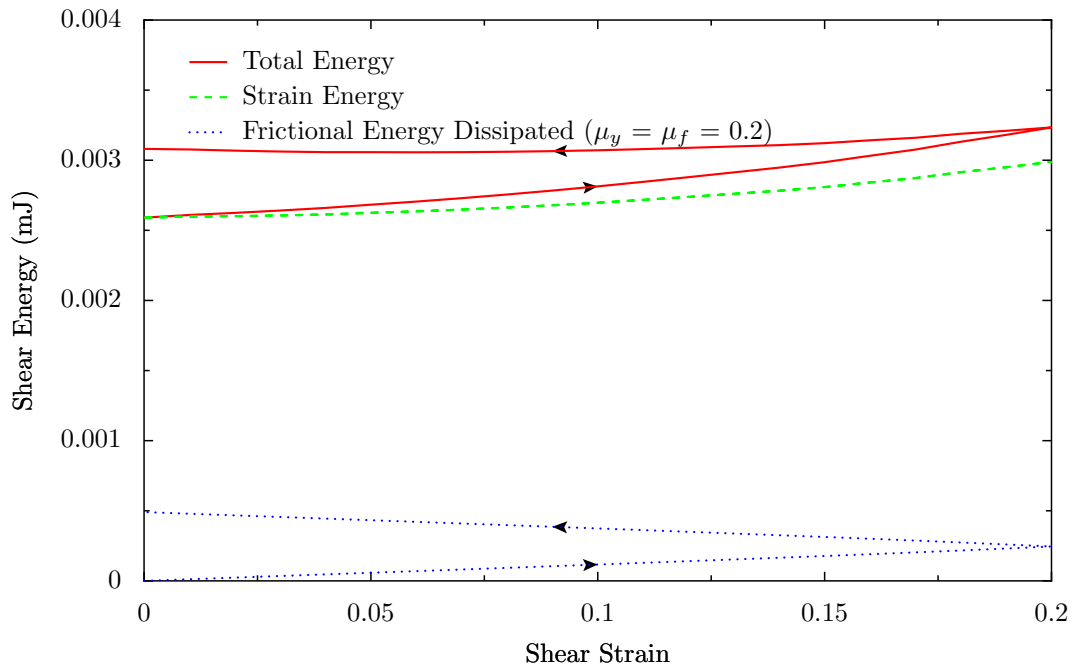


Figure 4.41: Effect of  $\mu_y$  and shear strain on frictional energy dissipated at  $\mu_f = 1$

In order to compare against experimental results, it is necessary to convert the energies into forces as described in Section 4.5.4. Figure 4.42 shows a graph of strain and frictional energy versus shear strain for fixed coefficients of friction. Both the loading and

unloading curves are plotted and for the strain energy these curves overlap. In contrast the frictional energy dissipated always increases. The total energy represents the total work done on the fabric during shearing.



**Figure 4.42:** Energy vs. Shear Strain, arrows indicating loading and unloading

The energies have been converted to normalised shear forces and are shown in Figure 4.43. Normalised shear force is obtained by dividing the shear force by the width of the domain. The shear forces due to friction and strain energy have been separated to see the effect of each. The loading and unloading curves of each are also shown to demonstrate the effect of hysteresis. Again the forces due to strain energy overlap whereas the forces due to friction do not. One fact that stands out is that the curve for shear force due to strain energy is not smooth. This is due to the numerical differentiation performed on the strain energy curve which tends to amplify very small changes in the strain energy. These fluctuations have no physical meaning and should be ignored. Otherwise, the shape of the curve is similar to what one would expect to obtain from experiments. Figures 4.44 and 4.45 show the effect of varying the coefficient of friction.  $\mu_y$  and  $\mu_f$  are given the same value and varied together since the effect of varying each one independently has already been demonstrated. When  $\mu_y$  and  $\mu_f$  are equal, sliding occurs between fibres within a tow and not between crossing tows.

The shear force due to strain energy does not depend on the coefficient of friction whereas the shear force due to friction is scaled linearly with the coefficient of friction. It is convenient to separate these two quantities for comparison with experimental data. The Kawabata Evaluation System for fabrics [58, 59] identifies 3 quantities

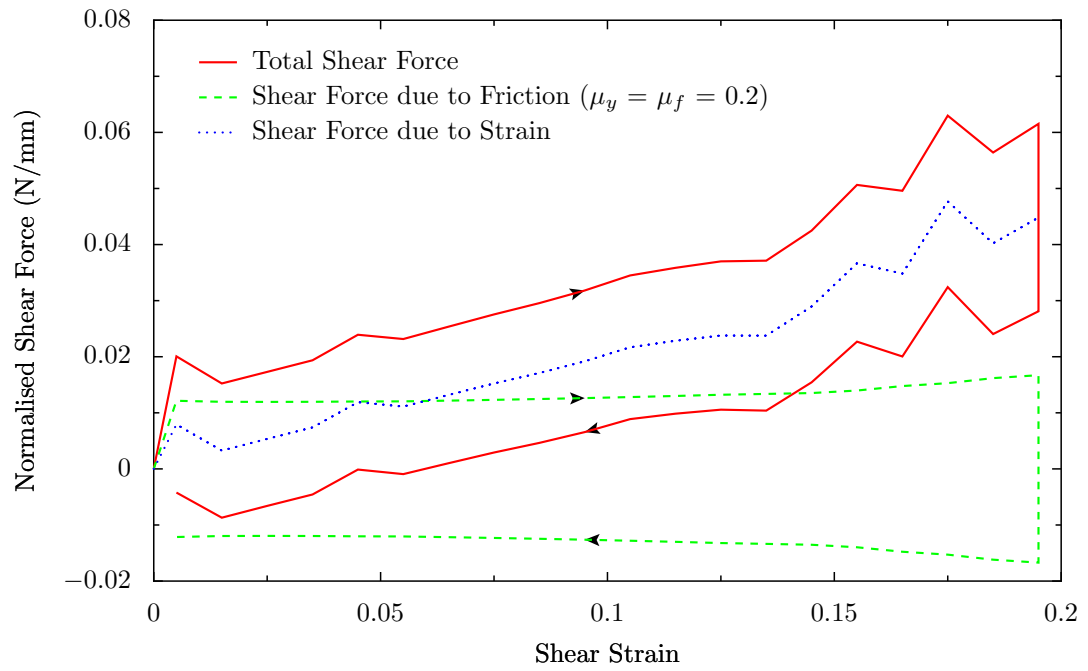


**Figure 4.43:** Normalised shear force vs. shear strain ( $\mu_y = \mu_f = 0.2$ )

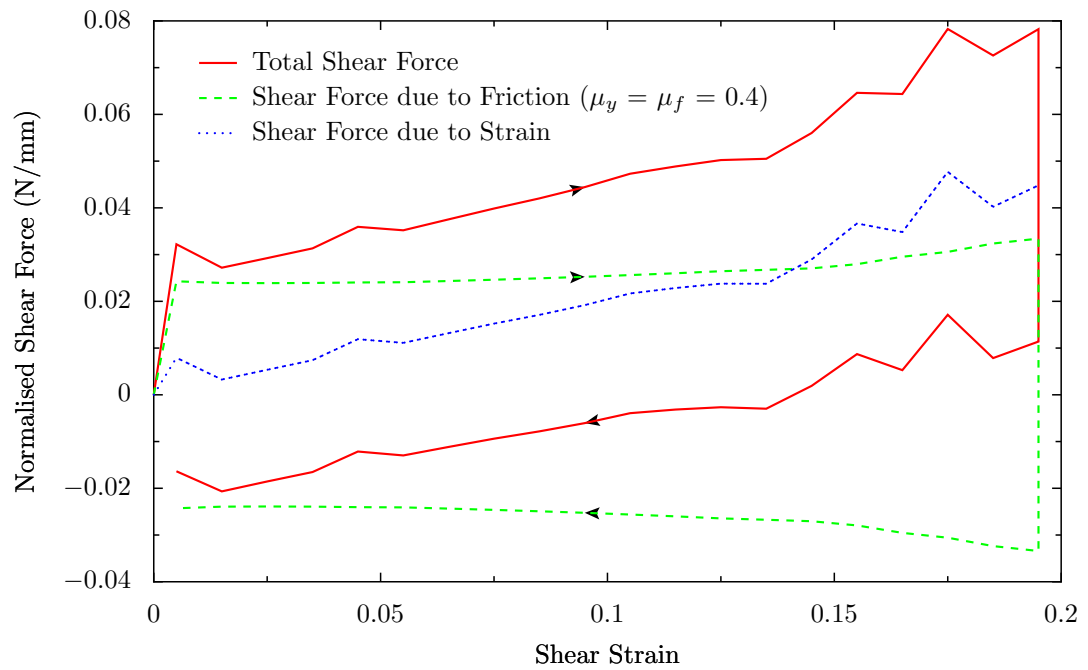


**Figure 4.44:** Normalised shear force vs. shear strain ( $\mu_y = \mu_f = 0.4$ )

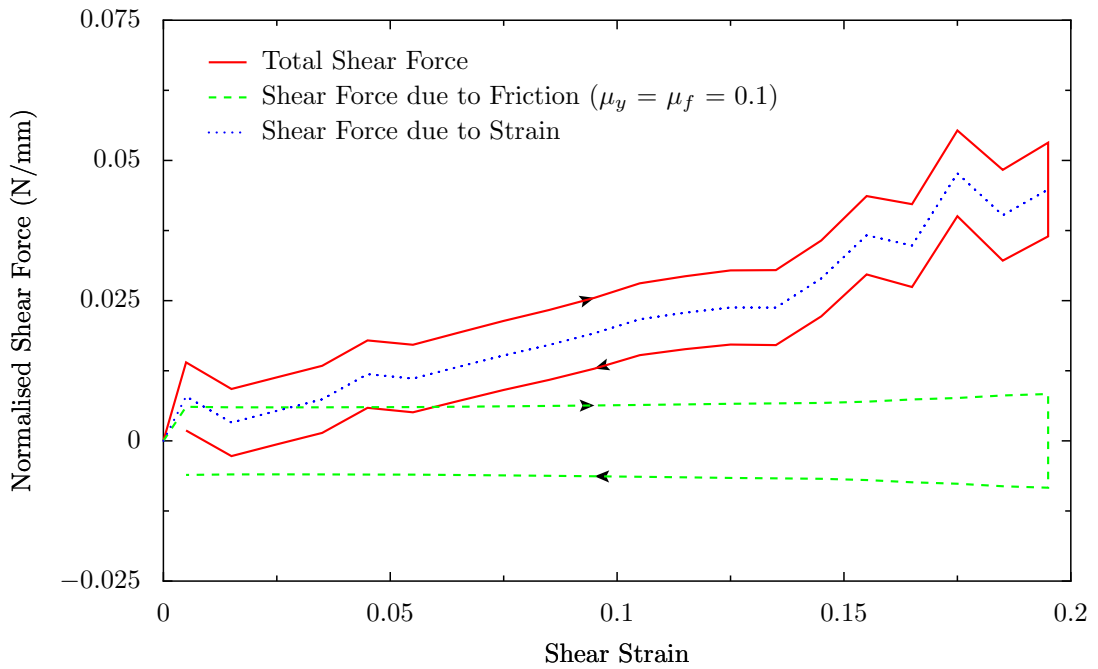


Figure 4.45: Normalised shear force vs. shear strain ( $\mu_y = \mu_f = 0.1$ )

from the curve: Shear stiffness  $G$  (cN/cm.degree), hysteresis of shear force at  $0.5^\circ$  of shear angle ( $2HG$ ) (cN/cm) and hysteresis of shear force at  $5^\circ$  of shear angle ( $2HG5$ ) (cN/cm). The quantities are illustrated in Figure 4.46. The shear stiffness  $G$  relates to the shear forces due to strain energy and hysteresis values  $2HG$  and  $2HG5$  relate to the shear forces due to friction. KES-f data were obtained for the polyester fabric by the University of Manchester and are shown in Table 4.5.

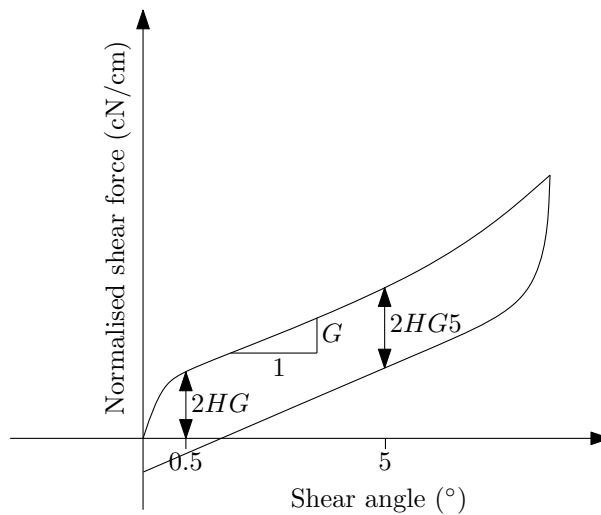


Figure 4.46: Kawabata Evaluation System for fabrics shear parameters [59]

The same polyester fabric was tested with different surface treatments to investigate their effect on mechanical properties. The first set of data is for untreated yarns, the

**Table 4.5:** KES-f experimental shear data

Fabric	$G$ (cN/cm.degree)	$2HG$ (cN/cm)	$2HG5$ (cN/cm)
Untreated	3.67	7.11	20.34
Treatment A	2.71	5.26	12.15
Treatment B	0.87	3.26	5.21

two other sets have surface treatments labelled treatment A and B.

In order to compare results from the simulation it is necessary to convert shear strain to shear angle. The following equation relates shear strain to shear angle:

$$\tan \theta = \varepsilon_{xy} \quad (4.104)$$

This non-linear relationship makes the conversion troublesome, however for small angles  $\tan \theta \approx \theta$  when  $\theta$  is given in radians. The error introduced by this assumption is only 0.25% for the highest angle of interest ( $5^\circ$ ). The conversion then becomes a simple linear scaling of values:

$$1 \frac{\text{N}}{\text{mm}} = \frac{1000\pi}{180} \frac{\text{cN}}{\text{cm.degree}} \quad (4.105)$$

The values for  $G$ ,  $2HG$  and  $2HG5$  from the simulation converted to the same units as the KES-f data are shown in Table 4.6.

**Table 4.6:** KES-f predicted shear data

Range	$G$ (cN/cm.degree)	$2HG$ (cN/cm)	$2HG5$ (cN/cm)
$\mu_f \leq 3.33 \mu_y$	3.53	$60.7 \mu_f$	$125 \mu_f$
$\mu_f \geq 3.33 \mu_y$	3.53	$202 \mu_y$	$415 \mu_y$

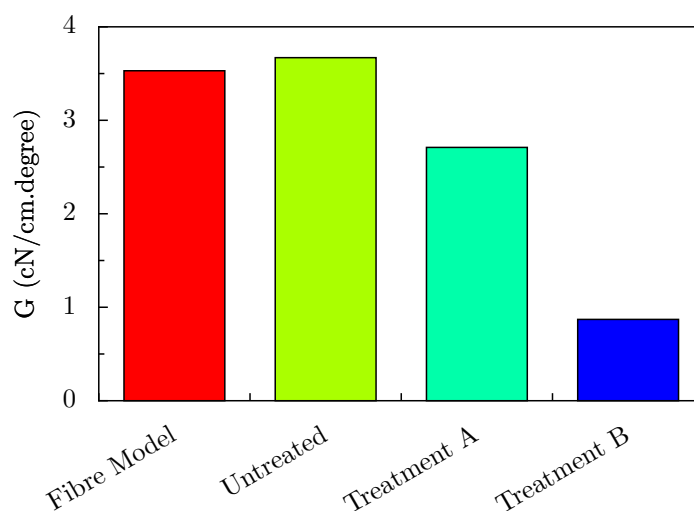
**Figure 4.47:** Comparison between model and experimental data for  $G$

Figure 4.47 illustrates the values of  $G$  for the KES-f experimental data and the simulation. The agreement is very good between the untreated experimental case and the fibre model. Without further knowledge of the type of treatment applied to the fabric, the treated fabrics cannot be modelled. According to the model, the friction between the yarns should have a negligible affect on the value of  $G$  because the shear force due to friction is almost constant compared to the shear force due to fibre bending. However, it is possible that the Young's modulus of the fibres may have been reduced during the treatment which would result in a reduction in  $G$ .

In order to compare results for  $2HG$  and  $2HG5$  a coefficient of friction is needed for the fibres. Using the KES-f system, a coefficient of friction  $MIU$  between a flat surface and the fabric was obtained and is shown in Table 4.7.  $MMD$  represents the Mean Deviation of the coefficient of friction.

**Table 4.7:** KES-f experimental friction data

Fabric	$MIU$	$MMD$
Untreated	0.124	0.0255
Treatment A	0.131	0.017
Treatment B	0.129	0.0174

The experimental data does not seem consistent since the coefficient of friction of  $MIU$  increases with both surface treatments whereas the hysteresis values  $2HG$  and  $2HG5$  reduce with both surface treatments. An increase in coefficient of friction  $MIU$  is expected to result in an increase in hysteresis values  $2HG$  and  $2HG5$ . Potluri [100] noted that in his experience the KES friction tester is not a particularly sensitive instrument. It should also be noted that the coefficient of friction used within the simulation should be that between two polyester fibres. This is not necessarily the same as that measured by the KES-f system.

However, using the value  $MIU$  for the untreated fibres in the simulation (with  $\mu_f = \mu_y$ ), values for  $2HG$  and  $2HG5$  were obtained and are shown in Figures 4.48 and 4.49. Again very good agreement can be seen between the model and the untreated fabric experimental data for  $2HG$ . The agreement for  $2HG5$  is not quite so good but the value from the simulation lies between the experimental values of the 3 fabrics.

Since the coefficient of friction obtained from the experimental data is not considered to accurately represent the coefficient of friction between fibres, it makes sense to calculate this value from the simulation using an inverse method (by combining results from Tables 4.5 and 4.6). The results are shown in Table 4.8 where  $\mu_f$  and  $\mu_y$  are again assumed to be equal. Two calculations are made, the first based on  $2HG$  the second

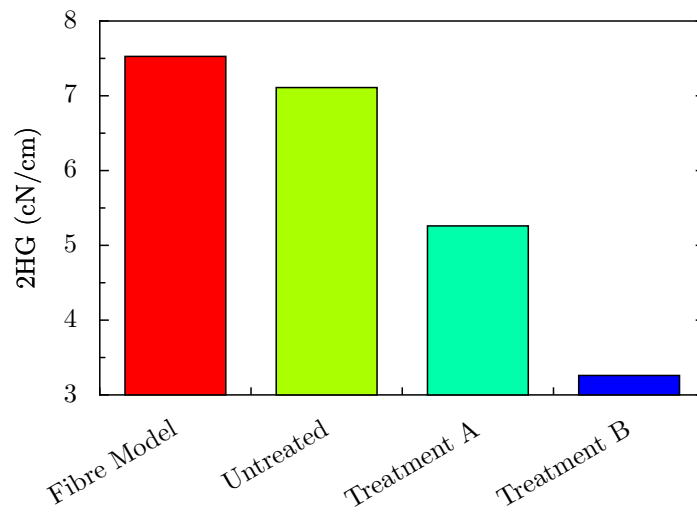


**Figure 4.48:** Comparison between model and experimental data for 2HG with  $\mu_f = \mu_y = 0.124$

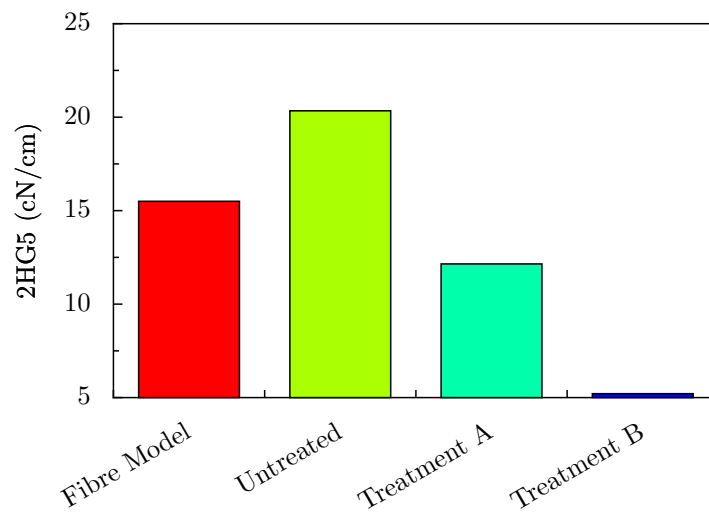


**Figure 4.49:** Comparison between model and experimental data for 2HG5 with  $\mu_f = \mu_y = 0.124$

based on 2HG5. The difference and mean of the two predictions is shown. The calculated coefficients of friction decrease with surface treatments as expected, in contrast to measurements from the KES-f system.

**Table 4.8:** Calculated coefficients of friction ( $\mu_f = \mu_y$ )

Fabric	From 2HG	From 2HG5	Mean	Difference
Untreated	0.117	0.162	0.139	32.4%
Treatment A	0.0866	0.0972	0.0919	11.5%
Treatment B	0.0537	0.0417	0.0477	25.2%

#### 4.5.6 Conclusions

The computational model developed has proven to be able to predict accurately the shear behaviour of the polyester fabric. No fitting parameters have been used to achieve this prediction. Elastic strain energy stored in the fibres and frictional energy dissipated during shear were both obtained from the model. These energies were then used to infer shear forces applied to the unit cell. A plot of shear force versus shear strain was obtained with the components due to fibre bending and fibre sliding separated out. The values obtained from the graph were compared to KES-f experimental data of the fabric under three different surface treatment states. Good agreement was shown for shear stiffness and hysteresis when compared against the untreated fabric. The coefficient of friction between the fibres was calculated for both treated fabrics using an inverse method.

The model was found to be more suitable for predicting the shear behaviour of a small unit cell than predicting compaction of a tow. This is believed to be because the boundary conditions were satisfactorily modelled for the shear case but not for the tow compaction case. With further work, the boundary conditions for the tow compaction case could be improved to give better results.



# Mechanical modelling of fabric unit cells

## 5.1 Introduction

This chapter is a theoretical study of the mechanical behaviour of textiles using finite element analysis [124, 145]. The method is designed to be sufficiently general that it can be applied to any type of fabric. Analytical solutions exist for simple textile structures, however these analytical methods are always aimed at a particular type of fabric and a particular mode of deformation. Extensions of these solutions to other fabric types or deformation modes either require substantial additional work or are not feasible. In contrast finite element analysis is very general; once the method has been developed for one fabric structure it can be extended to any type of fabric as long as it has a repeatable unit cell. In order to keep a general solution method, fabric symmetry should not be exploited since not all fabrics contain symmetries and certainly not the same symmetries. Instead periodic boundary conditions may be used which will be applicable to any repeatable unit cell no matter what the fabric type. This generality is obtained at the sacrifice of solution speed due to the increased mesh size where symmetries do exist. However with increases in computer processing speeds and the advent of parallel computing, the sacrifice is becoming less important.

## 5.2 Literature survey

### 5.2.1 Finite element analysis of fabric unit cells

The use of finite element analysis (FEA) in predicting mechanical properties of textile composites is well-established [25, 97, 109, 128]. However relatively little work has been done on predicting the mechanical properties of dry fabrics using FEA.

Tarfaoui and Akesbi [129] modelled the mechanical properties of a mono-filament plain weave with finite elements. The classic two dimensional geometrical models developed by Peirce [95] and Kemp [60] were extended to three dimensions. Volume meshes were then created from these geometries by linking a series of cross-sectional meshes together. Since the fabric modeled had mono-filament yarns, an isotropic material model was used avoiding issues such as material anisotropy and non-linearity. No comparison against experimental results was made and results were supplied in the form of minimum, maximum, and Tresca stresses for both Peirce's and Kemp's geometrical models. Unfortunately results in this form are very difficult to relate to experimental data.

Boisse et al. [10] used finite element analysis to model the behaviour of dry woven textiles under biaxial loads. The geometrical model consisted of cross-sections built of two straight vertical edges with a curved upper and lower surface presumably to provide a geometry easily meshed with high quality elements. The cross-section was then meshed with two rows of quadrilateral elements. For the biaxial simulations, the three shear moduli and three Poisson's ratios were set close to zero (zero values cause numerical difficulties during computation) and the transverse moduli were small in comparison with longitudinal modulus. The longitudinal modulus was determined via a tension test on one tow and an inverse identification was applied to obtain the non-linear transverse modulus. The finite element analysis gave good agreement with the experimental results for different ratios of biaxial loads.

Boisse et al. [11] later developed a finite element to model the behaviour of fabrics during forming. The approach consists of determining the behaviour of a fabric unit cell under biaxial tension and in-plane shear and using those properties to create a two dimensional element. Two approaches were explored in obtaining these properties. The first was to measure them from experiments on the fabrics and the second was through meso-scale finite element analysis as described in the previous paper. The finite element analysis of a plain woven fabric was performed using solid continuum elements. A number of issues were identified as being important to obtain accurate results:

- The fibre direction must be accurately represented due to the highly anisotropic material model involved (see Section 5.5.1). It was noted that commercial codes such as ABAQUS<sup>TM</sup>[51] do not correctly track the fibre directions during deformation without the use of custom code. Hagege [44], Hagege et al. [45] wrote a VUMAT for ABAQUS to deal with this issue.
- The transverse compaction behaviour is important in obtaining accurate results. The transverse modulus  $E_T$  was modelled with the following formula:

$$E_T = E_0 |\varepsilon_T^n| \varepsilon_L^m + E_\varepsilon \quad (5.1)$$

where  $E_0$ ,  $n$  and  $m$  are arbitrary constants to be determined by an inverse method. The value of  $E_\varepsilon$  is the initial transverse modulus supposedly also chosen arbitrarily.

- The shear modulus was chosen to be nearly equal to zero given the argument that the fibres can slide relatively easily. In fact the transverse shear behaviour of a tow is much more complex than this (see Section 5.4.2).
- Boundary conditions were applied by prescribing displacements causing the desired fabric deformation while restricting degrees of freedom to ensure periodicity. However in the case of the fabric shear, the displacements were over-constrained due to enforcing the yarn edges to remain in the plane perpendicular to the yarn normal. By doing so the effect of using a simplified transverse shear behaviour was reduced.
- A limitation was noted in modelling shear where the simulation was unable to complete when contact between adjacent yarns occurred. This was due to the limitations in the contact algorithm found in ABAQUS which is unable to deal with contact between sharp edges. Hence only the initial stages of fabric shear could be modelled. A further limitation not mentioned is that once the shear angle becomes large a periodic contact algorithm is necessary (see Section 5.4.6).

## 5.2.2 Experimental methods

Several experimental methods exist to characterise various mechanical properties of fabrics.

Kawabata [58], Kawabata and Niwa [59] developed the Kawabata Evaluation System for fabrics (KES-f) to characterize the mechanical properties of fabrics. The system is composed of 4 separate components: tensile and shear tester, pure bending tester,

compression tester and the surface tester. The tensile and shear tester is capable of measuring the tensile strain/force response of a fabric up to 500 gf/cm and measuring the shear response of a fabric up to 8 degrees of shear. The pure bending tester applies a constant curvature to the fabric and measures the bending moment up to a curvature of  $3 \text{ cm}^{-1}$ . The compression tester applies a through thickness force to the fabric of up to 50 gf/cm<sup>2</sup>. The surface tester measures the coefficient of friction between the fabric and a friction contactor, and measures the surface roughness with the roughness contactor.

However, the cost of the system is very high and it is only suitable for measuring mechanical properties at relatively low loads compared to the loads applied to textile composite preforms.

CSIRO Division of Wool Technology in Australia developed another set of instruments named Fabric Assurance by Simple Testing (FAST) for measuring mechanical properties of fabrics [89]. The FAST system is much cheaper and is composed of 3 components: compression meter, bending meter and the extension meter. The compression meter measures thickness of the fabric at 2 gf/cm<sup>2</sup> and 100 gf/cm<sup>2</sup> of pressure. This is done simply by adding weights to a measuring cup. The bending meter uses the cantilever bending principle, as described in British Standard Method (BS 3356:1961). However the bending meter provides a photocell to detect the leading edge of the sample, replacing the need for it to be done by eye. The extension meter operates on a simple lever principle with weights applied to the fabric to provide three different strain measurements. This system also operates at low loads and does not provide as much detailed information as the KES-f system.

Other experimental tests which aim to characterise a single mode of deformation are discussed below.

### **Tensile tests**

Tensile tests on fabrics can be carried out on standard testing equipment such as Instron and Hounsfield test frames. These setups are generally more suitable for larger loads compared to the more sensitive measurement capability provided by the KES-f system. In order to perform biaxial tensile tests a more sophisticated setup is required. Buet-Gautier and Boisse [12] describe a device capable of applying two different strains proportional to each other in two orthogonal directions. The ratio of the two strains is denoted  $k$ . This system is suitable for testing tensile properties of fabrics with high moduli, typically as found in textile composite preforms.

### Compression tests

Compression tests on fabrics can also be carried out on standard testing equipment where the fabric is placed between two parallel plates and the force measured with a load cell [103]. These setups are able to reach loads in the order of 1 MPa compared to 5 kPa on the KES-f system. However the pressure cannot generally be measured as accurately at low loads. For these tests to be completed successfully the degree of misalignment between the plates must be small especially for thin samples.

### Shear tests

Two methods of measuring the shear behaviour of fabrics at high shear levels are available, namely the picture frame test and bias extension test [47, 80, 144]. In the picture frame test, the fabric is clamped onto the four sides of a square frame. Bearings at the corners of the frame allow the frame to shear into a rhombus shape. Tensile forces are applied to two opposite corners of the frame to induce shear while measuring the reaction forces. A limitation of this method is that it is very sensitive to fabric misalignment and hence repeatability can be an issue.

The bias extension test involves clamping the fabric on only two sides in a similar manner to a simple extension test; however the fabric is placed such that yarns are oriented at  $45^\circ$  to the clamped edges. Tensile forces are then applied to the clamps to induce a shear deformation in the fabric. In order for this test to be valid, the length of the sample must be at least twice its width. The bias extension test is less sensitive to misalignment and does not require a picture frame to perform the test. The disadvantages are that the fabric tends to tear apart at high levels of shear and the results are more difficult to interpret. However Potluri et al. [98] devised a method to improve accuracy of the bias extension test up to higher levels of shear by using a wide-strip sample that is only partly clamped at the edges.

## 5.3 Experimental techniques

A compression rig was developed to test the fabric under high loads. The rig was mounted on a Hounsfield series S testing machine capable of measuring force up to an accuracy of 0.1 N. The fabric is placed on a static bottom plate while the top plate of diameter 100 mm moves vertically downwards at a rate of 1 mm/s until a force of 20 kN is reached. A compression LVDT with accuracy of 0.001 mm is mounted on the top plate to measure relative displacement between the two plates. The setup is illustrated

in Figure 5.1. The degree of parallelism was measured with slip gauges and it was determined that the angle between the two plates was  $0.082^\circ$ .



**Figure 5.1:** Fabric compression rig

The force measured was converted to pressure by dividing by the area of the top plate. The thickness of the fabric for a given force was calculated as the difference between the LVDT measurements with and without fabric placed between the plates. In order to obtain both sets of LVDT measurements the fabric compaction tests were followed by a compaction test without the fabric. Each test was performed 5 times and the standard deviation of the thickness values measured for a series of pressures were calculated.

## 5.4 Finite element method

This section will describe the explicit finite element analysis (FEA) code written by the author to predict mechanical properties of unit cells. Generally, an implicit FE method is preferable compared to an explicit method to solve static problems. However due to the complicated contacts present within dry textile structures the explicit method is thought to be more suitable.

The method involves treating yarns as regions of a continuum in which a given stress-strain relationship is assumed. By applying boundary conditions to the yarns, certain deformations can be imposed to the unit cell which replicate experimental tests and/or deformations that the fabric may undergo in its given application. The finite element method then predicts steady state equilibrium of the fabric for the given deformation.

In order to be able to calculate numerically the stresses and strains within a yarn it is

necessary to discretise the model. An important requirement is that each element has shared boundaries with its neighbours. The boundaries are composed of faces which are defined by edges which are in turn defined by points or nodes. Note that the nodes are shared between multiple elements.

The strain within each element is calculated based on the deformation of the element and the deformation of the element depends on the position of its nodes. Hence by imposing displacements to the nodes it is possible to induce strains in the elements. These strains result in a stress within the element which is calculated based on the stress-strain relationship (material model or constitutive model). Forces acting on the nodes can be extrapolated from the stress within the elements. When the model is in a steady state the total force acting on each node due to its surrounding elements should be equal to zero except at the nodes where displacements have been prescribed.

The difference between an explicit and implicit method is in how this steady state is arrived at. The explicit method calculates the state of the system at a later time from the state of the system at the current time, while the implicit method finds it by solving an equation involving both the current state of the system and the later one. For simple linear cases the implicit method can find a solution in a single iteration whereas the explicit method requires a number of iterations in order to arrive at the solution. However the computational time required to perform a single implicit iteration is far greater than that required to perform an explicit iteration.

In order to gain a better understanding of the finite element method and have complete freedom to implement new algorithms, the decision to develop a new finite element analysis solver was made. The code was inspired by techniques from various open source finite element packages, notably **Impact** [37]. Unfortunately Impact was found to contain a number of bugs and poor programming practises in key areas of the software which lead the author to write his own code. The implementation was validated for a series of elements, deformation modes and material properties against the commercial finite element package ABAQUS<sup>TM</sup>[51] and was shown to be accurate. Results are shown in Appendix I.

Figure 5.2 shows the finite element program flowchart. The code was written in C++ in an object oriented manner with no use of external libraries.

#### 5.4.1 Element definition

In order to numerically represent strains in a body it is necessary to split the body into discrete elements. In this thesis the use of continuum elements is explored where the

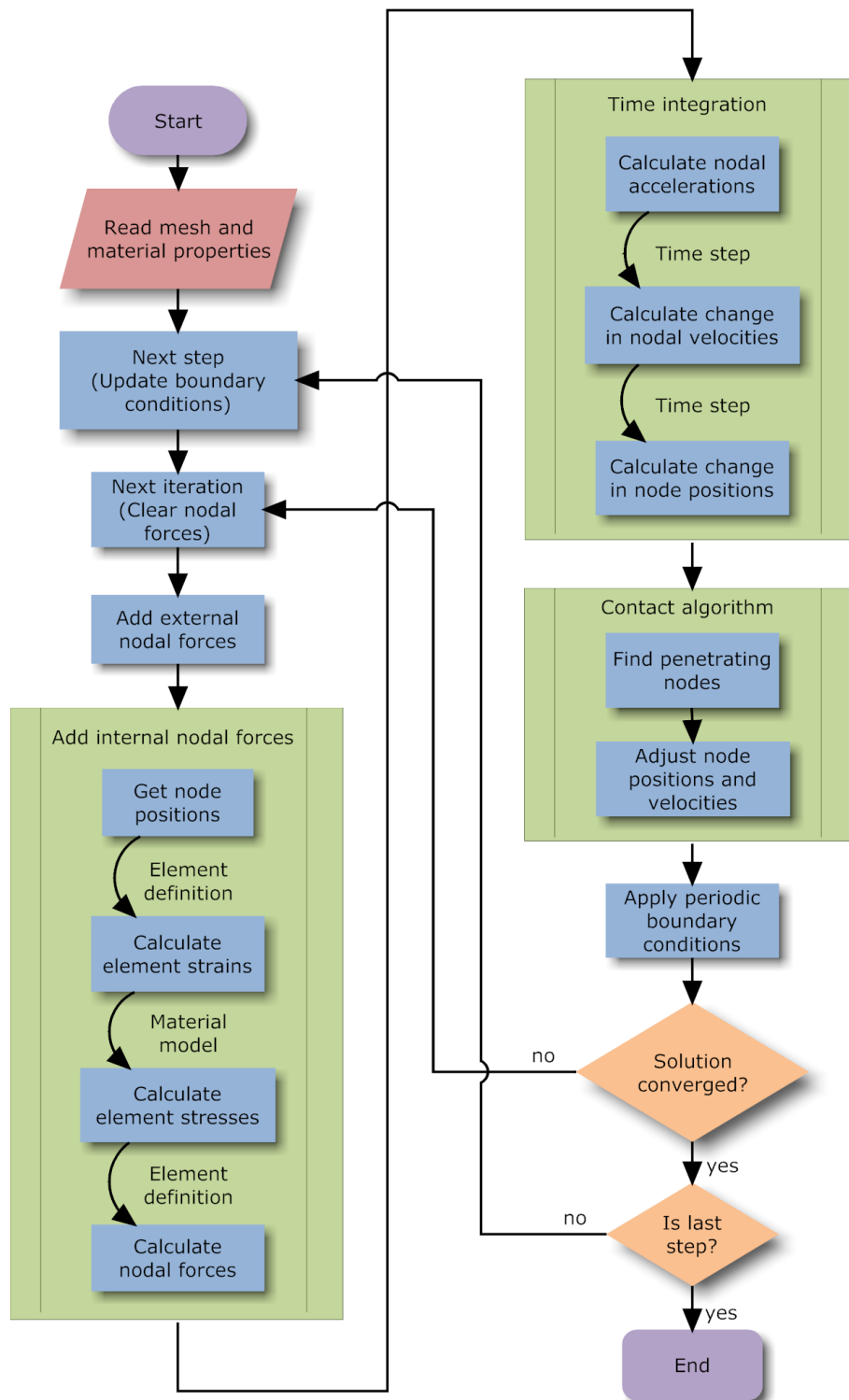


Figure 5.2: Finite element analysis program flowchart



body is split into a finite number of small volumes of given shape. The most common shapes used are hexahedron and tetrahedron, less common shapes include wedge and pyramid.

The element definition is responsible for interpolating values from the element's nodes to any position within the element. In the context of this thesis, nodal displacements are interpolated and integrated to obtain the element strain. A brief overview of the procedure is described in this section; a more detailed explanation can be found in standard finite element analysis text books [145]. The element definition is independent from the type of solver (explicit and implicit), however due to the difference in nature between the explicit and implicit methods, element definition optimisations are often targeted at one of the two methods. Therefore it is common to find elements specific to explicit or implicit solvers in commercial code such as ABAQUS<sup>TM</sup>[51].

The displacement  $\vec{u}$  of any point  $x$  within an element is calculated as:

$$\vec{u}(x) = \mathbf{N}(x)\mathbf{q} \quad (5.2)$$

where  $\mathbf{N}$  is 1-by- $m$  matrix called the shape function matrix and  $\mathbf{q}$  is a  $m$ -by- $n$  matrix containing the nodal displacements.  $m$  represents the number of nodes of the element and  $n$  represents the number of dimensions. For example, given a 3-noded triangular element in two dimensions with nodal displacements  $\vec{u}_1$ ,  $\vec{u}_2$  and  $\vec{u}_3$ , Equation 5.2 becomes:

$$\begin{bmatrix} \vec{u}_x & \vec{u}_y \end{bmatrix} = \begin{bmatrix} \mathbf{N}_{1,1} & \mathbf{N}_{1,2} & \mathbf{N}_{1,3} \end{bmatrix} \begin{bmatrix} \vec{u}_{1x} & \vec{u}_{1y} \\ \vec{u}_{2x} & \vec{u}_{2y} \\ \vec{u}_{3x} & \vec{u}_{3y} \end{bmatrix} \quad (5.3)$$

The values in the matrix  $\mathbf{N}$  depend on the position of the nodes and the type of element [145]. The strain at any point  $x$  in the element can then be calculated as a function of the displacement field  $\vec{u}$ . There are two ways in which this can be done, as described in Section 5.4.2. Note that in linear elements such as the 3 noded triangle and 4 noded tetrahedron, the strain over the entire element is constant. 4 noded quadrilateral elements, 6 noded wedge elements and 8 noded hexahedral elements are often referred to as linear elements although the interpolation function is not linear resulting in a non-constant strain over the element. Nevertheless the strain must be a continuous function of position across the element and the mass within an element must stay within the element. This causes problems when attempting to model shear of a yarn as a continuum.

Figure 5.3 illustrates an idealised section of tow containing four parallel fibres within a single quadrilateral element. The undeformed tow is shown (a), as is the tow sheared as a continuum element (b) and the tow sheared as it would in reality (c). Note that in

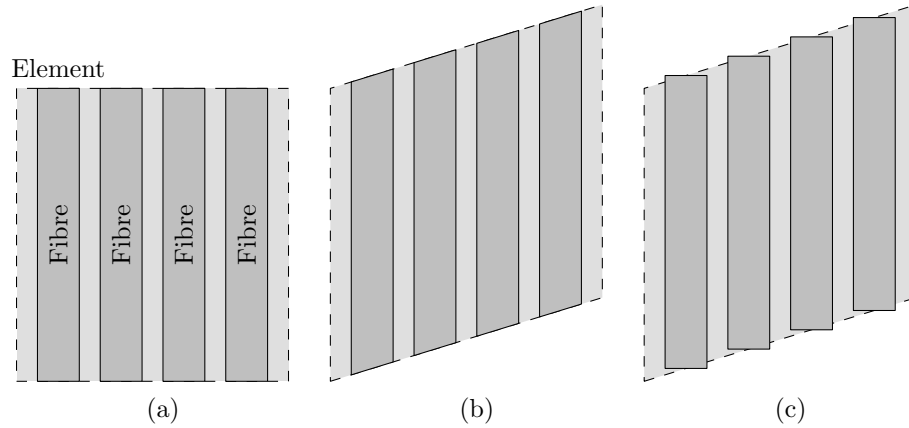


**Figure 5.3:** Element of a yarn under shear

the last case part of the fibre mass crosses the element boundary. This occurs because fibres are able to slide past each other without inducing any shear strain in the fibres themselves.

In essence the shear strain of an element does not accurately represent the strains of the fibres contained within it. Hence the model will be unable to accurately predict the behaviour of a fabric where internal fibre strains are important, notably in bending of a yarn.

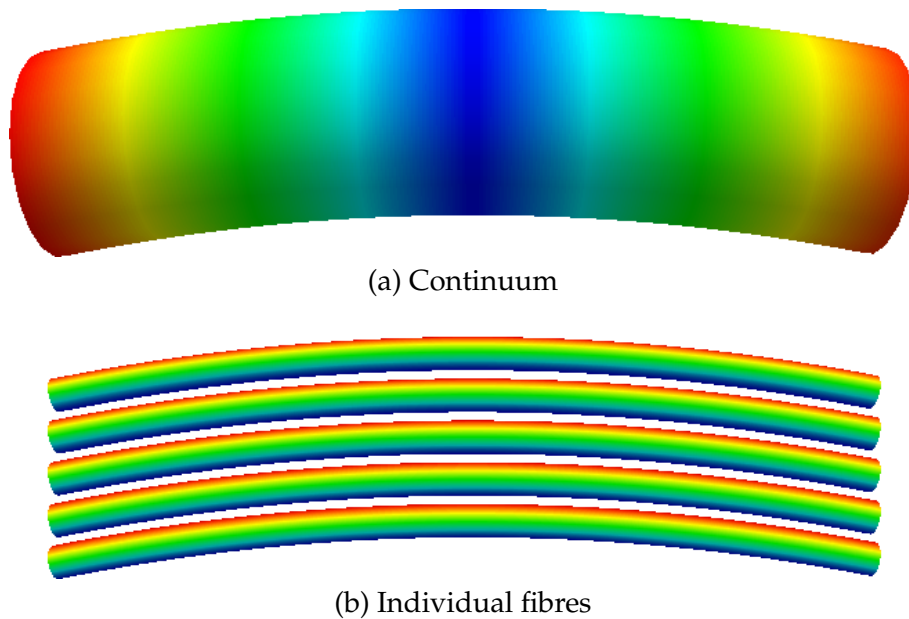


**Figure 5.4:** Tow bending with strains displayed as a colour map (a - shear strain, b - tensile strain)

This limitation is illustrated in Figure 5.4 where a tow under a bending deformation treated as a continuum (a) and as individual fibres (b) is shown. The color represents

the magnitude of shear and tensile strain respectively. The tow treated as a continuum contains no strains half way along the length of the tow and highest shear strains at the edges. The fibres on the other hand contain no strains about their neutral axis, high compressive strains towards the bottom and high tensile strains at the top.

This figure illustrates the very different strains that occur within the fibres and the continuum that is supposed to represent them. The shear strain occurring in the continuum gives a measure of the amount of sliding occurring between fibres, it does not however give any measure of strain contained within the fibres. The tendency for the tow to straighten itself is governed by these fibre strains. Hence the tow modelled as a continuum is unable to accurately model the straightening behaviour of a tow under bending deformation. The consequences of this will be discussed further in the relevant sections.

## 5.4.2 Material model

The material model describes the stress of yarn as a function of its strain and ultimately defines what forces result from given displacements. This presents significant problems when modelling the mechanical behaviour of dry textiles.

### Strain

To begin with, it is necessary to fully understand the meaning of strain before a material model can be derived. Strain  $\varepsilon$  represents the deformation of a body, in the simple one dimensional case it only has one component and perhaps the most familiar definition of it is known as **engineering strain**:

$$\varepsilon = \frac{L_1 - L_0}{L_0} \quad (5.4)$$

where  $L_0$  is the length of a body before undergoing uniform deformation, and  $L_1$  is the length after deformation. An alternative definition of strain, known as **logarithmic strain** is:

$$\varepsilon = \ln \left( \frac{L_1}{L_0} \right) \quad (5.5)$$

For small strains these two definitions are equivalent. The advantage of logarithmic strain over engineering strain is that strains can be added. For example, suppose the body were to undergo a series of two deformations from length  $L_0$  to  $L_1$  and then to  $L_1$  to  $L_2$ . The total engineering strain cannot be expressed as the sum of the two

components of engineering strain:

$$\frac{L_2 - L_0}{L_0} \neq \frac{L_1 - L_0}{L_0} + \frac{L_2 - L_1}{L_1} \quad (5.6)$$

But total logarithmic strain can be expressed as the sum of their components:

$$\ln\left(\frac{L_2}{L_0}\right) = \ln\left(\frac{L_1}{L_0}\right) + \ln\left(\frac{L_2}{L_1}\right) \quad (5.7)$$

The use of engineering or logarithmic strain is one of convenience. However it is important to stay consistent when defining the material model. If logarithmic strain is used then stress should be defined as a function of logarithmic strain. If engineering strain is used, then stress should be defined as a function of engineering strain.

If the deformation in the body is not uniform, then the strain will vary throughout the length of body and this simplified equation does not apply. To derive a new expression for strain that takes into account non-uniform deformation it is convenient to express the displacement of a point in the body by a vector  $\vec{u}$  as a function of position  $x$ . The **engineering strain** can then be expressed as:

$$\varepsilon = \frac{d\vec{u}}{dx} \quad (5.8)$$

Noting that  $\vec{u}$  is a function of position  $x$ ,  $\varepsilon$  is also a function  $x$ . This use of displacement vector  $\vec{u}$  the makes it easy to extend into three dimensions. The direct strains  $\varepsilon_x$ ,  $\varepsilon_y$  and  $\varepsilon_z$  can be expressed as:

$$\varepsilon_x = \frac{\partial \vec{u}_x}{\partial x} \quad (5.9)$$

$$\varepsilon_y = \frac{\partial \vec{u}_y}{\partial y} \quad (5.10)$$

$$\varepsilon_z = \frac{\partial \vec{u}_z}{\partial z} \quad (5.11)$$

In three dimensions, shear deformations are possible and they are represented by shear strains  $\varepsilon_{xy}$ ,  $\varepsilon_{yz}$  and  $\varepsilon_{zx}$ . To complicate matters a different definition of shear strain known as engineering shear strains  $\gamma_{xy}$ ,  $\gamma_{yz}$  and  $\gamma_{zx}$  also exists representing the same thing. They are defined as:

$$\varepsilon_{xy} = \varepsilon_{yx} = \frac{\gamma_{xy}}{2} = \frac{\gamma_{yx}}{2} = \frac{1}{2} \left( \frac{\partial \vec{u}_x}{\partial y} + \frac{\partial \vec{u}_y}{\partial x} \right) \quad (5.12)$$

$$\varepsilon_{yz} = \varepsilon_{zy} = \frac{\gamma_{yz}}{2} = \frac{\gamma_{zy}}{2} = \frac{1}{2} \left( \frac{\partial \vec{u}_y}{\partial z} + \frac{\partial \vec{u}_z}{\partial y} \right) \quad (5.13)$$

$$\varepsilon_{zx} = \varepsilon_{xz} = \frac{\gamma_{zx}}{2} = \frac{\gamma_{xz}}{2} = \frac{1}{2} \left( \frac{\partial \vec{u}_z}{\partial x} + \frac{\partial \vec{u}_x}{\partial z} \right) \quad (5.14)$$

Again it is a matter of convenience which definition is used as long as consistency is maintained. The deformation of any point in a body is defined by these 6 unique strain components  $\varepsilon_x, \varepsilon_y, \varepsilon_z, \varepsilon_{xy}, \varepsilon_{yz}$  and  $\varepsilon_{zx}$ .

The strain definitions presented above are known as small strain theory because they are only valid for small deformations. If the body undergoes a rigid body rotation the above strain definition will result in non-zero strains. Since the stresses are defined as a function of strain, this will result in non-zero stresses in the body. This is not a realistic model, since rigid body rotation should not induce stresses into a body.

In some applications with negligible rotation it is acceptable to use these strain definitions, but that is not the case for dry textile mechanics since yarns undergo large rotations during shear. A different definition of strain needs to be derived which is not affected by rotation using finite deformation tensors.

Suppose the position of a particle in the undeformed state of a body is denoted by  $\mathbf{X}$  and its position in the deformed state is denoted by  $\mathbf{x}$ . If  $d\mathbf{X}$  is a line segment joining two nearby particles in the undeformed state and  $d\mathbf{x}$  is the line segment joining the same two particles in the deformed state. Line segments  $d\mathbf{x}$  and  $d\mathbf{X}$  can be related by a linear transformation  $\mathbf{F}$ :

$$d\mathbf{x} = \mathbf{F}d\mathbf{X} \quad (5.15)$$

where  $\mathbf{F}$  is known as the deformation gradient and can be expressed as:

$$\mathbf{F} = \frac{\partial \mathbf{x}}{\partial \mathbf{X}} \quad (5.16)$$

Or in index notation:

$$F_{ij} = \frac{\partial x_i}{\partial X_j} \quad (5.17)$$

The deformation gradient  $\mathbf{F}$  is a second order tensor and contains information about both the stretch and rotation of the body. If the stretch can be separated from the rotation, then a definition of strain based on stretch alone can be obtained. This can be achieved with the polar decomposition theorem [20, 33]. The deformation gradient  $\mathbf{F}$  can be expressed as the multiple of a rotation tensor  $\mathbf{R}$  and a stretch tensor  $\mathbf{U}$ :

$$\mathbf{F} = \mathbf{R}\mathbf{U} \quad (5.18)$$

The stretch tensor  $\mathbf{U}$  is not affected by any rotations and will remain identity when a body undergoes rigid body rotation. Strains can be extracted from  $\mathbf{U}$  but first the principal stretches and stretch directions must be obtained. This is accomplished by using the spectral decomposition theorem [5, 46].

$$\mathbf{U} = \sum_{i=1}^3 \lambda_i \vec{\mathbf{N}}_i \otimes \vec{\mathbf{N}}_i \quad (5.19)$$

where  $\lambda_i$  are eigenvalues representing the principal stretches and  $\vec{N}_i$  are eigenvectors representing the principal stretch directions. The principal **logarithmic strains**  $\varepsilon_i$  are defined as:

$$\varepsilon_i = \ln(\lambda_i) \quad (5.20)$$

The principal strain directions are the same as the principal stretch directions. The strains can then be expressed in any coordinate system by transforming the principal strains into that coordinate system with the aid of the principal strain directions.

Both small strain and large strain theories have been implemented in the finite element code for validation purposes. However for all the simulations, the latter is used and all references to strain from here on will be to logarithmic strain. In ABAQUS<sup>TM</sup>[51] small strain theory is referred to as linear geometry and large strain theory is referred to as non-linear geometry.

### Stress

Stress is the internal distribution of force per unit area that balances and reacts to external loads applied to a body. Stresses are calculated as a function of the strain state and this relationship is called the material model. If the material modelled is perfectly elastic then the state of stress within a body depends only on the state of strain at the current point in time. However, if the material exhibits a plastic behaviour then the state of stress also depends on the strain history. That is to say all deformations taken place up to the current moment in time affect the current state of stress.

Yarns are not completely anisotropic, they are termed transversely isotropic. This means that there exists a plane of symmetry where the stress response is isotropic in that plane of symmetry. This plane of symmetry is perpendicular to the yarn direction  $\mathbf{S}'$ . If the material is assumed to be linear elastic, the stress can be defined as a function of strain with 5 constants. The constants are longitudinal modulus  $E_L$ , transverse modulus  $E_T$ , transverse Poisson's ratio  $\nu_{TT}$ , transverse-longitudinal Poisson's ratio  $\nu_{TL}$  and transverse-longitudinal shear modulus  $G_{TL}$ .

From these 5 constants, the longitudinal-transverse Poisson's ratio  $\nu_{LT}$  and transverse shear modulus  $G_{TT}$  can be calculated as:

$$\nu_{LT} = \frac{\nu_{TL}E_L}{E_T} \quad (5.21)$$

$$G_{TT} = \frac{E_T}{2(1 + \nu_{TT})} \quad (5.22)$$

Defining the z axis as being parallel to the yarn direction  $\mathbf{S}'$  and axes x, y such that all three axes are all orthogonal to each other, the stress can be related to strain by the

following stiffness matrix:

$$\begin{bmatrix} \sigma_x \\ \sigma_y \\ \sigma_z \\ \sigma_{xy} \\ \sigma_{yz} \\ \sigma_{zx} \end{bmatrix} = \begin{bmatrix} \frac{E_T(1-\nu_{TL}\nu_{LT})}{\Delta} & \frac{E_T(\nu_{TT}+\nu_{TL}\nu_{LT})}{\Delta} & \frac{E_L(\nu_{TL}+\nu_{TT}\nu_{TL})}{\Delta} & 0 & 0 & 0 \\ \frac{E_T(\nu_{TT}+\nu_{TL}\nu_{LT})}{\Delta} & \frac{E_T(1-\nu_{TL}\nu_{LT})}{\Delta} & \frac{E_L(\nu_{TL}+\nu_{TT}\nu_{TL})}{\Delta} & 0 & 0 & 0 \\ \frac{E_T(\nu_{TL}+\nu_{TT}\nu_{TL})}{\Delta} & \frac{E_T(\nu_{TL}+\nu_{TT}\nu_{TL})}{\Delta} & \frac{E_L(1-\nu_{TT}^2)}{\Delta} & 0 & 0 & 0 \\ 0 & 0 & 0 & G_{TT} & 0 & 0 \\ 0 & 0 & 0 & 0 & G_{TL} & 0 \\ 0 & 0 & 0 & 0 & 0 & G_{TL} \end{bmatrix} \begin{bmatrix} \varepsilon_x \\ \varepsilon_y \\ \varepsilon_z \\ \gamma_{xy} \\ \gamma_{yz} \\ \gamma_{zx} \end{bmatrix} \quad (5.23)$$

where  $\Delta$  is defined as:

$$\Delta = (1 + \nu_{TT})(1 - \nu_{TT} - 2\nu_{TL}\nu_{LT}) \quad (5.24)$$

Note that if all the Poisson's ratios are set to 0 then the stiffness matrix simply becomes:

$$\begin{bmatrix} \sigma_x \\ \sigma_y \\ \sigma_z \\ \sigma_{xy} \\ \sigma_{yz} \\ \sigma_{zx} \end{bmatrix} = \begin{bmatrix} E_T & 0 & 0 & 0 & 0 & 0 \\ 0 & E_T & 0 & 0 & 0 & 0 \\ 0 & 0 & E_L & 0 & 0 & 0 \\ 0 & 0 & 0 & G_{TT} & 0 & 0 \\ 0 & 0 & 0 & 0 & G_{TL} & 0 \\ 0 & 0 & 0 & 0 & 0 & G_{TL} \end{bmatrix} \begin{bmatrix} \varepsilon_x \\ \varepsilon_y \\ \varepsilon_z \\ \gamma_{xy} \\ \gamma_{yz} \\ \gamma_{zx} \end{bmatrix} \quad (5.25)$$

Defining the moduli as constants restricts the material model to linear elastic materials. However the mechanical behaviour of a yarn is highly non-linear, hence the moduli need to vary based on strain.

**Longitudinal behaviour** The longitudinal modulus  $E_L$  can be approximated in terms of fibre volume fraction  $V_f$  and fibre modulus  $E_f$  by the following equation:

$$E_L = E_f V_f \quad (5.26)$$

This is assuming all fibres within a tow are perfectly parallel and hence no stiffening of the yarn occurs due to fibre straightening at low strains.

The longitudinal modulus  $E_L$  defined in Equation 5.26 depends on volume fraction  $V_f$  and volume fraction will vary at each point in the yarn during deformation. Therefore it is necessary to calculate a different value of  $E_L$  for each element in the model depending on the element's volume fraction. The volume fraction of an element can be calculated as a function of element strains  $\varepsilon_x$  and  $\varepsilon_y$ . Figure 5.5 illustrates a small portion of a yarn cross-section of width  $w$  and height  $h$  under strains  $\varepsilon_x$  and  $\varepsilon_y$  (Note this uses the logarithmic definition of strain).

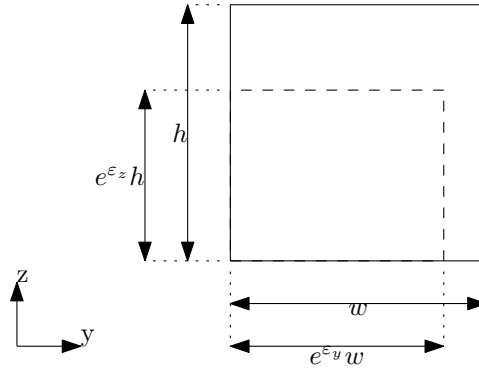


**Figure 5.5:** Strained cross-section of yarn

The area of the undeformed section of yarn  $A_0$  is defined as:

$$A_0 = wh \quad (5.27)$$

The deformed area  $A$  is defined as:

$$A = e^{\epsilon_x} e^{\epsilon_y} wh \quad (5.28)$$

At this point it is convenient to define a transverse strain  $\epsilon_T$  which measures the ratio of change of cross-sectional area defined as:

$$\epsilon_T = \epsilon_x + \epsilon_y \quad (5.29)$$

Equation 5.28 then becomes:

$$A = e^{\epsilon_T} wh \quad (5.30)$$

Supposing the area occupied by fibres is  $A.F.$  and remains constant during deformation, the fibre area fraction before deformation  $A_{f0}$  and area fraction after deformation  $A_f$  can be calculated as:

$$A_{f0} = \frac{A.F.}{A_0} \quad (5.31)$$

$$A_f = \frac{A.F.}{A} \quad (5.32)$$

Combining the above equations, the area fraction after deformation  $A_f$  can be expressed as:

$$A_f = \frac{A_{f0}}{e^{\epsilon_T}} \quad (5.33)$$

For a typical yarn, the longitudinal modulus is far greater than the transverse modulus so it is reasonable to assume that the longitudinal strain  $\epsilon_z$  is negligible compared to the



transverse strain  $\varepsilon_T$ . Given this assumption the volume fraction  $V_f$  and area fraction  $A_f$  represent the same quantity and so the following equation also holds:

$$V_f = \frac{V_{f0}}{e^{\varepsilon_T}} \quad (5.34)$$

**Transverse behaviour** In Chapter 4 it was shown that the pressure applied to a tow during compaction can be characterised as a function of volume fraction  $V_f$  by a power law:

$$P = aV_f^b \quad (5.35)$$

where  $P$  is the transverse pressure applied and  $a$  and  $b$  are constants used to fit a curve to experimental data. In order to create a material model based on Equation 5.35 it is necessary to convert it into the form of a transverse modulus  $E_T$  as a function of strain. Substituting Equation 5.34 into Equation 5.35 the following expression can be obtained:

$$P = a \left( \frac{V_{f0}}{e^{\varepsilon_T}} \right)^b \quad (5.36)$$

The stress within the tow is equal and opposite to the pressure applied to it, hence  $P$  can be interchanged with negative transverse stress  $-\sigma_T$ . However it should be noted that if this equation is used directly the transverse stress  $\sigma_T$  is not 0 when transverse strain  $\varepsilon_T$  is 0. This is not physically correct and will cause problems in the simulation, so an additional term is added. Transverse stress is thus defined as:

$$\sigma_T = -a \left( \frac{V_{f0}}{e^{\varepsilon_T}} \right)^b + a(V_{f0})^b \quad (5.37)$$

The effect of the additional term  $a(V_{f0})^b$  on  $\sigma_T$  is negligible at high levels of compaction. The transverse modulus  $E_T$  can then be defined:

$$E_T(\varepsilon_T) = \frac{\sigma_T}{\varepsilon_T} = \frac{-a \left( \frac{V_{f0}}{e^{\varepsilon_T}} \right)^b + a(V_{f0})^b}{\varepsilon_T} \quad (5.38)$$

Note that when  $\varepsilon_T$  is 0,  $E_T$  is undefined causing numerical errors. So an alternate definition for  $E_T$  is needed when  $\varepsilon_T$  is close to 0:

$$E_T(0) = \lim_{\varepsilon_T \rightarrow 0} \frac{\sigma_T}{\varepsilon_T} = \frac{d\sigma_T}{d\varepsilon_T} = ab \left( \frac{V_{f0}}{e^{\varepsilon_T}} \right)^b \quad (5.39)$$

Figure 5.6 illustrates how the values of  $E_T$ ,  $-\sigma_T$  and  $P$  vary as a function of  $V_f$  and  $\varepsilon_T$  for a typical glass tow. The coefficients  $a$  and  $b$  are taken from Figure 4.31 in Chapter 4 ( $a = 1151$ ,  $b = 12.24$ ). The initial fibre volume fraction of the tow  $V_{f0}$  is arbitrarily chosen

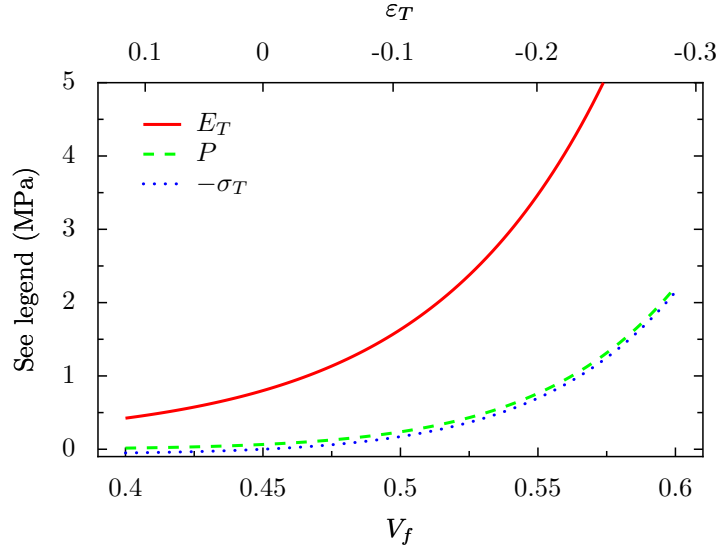


**Figure 5.6:** Transverse compaction material model

as 0.45 for illustration purposes. Note that  $-\sigma_T$  is slightly offset vertically from  $P$  due to the adjustment made to ensure  $\sigma_T$  is zero at  $\varepsilon_T = 0$ . As can be seen from the graph this offset is negligible especially at higher volume fractions.

The reason for deriving an expression for  $E_T$  in terms of strain rather than setting the element stress directly from Equation 5.37 is that two different values of stress  $\sigma_x$  and  $\sigma_y$  must be defined for the two orthogonal directions. However, by assuming a transversely isotropic material model, only a single value of  $E_T$  is needed:

$$E_T = E_x = E_y \quad (5.40)$$

The values of  $\sigma_x$  and  $\sigma_y$  are then obtained with the following equations (assuming Poisson's ratios are 0):

$$\sigma_x = \varepsilon_x E_T \quad (5.41)$$

$$\sigma_y = \varepsilon_y E_T \quad (5.42)$$

In the case where  $\varepsilon_x$  is 0, the magnitude of  $\sigma_y$  corresponds to the value of pressure measured from the uniaxial experimental compression of a tow and conversely for the case when  $\varepsilon_y$  is zero. In the case where neither  $\varepsilon_x$  nor  $\varepsilon_y$  is 0, the values of  $\sigma_x$  and  $\sigma_y$  are determined by the conditions imposed by assuming a transversely isotropic material. No experimental data is available on bi-axial compression of a yarn hence this is considered to be the most suitable assumption.

Figure 5.7 illustrates how the values of transverse modulus  $E_T$  and transverse stresses  $\sigma_x$  and  $\sigma_y$  vary as a function of transverse strains  $\varepsilon_x$  and  $\varepsilon_y$  based on the parameters used to generate Figure 5.6.

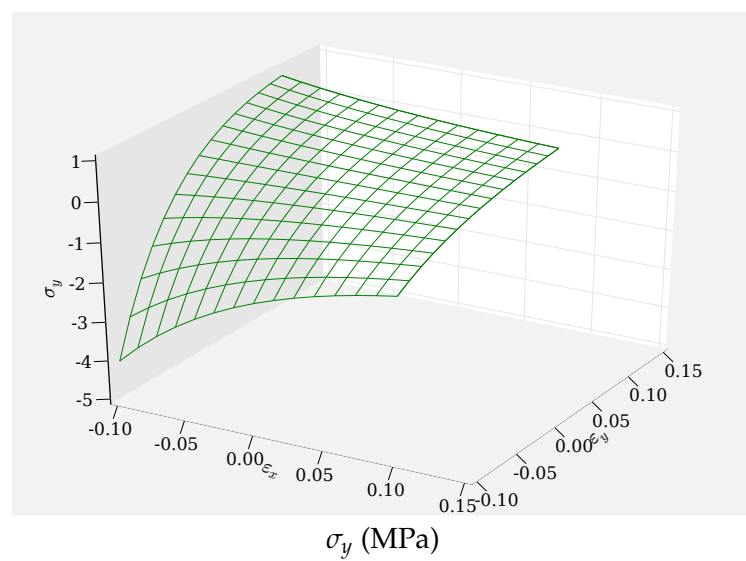
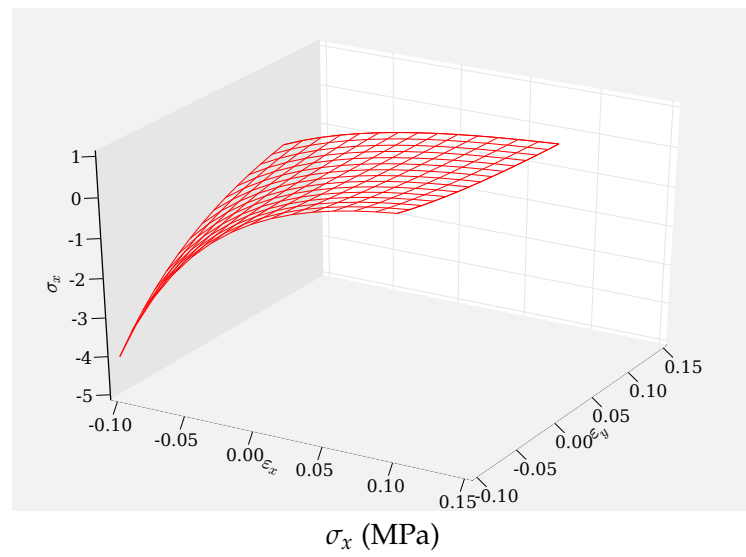
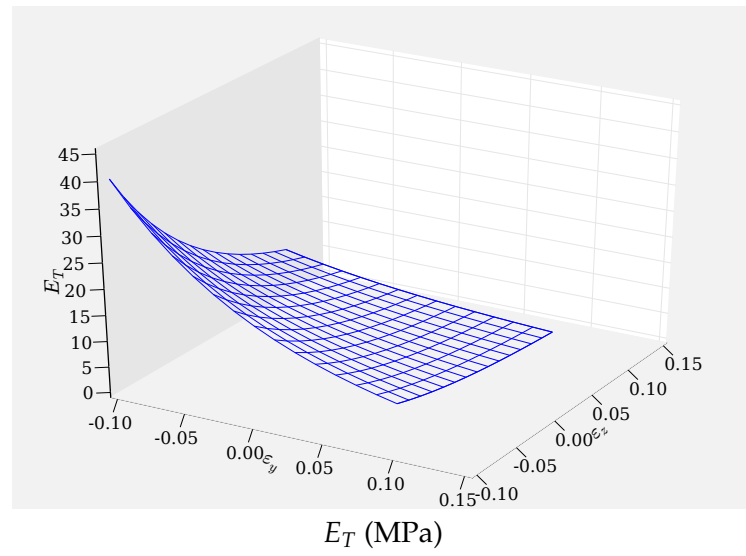


**Figure 5.7:** Plot of  $E_T$ ,  $\sigma_x$  and  $\sigma_y$  as a function of  $\epsilon_x$  and  $\epsilon_y$

**Transverse longitudinal shear behaviour** The transverse-longitudinal shear behaviour of a tow is governed mainly by the sliding of fibres past each other. As such this cannot accurately be represented by an elastic modulus  $G_{TL}$  alone. Energy dissipated through frictional sliding of fibres is not recoverable and should thus be modelled as a plastic deformation. However no experimental studies to date have been conducted on characterising the shear behaviour of individual tows primarily due to the difficulties involved in performing such a task. Due to this lack of experimental data, the transverse-longitudinal shear behaviour is simply characterised by an elastic modulus  $G_{TL}$  chosen so that simulations remain stable. In many cases this shear behaviour is not important to overall mechanical properties as will be shown in Sections 5.6 and 5.7.

It is also important to remember that the shear strain of the continuum element does not accurately represent the shear strains of the fibres within it. Therefore no matter how accurately the fibre sliding is modelled the internal stresses of the fibres can never be modelled accurately. Neglecting these internal fibre stresses will result in inaccurate overall mechanical property predictions when these internal fibre stresses become significant (i.e. in bending). It is therefore the opinion of the present author that modelling the sliding effect of fibres is of limited value in the absence of a model incorporating the internal fibre stresses.

### 5.4.3 Time integration and damping

In contrast to the implicit method, the explicit method includes the dynamic response of a system. Nodes therefore have mass, velocity and acceleration in addition to displacement and force present in the implicit method. The reason for using an explicit method over an implicit method is not to characterise the dynamic response, it is merely that the explicit method is better able to deal with the complex system of contacts. Unfortunately by using an explicit method there are various additional complications that must be addressed which are discussed in this section.

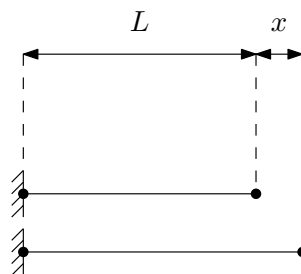


Figure 5.8: Truss element diagram

The explicit method includes an additional dimension over the implicit method, time.

This is best illustrated with a simple example. Consider a truss element fixed at one end with one degree of freedom  $x$ , initial length  $L$ , initial extension  $x_0$ , cross-sectional area  $A$ , Young's modulus  $E$  and mass  $m$  (Figure 5.8). The displacement  $x$  can be calculated as a function of time by solving the following ordinary differential equation [96]:

$$\frac{m}{2} \frac{d^2y}{dx^2} + c \frac{dy}{dx} + \frac{EA}{L} x = 0 \quad (5.43)$$

where  $c$  is the damping, the exact solution for a truss with properties shown in Table 5.1 is illustrated in Figure 5.9.

**Table 5.1:** Truss example parameters

$E$	$A$	$L$	$x_0$	$m$
72000 MPa	0.1 mm <sup>2</sup>	10 mm	1 mm	2 kg

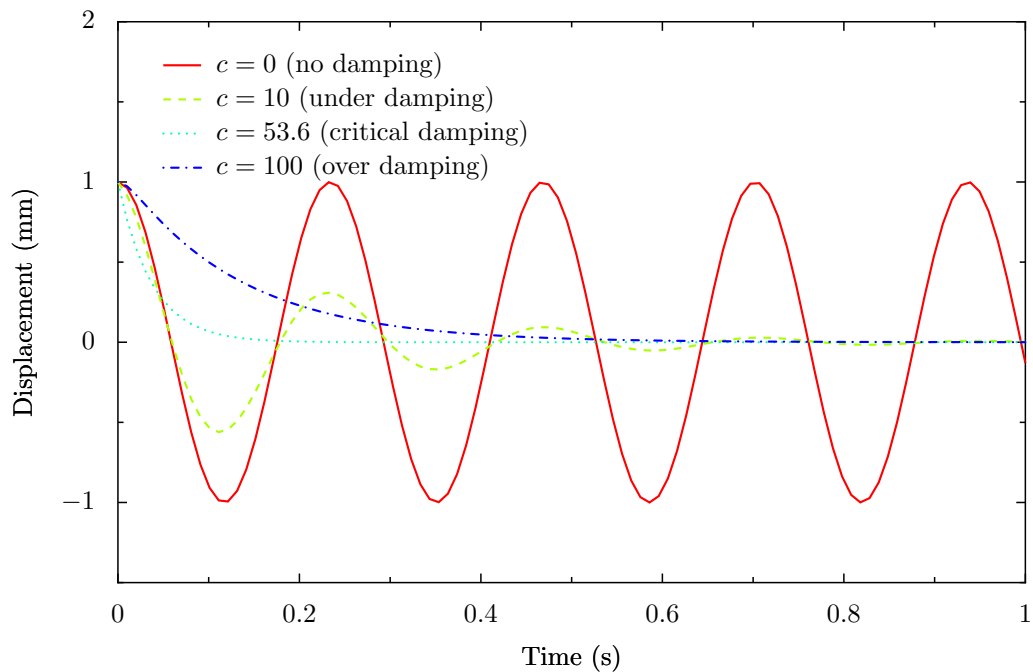


**Figure 5.9:** Graph of truss node displacement as a function of time

This truss element acts exactly like a mass on a spring and without damping it oscillates indefinitely. As stated previously the dynamic response of the system is of no concern; however by introducing damping the steady state of static equilibrium can be obtained after a certain period of time. In this case the steady state solution is trivial ( $x = 0$ ). The amount of time to reach the steady state depends on the damping value  $c$  as shown in Figure 5.9. A critical damping value  $c_c$  is defined by the following equation [94]:

$$c_c = 2\sqrt{\frac{EA m}{2L}} \quad (5.44)$$

When  $c < c_c$  then the system is said to be under damped, when  $c = c_c$  then it is critically damped and when  $c > c_c$  it is over damped. The steady state solution is obtained after the shortest time period when the system is critically damped thus this is the most suitable value of damping to use. Note that the value of  $c$  is irrelevant to the final steady state solution.

An implicit method would simply calculate the steady state solution in a single step without dealing with mass and time. However the explicit method must arrive at the solution over a series of iterations. The state of the system is approximated at a discrete series of times  $t_i$ . The state of the system at any given time is calculated from the state of the system at the previous time using Euler integration [67]. The acceleration  $\vec{a}$ , velocity  $\vec{V}$  and displacement  $\vec{x}$  of each node is calculated by the following equations:

$$\vec{a}(t_i) = \frac{\vec{F}(t_i)}{m} - c\vec{V}(t_{i-1}) \quad (5.45)$$

$$\vec{V}(t_i) = \vec{V}(t_{i-1}) + \vec{a}(t_i)\Delta t_i \quad (5.46)$$

$$\vec{x}(t_i) = \vec{x}(t_{i-1}) + \vec{V}(t_i)\Delta t_i \quad (5.47)$$

where  $\Delta t_i$  is known as the time step and is defined as:

$$\Delta t_i = t_i - t_{i-1} \quad (5.48)$$

In this one dimensional example the force is a scalar and is defined as:

$$F = -\frac{EAx}{L} \quad (5.49)$$

The choice of a suitable time step is critical in minimising the CPU time necessary to obtain a solution and maintaining simulation stability. Figure 5.10 illustrates the explicit approximation of the solution to Equation 5.43 with a damping of 10 and parameters shown in Table 5.1 compared to the exact solution.

A stability limit  $\zeta$  can be defined by the Courant-Friedrichs-Levy conditions [21, 22]:

$$\zeta = \frac{L_c}{v} \quad (5.50)$$

where  $L_c$  is the characteristic length chosen as the minimum edge length of an element and  $v$  is the speed of sound through the material defined as:

$$v = \sqrt{\frac{E}{\rho}} \quad (5.51)$$

This stability limit corresponds to the maximum time step permissible before the simulation becomes unstable; above this limit the simulation may diverge from the solution and hence become unstable as illustrated in Figure 5.10. In the case where an anisotropic material model is used as will be discussed in Section 5.4.2, the Young's modulus used in Equation 5.51 must be the largest modulus corresponding to the yarn longitudinal modulus  $E_L$ .

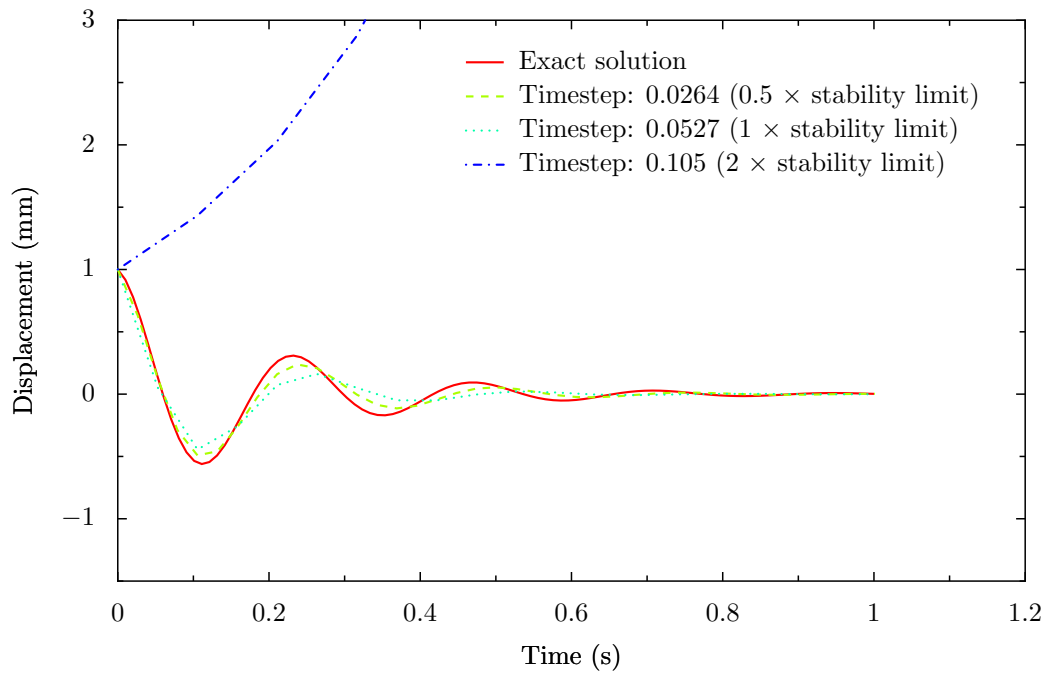


Figure 5.10: Graph of truss node displacement as a function of time

#### 5.4.4 Incremental loading

When characterising mechanical properties it is generally desirable to obtain data starting from the undeformed state up until the final deformed state. For example in a compaction simulation, the compaction pressure should be obtained as a function of fabric thickness or volume fraction. In order to obtain this data it is necessary to apply small deformations over a series of steps until the final deformation is reached. At each step the boundary conditions remain constant and the explicit calculation is performed until a steady state of equilibrium is reached. The number of steps performed does not affect the results, it simply determines how many data points are obtained. If only the final deformed state is of interest the simulation can be completed in a single step.

When passing from one step to the next, a linear transformation representing the change in deformation is applied to the nodes as an approximation to the steady state solution. By doing so the system is likely to be in a state closer to the steady state solution which allows for faster convergence and avoids large deformations of elements at the boundary.

In order to determine when the system reaches a steady state a convergence criterion is needed. In theory the steady state is only reached when the kinetic energy  $K.E.$  in the system is zero. However due to numerical errors this is unlikely to ever occur. Instead the convergence criterion is based on the ratio of kinetic energy  $K.E.$  to internal element

strain energy  $U$ :

$$\frac{K.E.}{U} \leq t \quad (5.52)$$

where  $t$  is a tolerance set to 0.001 in this implementation. In addition to this a minimum and maximum number of iterations are specified to ensure the simulation does not pass on to the next step prematurely or run indefinitely. However if the maximum number of iterations is reached the results may not be accurate.

#### 5.4.5 Contact algorithm

A major difficulty involved with modelling textile structures is modelling the contacts between yarns. This is a particular issue in the modelling of textiles and is the reason for the choice of an explicit finite element system over an implicit one. Contact algorithms in an implicit system are extremely complicated and memory intensive compared to those of an explicit system. For the complicated contacts involved with textile fabrics, it is impractical to use implicit contact algorithms as these tend not to behave in a stable manner. As a further complication, the repeating nature of the problem requires special contact code to deal with repeated unit cells.

#### Contact locations

In order to prepare to deal with contacts, the surface of the tows must be defined for convenience, in the form of triangles. This is because collision detection between triangles is simpler than other alternatives such as a non-planar quadrilateral based surface definition. This also provides an easy way to render the tows for visualisation. Initially a completely generic contact algorithm was implemented but this was found to be problematic when penetration becomes too severe and especially in the case where parallel yarns with sharp edges come in to contact. So taking advantage of the planar nature of textiles a new contact algorithm was developed. Unfortunately this algorithm does somewhat restrict the generality of the method (e.g. it is not suitable for weft knits).

In most textiles there are two types of contact that can occur, namely contact between parallel yarns and contact between crossing yarns. Any two yarns will only come into contact by one of the two mechanisms defined above, not both. Yarns running parallel to each other will only have side contacts and will not pass above or below each other, similarly yarns crossing above or below each other will not come into contact sideways. Thus a table can be built showing the relationship between yarns in the unit cell model. Possible relationships are *Beside*, *Above*, *Below* and *N/A*. The final category relates to the



relationship between a yarn with itself. This table is generated automatically based on the geometry given before deformation. Elements are given group numbers which identify which yarn the element belongs to. The groups are assembled by finding all elements which are connected to each other through common nodes. This relationship table will be used by the contact algorithm as will be seen later.

To illustrate this a table is constructed for a simple plain weave and as shown in Figure 5.11. The yarns in the fabric are numbered from one to four, Table 5.2 shows the relationship between the yarns. The table should be read as the yarn number in the left column relative to the yarn number in the top row. For example, yarn 1 is below yarn 3 and yarn 3 is above yarn 1. The table is almost symmetric except that if element  $ij$  is *Below* then element  $ji$  is *Above* and vice versa.

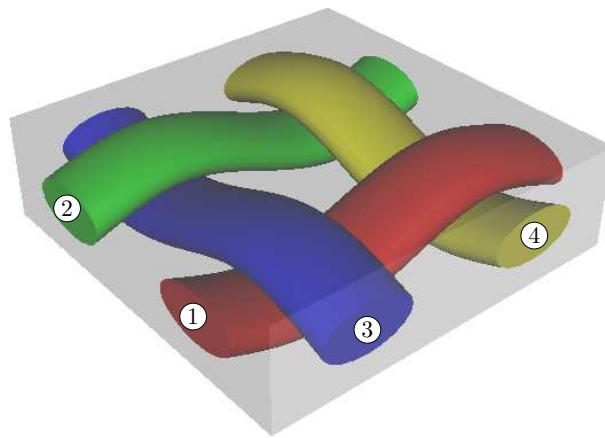


**Figure 5.11:** Plain woven fabric with yarns numbered 1 to 4

**Table 5.2:** Contact table

	Yarn 1	Yarn 2	Yarn 3	Yarn 4
Yarn 1	N/A	Beside	Below	Above
Yarn 2	Beside	N/A	Above	Below
Yarn 3	Above	Below	N/A	Beside
Yarn 4	Below	Above	Beside	N/A

As described earlier, the finite element model consists of a number of elements  $e_i$  constructed from nodes  $\mathbf{n}_i$  and the surface of the yarns is defined by a number of triangle surface elements  $T_i$ . The contact algorithm attempts to prevent the nodes of a yarn from penetrating the surface elements of the other yarns. Two algorithms exist, the first to deal with yarns crossing over each other and the second to deal with yarns side by side.

**Crossing contacts** Each node is processed one by one, determining if the node is penetrating another yarn. This process is typically very CPU intensive and needs to be performed in an efficient way. It is done in a series of stages where the fastest methods capable of discarding contacts are applied first.

The first stage is to project a line parallel to the  $z$  axis that passes through node  $\mathbf{n}_i$  where the  $z$  axis is the through thickness axis. A list of surface triangles that intersect with this line is obtained. If the surface triangle belongs to the same yarn as the node then it is discarded, hence self intersections are ignored. For all the fabrics modelled in Chapter 3 this is a perfectly valid assumption. This stage can be a rather slow process and Appendix J describes a method to greatly optimise this process making it run at an acceptable time scale through the use of a quadtree.

The second stage is to determine if the node has penetrated through any of the triangles listed by observing the position of the node relative to the triangles. This is best illustrated with an example, Figure 5.12 shows a yarn with a vertical line projected through it. Two triangles  $A$  and  $B$  are drawn with normals  $\vec{\mathbf{N}}_A$  and  $\vec{\mathbf{N}}_B$  respectively. The node  $\mathbf{n}_i$  may lie anywhere along the length of the line  $L$ .

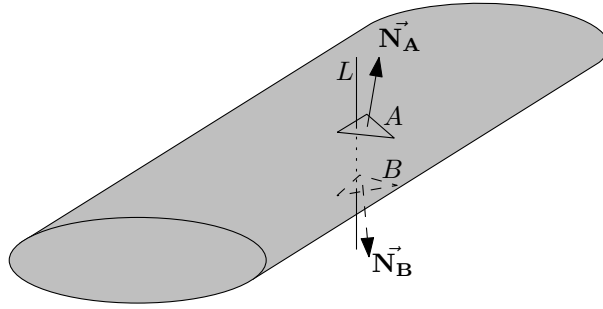


**Figure 5.12:** Yarn with vertical line intersecting two surface triangles

The node position can be categorized into three regions: the region above triangle  $A$ , the region between triangle  $A$  and  $B$  and finally the region below triangle  $B$ . In order to define these regions mathematically, the signed distance  $d$  between a node  $\mathbf{n}_i$  and the plane described by triangle  $T_i$  can be expressed as:

$$d = \vec{\mathbf{N}}_{T_i} \cdot (\mathbf{n}_i - \mathbf{P}_i) \quad (5.53)$$

where  $\mathbf{P}_i$  is one of the nodes of  $T_i$  and  $\vec{\mathbf{N}}_{T_i}$  is the normal of triangle  $T_i$ . If  $d$  is positive,  $\mathbf{n}_i$  is said to lie in front of triangle  $T_i$ , if  $d$  is negative,  $\mathbf{n}_i$  is said to lie behind triangle  $T_i$  and if  $d$  is 0 then  $\mathbf{n}_i$  lies on triangle  $T_i$ .

So the region above triangle  $A$  corresponds to when  $\mathbf{n}_i$  lies in front of triangle  $A$  and behind triangle  $B$ . Similarly the region below triangle  $B$  corresponds to when  $\mathbf{n}_i$  lies

in front of triangle  $B$  and behind triangle  $A$ . Finally the region between triangles  $A$  and  $B$  corresponds to when  $\mathbf{n}_i$  is behind both triangles  $A$  and  $B$ . If  $\mathbf{n}_i$  lies behind both triangles  $A$  and  $B$  the node has clearly penetrated the surface of the yarn. However there is another case where the node can penetrate the surface. That is if a node begins in front of triangle  $A$  and during the course of the simulation ends up in front of triangle  $B$  thus completely passing through the yarn.

It is not sufficient to establish whether or not contact has occurred, it is also necessary to determine which surface the node penetrated first. The standard approach to this is to find the closest surface triangle  $T_i$  to  $\mathbf{n}_i$ . However once  $\mathbf{n}_i$  has penetrated further than half the tow thickness (i.e. half way between triangles  $A$  and  $B$ ), the closest surface triangle will be the one on the opposite face of the yarn. When contact forces are applied, they will be in the wrong direction and once this happens there is no chance of recovery.

In order to solve this problem the table which describes the relationship of each yarn relative to another is used to remove offending triangles from the list of possible contacts. If  $\mathbf{n}_i$  belongs to a yarn which is *Above* the yarn owning triangle  $T_i$  and the triangle's normal  $z$  component  $\vec{N}_{T_i z}$  is negative then triangle  $T_i$  is discarded from possible contacts. Conversely if  $\mathbf{n}_i$  belongs to a yarn which is *Below* the yarn owning triangle  $T_i$  and  $\vec{N}_{T_i z}$  is positive  $T_i$  is discarded. In other words, nodes from a yarn that started out above another yarn cannot contact with the bottom surface of that yarn and vice versa. Note that contact between yarns side by side are handled in a different way so yarns found to be *Beside* are also discarded.

After removing the offending triangles, there should only be one triangle remaining. If the node lies behind it then contact occurs, if not then there is no contact. When contact occurs, forces need to be applied to both  $\mathbf{n}_i$  and  $T_i$ .

**Side contacts** Side contacts are more difficult to deal with than crossing contacts due to the sharp edges present at the edge of yarns. Contact algorithms are much better at handling contacts between smooth surfaces. Contacts between a smooth and sharp surface are also manageable but general contact algorithms perform poorly when faced with contacts between two sharp surfaces. In order to deal with the problem, a simplification has to be made.

If it is assumed that yarns that begin side by side never become overlapped during deformation, then the problem becomes much simpler. This is a valid assumption for the fabrics and deformation modes observed in this thesis. Using this assumption the yarns can be projected onto the  $x$ - $y$  plane and contacts identified in 2 dimensions.

Similarly to the 3 dimensional case where a number of triangles  $T_i$  represent the yarn surface, a number of line segments  $l_i$  are identified from  $T_i$ 's edges that represent the edges of the yarns.

Each node is processed one by one, determining if the node is penetrating another yarn which has the property *Beside* defined from the relationship table. This is achieved by finding the closest segment  $l_i$  to the node  $\mathbf{n}_i$ . In this case it is sufficient to obtain the closest line segments since it is very unlikely that a node will penetrate further than half the width of a yarn. That is because the yarn width is much greater than the yarn thickness for the fabrics presented in this thesis. Each segment  $l_i$  has a normal  $\vec{\mathbf{N}}_{l_i}$  that points towards the exterior of the yarn. The signed distance between  $\mathbf{n}_i$  and  $l_i$  is defined as:

$$d = \vec{\mathbf{N}}_{l_i} \cdot (\mathbf{n}_i - \mathbf{P}_i) \quad (5.54)$$

where  $\mathbf{P}_i$  is one of the nodes of the line segment  $l_i$ . If  $d$  is positive then no contact occurs, if  $d$  is negative then contact occurs. Contact forces must then be applied between penetrating nodes  $\mathbf{n}_i$  and lines  $l_i$ .

### Contact forces

When two bodies come into contact an equal and opposite force results at the contact surface. In the finite element model, these forces must be applied at the nodes. Several algorithms exist to avoid penetration. One of the simplest is the penalty method. In this method a complete penetration is not prevented. Instead a force  $\vec{\mathbf{F}}$  is applied which has magnitude  $F$  defined as a function of the penetration distance  $d$ . For example:

$$F = Kd \quad (5.55)$$

where  $K$  is a constant that represents the contact stiffness. The stiffer the contact the less penetration will occur however if the contact is too stiff instabilities will occur. Generally this parameter is chosen such that the contact is as stiff as possible without causing instabilities. The direction of the force is given by the contact surface normal. So in the case of contact with a triangle facet  $T_i$ , the facet normal  $\vec{\mathbf{N}}_{T_i}$  is used:

$$\vec{\mathbf{F}} = F\vec{\mathbf{N}}_{T_i} \quad (5.56)$$

Or in the case of contact with a line segment  $l_i$ , the line segment normal  $\vec{\mathbf{N}}_{l_i}$  is used:

$$\vec{\mathbf{F}} = F\vec{\mathbf{N}}_{l_i} \quad (5.57)$$

The forces must be applied between a node  $\mathbf{n}_i$  and either a triangle facet  $T_i$  or line segment  $l_i$  depending on whether crossing or side contact has occurred. However, since in the finite element model forces can only be applied to nodes it is necessary to transfer forces from  $T_i$  or  $l_i$  to its nodes. The way in which this is done is described for the more complicated triangle facet case. The same method can be applied to the line segment.

A contact force  $\vec{\mathbf{F}}$  acting at point  $\mathbf{P}$  on  $T_i$  can be split in to three equivalent forces  $\vec{\mathbf{F}}_1$ ,  $\vec{\mathbf{F}}_2$  and  $\vec{\mathbf{F}}_3$  acting at the triangle's nodes  $\mathbf{P}_1$ ,  $\mathbf{P}_2$  and  $\mathbf{P}_3$  respectively. This needs to be done in such a way that the resultant force of  $\vec{\mathbf{F}}_1$ ,  $\vec{\mathbf{F}}_2$  and  $\vec{\mathbf{F}}_3$  acting on  $T_i$  is equal to the force  $\vec{\mathbf{F}}$ . Furthermore the moment at point  $\mathbf{P}$  caused by forces  $\vec{\mathbf{F}}_1$ ,  $\vec{\mathbf{F}}_2$  and  $\vec{\mathbf{F}}_3$  must be zero.

There are an infinite number of solutions that would satisfy these conditions, but the one which minimises the sum of the magnitudes of forces  $\vec{\mathbf{F}}_1$ ,  $\vec{\mathbf{F}}_2$  and  $\vec{\mathbf{F}}_3$  is when  $\vec{\mathbf{F}}_1$ ,  $\vec{\mathbf{F}}_2$  and  $\vec{\mathbf{F}}_3$  are scalar multiples of  $\vec{\mathbf{F}}$  such that:

$$\vec{\mathbf{F}}_1 = c_1 \vec{\mathbf{F}} \quad (5.58)$$

$$\vec{\mathbf{F}}_2 = c_2 \vec{\mathbf{F}} \quad (5.59)$$

$$\vec{\mathbf{F}}_3 = c_3 \vec{\mathbf{F}} \quad (5.60)$$

Since the sum of  $\vec{\mathbf{F}}_1$ ,  $\vec{\mathbf{F}}_2$  and  $\vec{\mathbf{F}}_3$  must be equal to  $\vec{\mathbf{F}}$  the following constraint on the coefficients  $c_1$ ,  $c_2$  and  $c_3$  applies:

$$c_1 + c_2 + c_3 = 1 \quad (5.61)$$

The moment  $\vec{\mathbf{M}}_{\mathbf{P}}$  at point  $\mathbf{P}$  due to forces  $\vec{\mathbf{F}}_1$ ,  $\vec{\mathbf{F}}_2$  and  $\vec{\mathbf{F}}_3$  can be expressed as

$$\vec{\mathbf{M}}_{\mathbf{P}} = (\mathbf{P}_1 - \mathbf{P}) \times \vec{\mathbf{F}}_1 + (\mathbf{P}_2 - \mathbf{P}) \times \vec{\mathbf{F}}_2 + (\mathbf{P}_3 - \mathbf{P}) \times \vec{\mathbf{F}}_3 \quad (5.62)$$

By substituting Equations 5.58 to 5.60 into Equation 5.62:

$$\vec{\mathbf{M}}_{\mathbf{P}} = c_1(\mathbf{P}_1 - \mathbf{P}) \times \vec{\mathbf{F}} + c_2(\mathbf{P}_2 - \mathbf{P}) \times \vec{\mathbf{F}} + c_3(\mathbf{P}_3 - \mathbf{P}) \times \vec{\mathbf{F}} \quad (5.63)$$

which can be re-arranged to:

$$\vec{\mathbf{M}}_{\mathbf{P}} = c_1(\mathbf{P}_1 \times \vec{\mathbf{F}}) + c_2(\mathbf{P}_2 \times \vec{\mathbf{F}}) + c_3(\mathbf{P}_3 \times \vec{\mathbf{F}}) - (c_1 + c_2 + c_3)(\mathbf{P} \times \vec{\mathbf{F}}) \quad (5.64)$$

The moment  $\vec{\mathbf{M}}_{\mathbf{P}}$  should be 0, and using Equation 5.61 the following expression can be obtained:

$$\mathbf{P} \times \vec{\mathbf{F}} = (c_1 \mathbf{P}_1 + c_2 \mathbf{P}_2 + c_3 \mathbf{P}_3) \times \vec{\mathbf{F}} \quad (5.65)$$

which leads to the following equation:

$$\mathbf{P} = c_1 \mathbf{P}_1 + c_2 \mathbf{P}_2 + c_3 \mathbf{P}_3 \quad (5.66)$$

Expanding the equation out into the Cartesian coordinate system the following set of simultaneous equations are obtained:

$$\mathbf{P}_x = c_1\mathbf{P}_{1x} + c_2\mathbf{P}_{2x} + c_3\mathbf{P}_{3x} \quad (5.67)$$

$$\mathbf{P}_y = c_1\mathbf{P}_{1y} + c_2\mathbf{P}_{2y} + c_3\mathbf{P}_{3y} \quad (5.68)$$

$$\mathbf{P}_z = c_1\mathbf{P}_{1z} + c_2\mathbf{P}_{2z} + c_3\mathbf{P}_{3z} \quad (5.69)$$

The coefficients  $c_1$ ,  $c_2$  and  $c_3$  can then be solved using Cramer's rule [91] given the positions of points  $\mathbf{P}$ ,  $\mathbf{P}_1$ ,  $\mathbf{P}_2$  and  $\mathbf{P}_3$  alone. The forces  $\vec{\mathbf{F}}_1$ ,  $\vec{\mathbf{F}}_2$  and  $\vec{\mathbf{F}}_3$  are then obtained from Equations 5.58, 5.59 and 5.60. The coefficients  $c_1$ ,  $c_2$  and  $c_3$  are also known as barycentric coordinates or area coordinates [23].

**Friction** So far forces have been applied parallel to the surface normal. This accounts for direct contact forces, however in order to account for frictional forces between yarns an additional frictional component must be added. The Coulomb frictional model can be applied where friction force magnitude  $F$  is given by the following equation:

$$F = \mu N \quad (5.70)$$

where  $N$  is the magnitude of the normal force. The direction of the frictional force  $\vec{\mathbf{F}}$  is opposite to that of the relative motion. There is however a limit to the magnitude of the frictional force that can be applied. Frictional force only applies to prevent relative motion, it should never be large enough to causes a change in direction of relative motion.

The simulation is performed over a series of iteration or time steps  $\Delta t$ , and during those time steps the forces remain constant. It is feasible that a frictional force  $\vec{\mathbf{F}}$  that was preventing relative motion at the start of a time step is in fact aiding relative motion at the end of the time step because the relative motion has changed during the time step. At the next time step the frictional force  $\vec{\mathbf{F}}$  will be reversed, however without applying limits to the magnitude of  $\vec{\mathbf{F}}$  the contacting surface will oscillate and never reach a state where the relative motion is zero.

In order to avoid this problem, it is necessary to calculate the magnitude of the frictional force  $F_{max}$  necessary to stop relative motion between the two surfaces at the end of the time step. The frictional force obtained from Coulomb's model should then be limited to  $F_{max}$ . To accurately perform this calculation it is necessary to take into account all other forces that may be acting on the contacting nodes. Unfortunately due to the nature of the explicit method, this information is not available. Instead  $F_{max}$  is estimated without taking into account these other forces.

As explained in Section 5.4.5, nodes come in to contact with either triangle facets or line elements. The point of contact can be identified and any forces acting on the triangle facet or line segment are applied to the facet's or segment's nodes. Similarly values can be interpolated from the nodes to obtain properties at any given position on the surface. As an example, suppose node **A** contacts with a triangle facet at point **B**. the velocity and mass of **A** are known since they are properties of the node. The velocity and mass of **B** are not known directly because **B** does not correspond to a node, however they can be interpolated. The velocity  $\vec{V}_B$  is interpolated as follows:

$$\vec{V}_B = c_1\vec{V}_1 + c_2\vec{V}_2 + c_3\vec{V}_3 \quad (5.71)$$

where  $\vec{V}_1$ ,  $\vec{V}_2$  and  $\vec{V}_3$  are the velocities of the nodes of the triangle facet. Mass  $m_B$  is interpolated as:

$$m_B = c_1m_1 + c_2m_2 + c_3m_3 \quad (5.72)$$

where  $m_1$ ,  $m_2$  and  $m_3$  are the masses of the nodes of the triangle facet. The coefficients  $c_1$ ,  $c_2$  and  $c_3$  are the same those derived in Section 5.4.5.

Now the force  $F_{max}$  necessary to prevent sliding motion between node **A** and point **B** can be derived. Given frictional forces  $\vec{F}_A$  and  $\vec{F}_B$  acting on **A** and **B** respectively where:

$$\vec{F}_A = -\vec{F}_B \quad (5.73)$$

The accelerations  $\vec{a}_A$  and  $\vec{a}_B$  of **A** and **B** are:

$$\vec{a}_A = \frac{\vec{F}_A}{m_A} \quad (5.74)$$

$$\vec{a}_B = \frac{\vec{F}_B}{m_B} \quad (5.75)$$

where  $m_A$  and  $m_B$  are the masses of **A** and **B**. Suppose the velocities  $\vec{V}_{A_i}$  and  $\vec{V}_{B_i}$  of **A** and **B** are known at time  $t_i$ . The velocities  $\vec{V}_{A_{i+1}}$  and  $\vec{V}_{B_{i+1}}$  of **A** and **B** at the next time step  $t_{i+1}$  due to accelerations  $\vec{a}_A$  and  $\vec{a}_B$  are:

$$\vec{V}_{A_{i+1}} = \vec{V}_{A_i} + \vec{a}_A(t_{i+1} - t_i) \quad (5.76)$$

$$\vec{V}_{B_{i+1}} = \vec{V}_{B_i} + \vec{a}_B(t_{i+1} - t_i) \quad (5.77)$$

If the relative motion between **A** and **B** is to be stopped at time step  $t_{i+1}$  then the following equation applies:

$$\vec{V}_{A_{i+1}} = \vec{V}_{B_{i+1}} \quad (5.78)$$

By re-arranging and combining the above equations, expressions for the frictional forces  $\vec{F}_A$  and  $\vec{F}_B$  necessary to prevent relative motion over one time step are obtained:

$$\vec{F}_A = \frac{(\vec{V}_{B_i} - \vec{V}_{A_i})m_A m_B}{(t_{i+1} - t_i)(m_A + m_B)} \quad (5.79)$$

$$\vec{F}_B = \frac{(\vec{V}_{A_i} - \vec{V}_{B_i})m_A m_B}{(t_{i+1} - t_i)(m_A + m_B)} \quad (5.80)$$

And  $F_{max}$  is the magnitude of  $\vec{F}_A$  and  $\vec{F}_B$ :

$$F_{max} = \|\vec{F}_A\| = \|\vec{F}_B\| \quad (5.81)$$

### 5.4.6 Periodicity

#### Boundary conditions

For unit cell models to simulate the behaviour of a large fabric many times the size of a single unit cell, it is necessary to apply periodic boundary conditions. By applying such boundary conditions the model is equivalent to an infinitely large fabric undergoing uniform deformation. If a large fabric needs to be modelled with non-uniform deformation as is usually the case, the unit cell model is still useful. But a macroscopic model is required which takes effective properties from the unit cell models in a multi-scale modelling approach.

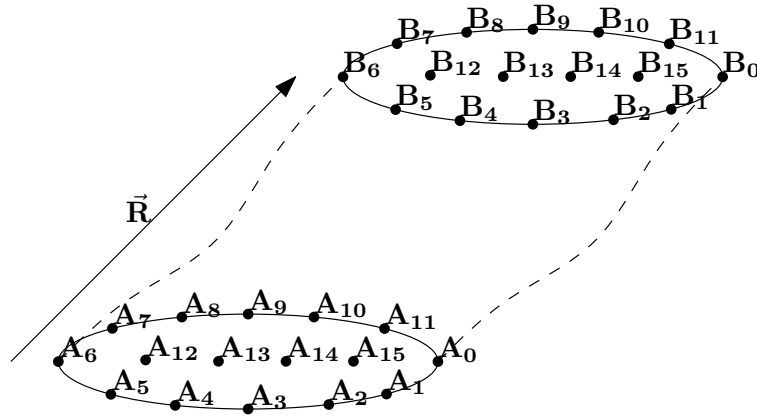


Figure 5.13: Periodic boundary constraints

The repeat vectors  $\vec{R}$  described in Chapter 2 are used to enforce the periodic boundary conditions. Figure 5.13 illustrates a section of a periodic yarn, where the yarn is repeatable along the repeat vector  $\vec{R}$ . Nodes  $A_i$  and  $B_i$  lie on opposite sides of the yarn section. Their positions are initially related by the following equation:

$$\mathbf{B}_i = \mathbf{A}_i + \vec{R} \quad (5.82)$$



This is a requirement for applying periodic boundary conditions and it is a consideration to be taken into account when the mesh is created for the yarn.

In order for the yarn to remain periodic during the simulation, Equation 5.82 must remain valid. This is enforced at the end of each iteration. Suppose the position of nodes  $\mathbf{A}_i$  and  $\mathbf{B}_i$  become  $\mathbf{A}'_i$  and  $\mathbf{B}'_i$  at the end of an iteration. The error vector  $\vec{\mathbf{E}}_i$  between nodes can be expressed as:

$$\vec{\mathbf{E}}_i = \mathbf{A}'_i + \vec{\mathbf{R}} - \mathbf{B}'_i \quad (5.83)$$

where  $\vec{\mathbf{E}}_i$  represents how far the nodes have moved apart thus invalidating the periodicity condition. If  $\vec{\mathbf{E}}_i$  is zero then no further action is required. Otherwise the positions of  $\mathbf{A}'_i$  and  $\mathbf{B}'_i$  must be adjusted to restore periodicity. By moving both nodes by the same distance, the adjusted positions  $\mathbf{A}''_i$  and  $\mathbf{B}''_i$  are calculated as:

$$\mathbf{A}''_i = \mathbf{A}'_i - \frac{\vec{\mathbf{E}}_i}{2} \quad (5.84)$$

$$\mathbf{B}''_i = \mathbf{B}'_i + \frac{\vec{\mathbf{E}}_i}{2} \quad (5.85)$$

This method of applying boundary conditions is very convenient when certain deformations are to be applied. For example, suppose the vector  $\vec{\mathbf{R}}$  is parallel to the  $\vec{\mathbf{X}}$  axis, to apply a longitudinal tensile strain  $\varepsilon_x$  the vector  $\vec{\mathbf{R}}$  can be redefined as  $\vec{\mathbf{R}}'$ :

$$\vec{\mathbf{R}}' = \varepsilon_x \vec{\mathbf{R}} \quad (5.86)$$

Shear can also be modelled using repeat vectors. Given a unit cell with two repeat vectors  $\vec{\mathbf{R}}_1$  and  $\vec{\mathbf{R}}_2$  parallel to axes  $\vec{\mathbf{X}}$  and  $\vec{\mathbf{Y}}$  respectively, vectors  $\vec{\mathbf{R}}'_1$  and  $\vec{\mathbf{R}}'_2$  can be defined as:

$$\vec{\mathbf{R}}'_1 = \vec{\mathbf{R}}_1 + \varepsilon_{xy} \|\vec{\mathbf{R}}_1\| \vec{\mathbf{Y}} \quad (5.87)$$

$$\vec{\mathbf{R}}'_2 = \vec{\mathbf{R}}_2 + \varepsilon_{xy} \|\vec{\mathbf{R}}_2\| \vec{\mathbf{X}} \quad (5.88)$$

In some cases it may be desirable to leave a repeat vector unconstrained, for example to model tension of a unit cell with two repeat vectors  $\vec{\mathbf{R}}_1$  and  $\vec{\mathbf{R}}_2$ . A tensile strain may be applied to vector  $\vec{\mathbf{R}}_1$  leaving vector  $\vec{\mathbf{R}}_2$  unconstrained allowing the fabric to shrink along  $\vec{\mathbf{R}}_2$  as  $\vec{\mathbf{R}}_1$  grows. This can be accomplished by calculating a new repeat vector  $\vec{\mathbf{R}}'_2$  based on the error vectors  $\vec{\mathbf{E}}_{2i}$ :

$$\vec{\mathbf{R}}'_2 = \vec{\mathbf{R}}_2 + \frac{1}{n} \sum_{i=1}^n \vec{\mathbf{E}}_{2i} \quad (5.89)$$

where  $n$  is the number constrained node pairs.

### Contacts

The description of the contact algorithm in Section 5.4.5 did not discuss issues that may occur when dealing with a periodic unit cell. To illustrate the issues that may arise, a simple hypothetical orthogonal non-crimp fabric unit cell is displayed in Figure 5.14 (stitching is not shown). The contact region is highlighted for different levels of shear strain  $\varepsilon_{xy}$ .

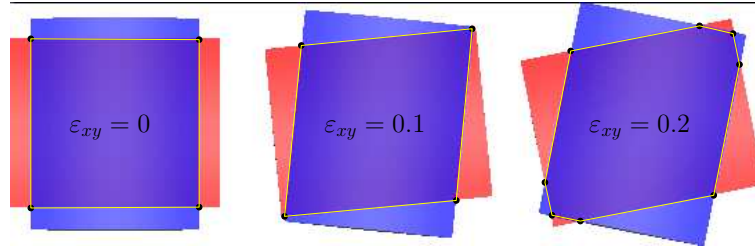


**Figure 5.14:** Shear of an orthogonal non-crimp fabric unit cell

The shape of the contact region starts as a square and as the unit cell is sheared the contact region should remain as a rhombus. From the figure it is clear that at 0.2 of shear strain, the contact region is no longer a rhombus. The reason for this is that the contacts between repeated segments of yarns (not illustrated on the figure) are neglected. This is an issue that is also apparent in more complex unit cells and this must be addressed in order to have a robust model.

During deformation nodes may leave the domain as illustrated in the above case. In order to keep all nodes constrained within the domain without restricting deformation, it is necessary to re-mesh. This is a very CPU intensive task and would result in loss of precision due to the need to map interpolated stresses and strains from elements of the previous mesh to the new mesh. A better solution exists that does not require nodes to be confined to a set domain. The contact algorithm is modified to deal with this.

Suppose contact between node  $\mathbf{n}_i$  and triangle  $T_i$  is to be determined within a unit cell with repeat vectors  $\vec{\mathbf{R}}_1$  and  $\vec{\mathbf{R}}_2$ . The absolute relative vector  $\vec{\mathbf{V}}_a$  between the node  $\mathbf{n}_i$  and the centre of the triangle  $\mathbf{T}_{ic}$  can be expressed as:

$$\vec{\mathbf{V}}_a = \mathbf{T}_{ic} - \mathbf{n}_i \quad (5.90)$$

It is important to remember that each segment of yarn in a domain is periodic and an infinite number of these segments exist in space outside of the domain offset by integer multiples of the repeat vectors. Therefore there exist an infinite number of vectors  $\vec{\mathbf{V}}$  that represent the position of node  $\mathbf{n}_i$  relative to triangle centre  $\mathbf{T}_{ic}$  since an infinite number of both  $\mathbf{n}_i$  and  $\mathbf{T}_{ic}$  exist in space. The shortest vector  $\vec{\mathbf{V}}_m$  of all vectors  $\vec{\mathbf{V}}$

represents the shortest distance between node  $\mathbf{n}_i$  and triangle centre  $\mathbf{T}_{ic}$ . If vector  $\vec{\mathbf{V}}_m$  can be calculated then contact between repeated yarns can be accounted for.

In order to determine  $\vec{\mathbf{V}}_m$ , the vector  $\vec{\mathbf{V}}_a$  must be expressed in terms of repeat vectors  $\vec{\mathbf{R}}_1$  and  $\vec{\mathbf{R}}_2$ :

$$\vec{\mathbf{V}}_a = C_1\vec{\mathbf{R}}_1 + C_2\vec{\mathbf{R}}_2 + C_3\vec{\mathbf{Z}} \quad (5.91)$$

where  $C_1$ ,  $C_2$  and  $C_3$  are scalar coefficients and  $\vec{\mathbf{Z}}$  is parallel to the  $z$  axis (through thickness axis). Expanding this equation into  $x$ ,  $y$  and  $z$  components and solving the simultaneous equations the values of  $C_1$ ,  $C_2$  and  $C_3$  can be calculated. A new vector  $\vec{\mathbf{W}}$  can be defined which is an integer multiple of the repeat vectors:

$$\vec{\mathbf{W}} = [C_1]\vec{\mathbf{R}}_1 + [C_2]\vec{\mathbf{R}}_2 \quad (5.92)$$

where the square brackets  $[\ ]$  represent the nearest integer function. Vector  $\vec{\mathbf{V}}_m$  can then be expressed as:

$$\vec{\mathbf{V}}_m = \vec{\mathbf{V}}_a - \vec{\mathbf{W}} \quad (5.93)$$

The length of vector  $\vec{\mathbf{V}}_m$  represents the closest distance between node  $\mathbf{n}_i$  and triangle centre  $\mathbf{T}_{ic}$ .

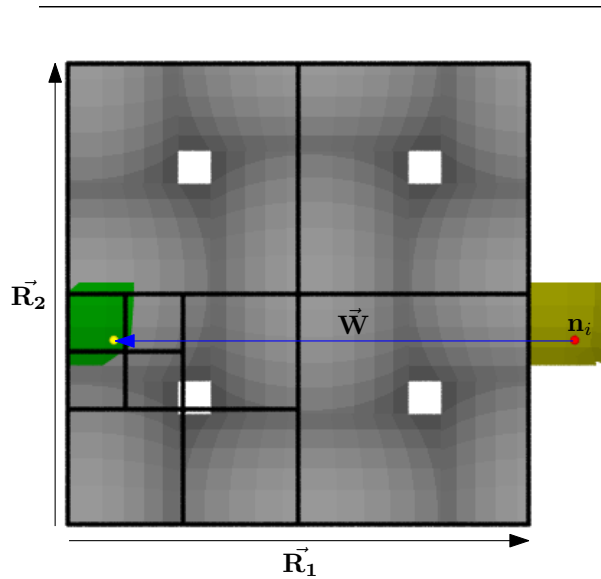


**Figure 5.15:** Point outside the domain contacting with the fabric

Contacts can be applied as described in Section 5.4.5 except node  $\mathbf{n}_i$  must be displaced by vector  $\vec{\mathbf{W}}$  before applying the contact algorithm. Figure 5.15 illustrates the process and demonstrates how it can be combined with the quadtree optimisation which is described in Appendix J. The surface mesh of a plain woven fabric unit cell contained within a domain is shown. The node  $\mathbf{n}_i$  situated outside the domain is translated by

vector  $\vec{W}$  to check contacts with triangles inside the domain. The triangles found within the vicinity of the translated node (illustrated in green) are translated by vector  $-\vec{W}$  and shown in yellow for visualisation purposes.

## 5.5 Fabric meshes

In order to perform the finite element analyses, the geometry of the fabrics must be meshed. This process is accomplished within TexGen using quadrilateral mesh generation as described in Section 2.9. Three meshes have been created for each fabric, a coarse, medium and fine mesh. Table 5.3 shows the number of nodes and elements in each mesh and Figure 5.16 displays the meshes, where the elements have been shrunk for visualisation purposes.

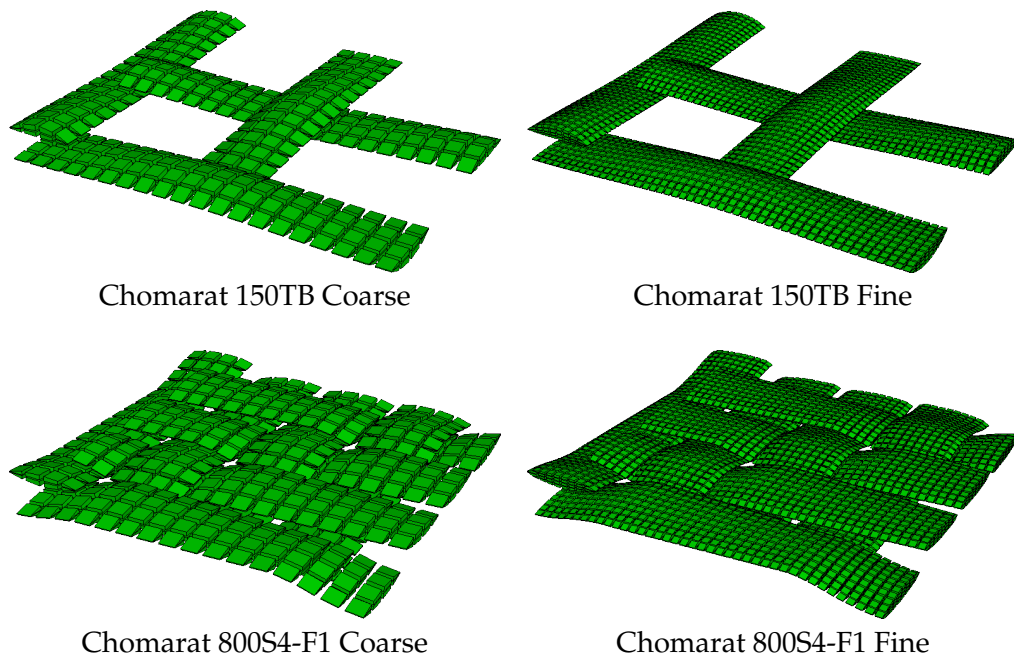


Figure 5.16: Fabric meshes

Table 5.3: Fabric mesh statistics

Fabric	Mesh density	Number of Nodes	Number of Elements
Chomarat 150TB	Coarse	814	560
	Medium	5220	3520
	Fine	7380	5632
Chomarat 800S4-F1	Coarse	1496	1024
	Medium	9512	6400
	Fine	13448	10240

### 5.5.1 Fibre direction

Due to the regular meshing technique used (Section 2.9), the fibre orientation can be obtained from the element itself. Yarn cross-sections meshed with triangular and quadrilateral elements are linked together along the fibre direction to create wedge and hexahedral elements. Suppose a triangle formed by 3 nodal coordinates  $\mathbf{P}_1$ ,  $\mathbf{P}_2$  and  $\mathbf{P}_3$  is linked to triangle with nodal coordinates  $\mathbf{P}_1'$ ,  $\mathbf{P}_2'$  and  $\mathbf{P}_3'$  to create a wedge element. The fibre direction  $\vec{\mathbf{V}}$  is calculated as:

$$\vec{\mathbf{V}} = \left\| \sum_{i=1}^n (\mathbf{P}_i' - \mathbf{P}_i) \right\| \quad (5.94)$$

where  $n$  is 3 in this case. The same equation can be applied to hexahedral elements formed by 2 quadrilateral elements in which case  $n$  would be 4.

## 5.6 Fabric compression

The finite element method described in this chapter was used to predict the mechanical behaviour of a fabric under compression. In order to simulate this deformation behaviour two planes are created, one above the fabric and the other below. All of the nodes within the model are restricted to lie between these two planes. The planes are moved closer together over a number of steps keeping track of the contact forces between the fabric and the planes.

### 5.6.1 Chomarar 150TB

Table 5.4 shows the simulation parameters used for the compaction of the Chomarar 150TB fabric. The coefficients  $a$  and  $b$  for transverse compaction are taken from Figure 4.31 in Chapter 4. The initial fibre volume fraction  $V_{f_0}$  is taken from Chapter 3.

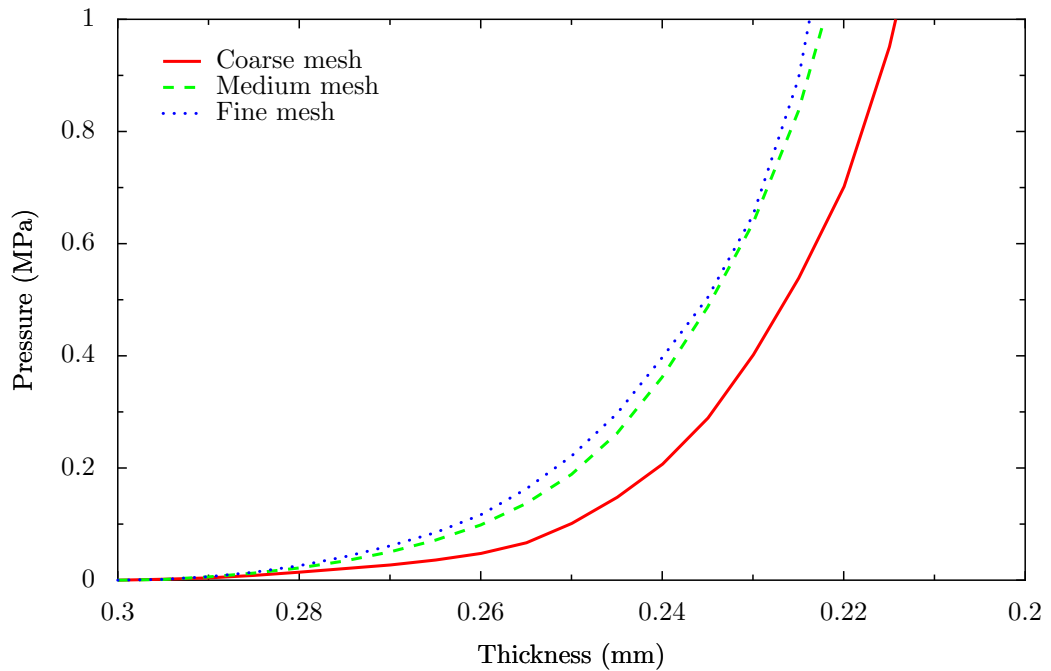
Appendix K contains graphs justifying the value of the contact stiffness and showing that the model is not sensitive to  $G_{TL}$ , damping, number of steps and coefficient of friction.

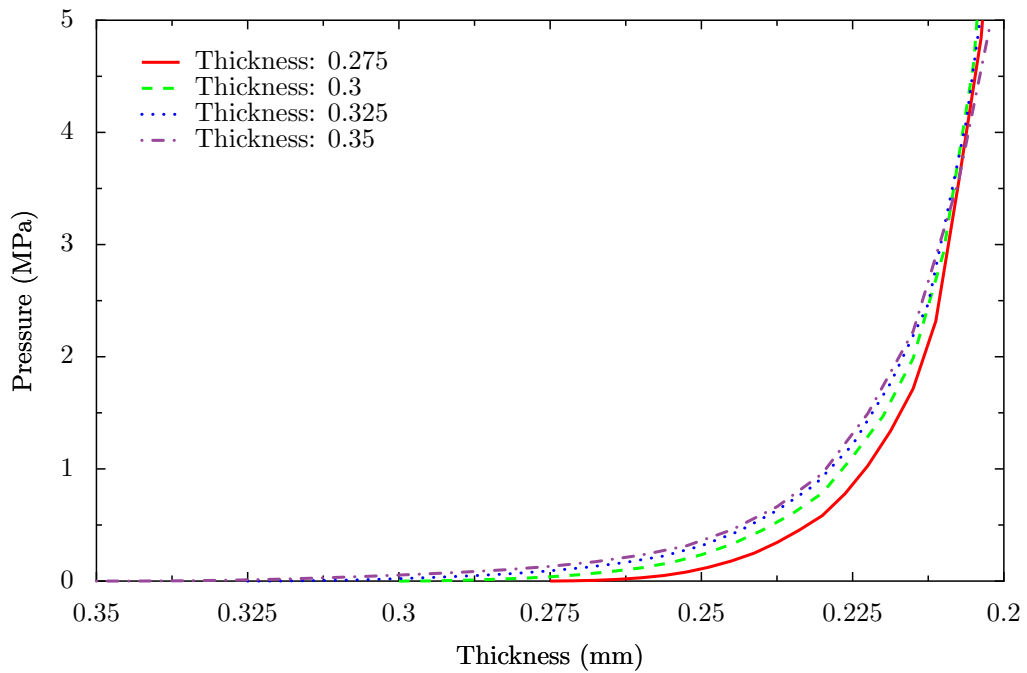
Figure 5.17 shows the results of varying the mesh density. There is a clear difference between the coarse mesh and the other two, however the medium and fine meshes show similar results. It can be concluded from this graph that the medium mesh density is sufficient to provide accurate results hence further simulations are performed using this mesh density.

Figure 5.18 shows the results of varying the fabric thickness. Note that the original fibre

**Table 5.4:** Chomarar simulation parameters

Properties	Parameter	Value
Transverse	$a$	1151.09
	$b$	12.2435
Longitudinal	$E_f$	$73 \times 10^3$ MPa
Shear	$G_{TL}$	$G_{TT}$ (Equation 5.22)
General	$\nu_{TT}$	0
	$\nu_{TL}$	0
	$V_{f0}$	0.55
	Steps	20
	Damping	$100 \text{ s}^{-1}$
	Contact algorithm	Penalty method
	Contact stiffness	100000
Coefficient of friction	0.3	

**Figure 5.17:** Pressure vs. thickness for different mesh densities



**Figure 5.18:** Pressure vs. thickness for different fabric thicknesses

volume fraction has been adjusted with thickness such that all three models contain the same mass of fibre. The values of volume fraction with change in thickness are shown in Table 5.5. It can be seen that the curves tend to converge at higher pressure levels showing that the initial thickness measurement of the fabric is not important as long as the mass of fibre remains the same. This is a positive finding since the initial fabric thickness is a difficult quantity to measure (see Chapter 3) whereas the mass of fibre is easy to quantify.

**Table 5.5:** Thickness and fibre volume fraction

Thickness $T$	0.275	0.3	0.325	0.35
Original volume fraction $V_{f0}$	0.610	0.559	0.516	0.479

The experimental results obtained from the compaction rig described in Section 5.3 are shown in Figure 5.19. An anomaly is noticeable on the graph, probably due to misalignment of the plates, which is more critical for this fabric due to its low thickness. At higher pressures the plates align themselves and the data is thought to be accurate as the curve follows the expected power law. Compaction tests on 3 layers of fabric were also performed, however the pressure needed to compact each fabric layer to the same thickness is less due to fabric nesting. Since the finite element analysis simulates a single layer of fabric, the single layer compaction test is more suitable for comparison.

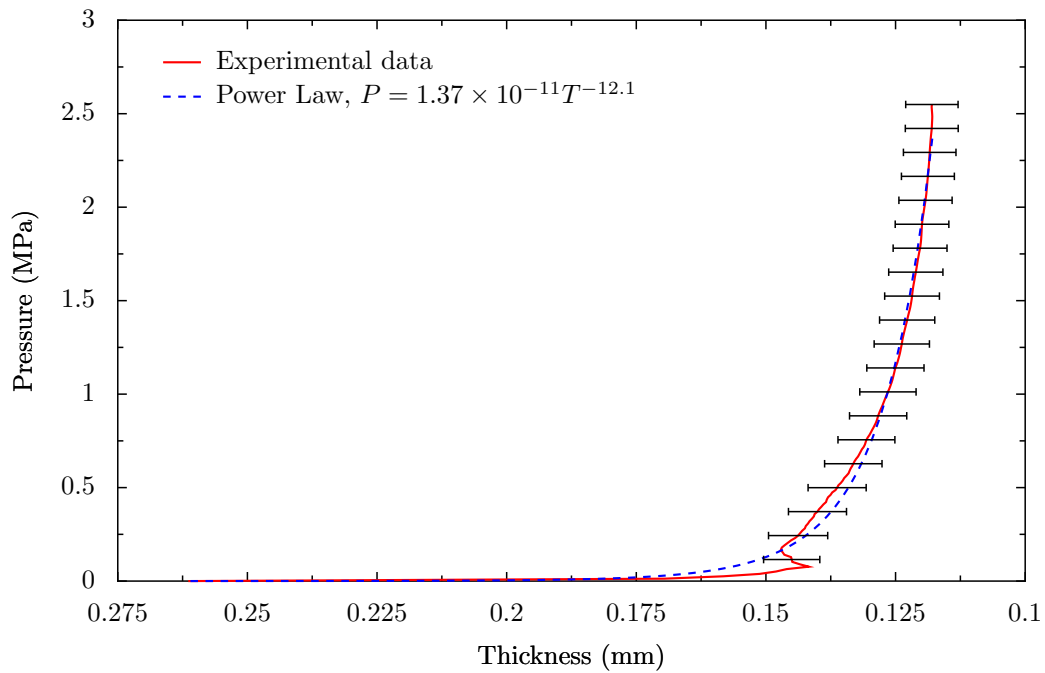


**Figure 5.19:** Compression rig pressure vs. thickness data (error bars represent the standard deviation of thickness over the 5 tests performed)

It can be seen (Figure 5.20) that the finite element results do not compare well with the experimental results for this fabric. The main reason for this is thought to be that the material model was derived from experimental data by McBride [88] where the initial fibre volume fraction was 0.35, and the maximum volume fraction was 0.6. The initial tow volume fraction for the Chomarac 150TB fabric is 0.55 and this will increase beyond 0.6 as the fabric compresses. It is unreasonable to assume that the material model will be accurate in this untested range. It is likely that the tows tested by McBride exhibit a different compaction response from the tows in this fabric due to the large difference in initial volume fraction despite the fact that they are both composed of E-glass fibres. The degree of fibre misalignment may also be different due to differences in the tow manufacturing process which will affect compaction behaviour (Chapter 4). It should also be noted that the experiments performed by McBride were on stacks of tows rather than individual tows. Furthermore the micrographs in Chapter 3 suggested that the initial fibre volume fraction may be lower than calculated from mass considerations. Irrespective of the source(s) of the error, the parameter  $a$  can be modified to correct for this.

Figure 5.20 shows four curves:

- Results of the FE model using McBride's yarn compaction data
- Results of the FE model where the material model parameter  $a$  is changed to 1.0



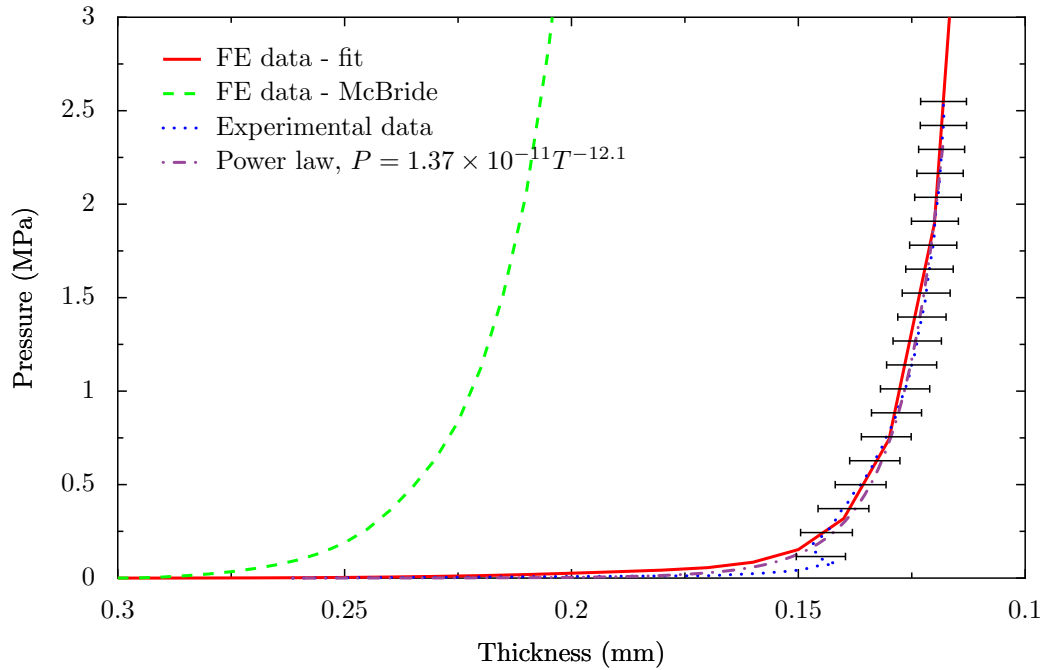


**Figure 5.20:** Chomarat 150TB Compression pressure vs. thickness comparison

while everything else is kept the same

- Experimental data obtained from the compression rig
- A power law fit to the experimental data

A virtually perfect fit to the experimental data has been obtained by fitting the single parameter  $a$ .

### 5.6.2 Chomarat 800S4-F1

The simulation parameters used for the compaction of the Chomarat 800S4-F1 fabric are the same as those used for the Chomarat 150TB fabric shown in Table 5.4 except  $V_{f0}$  is 0.411 (see Chapter 3). The results of the FE compaction test compared against experimental results is shown in Figure 5.21. Considering these results have been obtained without any parameter fitting the agreement is reasonably good. The initial linear region in the FE curve is thought to be due to buckling of the yarns during compression. The continuum model is unable to accurately represent buckling of yarns and stiffness is most likely over predicted (this source of inaccuracy was negligible in the Chomarat 150TB fabric because of its low crimp). This may have caused the increased compressional resistance found compared to the experimental results. However apart from this offset the shape of the curve is very similar to the experimental curve.

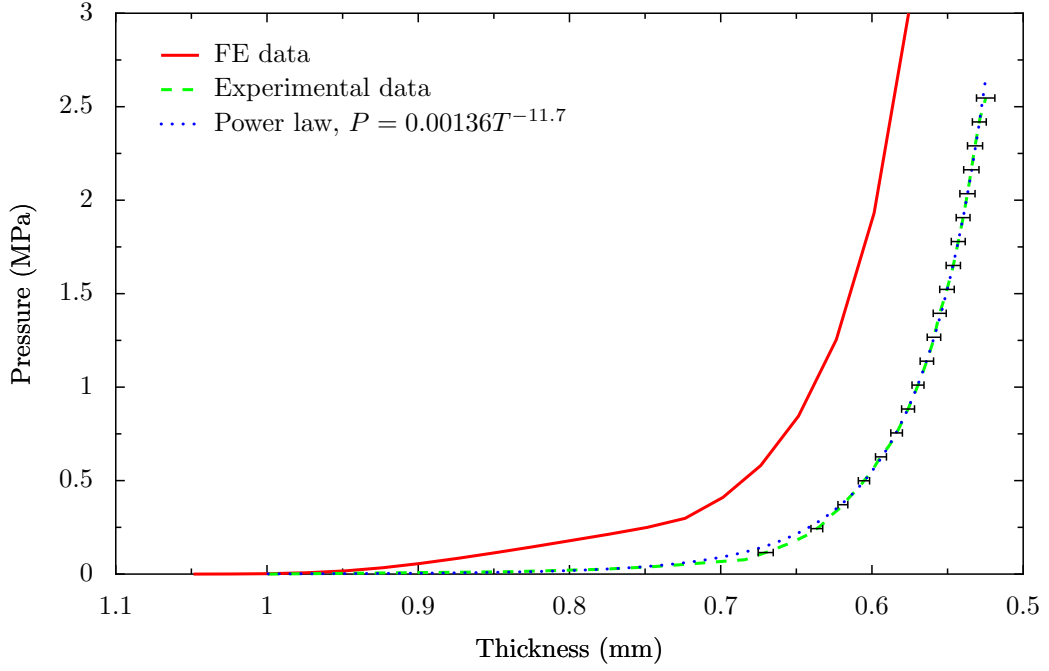


**Figure 5.21:** Chomarat 800S4-F1 compression pressure vs. thickness comparison (error bars represent the standard deviation of thickness over the 5 tests performed)

## 5.7 Fabric tension

The behaviour of fabrics under uniaxial and biaxial loads is analysed in this section. This is achieved by applying strains to the repeat vectors (Section 5.4.6). A biaxial ratio  $k$  is defined as:

$$k = \frac{\varepsilon_2}{\varepsilon_1} \quad (5.95)$$

where  $\varepsilon_1$  is the primary fabric strain and  $\varepsilon_2$  is the secondary fabric strain. The primary and secondary fabric strains correspond either to the warp or weft fabric strains depending on whether warp or weft force is plotted. For the case of uniaxial tension the biaxial ratio  $k$  is 0.

For comparison purposes a simple linear approximation to the fabric tensile behaviour can be made based on the assumption that all fibres are perfectly straight. Given the areal densities of warp and weft yarns  $\rho_{Ax}$  and  $\rho_{Ay}$  and the fibre density  $\rho_f$ , the volume of warp and weft fibres  $V.F_x$  and  $V.F_y$  in a unit area of fabric can be calculated as:

$$V.F_x = \frac{\rho_{Ax}}{\rho_f} \quad (5.96)$$

$$V.F_y = \frac{\rho_{Ay}}{\rho_f} \quad (5.97)$$

The warp and weft tensile forces  $F_x$  and  $F_y$  per unit length of fabric can be calculated

as a function of warp and weft strains  $\varepsilon_x$  and  $\varepsilon_y$  given fibre modulus  $E_f$ :

$$F_x = E_f V.F.x \varepsilon_x \quad (5.98)$$

$$F_y = E_f V.F.y \varepsilon_y \quad (5.99)$$

Note that if the fabric is balanced then the areal densities of warp and weft yarns  $\rho_{A_x}$  and  $\rho_{A_y}$  are equal to half the areal density of the fabric  $\rho_A$ .

### 5.7.1 Chomarat 150TB

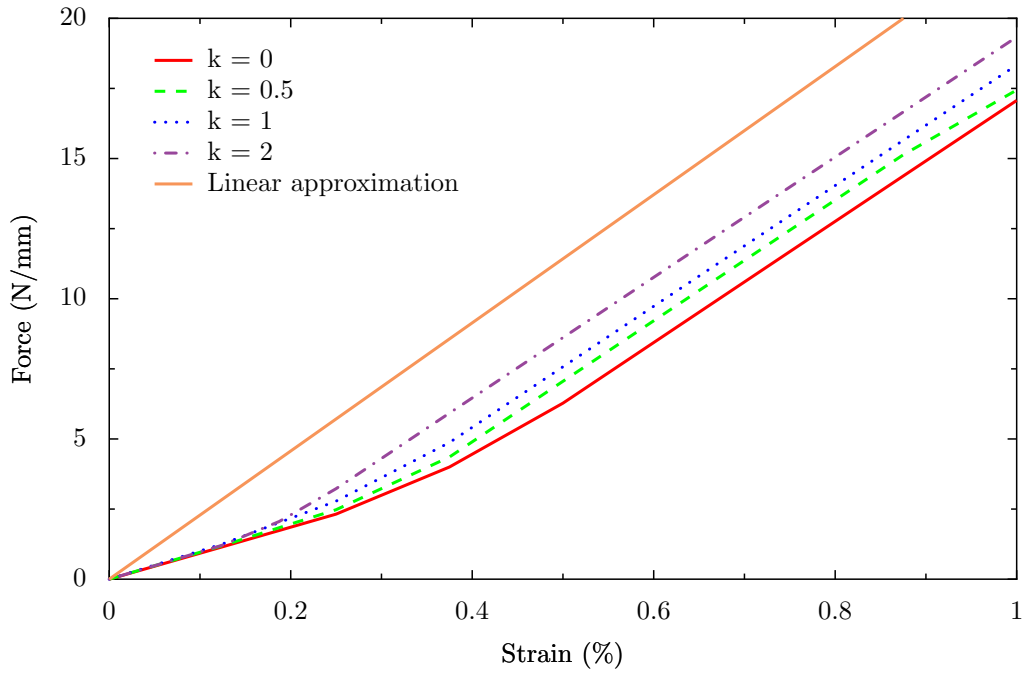


**Figure 5.22:** Chomarat 150TB warp tension for different biaxial ratios  $k$

The simulation parameters are kept the same as for the compression tests. These parameters are shown in Table 5.4 with the revised material parameter  $a$  of 1.0. Figures 5.22 and 5.23 display the results of the warp and weft biaxial tension finite element simulations respectively and Figure 5.24 shows a visual representation of the simulation. From the graphs it can be seen that there is an initial non-linear region which corresponds to the straightening of the yarns. This region is larger for the weft direction due to the higher crimp in this direction. The extent of the straightening region also depends on the biaxial ratio  $k$ . Higher values of  $k$  limit the amount of uncrimping that occurs thus limiting the extent of the non-linear region. At higher levels of strain the curve becomes linear where the gradient is equal to the linear approximation. This is the region where no further uncrimping occurs. The same trends have been shown by Boisse et al. [10] with a slightly less general modelling approach.

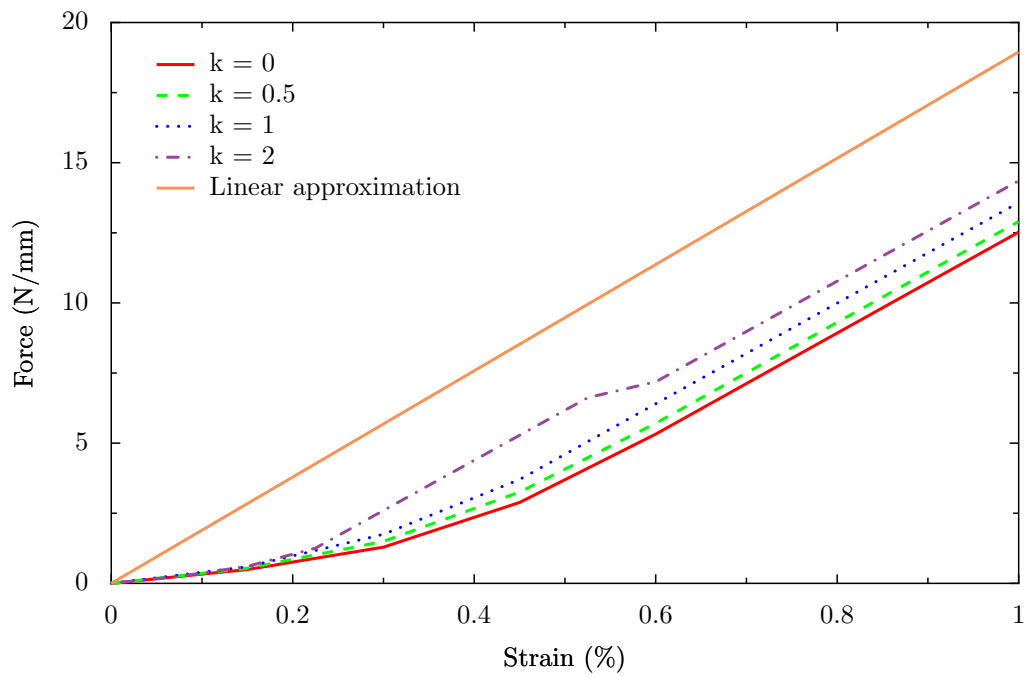


Figure 5.23: Chomarat 150TB weft tension for different biaxial ratios  $k$

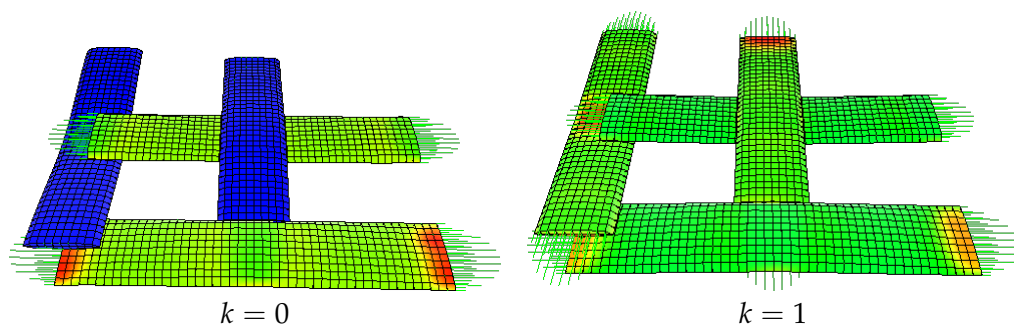


Figure 5.24: Chomarat 150TB under uniaxial and biaxial tension (colours represent von mises stresses)

## 5.7.2 Chomar 800S4-F1

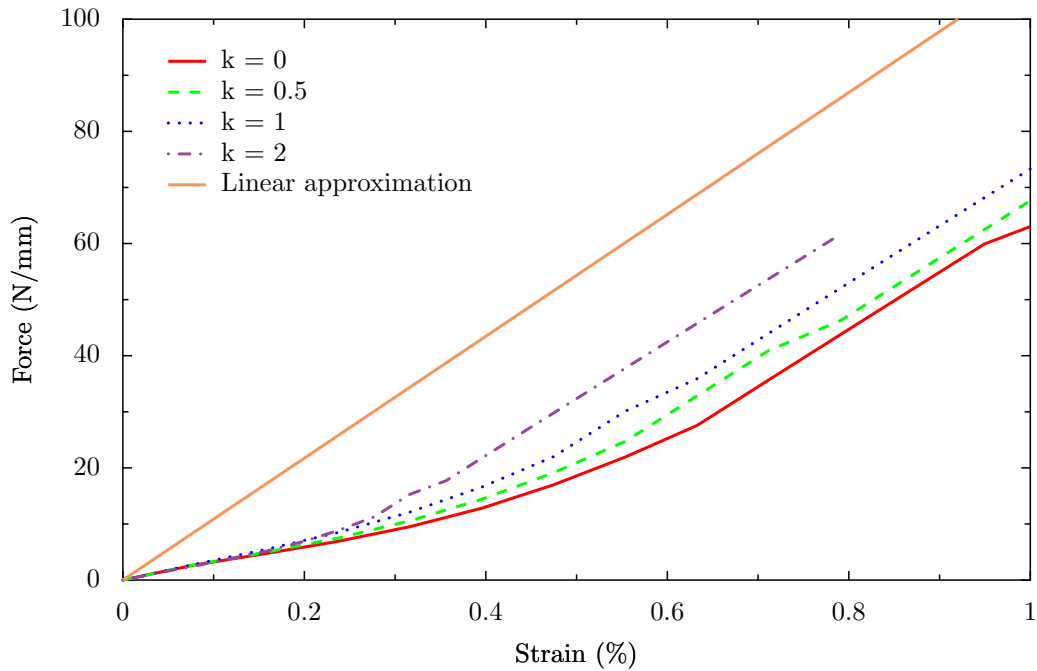


Figure 5.25: Chomar 800S4 tension for different biaxial ratios  $k$

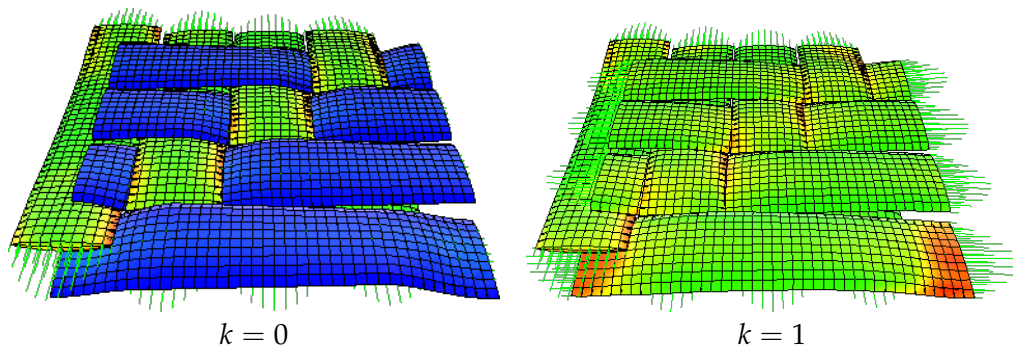


Figure 5.26: Chomar 800S4-F1 under uniaxial and biaxial tension (colours represent von mises stresses)

Since the Chomar 800S4-F1 is a balanced fabric, the graphs for tension along the warp and weft directions are the same. Figure 5.25 shows the results of the tension for this fabric using the same parameters as for the compaction simulation. Figure 5.26 shows a visual representation of the simulation. The curves are similar to those for Chomar 150TB except that the initial non-linear region is larger. This is expected, due to the larger amount of crimp present in the fabric.

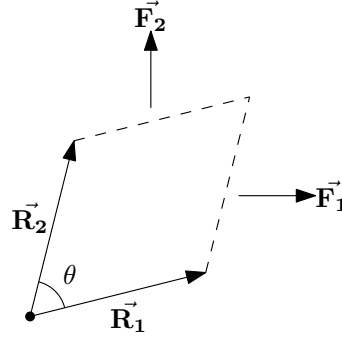


Figure 5.27: Shear force diagram

## 5.8 Fabric shear

The modelling of fabrics under shear loading is attempted in this section. This is achieved by reducing the angle between the repeat vectors from 90 degrees. The shear angle  $\alpha$  is measured as the change in angle between the repeat vectors:

$$\alpha = 90 - \theta \quad (5.100)$$

where  $\theta$  is the angle between the repeat vectors  $\vec{R}_1$  and  $\vec{R}_2$  as illustrated in Figure 5.27. The value of  $\theta$  can be calculated from the repeat vectors  $\vec{R}_1$  and  $\vec{R}_2$  as:

$$\theta = \cos^{-1} \frac{\vec{R}_1 \cdot \vec{R}_2}{\|\vec{R}_1\| \|\vec{R}_2\|} \quad (5.101)$$

The shear force  $F$  is calculated as the projection of the reaction forces  $\vec{F}_1$  and  $\vec{F}_2$  to the repeat vector directions  $\vec{R}_2$  and  $\vec{R}_1$  respectively:

$$F = \frac{\vec{F}_1 \cdot \vec{R}_2}{\|\vec{R}_2\|} = \frac{\vec{F}_2 \cdot \vec{R}_1}{\|\vec{R}_1\|} \quad (5.102)$$

where the reaction forces  $\vec{F}_1$  and  $\vec{F}_2$  are calculated as the sum of the reaction forces of the nodes on the unit cell boundary.

For comparison purposes a normalised shear force  $F_N$  is calculated as the division of the shear force by the edge length of the unit cell:

$$F_N = \frac{F}{\|\vec{R}_1\|} = \frac{F}{\|\vec{R}_2\|} \quad (5.103)$$

Picture frame experimental data for the Chomarat fabrics was taken from Souter [125].

### 5.8.1 Chomarat 150TB

Initially the shear simulation was run with the same material properties as for the tensile simulations. However the simulation became unstable and was unable to complete.

In order to address the issue, the shear modulus  $G_{TL}$  was given a new value calculated using the following equation:

$$G_{TL} = \frac{E_L}{2(1 + \nu_{TL})} \quad (5.104)$$

where the value of Poisson's ratio  $\nu_{TL}$  is 0. This increase in shear modulus allowed the simulation to complete. The difference between the two cases can clearly be seen visually in Figure 5.28. In the first case the yarn shears by the same amount as the fabric due to its low shear resistance, in the second case the high shear modulus prevents the yarn from shearing at all and instead it rotates.

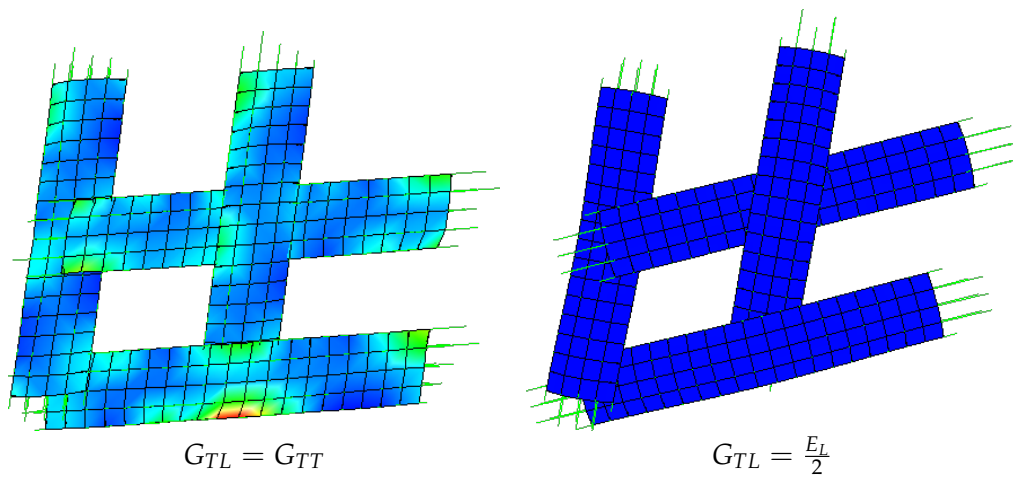


**Figure 5.28:** Chomarat 150TB under shear with different values of  $G_{TL}$

As discussed in Section 5.4.2, the shear behaviour of a yarn is governed mainly by sliding of fibres past each other. Thus the concept of a shear modulus is not suitable and neither of these two shear moduli capture the true behaviour of the yarn. Results of the latter case compared against experimental results are shown in Figure 5.29.

The finite element model exhibits an increased shear force at higher shear angles when the locking angle is approached. In the experiment this increase in shear stiffness occurs gradually whereas in the model there is a sharp change. The sharp change is thought to be due to the incorrect modelling of the axial shear and bending behaviour of the yarns. Before the locking angle is reached the fit to experimental data is surprisingly good since little yarn bending occurs up to this point.

### 5.8.2 Chomarat 800S4-F1

Similar problems were encountered when modelling the shear behaviour of the Chomarat 800S4-F1 fabric. The simulation was unable to complete given the original shear modulus. Results of the shear simulation with shear modulus  $G_{TL}$  defined by Equation 5.104 compared against experimental results are shown in Figure 5.30. The fabric

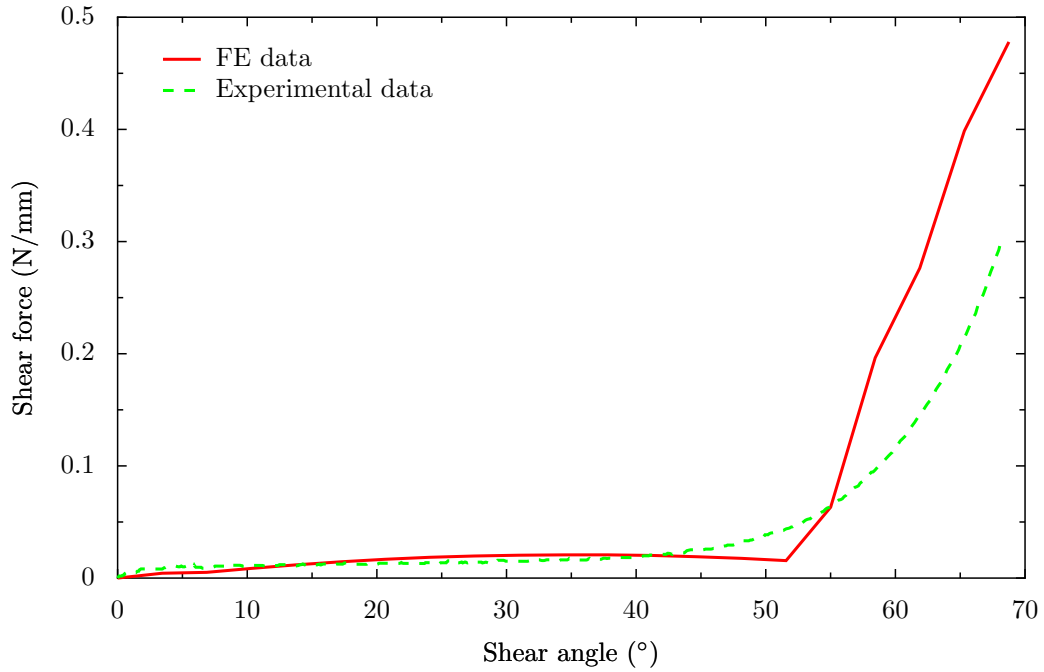


Figure 5.29: Chomarat 150TB shear

shear force response is clearly too high compared to the experimental data due to the excessively high bending rigidity of the yarn.

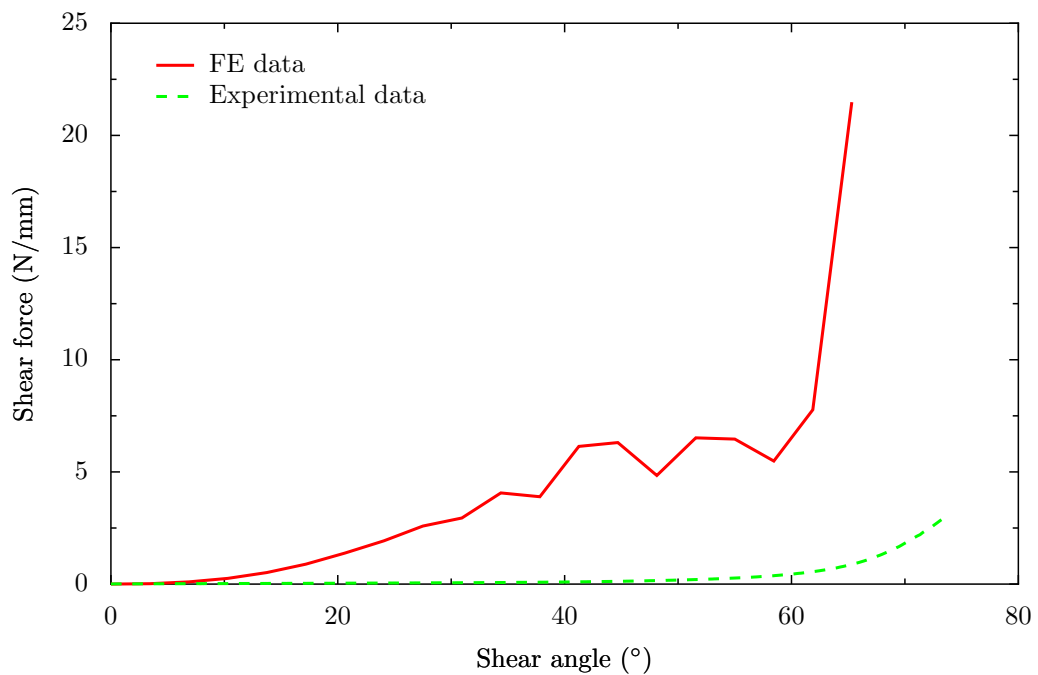


Figure 5.30: Chomarat 800S4-F1 shear

In order to reduce the bending rigidity the shear modulus  $G_{TL}$  was reduced in unison with the longitudinal modulus  $E_L$  and results are shown in Figure 5.31. The magnitude of the fabric shear force is reduced as expected, however the simulation was not able



converge due to the small magnitude of the forces involved. The simulation became unstable in all cases before reaching the prescribed maximum shear angle.

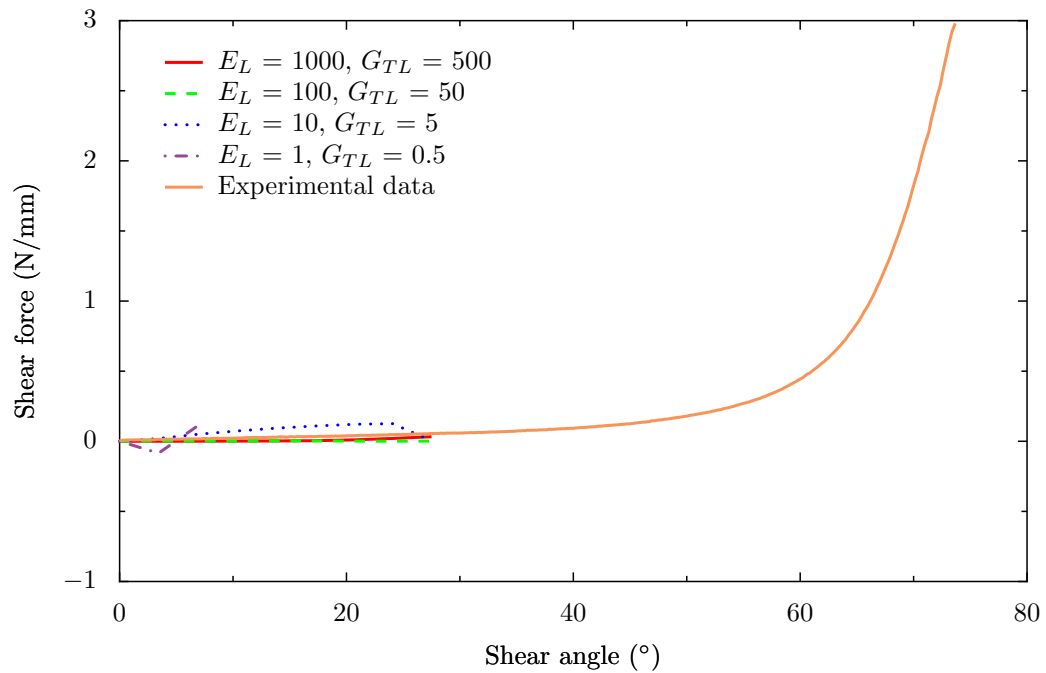


Figure 5.31: Chomarat 800S4-F1 shear varying  $G_{TL}$  and  $E_L$

## 5.9 Conclusions

In this chapter the mechanical properties of textile fabrics were analysed using finite element analysis, modelling the yarns as 3D continuum elements. An explicit method was used in order to alleviate issues with contacts present in implicit methods. A transversely isotropic material model was used for the yarns. Non-linear moduli were used for both the transverse and longitudinal directions. Poisson ratios of 0 were assumed for simplicity and the transverse longitudinal shear modulus  $G_{TL}$  was assumed to be constant. However it was demonstrated that the bending behaviour of yarns cannot be accurately modelled by representing the yarns as continuum elements alone. This became apparent when modelling the shear behaviour of fabrics. A satisfactory fit to experimental shear data could not be achieved using this model for large shear deformations.

Nevertheless the bending of yarns is negligible in compression and tension of fabrics, thus the model was found to be accurate in these deformation modes. The compression of two Chomarat fabrics was modelled and compared against experimental data. Given an accurate fitted transverse yarn material model a close fit to the experimental

data was achieved. Tensile loading of the same two fabrics was modelled and validated against a simple linear approximation of the expected fabric tensile modulus. After the un-crimping process the effective tensile modulus agreed with the linear approximation. Predictions were made for different bi-axial tensile strain ratios which produced results in line with published measurements.

Further work in this area should address the issue of the inability to accurately model the bending behaviour of yarns. One possible avenue of research might include embedding truss elements within the continuum elements which would represent either individual fibres or small groups of fibres. These truss elements could then represent the tensile and flexural behaviour of the fibres while the continuum elements would represent the transverse compaction behaviour and frictional sliding of fibres with an elastic-plastic model.

# Discussion and conclusions

## 6.1 Introduction

The aim of this chapter is to discuss the findings of the work presented in this thesis as a whole, to highlight the significant conclusions and to make recommendations for future study in the field, based on perceived limitations of the techniques suggested.

## 6.2 Discussion

The work presented in this thesis is aimed at characterising and modelling the geometry of textile fabrics and developing methods to predict the mechanical properties of fabrics at the micro and mesoscopic scales.

### 6.2.1 Geometric modelling

A generic method to define the geometry of all types of fabrics has been developed where geometry definition is split into two stages. The first stage consists of specifying the yarn centreline (or the yarn path) defined by a series of nodes on the centreline which are interpolated with a spline. In this way any desired path can be approximated and a higher degree of fit to the desired path can be obtained by increasing the number of points. However for the woven fabrics presented in this thesis it was found that only one point per cross-over was necessary to obtain a good fit to the real fabric.

The second stage is to define the cross-section of the yarn which can be done independently from the yarn path definition. Cross-sections are defined in two dimensions as parametric equations and a series of cross-sections defined in this way are presented: ellipse, power ellipse and lenticular. However any cross-section which can be defined

as a parametric equation is suitable. The cross-sections can then be assigned at discrete points along the length of the yarn and interpolated between these points.

The geometric model defines the yarn surface and volume suitable for use in various numerical analysis techniques such as finite element analysis, boundary element analysis, finite difference, etc. The geometric modelling algorithms have been implemented in the TexGen software package and this is used to create models of four woven fabrics presented in Chapter 3. Cross-section images of the fabrics were obtained using optical microscopy and scanning electron microscopy. Full three dimensional volumetric data of the fabrics were also obtained using microtomography. This data was used as both input and validation.

Difficulties were encountered in defining the boundary of the yarns in the cotton fabric due to the large number of stray fibres present. Other than this fundamental issue there were no limitations in representing the observed yarn shapes with the modelling techniques presented. The accuracy of the model is essentially determined by the accuracy of the input parameters. Features common to all the observed fabrics were identified and algorithms developed such that they are applicable to woven fabrics in general. More specifically an interference correction algorithm applicable to woven fabrics was developed and the location and magnitude of yarn rotations characterised.

### **6.2.2 Mechanical modelling**

At the microscopic scale, an original numerical technique was developed for predicting the mechanical behaviour of tows. The method involves modelling fibres within a tow following the Euler-Bernoulli beam equations. The number of fibres that can be modelled in a yarn is limited by the computational requirements. Compaction of a tow was simulated by applying a linear transformation to the fibres contained within it. It was found that averaging results over a large number of small tow sections provides similar trends to experimental results. It is computationally cheaper to perform a large number of small scale simulations than a single large scale simulation hence the former approach was adopted. Results were compared against experimental results and analytical models found in the literature. The pressure versus volume fraction curves of the simulation and experimental data were both found to fit closely to a power law hence showing that the trends are accurately predicted. Unfortunately the scale of the pressures predicted was found to be several orders of magnitude lower than experimental results. This is thought to be due to the assumption that the fibres are initially straight and consequently the inability to correctly model the longitudinal boundary conditions. However to the knowledge of the author there is currently no model able

to accurately predict the scale of the compaction pressure without fitting parameters.

The model was also used to simulate the shear behaviour of a polyester plain woven fabric. Results were compared against KES-f measurements of the modelled fabric. The shear response behaviour was decomposed into two parts, the first part caused by frictional sliding between fibres and the second part caused by elastic bending of the fibres. In contrast to the compaction simulation, the model showed very good predictive capabilities for the overall shear behaviour including hysteresis when compared against KES-f data. This is thought to be due to the accurate modelling of the longitudinal boundary conditions, as here a complete fabric unit cell was modelled with periodic boundary conditions.

At the mesoscopic scale, an explicit finite element analysis solver was implemented to predict the mechanical properties of fabrics under compression, tensile and in-plane shear deformations. The two Chomarac woven fabrics modelled using TexGen were simulated with the FE solver. It was found that very good agreement between FE results and experimental data can be obtained for compaction given an accurate transverse material model. Using yarn material properties obtained from McBride [88] a reasonably close fit to experimental data was found for the Chomarac 800S4-F1 fabric, however the material properties were found not to be suitable for the Chomarac 150TB fabric. The biaxial tensile behaviour of fabrics was found to follow trends presented by Boisse et al. [10]. However, the fabric shear behaviour could not be accurately modelled with the finite element method presented in this chapter due to the inability of the continuum elements to accurately represent the axial shear behaviour of yarns.

### 6.3 Conclusions

The conclusions gained from this thesis are summarised below.

- The geometry of any textile fabric can be represented in a generic way by specifying yarn path and yarn cross-sections independently.
- Characterisation of fabric geometry is difficult due to the large variability observed in measurement of fabric parameters. However given accurate input measurements an accurate geometric model of the fabric can be created.
- A number of assumptions about the path and shape of the cross-sections were made for 2D woven fabrics in general and validated against four different fabrics. Algorithms were implemented in TexGen to create 2D woven fabric geometric

models using these assumptions with minimal input data. To avoid penetration between tows.

- Prediction of tow compaction behaviour involves modelling a complex system of fibre contacts and fibre bending. The numerical approach presented in this thesis shows promising trends.
- Fibre sliding is inevitable during shearing of fabrics and two possible distinct modes of sliding were identified: the sliding between fibres within a tow (intra-tow) and sliding between fibres between tows (inter-tow). For the polyester fabric modelled it was shown that only one mode occurs depending on the ratio of intra-tow coefficient of friction and inter-tow coefficient of friction.
- Prediction of fabric shear properties for low filament count tows where individual fibres were modelled showed good agreement with experimental results without any fitting parameters. It was shown that the force response could be separated into two components, the frictional forces between fibres caused by sliding and the internal stresses created by elastic deformation of the fibres due to bending.
- A flaw in the use of solid continuum finite elements to model the behaviour of dry fabrics where bending or axial shear of yarns plays a significant role was identified. The internal fibre strains are not correctly represented by the continuum elements.

## 6.4 Recommendations for further work

In terms of geometrical modelling of unit cells the following areas of further research may be constructive.

- In this thesis the geometric modelling techniques presented have only been applied and validated for two dimensional woven fabrics. It would be advantageous to apply the same systematic approach to the full spectrum of textile fabrics using the same modelling strategy. The findings should be implemented in TexGen in order to provide a comprehensive modelling tool capable of creating textile unit cell models with a minimum of input parameters suitable for both research and industrial purposes.
- The geometric models created by TexGen are of little utility on their own. In order to perform numerical analysis with these models it is necessary to export them

to different software packages which can be troublesome and time consuming resulting in a considerable reduction in research efficiency. Further work spent on providing a simple interface between TexGen with commercial and research tools through the use of standard file formats would alleviate this issue.

- The use of microtomography is potentially very powerful in characterising textile geometry. The development of algorithms to analyse volumetric data provided by  $\mu$ CT could result in automatic identification of yarn centrelines and cross-sectional shapes which could be used to create highly accurate TexGen geometric models. A series of models could be created in this way and analysed to characterise fabric variability. Using this data, algorithms could be devised to create batches of non-idealised geometric models of fabrics without the need for additional  $\mu$ CT measurements.

Recommendations for future work on modelling the mechanical behaviour of tows is listed below.

- Preliminary work was performed on the use of microtomography to characterise the fibre distribution within tows (not presented in this thesis). Revisiting this work would provide a more accurate initial fibre distribution for use in the tow compaction model.
- The longitudinal boundary conditions of the tow compaction model should be improved. Either mirrored or periodic boundary conditions should be used and consequently a change in the assumption that fibres are initially straight is required. The initial shape could be modelled as the shape described by a fibre with a single force applied at a position along the length of the fibre. By describing initially curved fibres the number of fibre to fibre contacts should increase thus bringing the predicted compaction pressure closer to the experimental results.
- The Euler-Bernoulli beam equations may be replaced or extended to model the tensile and possibly torsional behaviour of the fibres. By doing so the tensile behaviour of yarns may be modelled and Poisson's ratio may be characterised.

Future work on finite element modelling of textile fabric unit cells is identified below.

- Although the task of programming a finite element analysis code without the use of any external libraries is a rewarding learning experience and allows complete

freedom it almost certainly results in sub-optimal code. Since the performance of finite element analysis code is critical in obtaining results in a timely manner the resulting code is of limited use. Therefore it would be beneficial to implement the algorithms presented in this thesis in existing optimised, validated and robust finite element software such as ABAQUS<sup>TM</sup>[51] where possible.

- A fundamental issue with modelling yarns with solid continuum elements for use in finite element analysis was identified. The internal strains within fibres are not captured accurately which means the behaviour of the fabric cannot be predicted when the fabric deforms such that these strains become important. Development of a finite element which can capture the internal fibre strains either by replacing the continuum elements or by working in conjunction with them may solve the issue. This may be achieved by embedding truss elements inside the continuum elements to represent each individual fibre or a group of fibres. The truss elements could represent the tensile and flexural modulus of the fibres while the continuum elements could represent the compressive modulus and frictional sliding between fibres as a plastic deformation.
- The finite element analysis techniques described in this thesis are applicable to all fabric types except for the contact algorithm which may need modification for certain fabric types such as weft knits. Future work may include developing the analysis technique and validation for different fabric types.



# References

- [1] S. Adanur and T. Liao. 3d modeling of textile composite preforms. *Composites Part B: Engineering*, 29:787–93, November 1998.
- [2] Ahlberg, Nielson, and Walsh. *The Theory of Splines and Their Applications*. New York, Academic Press, 1967.
- [3] H. Ainsworth. HXA7241 octree c++ general component, 2005. URL <http://www.hxa7241.org/articles/articles.html>. [Online; accessed 23-April-2007].
- [4] H. Anton, I. Bivens, and S. Davis. *Calculus: Multivariable*. John Wiley and Sons, 8th edition, November 2004.
- [5] S. Axler. *Linear Algebra Done Right*. Springer, 2nd edition, 2004.
- [6] Bartels, Beatty, and Barsky. *An Introduction to Splines for Use in Computer Graphics and Geometric Modeling*. Morgan Kaufmann, 1987.
- [7] D. Beazley and M. Matus. SWIG, 2007. URL <http://www.swig.org/>. [Online; accessed 23-April-2007].
- [8] G. A. Bingham, R. J. M. Hague, C. J. Tuck, A. C. Long, J. J. Crookston, and M. N. Sherburn. Rapid manufactured textiles. *Int. J. Computer Integrated Manufacturing*, 21(1):96–105, 2007.
- [9] O. A. R. Board, D. Shreiner, M. Woo, J. Neider, and T. Davis. *OpenGL Programming Guide: The Official Guide to Learning OpenGL*. Addison-Wesley, 2005.
- [10] P. Boisse, K. Buet, A. Gasser, and J. Launay. Meso/macro-mechanical behaviour of textile reinforcements for thin composites. *Composites Science and Technology*, 61:395–401, 2001.
- [11] P. Boisse, B. Zouari, and J.-L. Daniel. Importance of in-plane shear rigidity in finite element analyses of woven fabric composite preforming. *Composites: Part A*, 37:2201–12, 2006.

## REFERENCES

- [12] K. Buet-Gautier and P. Boisse. Experimental analysis and modeling of biaxial mechanical behavior of woven composite reinforcements. *Exp Mech*, 41:260–9, 2001.
- [13] R. L. Burden and J. D. Faires. *Numerical Analysis*. Brooks/Cole, 2000.
- [14] Z. Cai and T. G. Gutowski. The 3-d deformation behaviour of a lubricated fiber bundle. *Journal of Composite Materials*, 26(8):1207–37, 1992.
- [15] G. A. Carnaby and N. Pan. Theory of the compression hysteresis of fibrous assemblies. *Textile Research Journal*, 59(5):275–84, 1989.
- [16] G. A. Carnaby and R. Postle. Discrete fiber versus continuum models in the mechanics of staple yarns. *Journal of Applied Polymer Science: Applied Polymer Symposium*, 47(Sci. Technol. Fibers Relat. Mater.):341–54, 1991.
- [17] S. H. Chang, S. B. Sharma, and M. P. F. Sutcliffe. Microscopic investigation of tow geometry of a dry satin weave fabric during deformation. *Composites Science and Technology*, 63:99–111, January 2003.
- [18] S. H. Chang, M. P. F. Sutcliffe, and S. B. Sharma. Microscopic investigation of tow geometry changes in a woven prepreg material during draping and consolidation. *Composites Science and Technology*, 64:1701–07, August 2004.
- [19] T. Charlton. *Energy Principles in Theory of Structures*. Oxford University Press, 1973.
- [20] J. B. Conway. *A Course in Functional Analysis*. Springer-Verlag, 2nd edition, 1990.
- [21] R. Courant, K. Friedrichs, and H. Lewy. Über die partiellen differenzengleichungen der mathematischen physik. *Mathematische Annalen*, 100:32–74, 1928.
- [22] R. Courant, K. Friedrichs, and H. Lewy. On the partial difference equations of mathematical physics. *IBM Journal*, pages 215–234, March 1967.
- [23] H. S. M. Coxeter, editor. *Introduction to Geometry*. Wiley, New York, 2nd edition, 1969.
- [24] J. J. Crookston, M. N. Sherburn, L. G. Zhao, J. W. Ooi, A. C. Long, and I. A. Jones. Finite element analysis of textile composite unit cells using conventional and novel techniques. In *15th Int. Conf. on Composite Materials*, Durban, South Africa, June 2005.

## REFERENCES

- [25] J. J. Crookston, W. Ruijter, A. C. Long, and I. A. Jones. Modelling mechanical performance including damage development for textile composites using a grid-based fe method with adaptive mesh refinement. In *8th International Conference on Textile Composites*, page T09, Nottingham, UK, October 2006.
- [26] J. I. Curiskis and G. A. Carnaby. Continuum mechanics of the fiber bundle. *Textile Research Journal*, 55:334–44, 1985.
- [27] M. Cybulska, T. Florczak, and T. Lodz. 3D graphics in textile designing. In *AUTEX 2006 World Textile Conference*, Raleigh, North Carolina, US, June 2006.
- [28] A. de Moivre. *The Doctrine of Chances*. A. Millar, 2nd edition, 1738.
- [29] F. Desplentere. *Multiscale modelling of stochastic effects in mould filling simulations for thermoplastic composites*. PhD thesis, Catholic University of Leuven, January 2007.
- [30] F. Desplentere, S. Lomov, D. Woerdeman, I. Verpoest, M. Wevers, and A. Bogdanovich. Micro-ct characterization of variability in 3d textile architecture. *Composites Science and Technology*, 65:1920–30, October 2005.
- [31] R. G. Djaja, G. A. Carnaby, P. J. Moss, A. J. Carr, and D. H. Lee. A tangent compliance matrix for an oriented assembly of fibres. *Wool Research Organisation of New Zealand Communication*, C111, 1989.
- [32] R. G. Djaja, P. J. Moss, and A. J. Carr. Finite element modeling of an oriented assembly of continuous fibers. *Textile Research Journal*, 62:445–57, 1992.
- [33] R. G. Douglas. On majorization, factorization, and range inclusion of operators on hilbert space. *Proceedings of the American Mathematical Society*, 17(2):413–415, April 1966.
- [34] J. P. Dunkers, R. S. Parnas, C. G. Zimba, R. C. Peterson, K. M. Flynn, J. G. Fujimoto, and B. E. Bouma. Optical coherence tomography of glass reinforced polymer composites. *Composites Part A: Applied Science and Manufacturing*, 30:139–45, February 1999.
- [35] J. P. Dunkers, F. R. Phelan, D. P. Sanders, M. J. Everett, W. H. Green, D. L. Hunston, and R. S. Parnas. The application of optical coherence tomography to problems in polymer matrix composites. *Optics and Lasers in Engineering*, 35:135–47, March 2001.
- [36] D. Eberly. *3D Game Engine Design*. Morgan Kaufmann, 2001.

## REFERENCES

- [37] J. Forssell and Y. Mikhaylovskiy. Impact Finite Element Program, 2007. URL <http://impact.sourceforge.net/>. [Online; accessed 23-April-2007].
- [38] M. Gardner, editor. *Mathematical Carnival*. Vintage, 1977.
- [39] R. Graham, D. Knuth, and O. Patashnik. *Concrete Mathematics*. Addison-Wesley, 1999.
- [40] P. Grosberg. The strength of twistless slivers. *Journal Textile Institute*, 54:223–33, 1963.
- [41] P. Grosberg and P. A. Smith. The strength of slivers of relatively low twist. *Journal Textile Institute*, 57:15–23, 1966.
- [42] T. G. Gutowski and G. Dillon. The elastic deformation of lubricated carbon fiber bundles: comparison of theory and experiments. *Journal of Composite Materials*, 26(16):2330–47, 1992.
- [43] T. G. Gutowski, Z. Cai, S. Bauer, D. Boucher, J. Kingery, and S. Wineman. Consolidation experiments for laminate composites. *Journal of Composite Materials*, 21(7):650–69, 1987.
- [44] B. Hagege. *Simulation du comportement mecanique des renforts fibreux en grandes transformations: application aux renforts tricotes*. PhD thesis, ENSAM Paris, 2004.
- [45] B. Hagege, P. Boisse, and J. Billoët. Analysis and simulation of the constitutive behavior of fibrous reinforcements. In *Esaform 7 conference*, pages 317–20, Trondheim, Norway, April 2004.
- [46] P. R. Halmos. What does the spectral theorem say? *The American Mathematical Monthly*, 70(3):241–247, March 1963.
- [47] P. Harrison, M. J. Clifford, A. C. Long, and C. D. Rudd. A constituent-based predictive approach to modelling the rheology of viscous textile composites. *Composites Part A: Applied Science and Manufacturing*, 35:915–31, July 2004.
- [48] J. W. S. Hearle. The challenge of changing from empirical craft to engineering design. In *International Textile Design and Engineering Conference*, Edinburgh, September 2003.
- [49] J. W. S. Hearle. Engineering design of textiles. *Indian Journal of Fibre and Textile Research*, 31(1):142–49, March 2006.

## REFERENCES

- [50] J. W. S. Hearle and W. J. Shanahan. An energy method for calculations in fabric mechanics. *Journal Textile Institute*, 69(4):81–110, 1978.
- [51] Hibbit, Karlsson, and Sorensen. *Abaqus Standard*. HKS Inc., 2007.
- [52] S. Hind, D. Raizenne, and F. Robitaille. Prediction of the effective transverse thermal conductivity of carbon based textile composites with varying constituent properties and reinforcement geometry. In *Proc. Canada Japan Workshop on Composites*, Toronto, Canada, 2006.
- [53] S. Hind, F. Robitaille, and D. Raizenne. Parametric unit cell modelling of the effective transverse thermal conductivity of carbon plain weave composites. In *Proc. International Conference on Textile Composites (TEXCOMP-8)*, Nottingham, UK, October 2006.
- [54] J. Hofstee and F. van Keulen. 3-d geometric modeling of a draped woven fabric. *Composite Structures*, 54:179–95, November/December 2001.
- [55] M. Itoh and T. Komori. An extension of the theory of the deformation of fiber assemblies. *Sen'i Gakkaishi*, 47(11):563–72, 1991.
- [56] I. A. Jones, A. C. Long, J. J. Crookston, M. Sherburn, W. Ruijter, and J. Ooi. Modelling of woven technical textile deformations and textile composite properties at the fibre and tow scale. In *Technical Textiles Ú The Innovative Approach*, Manchester, UK, April 2006.
- [57] O. Kallmes and H. Corte. The structure of paper, i. the statistical geometry of an ideal two-dimensional fibre network. *Tappi*, 43:737–52, 1960.
- [58] S. Kawabata. The development of the objective measurement of fabric handle. In *1st Japan-Australia Symposium on Objective Specification of Fabric Quality, Mechanical Properties, and Performance*, pages 31–59, Kyoto, Japan, 1982.
- [59] S. Kawabata and M. Niwa. Fabric performance in clothing manufacture. *Journal Textile Institute*, 80(1):19–50, 1989.
- [60] A. Kemp. An extension of peirce's cloth geometry to the treatment of nonlinear threads. *Journal Textile Institute*, 49:44–8, 1958.
- [61] S. Kimball and P. Mattis. GIMP, 2007. URL <http://www.gimp.org/>. [Online; accessed 23-April-2007].
- [62] Kincaid, David, and W. Cheney. *Numerical Analysis*. Brooks/Cole, 3rd edition, 1987.

## REFERENCES

- [63] T. Komori and M. Itoh. A new approach to the theory of the compression of fiber assemblies. *Textile Research Journal*, 61(7):420–28, 1991.
- [64] T. Komori and M. Itoh. Theory of the general deformation of fiber assemblies. *Textile Research Journal*, 61(10):588–94, 1991.
- [65] T. Komori and K. Makishima. Numbers of fibre-to-fibre contacts in general fibre assemblies. *Textile Research Journal*, 47:13–17, 1977.
- [66] T. Komori, M. Itoh, and A. Takaku. A model analysis of the compressibility of fiber assemblies. *Textile Research Journal*, 62:567–74, 1992.
- [67] J. D. Lambert. *Numerical Methods for Ordinary Differential Systems*. John Wiley & Sons, Chichester, 1991.
- [68] H. L. Langhaar. *Energy Methods in Applied Elasticity*. Krieger, 1989.
- [69] D. H. Lee and G. A. Carnaby. Compressional energy of the random fiber assembly part i: Theory. *Textile Research Journal*, 64(4):185–91, 1992.
- [70] D. H. Lee and J. K. Lee. Initial compressional behaviour of fibre assembly. *Objective measurement applications to product design and process control*, pages 613–22, 1985.
- [71] D. H. Lee and J. K. Lee. The application of the orientation density function to the mechanics of fibrous assembly. *The application of Mathematics and Physics in the Wool Industry*, pages 171–80, 1988.
- [72] D. H. Lee, G. A. Carnaby, and S. K. Tandon. An energy analysis of the compression of a random fibre assembly. In *8th International Wool Textile Conference*, volume V, pages 34–44, Christchurch, New Zealand, 1990.
- [73] D. H. Lee, G. A. Carnaby, and S. K. Tandon. Compressional energy of the random fiber assembly part ii: Evaluation. *Textile Research Journal*, 62(5):258–65, 1992.
- [74] K. Lee. Private communicator. Unilever, 2005.
- [75] S. V. Lomov and I. Verpoest. Compression of woven reinforcements: a mathematical model. *Journal of Reinforced Plastics and Composites*, 19(16):1329–50, 2000.
- [76] S. V. Lomov and I. Verpoest. Modelling of the internal structure and deformability of textile reinforcements: Wisetex software. In *10th European Conference Composite Materials*, pages 336 – 44, Brugge, Belgium, June 2002.

## REFERENCES

- [77] S. V. Lomov, G. Huysmans, Y. Luo, R. S. Parnas, A. Prodromou, I. Verpoest, and F. R. Phelan. Textile composites: modelling strategies. *Composites, Part A: Applied Science and Manufacturing*, 32A(10):1379–94, 2001.
- [78] S. V. Lomov, G. Huysmans, and I. Verpoest. Hierarchy of textile structures and architecture of fabric geometric models. *Textile Research Journal*, 71(6):534–43, 2001.
- [79] S. V. Lomov, R. S. Parnas, S. B. Ghosh, I. Verpoest, and A. Nakai. Experimental and theoretical characterization of the geometry of two-dimensional braided fabrics. *Textile Research Journal*, 72(8):706–12, 2002.
- [80] A. Long, editor. *Design and manufacture of textile composites*. Woodhead Publishing Limited & CRC Press LLC, 2005.
- [81] A. C. Long, C. C. Wong, M. Sherburn, and F. Robitaille. Modelling the effect of fibre architecture on permeability for multi-layer preforms. In *25th SAMPE Europe International Conference*, pages 325–30, Paris, France, March/April 2004.
- [82] A. C. Long, C. C. Wong, M. Sherburn, and F. Robitaille. Prediction of permeability distributions for textile reinforcements. In *7th Int. Conf. On Textile Composites*, Yamagata, Japan, September 2004.
- [83] W. Lorensen and H. Cline. Marching cubes: A high-resolution 3d surface reconstruction algorithm. *ACM Computer Graphics*, 21(4):163–170, 1987.
- [84] A. E. H. Love. *General theory of the bending and twisting of thin rods*. A treatise on the mathematical theory of elasticity. Dover Publications, 4 edition, 1944.
- [85] F. Lundh. Python imaging library, 2007. URL <http://www.pythonware.com/products/pil>. [Online; accessed 21-June-2007].
- [86] K. Martin, W. Schroeder, and B. Lorensen. Visualization Toolkit, 2007. URL <http://www.vtk.org/>. [Online; accessed 23-April-2007].
- [87] T. Matsuo. *Study on the mechanical property of fiber assemblies*. PhD thesis, Tokyo Institute of Technology, 1968.
- [88] T. M. McBride. *The large deformation behaviour of woven fabric and microstructural evolution in formed textile composites*. PhD thesis, Boston University, 1997.
- [89] P. Minazio. Fast - fabric assurance by simple testing. *International Journal of Clothing Science and Technology*, 7:43–8, 1995.

## REFERENCES

- [90] T. Möller. A fast triangle-triangle intersection test. *Journal of Graphics Tools*, 2(2): 25–30, 1997.
- [91] T. Muir, editor. *The Theory of Determinants in the Historical Order of Development*, volume 1. New York: Dover, 1960.
- [92] N. Pan and G. A. Carnaby. The initial shear modulus of a unit cell of wool fibres. *Wool Research Organisation of New Zealand Communication*, C106, 1988.
- [93] N. Pan and G. A. Carnaby. Micromechanics of wool fibre assemblies in compression. *The application of Mathematics and Physics in the Wool Industry*, pages 181–91, 1988.
- [94] A. Papoulis, editor. *Probability, Random Variables, and Stochastic Processes*. McGraw-Hill, New York, 1984.
- [95] F. Peirce. The geometry of cloth structure. *Journal Textile Institute*, 28(3):45–96, 1937.
- [96] A. D. Polyanin and V. F. Zaitsev, editors. *Handbook of Exact Solutions for Ordinary Differential Equations*. Chapman & Hall/CRC Press, 2nd edition, 2003.
- [97] P. Potluri and V. Thammandra. Influence of uniaxial and biaxial tension on meso-scale geometry and strain fields in a woven composite. *Composite Structures*, 77: 405–18, February 2007.
- [98] P. Potluri, D. P. Ciurezu, and R. Ramgulam. Measurement of meso-scale shear deformations for modelling textile composites. *Composites Part A: Applied Science and Manufacturing*, 37:303–14, February 2006.
- [99] P. Potluri, I. Parlak, R. Ramgulam, and T. Sagar. Analysis of tow deformations in textile preforms subjected to forming forces. *Composites Science and Technology*, 66:297–305, February 2006.
- [100] P. Potluri, P. Patel, and J. Leung. Effect of treatments on frictional behaviour of cotton and polyester fabrics. Technical report, Textile Composites Group, University of Manchester, 2006.
- [101] T. J. Reinhard, C. A. Dostal, M. S. Woods, H. J. Frissel, and A. W. Ronke, editors. *Engineered Materials Handbook*. ASM International, 1987.
- [102] W. W. Roberts and N. B. Beil. Fibrous assemblies: modeling / computer simulation of compressional behaviour. In *International Textile Design and Engineering Conference*, Edinburgh, 2003.



## REFERENCES

- [103] F. Robitaille and R. Gauvin. Compaction of textile reinforcements for composites manufacturing. ii: compaction and relaxation of dry and h<sub>2</sub>o-saturated woven reinforcements. *Polymer Composites*, 19(5):543–57, 1998.
- [104] F. Robitaille, B. J. Souter, A. C. Long, and C. D. Rudd. A geometrical model for textile preforms. In *19th SAMPE Europe International Conference*, pages 151–62, Paris, France, April 1998.
- [105] F. Robitaille, B. R. Clayton, A. C. Long, B. J. Souter, and C. D. Rudd. Geometric modelling of industrial preforms: Woven and braided textiles. *Journal of Materials: Design and Applications, Proc. Institution of Mechanical Engineers (Part L)*, 213: 69–84, 1999.
- [106] F. Robitaille, B. R. Clayton, A. C. Long, B. J. Souter, and C. D. Rudd. Geometric modelling of industrial preforms: Warp-knitted and multiple layer textiles. *Journal of Materials: Design and Applications, Proc. Institution of Mechanical Engineers (Part L)*, 214:71–90, 2000.
- [107] F. Robitaille, A. C. Long, and C. D. Rudd. Geometric modelling of textiles for prediction of composite processing and performance characteristics. *Plastics, Rubber and Composites*, 31(2):66–75, 2002.
- [108] F. Robitaille, A. Long, M. Sherburn, C. Wong, and C. Rudd. Predictive modelling and performance properties of textile composite unit cells: current status and perspectives. In *ECCM-11 (European Conf. on Composite Materials, Spn. ESCM: European Society for Composite Materials)*, Rhodes, Greece, May 2004.
- [109] W. Ruijter, J. Crookston, A. C. Long, and I. A. Jones. Computational meso-scale analysis of textile composites using adaptive finite element analysis. In *47th AIAA/ASME/AHS/ASC Structures, Structural Dynamics and Materials Conference*, Newport, RI, US, May 2006.
- [110] T. Sagar, P. Potluri, and J. Hearle. Energy approach to predict uniaxial/biaxial load-deformation of woven preforms. In *European Conference on Composite Materials 10*, Brugge, Belgium, June 2002.
- [111] T. Sagar, P. Potluri, and J. Hearle. Meso-scale modelling of interlaced fibre assemblies using energy method. *Computer material science*, 28:49–62, 2003.
- [112] O. C. S.A.S. Open CASCADE, 2007. URL <http://www.opencascade.org/>. [Online; accessed 23-April-2007].

## REFERENCES

- [113] M. Schatzman. *Numerical Analysis: A Mathematical Introduction*. Clarendon Press, 2002.
- [114] P. Schubel, N. Warrior, and C. Rudd. Surface roughness modelling of textile composites using texgen. In *Proceedings of the 8th International Conference on Textile Composites (TexComp 8)*, Nottingham, UK, October 2006.
- [115] K. Searles, G. Odegard, and M. Kumosa. Micro- and mesomechanics of 8-harness satin woven fabric composites: I - evaluation of elastic behavior. *Composites Part A: Applied Science and Manufacturing*, 32:1627–55, November 2001.
- [116] R. A. Serway and J. W. Jewett. *Physics for Scientists and Engineers*. Brooks/Cole, 6th edition, 2004.
- [117] M. Sherburn. TexGen v2, 2007. URL <http://www.nottingham.ac.uk/~emxmns/texgen.htm>. [Online; accessed 23-April-2007].
- [118] M. Sherburn. TexGen v3, 2007. URL <http://texgen.sourceforge.net>. [Online; accessed 23-April-2007].
- [119] M. Sherburn, F. Robitaille, A. Long, and C. Rudd. Geometric pre-processor for the calculation of physical properties of textiles. In *Industrial Simulation Conference*, pages 479–86, Malaga, Spain, June 2004.
- [120] M. N. Sherburn, A. C. Long, I. A. Jones, F. Robitaille, J. J. Crookston, and W. Ruijter. Mechanical properties of fibre assemblies and textile unit cells. In *15th Int. Conf. on Composite Materials*, Durban, South Africa, June 2005.
- [121] J. R. Shewchuk. Delaunay refinement algorithms for triangular mesh generation. *Computational Geometry: Theory and Applications*, 22(1–3):21–74, May 2002.
- [122] S. Sihn, Y. Wang, and E. Zhou. Computational modeling of 3-d textile composites. In *Fifteenth international conference on composite materials*, pages 329–30, Durban, South Africa, June/July 2005.
- [123] J. Smart. wxWidgets, 2007. URL <http://www.wxwidgets.org/>. [Online; accessed 23-April-2007].
- [124] I. M. Smith and D. V. Griffith. *Programming the Finite Element Method*. J. Wiley and Sons, 1982, 1988, 1998, 2004.
- [125] B. J. Souter. *Effects of fibre architecture on formability of textile preforms*. PhD thesis, University of Nottingham, 2001.

## REFERENCES

- [126] B. Stein. A point about polygons. *Linux Journal*, March 1997.
- [127] I. Stewart. *Galois Theory*. Chapman and Hall, 1989.
- [128] X. Tang, J. D. Whitcomb, A. D. Kelkar, and J. Tate. Progressive failure analysis of 2 x 2 braided composites exhibiting multiscale heterogeneity. *Composites Science and Technology*, 66:2580–90, November 2006.
- [129] M. Tarfaoui and S. Akesbi. A finite element model of mechanical properties of plain weave. *Colloids and Surfaces A: Physicochemical and Engineering Aspects*, 187–188:439–48, August 2001.
- [130] L. Thomason. TinyXml, 2007. URL <http://www.grinninglizard.com/tinyxml/>. [Online; accessed 23-April-2007].
- [131] A. Thorn. *DirectX 9 Graphics: The Definitive Guide to Direct 3D (Wordware Applications Library)*. Wordware Publishing, 2005.
- [132] S. P. Timoshenko and J. M. Gere. *Mechanics of Materials*. Brooks-Cole, 1972.
- [133] P. Tipler. *Physics for Scientists and Engineers*, volume 1. W. H. Freeman, 4th edition, 1998.
- [134] P. Tipler. *Physics for Scientists and Engineers: Mechanics, Oscillations and Waves, Thermodynamics*. W. H. Freeman, 5th edition, 2004.
- [135] G. van Rossum. Python, 2007. URL <http://www.python.org/>. [Online; accessed 23-April-2007].
- [136] C. M. van Wyk. Note on the compressibility of wool. *Journal Textile Institute*, 37: 285–82, 1946.
- [137] I. Verpoest and S. V. Lomov. Virtual textile composites software wisetex: Integration with micro-mechanical, permeability and structural analysis. *Composites Science and Technology*, 65:2563–74, 2005.
- [138] Y. Wang and X. Sun. Digital-element simulation of textile processes. *Composites Science and Technology*, 61:311–19, February 2001.
- [139] E. Witmer. Elementary bernoulli-euler beam theory. MIT Unified Engineering Course Notes, 1991, 1992.
- [140] C. C. Wong, A. C. Long, M. Sherburn, F. Robitaille, P. Harrison, and C. D. Rudd. Comparisons of novel and efficient approaches for permeability prediction based on the fabric architecture. *Composites Part A*, 37(6):847–57, 2006.

## REFERENCES

- [141] W. Wunderlich. *Mechanics of Structures: Variational and Computational Methods*. CRC, 2002.
- [142] M. Zako, Y. Uetsuji, and T. Kurashiki. Finite element analysis of damaged woven fabric composite materials. *Composites Science and Technology*, 63:507–16, 2003.
- [143] G. Zhou, X. Sun, and Y. Wang. Multi-chain digital element analysis in textile mechanics. *Composites Science and Technology*, 64:239–44, February 2004.
- [144] B. Zhu, T. Yu, and X. Tao. An experimental study of in-plane large shear deformation of woven fabric composite. *Composites Science and Technology*, 67:252–61, February 2007.
- [145] O. C. Zienkiewicz. *The Finite Element Method in Engineering Science*. McGraw-Hill, 1971, 1977.

# Appendices

## Area calculation

It is often necessary to evaluate the area of a cross-section, for example to calculate the area fraction of fibre to yarn. In this section the method to calculate this area will be discussed. The area  $A$  of a cross-section can be expressed as:

$$A = \iint_{\mathbf{a}} 1 \, dy \, dx \quad (\text{A.1})$$

Note that  $A$  is a scalar value and  $\mathbf{a}$  refers to a region of space. Taking the cross-section  $\mathbf{C}(t)$  defined as a closed counter-clockwise parametric equation between the limits  $0 \leq t \leq 1$ , the integral can be expressed using Green's theorem [4] as:

$$A = \int_0^1 \vec{\mathbf{F}} \times \mathbf{C}'(t) \, dt \quad (\text{A.2})$$

where  $\vec{\mathbf{F}}$  is defined as being any vector that satisfies the following equation:

$$\nabla \vec{\mathbf{F}} = 1 \quad (\text{A.3})$$

Possible values of  $\vec{\mathbf{F}}$  include but are not limited to  $(x, 0)$  and  $(0, y)$ . With  $\vec{\mathbf{F}} = (x, 0)$  Equation A.2 becomes:

$$A = \int_0^1 \mathbf{C}_x \mathbf{C}'_y \, dt \quad (\text{A.4})$$

Or with  $\vec{\mathbf{F}} = (0, y)$  Equation A.2 becomes:

$$A = - \int_0^1 \mathbf{C}'_x \mathbf{C}_y \, dt \quad (\text{A.5})$$

In practice the integral can be approximated using the Trapezium rule [13] where analytical solutions are not available. Given  $n$  points  $\mathbf{C}_i$  sampled along the length of the parametric curve  $\mathbf{C}(t)$ :

$$\mathbf{C}_i = \mathbf{C} \left( \frac{i}{n-1} \right) \quad (\text{A.6})$$

## APPENDIX A: AREA CALCULATION

The approximated area is:

$$A \approx \frac{1}{2} \sum_{i=1}^{n-1} (\mathbf{C}_{ix} + \mathbf{C}_{i+1x})(\mathbf{C}_{i+1y} - \mathbf{C}_{iy}) \quad (\text{A.7})$$

or

$$A \approx -\frac{1}{2} \sum_{i=1}^{n-1} (\mathbf{C}_{i+1x} - \mathbf{C}_{ix})(\mathbf{C}_{iy} + \mathbf{C}_{i+1y}) \quad (\text{A.8})$$

## Volume calculation

The volume of a yarn is a useful quantity to evaluate for example to calculate the volume fraction of fibre to yarn. The method is an extension of that used to calculate the cross-sectional area (see Appendix A). The volume  $V$  of a yarn can be expressed as:

$$V = \iiint_{\mathbf{v}} 1 \, dz \, dy \, dx \quad (\text{B.1})$$

Note that  $V$  is a scalar value and  $\mathbf{v}$  refers to a region of space. Suppose the yarn surface is defined by the parametric equation  $\mathbf{P}(u, v)$  with limits  $0 \leq u \leq 1$  and  $0 \leq v \leq 1$ , using the divergence theorem [4] the equation can be expressed as:

$$V = \int_0^1 \int_0^1 \vec{\mathbf{F}} \cdot \left( \frac{\partial \mathbf{P}}{\partial u} \times \frac{\partial \mathbf{P}}{\partial v} \right) \, dv \, du + \iint_{\mathbf{s}_a} \vec{\mathbf{F}} \cdot d\mathbf{s}_a + \iint_{\mathbf{s}_b} \vec{\mathbf{F}} \cdot d\mathbf{s}_b \quad (\text{B.2})$$

where  $\mathbf{s}_a$  and  $\mathbf{s}_b$  are two end cap surfaces which when combined with  $\mathbf{P}(u, v)$  form a completely closed boundary of  $v$ .  $d\mathbf{s}_a$  and  $d\mathbf{s}_b$  represent the outward pointing unit surface normals of surfaces  $\mathbf{s}_a$  and  $\mathbf{s}_b$  respectively.  $\vec{\mathbf{F}}$  is defined as any vector satisfying the following equation:

$$\nabla \cdot \vec{\mathbf{F}} = 1 \quad (\text{B.3})$$

Possible values of  $\vec{\mathbf{F}}$  include but are not limited to  $(x, 0, 0)$ ,  $(0, y, 0)$  and  $(0, 0, z)$ . Using  $\vec{\mathbf{F}} = (x, 0, 0)$ , the equation becomes:

$$V = \int_0^1 \int_0^1 \mathbf{P}_x \left( \frac{\partial \mathbf{P}}{\partial u_y} \frac{\partial \mathbf{P}}{\partial v_z} - \frac{\partial \mathbf{P}}{\partial u_z} \frac{\partial \mathbf{P}}{\partial v_y} \right) \, dv \, du + \iint_{\mathbf{s}_a} \mathbf{s}_{a_x} \cdot d\mathbf{s}_a + \iint_{\mathbf{s}_b} \mathbf{s}_{b_x} \cdot d\mathbf{s}_b \quad (\text{B.4})$$

Similar equations can be derived for other values of  $\vec{\mathbf{F}}$  not shown here. Although too complicated to solve analytically for general shapes an approximation can be obtained numerically. In order to do this  $\mathbf{P}(u, v)$  must be sampled as described in Section 2.8. From the sampled points a triangular mesh can be created, similarly triangular meshes



of the two end faces can also be created ensuring the normals point outwards. Given  $n$  triangles the approximated volume is:

$$V \approx \sum_{i=1}^n \iint_{\mathbf{s}_i} \vec{\mathbf{F}} \cdot d\mathbf{s}_i \quad (\text{B.5})$$

where  $\mathbf{s}_i$  is the surface of the  $i$ th triangle. Given vertices  $\mathbf{A}_i$ ,  $\mathbf{B}_i$  and  $\mathbf{C}_i$  for triangle  $i$  and vectors  $\vec{\mathbf{U}}_i$  and  $\vec{\mathbf{V}}_i$  defined as:

$$\vec{\mathbf{U}}_i = \mathbf{B}_i - \mathbf{A}_i \quad (\text{B.6})$$

$$\vec{\mathbf{V}}_i = \mathbf{C}_i - \mathbf{A}_i \quad (\text{B.7})$$

Any point on the surface of the triangle  $\mathbf{s}_i$  can be expressed in parametric form as:

$$\mathbf{s}_i(u, v) = \mathbf{A}_i + u\vec{\mathbf{U}}_i + v\vec{\mathbf{V}}_i \quad 0 \leq u \leq 1 \quad 0 \leq v \leq 1 - u \quad (\text{B.8})$$

The outward pointing unit surface normal  $d\mathbf{s}_i$  can then be expressed as:

$$d\mathbf{s}_i = \vec{\mathbf{U}}_i \times \vec{\mathbf{V}}_i dv du \quad (\text{B.9})$$

Using  $\vec{\mathbf{F}} = (x, 0, 0)$  Equation B.5 becomes:

$$V \approx \sum_{i=1}^n \int_0^1 \int_0^{1-u} (\mathbf{A}_{ix} + u\vec{\mathbf{U}}_{ix} + v\vec{\mathbf{V}}_{ix})(\vec{\mathbf{U}}_{iy} \vec{\mathbf{V}}_{iz} - \vec{\mathbf{U}}_{iz} \vec{\mathbf{V}}_{iy}) dv du \quad (\text{B.10})$$

Which can be written as:

$$V \approx \frac{1}{6} \sum_{i=1}^n (\mathbf{A}_{ix} + \mathbf{B}_{ix} + \mathbf{C}_{ix}) ((\mathbf{B}_{iy} - \mathbf{A}_{iy})(\mathbf{C}_{iz} - \mathbf{A}_{iz}) - (\mathbf{B}_{iz} - \mathbf{A}_{iz})(\mathbf{C}_{iy} - \mathbf{A}_{iy})) \quad (\text{B.11})$$

## Repeat limits

A yarn with  $n$  repeat vectors  $\vec{\mathbf{R}}_i$  covers an infinite region of space if no limits are placed on the number of times the yarn is repeated. Repeated yarns exist translated by vectors  $\vec{\mathbf{V}}_j$  defined as:

$$\vec{\mathbf{V}}_j = C_0\vec{\mathbf{R}}_0 + C_1\vec{\mathbf{R}}_1 + \cdots + C_{n-1}\vec{\mathbf{R}}_{n-1} \quad -\infty \leq C_i \leq \infty \quad (\text{C.1})$$

where the coefficients  $C_i$  are integers, and since they range from  $-\infty$  to  $\infty$ , the number of vectors  $\vec{\mathbf{V}}_j$  is infinite. For rendering and intersection purposes it is necessary to limit the yarn to a domain. The number of vectors  $\vec{\mathbf{V}}_j$  can be reduced to a finite number by limiting the coefficients  $C_i$  to a finite range:

$$a_i \leq C_i \leq b_i \quad (\text{C.2})$$

where  $a_i$  and  $b_i$  are referred to as the repeat limits. The repeat limits are calculated such that yarns repeated by vector  $\vec{\mathbf{V}}_j$  that intersect with the domain are not removed while minimising the number of vectors  $\vec{\mathbf{V}}_j$ . The number  $m$  of vectors  $\vec{\mathbf{V}}_j$  can be calculated as:

$$m = \prod_{i=0}^{n-1} (b_i - a_i + 1) \quad (\text{C.3})$$

Figure C.1 displays a simple example of a yarn with two repeat vectors  $\vec{\mathbf{R}}_0$  and  $\vec{\mathbf{R}}_1$ , and a box shaped domain.

The repeat vectors for this case can be found intuitively, they are:

$$a_0 = 1 \quad b_0 = 2 \quad a_1 = 0 \quad b_1 = 1 \quad (\text{C.4})$$

The number  $m$  of vectors  $\vec{\mathbf{V}}_j$  is 4 corresponding to 4 repeated yarns. An iterative algorithm is devised to calculate these repeat limits automatically. Note the example illustrated here is simple considering the repeat vectors  $\vec{\mathbf{R}}_i$  may not be orthogonal and

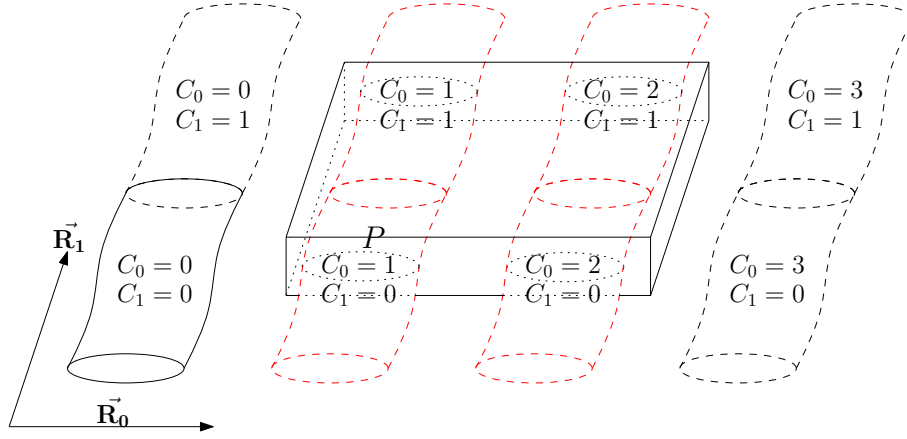


Figure C.1: Repeat limits example

the domain may not be a box shape nor aligned with the repeat vectors. The domain is defined by planes and as such can approximate any convex shape.

The algorithm operates as follows:

1. Set all repeat limits  $a_i$  and  $b_i$  to 0.
2. Repeat the following loop until all repeat limits  $a_i$  and  $b_i$  remain unchanged from one loop to the next
  - (a) For each repeat vector  $\vec{R}_i$  calculate repeat limits  $a_i$  and  $b_i$  as follows:
    - i. Set current repeat limits  $a_i$  and  $b_i$  to 0.
    - ii. Get a mesh of yarns repeated by vectors  $\vec{V}_j$  using repeat limits calculated so far and calculate the minimum  $A_a$  and maximum  $A_b$  of  $\mathbf{P}_k \cdot \frac{\vec{R}_i}{\|\vec{R}_i\|}$  for each point  $\mathbf{P}_k$  in the mesh.
    - iii. Get a mesh of the domain and calculate the minimum  $B_a$  and maximum  $B_b$  of  $\mathbf{P}_k \cdot \frac{\vec{R}_i}{\|\vec{R}_i\|}$  for each node  $\mathbf{P}_k$  in the mesh.
    - iv. Set current repeat limits to  $a_i = \lceil \frac{B_a - A_b}{\|\vec{R}_i\|} \rceil$  and  $b_i = \lfloor \frac{B_b - A_a}{\|\vec{R}_i\|} \rfloor$ . (Note:  $\lceil \cdot \rceil$  and  $\lfloor \cdot \rfloor$  are the ceiling and floor functions respectively [39]).

This algorithm can be slow when the yarn mesh is large hence to increase efficiency the yarn mesh in step 2-a-ii can be replaced with a mesh of the bounding box encompassing the yarn. This may result in a wider range for the repeat limits which could cause a loss in performance in further computations making use of the repeat limits, however this approach generally results in an overall faster execution time.

## Sample python scripts

The Python scripts used to create the fabrics illustrated in Chapter 1 are shown here:

**Listing D.1:** 2dweave.py

```
from TexGen.Core import *

# Create a 2x2 2D woven fabric with yarn spacing of 2 and thickness 0.3
Textile = CTextileWeave2D(2, 2, 2, 0.3);

# Set the weave pattern
Textile.SwapPosition(0, 0);
Textile.SwapPosition(1, 1);

# Adjust the yarn widths
Textile.SetYarnWidths(1.5);

# Create the domain and assign it
Domain = CDomainPlanes(XYZ(-1, -1, -10), XYZ(11, 11, 10))
Textile.AssignDomain(Domain)

# Add the textile
AddTextile('2DWeave', Textile)
```

Listing D.2: 3dweave.py

```

from TexGen.Core import *

# Create a 8x4 3D woven textile with yarn spacing of 5 and thickness of 7
Textile = CTextileWeave3D(8, 4, 5, 7);

# Add some warp and weft layers
Textile.AddYLayers(0, 1);
Textile.AddYLayers(2, 1);
Textile.AddYLayers(4, 1);
Textile.AddYLayers(6, 1);
Textile.AddXLayers();
Textile.AddYLayers();
Textile.AddXLayers();
Textile.AddYLayers();
Textile.AddXLayers();
Textile.AddYLayers();

# Set the weave pattern
Textile.PushUp(0, 0);
Textile.PushUp(1, 0);
Textile.PushDown(4, 0);
Textile.PushUp(7, 0);

Textile.PushUp(1, 1);
Textile.PushUp(2, 1);
Textile.PushUp(3, 1);
Textile.PushDown(6, 1);

Textile.PushDown(0, 2);
Textile.PushUp(3, 2);
Textile.PushUp(4, 2);
Textile.PushUp(5, 2);

Textile.PushDown(2, 3);
Textile.PushUp(5, 3);
Textile.PushUp(6, 3);
Textile.PushUp(7, 3);

# Set the yarn width and heights
Textile.SetYarnWidths(4);
Textile.SetYarnHeights(1);

# Assign the default domain
# Textile.AssignDefaultDomain()

```

## APPENDIX D: SAMPLE PYTHON SCRIPTS

```
# Create the domain and assign it
Domain = CDomainPlanes(XYZ(0, 0, -10), XYZ(40, 40, 10))
Textile.AssignDomain(Domain)

# Add the textile
AddTextile('3DWeave', Textile)
```

Listing D.3: triaxialbraid.py

```

from TexGen.Core import *
import math

# Create a textile
Textile = CTextile()

# Create a python list containing 3 yarns
Yarns = [CYarn(), CYarn(), CYarn()]

# Add nodes to the yarns to describe their paths
# First define the angled yarns
Yarns[0].AddNode(CNode(XYZ(0, 0, 0)))
Yarns[0].AddNode(CNode(XYZ(0.5, 0.2887, 0.2)))
Yarns[0].AddNode(CNode(XYZ(1, 0.5774, 0.2)))
Yarns[0].AddNode(CNode(XYZ(1.5, 0.8660, 0)))
Yarns[0].AddNode(CNode(XYZ(2, 1.1547, 0)))

Yarns[1].AddNode(CNode(XYZ(0, 0, 0.2)))
Yarns[1].AddNode(CNode(XYZ(0.5, -0.2887, 0)))
Yarns[1].AddNode(CNode(XYZ(1, -0.5774, 0)))
Yarns[1].AddNode(CNode(XYZ(1.5, -0.8660, 0.2)))
Yarns[1].AddNode(CNode(XYZ(2, -1.1547, 0.2)))

# Define a straight yarn
Yarns[2].AddNode(CNode(XYZ(-0.25, 0, 0.1)))
Yarns[2].AddNode(CNode(XYZ(-0.25, 0.57735, 0.1)))

# Create a lenticular section for the +- angled yarns
AngledSection = CSectionLenticular(0.45, 0.13)

# The section will be rotated at the appropriate points to avoid interference
# So create an interpolated yarn section
AngledYarnSection = CYarnSectionInterpPosition(True, True)
# This is the rotation angle defined
RotationAngle = math.radians(12)

# Add rotated sections at 1/8 and 5/8 of the way along the yarn
# at angles of +- RotationAngle
AngledYarnSection.AddSection(1.0/8.0, CSectionRotated(AngledSection, -
    RotationAngle))
AngledYarnSection.AddSection(5.0/8.0, CSectionRotated(AngledSection,
    RotationAngle))

# Add unrotated sections to the interpolation at intervals of 1/4

```

## APPENDIX D: SAMPLE PYTHON SCRIPTS

```
AngledYarnSection.AddSection(0.0/4.0, AngledSection)
AngledYarnSection.AddSection(1.0/4.0, AngledSection)
AngledYarnSection.AddSection(2.0/4.0, AngledSection)
AngledYarnSection.AddSection(3.0/4.0, AngledSection)

# Assign the rotating cross-section to the angled yarns
Yarns[0].AssignSection(AngledYarnSection)
Yarns[1].AssignSection(AngledYarnSection)
# Add repeats to those yarns
Yarns[0].AddRepeat(XYZ(2, 0, 0))
Yarns[1].AddRepeat(XYZ(2, 0, 0))

# Create a lenticular section for the straight yarns and assign it
StraightSection = CSectionLenticular(0.6, 0.15)
Yarns[2].AssignSection(CYarnSectionConstant(StraightSection))
# Add repeats for the straight yarn
Yarns[2].AddRepeat(XYZ(1, 0, 0))

# Loop over all the yarns in the list
for Yarn in Yarns:
    # Set the interpolation function
    Yarn.AssignInterpolation(CInterpolationCubic())
    # Set the resolution of the surface mesh created
    Yarn.SetResolution(20)
    # Add common repeat vector to the yarn
    Yarn.AddRepeat(XYZ(0, 0.57735, 0))
    # Add the yarn to our textile
    Textile.AddYarn(Yarn)

# Create a domain and assign it to the textile
Textile.AssignDomain(CDomainPlanes(XYZ(0+0.25, 0, -1), XYZ(4+0.25, 4, 1)))

# Add the textile
AddTextile("triaxialbraid", Textile)
```



Listing D.4: weftknit.py

```

from TexGen.Core import *
import math

# Create a textile
Textile = CTextile()

# Create a yarn
Yarn = CYarn()

# Define some constants
r = 1
sx = r*2.5
sy = r*10
ly = 0.75*(sx+r)

# Add nodes to the yarns to describe the yarn path
Yarn.AddNode(CNode(XYZ(0, 0, r)))
Yarn.AddNode(CNode(XYZ(sx+r, ly, 0)))
Yarn.AddNode(CNode(XYZ(sx, ly+0.5*sy, -r)))
Yarn.AddNode(CNode(XYZ(sx-r, ly+sy, 0)))
Yarn.AddNode(CNode(XYZ(2*sx, 2*ly+sy, r)))
Yarn.AddNode(CNode(XYZ(3*sx+r, ly+sy, 0)))
Yarn.AddNode(CNode(XYZ(3*sx, ly+0.5*sy, -r)))
Yarn.AddNode(CNode(XYZ(3*sx-r, ly, 0)))
Yarn.AddNode(CNode(XYZ(4*sx, 0, r)))

# Assign a constant circular cross-section
Section = CSectionEllipse(2*r, 2*r)
Yarn.AssignSection(CYarnSectionConstant(Section))

# Create some repeats
Yarn.AddRepeat(XYZ(4*sx, 0, 0))
Yarn.AddRepeat(XYZ(0, 2*sy, 0))

# Set the interpolation function
Yarn.AssignInterpolation(CInterpolationCubic())

# Set the resolution of the surface mesh created
Yarn.SetResolution(20)

# Add the yarn to our textile
Textile.AddYarn(Yarn)

# Translate the yarn and add it to the textile

```

## APPENDIX D: SAMPLE PYTHON SCRIPTS

```
# Note this could be part of the repeat vectors but is done
# like this to give the yarns different colours
Yarn.Translate(XYZ(0, sy, 0))
Textile.AddYarn(Yarn)

# Create a domain and assign it to the textile
Textile.AssignDomain(CDomainPlanes(XYZ(0, -ly, -2*r), XYZ(4*(4*sx), 4*sy-ly,
    2*r)))

# Add the textile
AddTextile("weftknit", Textile)
```

Listing D.5: ncf.py

```

from TexGen.Core import *

# Create a textile
Textile = CTextile()

# Create a python list containing 2 inlay yarns
Yarns = [CYarn(), CYarn()]

# Define some constants
w = 0.95
s = 1
h = 0.2

# Add nodes to the yarns to describe the yarn path
Yarns[0].AddNode(CNode(XYZ(0, 0, 0)))
Yarns[0].AddNode(CNode(XYZ(0, s, 0)))

Yarns[1].AddNode(CNode(XYZ(0, 0, h)))
Yarns[1].AddNode(CNode(XYZ(s, 0, h)))

# Loop over all the yarns in the list
for Yarn in Yarns:
    # Assign a power ellipse to the inlay yarns
    InlaySection = CSectionPowerEllipse(w, h, 0.5)
    Yarn.AssignSection(CYarnSectionConstant(InlaySection))
    # Add repeats
    Yarn.AddRepeat(XYZ(s, 0, 0))
    Yarn.AddRepeat(XYZ(0, s, 0))
    # Set the interpolation function
    Yarn.AssignInterpolation(CInterpolationCubic())
    # Set the resolution of the surface mesh created
    Yarn.SetResolution(40)
    # Add the yarn to our textile
    Textile.AddYarn(Yarn)

# Define some constants more constants for the stitching
a = 0.05
r = 0.025
u = 1.5*h+r
d = -0.5*h-r

# Create a stitch yarn
StitchYarn = CYarn()

```

## APPENDIX D: SAMPLE PYTHON SCRIPTS

```

# Create stitch yarn path, this path is quite complex and has been
# created with a fair amount of tweaking. Note that the tangents
# at the nodes have been specified for further control on the path.
StitchYarn.AddNode(CNode(XYZ(2*a, a, u), XYZ(1, 1, 0)))
StitchYarn.AddNode(CNode(XYZ(s+a, s-a, u), XYZ(1, 1, 0)))

StitchYarn.AddNode(CNode(XYZ(s+a, s, d), XYZ(0, 1, 0)))
StitchYarn.AddNode(CNode(XYZ(s+2*a, 2*s-a, d), XYZ(0, 1, 0)))

StitchYarn.AddNode(CNode(XYZ(s+a, 2*s, d+a), XYZ(-1, 0, 0)))
StitchYarn.AddNode(CNode(XYZ(s-a, 2*s, d+a), XYZ(-1, 0, 0)))

StitchYarn.AddNode(CNode(XYZ(s-2*a, 2*s-a, d), XYZ(0, -1, 0)))
StitchYarn.AddNode(CNode(XYZ(s-a, s, d), XYZ(0, -1, 0)))

StitchYarn.AddNode(CNode(XYZ(s-2*a, s+a, u), XYZ(-1, 1, 0)))
StitchYarn.AddNode(CNode(XYZ(-a, 2*s-a, u), XYZ(-1, 1, 0)))

StitchYarn.AddNode(CNode(XYZ(-a, 2*s, d), XYZ(0, 1, 0)))
StitchYarn.AddNode(CNode(XYZ(-2*a, 3*s-a, d), XYZ(0, 1, 0)))

StitchYarn.AddNode(CNode(XYZ(-a, 3*s, d+a), XYZ(1, 0, 0)))
StitchYarn.AddNode(CNode(XYZ(a, 3*s, d+a), XYZ(1, 0, 0)))

StitchYarn.AddNode(CNode(XYZ(2*a, 3*s-a, d), XYZ(0, -1, 0)))
StitchYarn.AddNode(CNode(XYZ(a, 2*s, d), XYZ(0, -1, 0)))

StitchYarn.AddNode(CNode(XYZ(2*a, 2*s+a, u), XYZ(1, 1, 0)))

# Add the repeat vectors for the stitching
StitchYarn.AddRepeat(XYZ(1, 0, 0))
StitchYarn.AddRepeat(XYZ(0, 2, 0))

# Assign a circular section to the stitch yarns
StitchSection = CSectionEllipse(2*r, 2*r)
StitchYarn.AssignSection(CYarnSectionConstant(StitchSection))
# Set the interpolation function to Bezier so that
# the yarn tangents specified above are respected
StitchYarn.AssignInterpolation(CInterpolationBezier())
# Set a lower surface mesh resolution that for the inlays,
# the stitching is so thin that a high resolution is not needed
StitchYarn.SetResolution(8)
# Translate the stitch yarn so that it falls between the inlay yarns
StitchYarn.Translate(XYZ(0.5*s, 0.5*s+r, 0))
# Add the yarn to our textile
Textile.AddYarn(StitchYarn)

```

## APPENDIX D: SAMPLE PYTHON SCRIPTS

```
# Create a domain and assign it to the textile
Textile.AssignDomain(CDomainPlanes(XYZ(0, 0, -1), XYZ(4*s, 4*s, 1)))

# Add the textile
AddTextile("ncf", Textile)
```

Listing D.6: createscreens.py

```

from TexGen.Core import *
from TexGen.Renderer import *
import Image

execfile('2dweave.py')
execfile('3dweave.py')
execfile('triaxialbraid.py')
execfile('weftknit.py')
execfile('ncf.py')

# Loop over all the textiles created above
for TextileName, Textile in GetTextiles().iteritems():
    # Get an instance of the CTexGenRenderer to render the textile
    Renderer = CTexGenRenderer()
    # Render our textile clipped to the domain
    Renderer.RenderTextile(Textile)
    # Set the background color to white
    Renderer.SetBackgroundColor(COLOR(1, 1, 1))
    # Set the camera position
    Renderer.ResetCamera(XYZ(0, 1.0, -1))

    # Start rendering in a window 640 x 480
    Width = 640
    Height = 480
    Renderer.Start(False, Width, Height)

    # Create a screenshot with 4 times magnification
    FileName = TextileName + ".png"
    Renderer.TakeScreenShot(FileName, 4)

    # Open the created image with the PIL library
    im = Image.open(FileName)
    # Resize it
    im.thumbnail((Width, Height), Image.ANTIALIAS)
    # Save it back to disk
    im.save(FileName)
    # This is done to get a better quality Anti-Aliased image

```

## Graphical user interface screenshots

Figures E.1, E.2 and E.3 show different menus in the TexGen GUI running under Windows. Figure E.4 shows the TexGen GUI running under Linux. At the time of writing the TexGen GUI only contains limited functionality for creating models and processing them. This aspect is still under development.

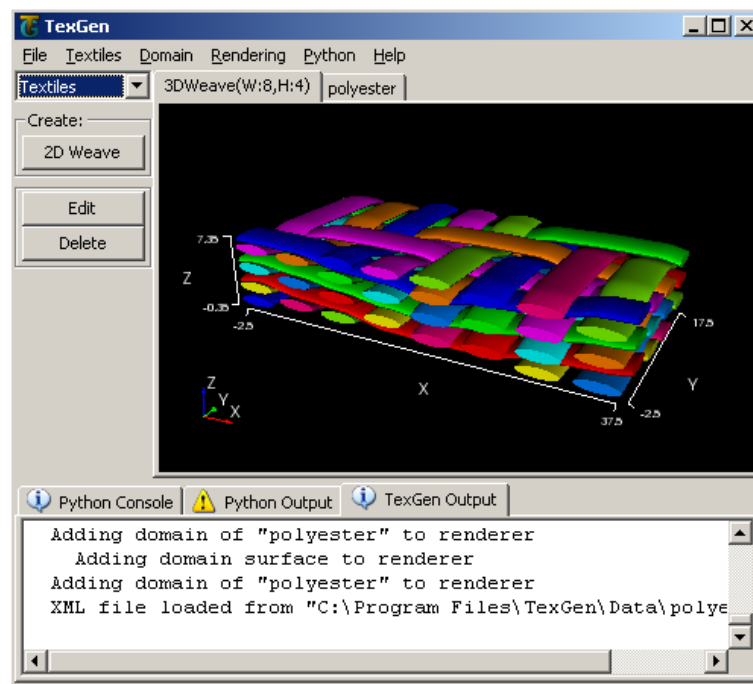


Figure E.1: TexGen GUI textiles page (Windows)

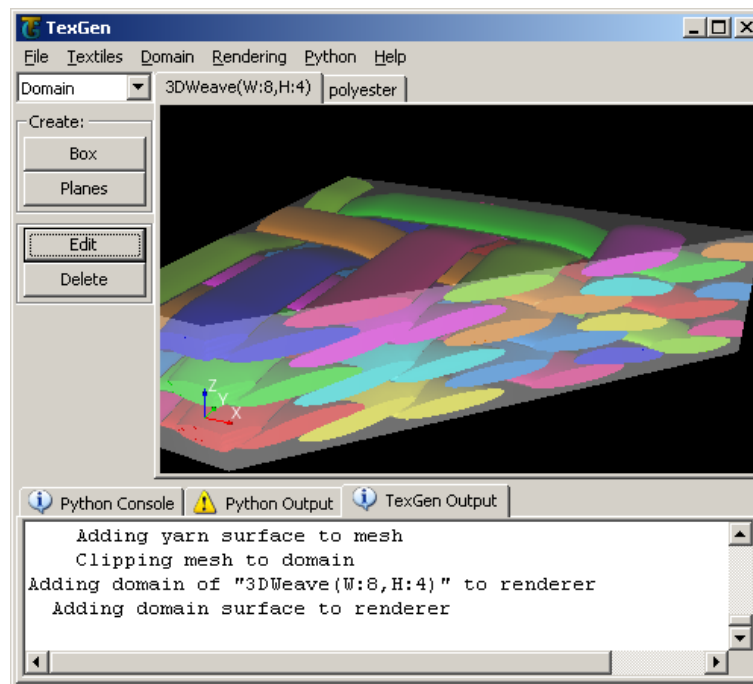


Figure E.2: TexGen GUI domain page (Windows)

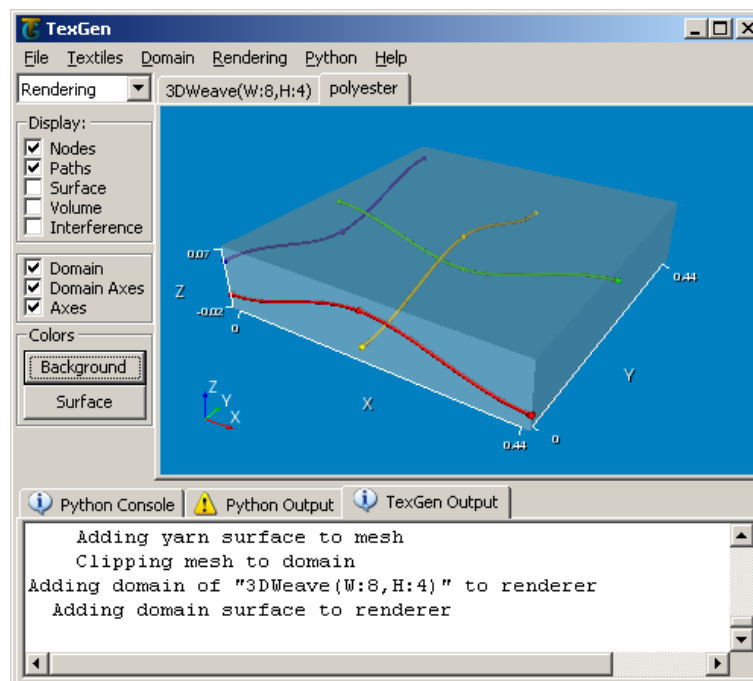


Figure E.3: TexGen GUI rendering page (Windows)



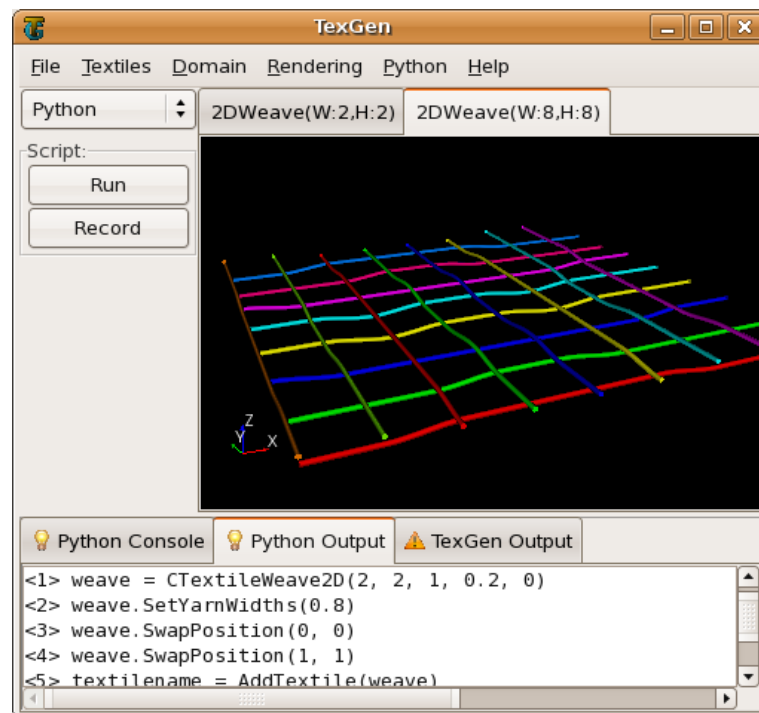


Figure E.4: TexGen GUI python page (Linux)

## Beam theory

Suppose a fibre of length  $L$  is supported at either end with some type of boundary condition yet to be decided. A force of magnitude  $P$  acts on the fibre at distance  $a$  from the end (Figure F.1).

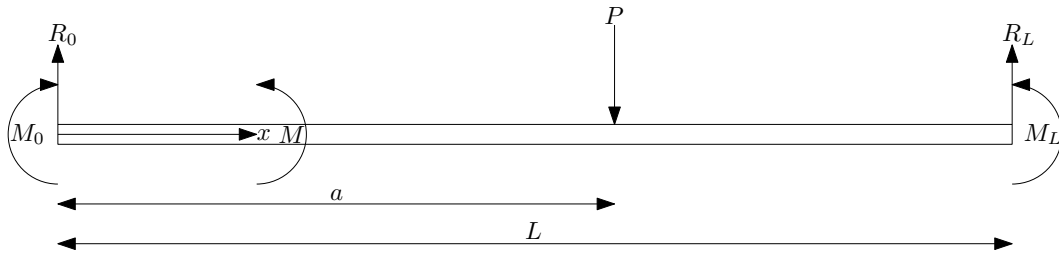


Figure F.1: Fibre modelled as a beam

If the fibre is in equilibrium then the sum of moments up to point  $x$  must be equal and opposite to the moment acting on the fibre at the point  $x$ . The fibre must be split into two parts with a different sets of equations for each. The first part denoted by subscript 1 applies for the range  $0 \leq x \leq a$ , the second part denoted by subscript 2 applies for the range  $a \leq x \leq l$ . The moment  $M$  is calculated as:

$$M_1(x) = R_0x + M_0 \quad (\text{F.1})$$

$$M_2(x) = R_0x - P(x - a) + M_0 \quad (\text{F.2})$$

Euler-Bernoulli's beam bending theory states that:

$$\frac{M}{I} = \frac{E}{R} \left( = \frac{\sigma}{y} \right) \quad (\text{F.3})$$

where  $I$  is the second moment of area,  $E$  is Youngs' modulus,  $R$  is the radius of curvature of the beam,  $\sigma$  is stress and  $y$  is distance from the neutral axis. The term  $\frac{\sigma}{y}$  will not be used in this derivation, it is simply included for completeness.

If deflection at any point  $x$  along the fibre is defined as  $v$ , it can be shown for small angles that:

$$\frac{1}{R} \approx \frac{d^2v}{dx^2} \quad (\text{F.4})$$

Assuming that deflection in the beam is always small:

$$\frac{d^2v}{dx^2_1}(x) = \frac{M_1}{EI} = \frac{R_0x}{EI} + \frac{M_0}{EI} \quad (\text{F.5})$$

$$\frac{d^2v}{dx^2_2}(x) = \frac{M_2}{EI} = \frac{R_0x}{EI} - \frac{P(x-a)}{EI} + \frac{M_0}{EI} \quad (\text{F.6})$$

Integrating once results in the slope of the fibre:

$$\frac{dv}{dx_1}(x) = \frac{R_0x^2}{2EI} + \frac{M_0x}{EI} + C_1 \quad (\text{F.7})$$

$$\frac{dv}{dx_2}(x) = \frac{R_0x^2}{2EI} - \frac{P(x-a)^2}{2EI} + \frac{M_0x}{EI} + C_3 \quad (\text{F.8})$$

Integrating again gives the deflection of the fibre:

$$v_1(x) = \frac{R_0x^3}{6EI} + \frac{M_0x^2}{2EI} + C_1x + C_2 \quad (\text{F.9})$$

$$v_2(x) = \frac{R_0x^3}{6EI} - \frac{P(x-a)^3}{6EI} + \frac{M_0x^2}{2EI} + C_3x + C_4 \quad (\text{F.10})$$

As the fibre must exhibit 0<sup>th</sup> and 1<sup>st</sup> order continuity, it follows that at  $x = a$ :

$$v_1(a) = v_2(a) \quad (\text{F.11})$$

$$\frac{dv}{dx_1}(a) = \frac{dv}{dx_2}(a) \quad (\text{F.12})$$

Solving these equations eliminates constants  $C_3$  and  $C_4$ :

$$C_1 = C_3 \quad (\text{F.13})$$

$$C_2 = C_4 \quad (\text{F.14})$$

A physical interpretation of values  $C_1$  and  $C_2$  can be found by obtaining expressions for  $\frac{dv}{dx}$  and  $v$  at  $x = 0$ :

$$\frac{dv}{dx_1}(0) = C_1 \quad (\text{F.15})$$

$$v_1(0) = C_2 \quad (\text{F.16})$$

So  $C_1$  represents the slope of the fibre at the origin while  $C_2$  represents the displacement at the origin of the fibre.

The magnitude of the reaction force  $R_0$  can be expressed in terms of moments  $M_0$  and  $M_L$  through static equilibrium of forces (Equation F.17) and moments (Equation F.18):

$$P = R_0 + R_L \quad (\text{F.17})$$

$$M_0 = M_L - Pa + R_LL \quad (\text{F.18})$$

The result is:

$$R_0 = \frac{P(L-a) - M_0 + M_L}{L} \quad (\text{F.19})$$

The second moment of area  $I$  of the fibre can be expressed in terms of its radius  $r$ :

$$I = \frac{\pi r^4}{4} \quad (\text{F.20})$$

Values  $C_1$ ,  $C_2$ ,  $M_0$  and  $M_L$  are constants that depend on the boundary conditions. If pinned boundary conditions are to be used the known constants are:

$$C_2 = M_0 = M_L = 0 \quad (\text{F.21})$$

The value of  $C_1$  can be determined by substituting the above constants into the equation  $v_2(L) = 0$ . Solving yields:

$$C_1 = -\frac{Pa(2L^2 - 3La + a^2)}{6EIL} \quad (\text{F.22})$$

For periodic boundary conditions the following equations would be used instead:

$$v_1(0) = C_2 = 0 \quad (\text{F.23})$$

$$v_2(L) = 0 \quad (\text{F.24})$$

$$\frac{dv}{dx_1}(0) = \frac{dv}{dx_2}(L) \quad (\text{F.25})$$

$$\frac{d^2v}{dx_1^2}(0) = \frac{d^2v}{dx_2^2}(L) \quad (\text{F.26})$$

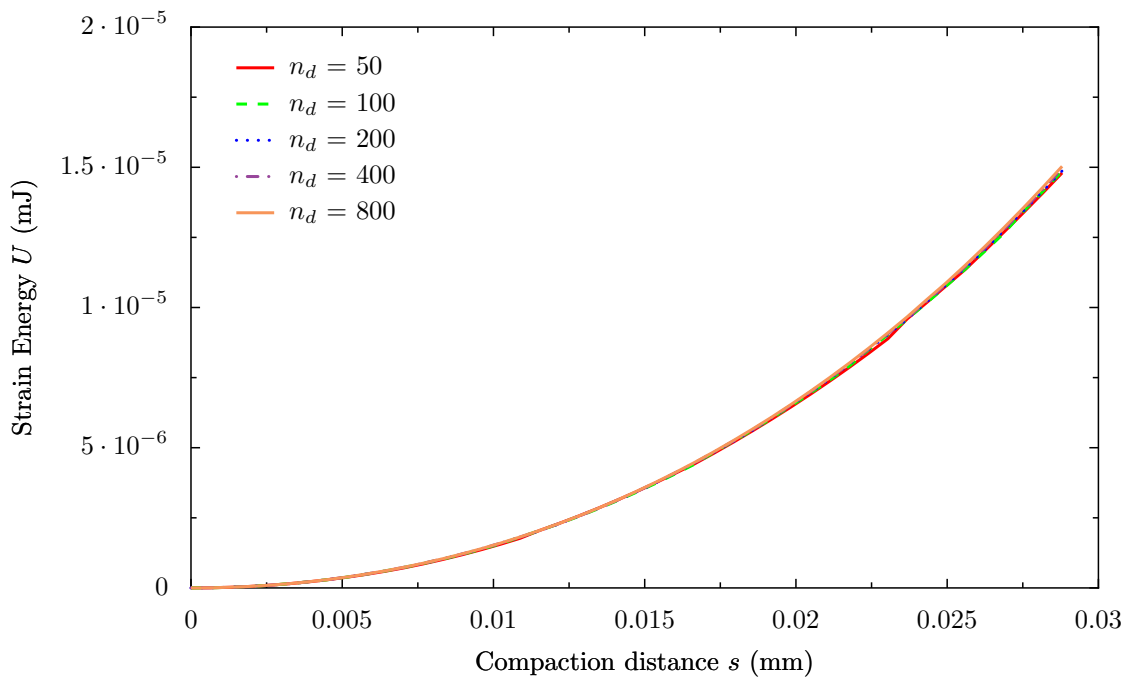
Solving for constants  $C_1$ ,  $M_0$  and  $M_L$ :

$$C_1 = -\frac{Pa(L^2 - 3La + 2a^2)}{12EIL} \quad (\text{F.27})$$

$$M_0 = -\frac{Pa(L-a)}{2L} \quad (\text{F.28})$$

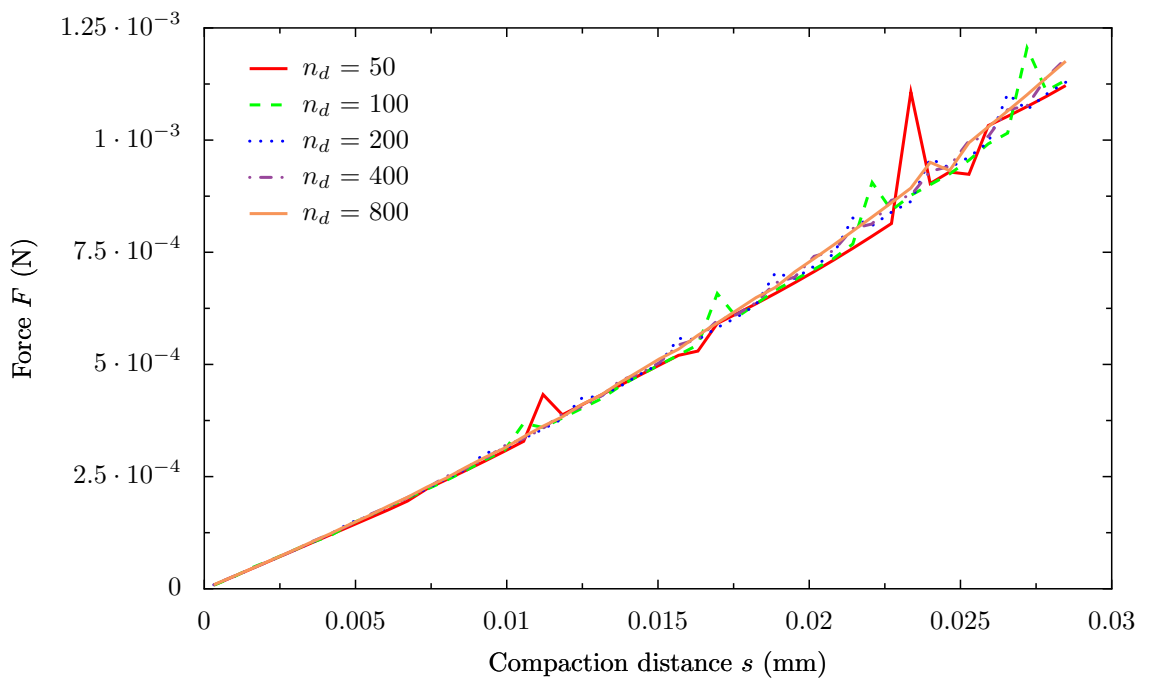
$$M_L = \frac{Pa(a-L)}{2L} \quad (\text{F.29})$$

## Test case tow compaction graphs



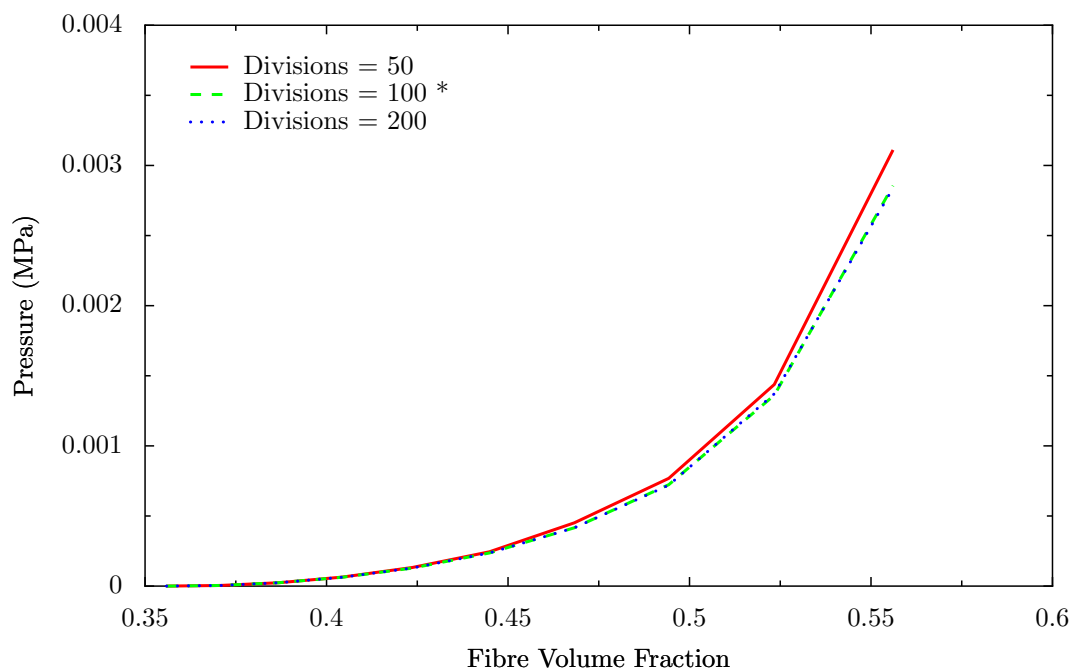
**Figure G.1:**  $U$  versus  $s$  for compaction test case varying  $n_d$

Figures G.1 and G.2 show the effect of varying the number of fibre length divisions  $n_d$  on the compaction test case described in Section 4.4.4. The energy curve  $U$  versus  $s$  is virtually identical for all cases, however small changes in energy  $U$  can have a fairly large effect on the gradient thus causing spikes in the force  $F$  versus  $s$  graph. The spikes are the largest but least frequent for  $n_d = 50$ . The magnitude of the spikes for  $n_d = 100$  is roughly halved while the frequency is doubled. And so on for larger number of fibre divisions until  $n_d = 800$  where the spikes have almost completely disappeared. These spikes occur when contact forces are transferred from one fibre length division to the next, therefore increasing the number of fibre length divisions smooths out the  $F$  versus  $s$  curve.



**Figure G.2:**  $F$  versus  $s$  for compaction test case varying  $n_d$

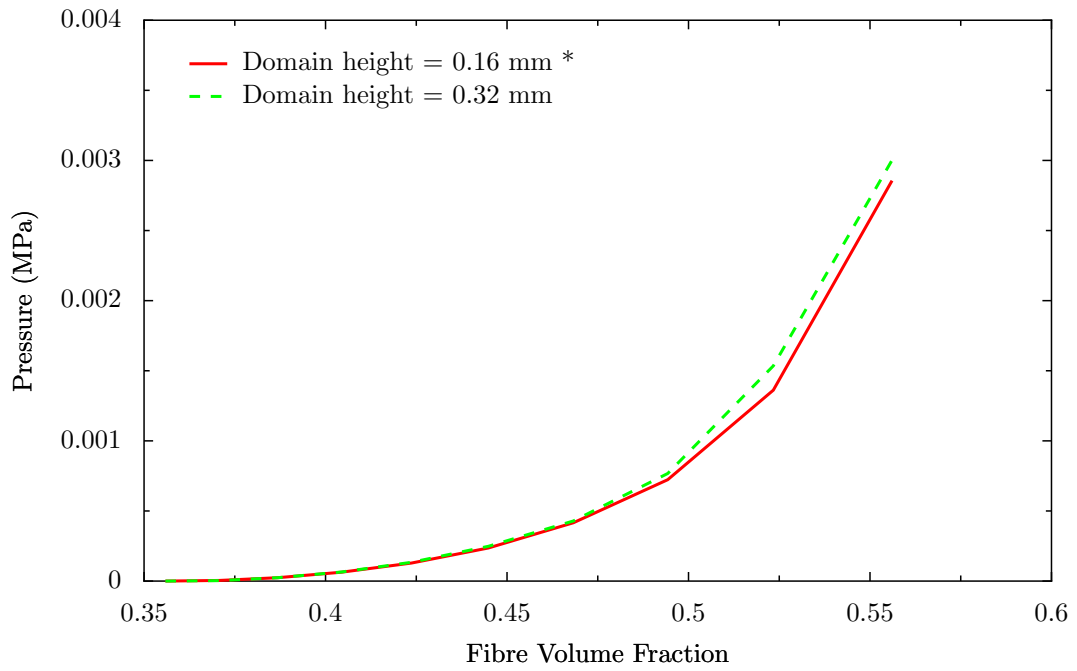
## Glass tow compaction graphs



**Figure H.1:** Pressure versus fibre volume fraction varying divisions

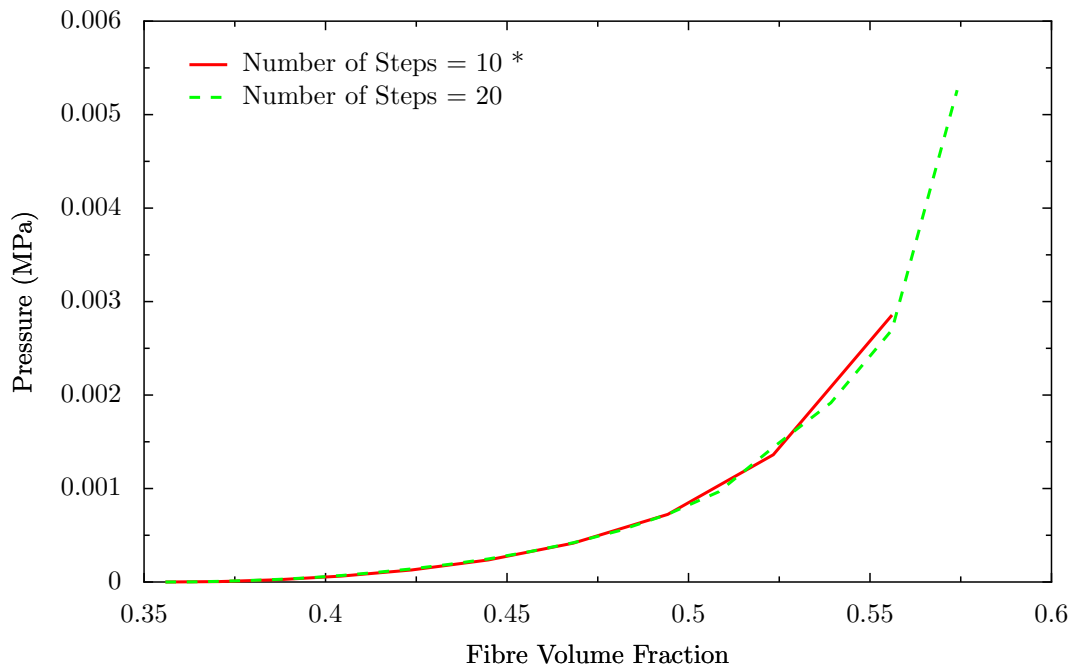
The effect of the number of fibre length divisions is shown in Figure H.1. This parameter does not significantly affect the results. Increasing the number of fibre length divisions should improve accuracy, however it also increases run time significantly. If the number of divisions is set too low then poor accuracy will result. 100 divisions provides a good compromise between the two.

Figure H.2 shows the effect of domain height. Again it can be seen that the height of the domain does not significantly affect the results. The lateral periodic boundary conditions help to ensure that this is the case. The run-time for running the simulation with a height of 0.32 mm is approximately 30 minutes whereas with a height of 0.16 mm the run-time is only a few minutes. It is therefore more efficient to run a large



**Figure H.2:** Pressure versus fibre volume fraction varying domain height

number of simulations on a small section of yarn.



**Figure H.3:** Pressure versus fibre volume fraction varying number of steps

Figure H.3 shows the effect of the number of steps on the results. This also does not affect the results. Increasing the number of steps will simply result in more data points being plotted, creating a smoother curve. However it also increases the run time. 10 steps gives a smooth enough curve and is fast enough to enable thousands of simula-



tions to be run in a relatively short period of time. If the number of steps is too small there is a danger that the simulation may become unstable and that fibres may pass through one another.

## Finite element code validation

A number of simulations were run in ABAQUS<sup>TM</sup>[51] implicit and explicit to compare against results from the in-house explicit code developed by the author (referred to as “FE CODE” in the tables). Single elements tests were performed on triangle, quadrilateral, wedge and hexahedral elements under shear and tensile deformations with different numbers of integration points. A patch test [145] was performed for quadrilateral, wedge and hexahedral elements. Results were compared using both small strain and large strain definitions referred to as linear and non-linear geometry in the tables. Isotropic and anisotropic material properties were also tested. Table I.1 contains a description of the elements tested in ABAQUS and Table I.2 contains a list of abbreviations used in the tables. The numbers 1, 2 and 3 each refer to one of three orthogonal axes. Not all combinations of the above were performed due to the very large number of tests required. The combinations of tests performed are illustrated in Tables I.3, I.4 and I.5.

**Table I.1:** ABAQUS elements

CPE3	3-node linear
CPE4	4-node bilinear
CPE4R	4-node bilinear, reduced integration with hourglass control
C3D6	6-node quadratic
C3D8	8-node biquadratic
C3D8R	8-node biquadratic, reduced integration

**Table I.2:** Table abbreviations

E	Strain
S	Stress
Max P	Maximum principal
Min P	Minimum principal
S Mises	Von Mises stress
RF	Reaction force
U	Displacement

**Table I.3:** ABAQUS Standard

	CPE3	CPE4	CPE4R	C3D6	C3D8	C3D8R
Linear Shear		x	x			
Linear Tension		x	x			
Linear Patch Test		x	x			
Non Linear Shear	x	x	x	x	x	
Non Linear Tension		x	x			
Non Linear Patch Test		x	x	x	x	
NL Shear Anisotropic					x	

**Table I.4:** ABAQUS Explicit

	CPE3	CPE4	CPE4R	C3D6	C3D8	C3D8R
Linear Shear			x			
Linear Tension			x			
Linear Patch Test			x			
Non Linear Shear			x			
Non Linear Tension			x			
Non Linear Patch Test			x			

**Table I.5:** In-house Implementation

	Triangle 3 IP	Quad 4 IP	Quad 1 IP	Wedge 2 IP	Hex 8 IP	Hex 1 IP
Linear Shear		x	x			
Linear Tension		x	x			
Linear Patch Test		x	x			
Non Linear Shear	x	x	x	x	x	
Non Linear Tension		x	x			
Non Linear Patch Test		x	x	x	x	
NL Shear Anisotropic					x	

APPENDIX I: FINITE ELEMENT CODE VALIDATION

**Table I.6:** ABAQUS STANDARD - CPE4 - SHEAR - LINEAR GEOMETRY

Integration Point	E11	E22	E12	E Max P	E Min P	S11	S22	S12	S Max P	S Min P	S Mises
1	0	0	0.1	0.05	-0.05	0	0	2143	2143	-2143	3712
2	0	0	0.1	0.05	-0.05	0	0	2143	2143	-2143	3712
3	0	0	0.1	0.05	-0.05	0	0	2143	2143	-2143	3712
4	0	0	0.1	0.05	-0.05	0	0	2143	2143	-2143	3712

Node	RF1	RF2	Magnitude
1	-1071	-1071	1515
2	-1071	1071	1515
3	1071	1071	1515
4	1071	-1071	1515

Internal Energy	107.1
-----------------	-------

**Table I.7:** ABAQUS STANDARD - CPE4 - SHEAR - NON-LINEAR GEOMETRY

Integration Point	E11	E22	E12	E Max P	E Min P	S11	S22	S12	S Max P	S Min P	S Mises
1	0.002496	-0.002496	0.09983	0.04998	-0.04998	106	-106	2139	2142	-2142	3710
2	0.002496	-0.002496	0.09983	0.04998	-0.04998	106	-106	2139	2142	-2142	3710
3	0.002496	-0.002496	0.09983	0.04998	-0.04998	106	-106	2139	2142	-2142	3710
4	0.002496	-0.002496	0.09983	0.04998	-0.04998	106	-106	2139	2142	-2142	3710

Node	RF1	RF2	Magnitude
1	-1016	-1022	1441
2	-1124	1128	1592
3	1016	1022	1441
4	1124	-1128	1592

Internal Energy	107.1
-----------------	-------

**Table I.8:** FE CODE - QUAD 4 INTEGRATION POINTS - SHEAR - LINEAR GEOMETRY

Integration Point	E11	E22	E12	E Max P	E Min P	S11	S22	S12	S Max P	S Min P	S Mises
1	0	0	0.1	0.05	-0.05	0	0	2143	2143	-2143	3712
2	0	0	0.1	0.05	-0.05	0	0	2143	2143	-2143	3712
3	0	0	0.1	0.05	-0.05	0	0	2143	2143	-2143	3712
4	0	0	0.1	0.05	-0.05	0	0	2143	2143	-2143	3712

Node	RF1	RF2	Magnitude
1	-1071	-1071	1515
2	-1071	1071	1515
3	1072	1071	1515
4	1072	-1071	1515

Internal Energy	107.1
-----------------	-------

**Table I.9:** FE CODE - QUAD 4 INTEGRATION POINTS - SHEAR - NON-LINEAR GEOMETRY

Integration Point	E11	E22	E12	E Max P	E Min P	S11	S22	S12	S Max P	S Min P	S Mises
1	0.002496	-0.002496	0.09983	0.04998	-0.04998	107	-107	2139	2142	-2142	3710
2	0.002496	-0.002496	0.09983	0.04998	-0.04998	107	-107	2139	2142	-2142	3710
3	0.002496	-0.002496	0.09983	0.04998	-0.04998	107	-107	2139	2142	-2142	3710
4	0.002496	-0.002496	0.09983	0.04998	-0.04998	107	-107	2139	2142	-2142	3710

Node	RF1	RF2	Magnitude
1	-1016	-1022	1441
2	-1123	1128	1592
3	1016	1022	1441
4	1123	-1128	1592

Internal Energy	107.1
-----------------	-------

APPENDIX I: FINITE ELEMENT CODE VALIDATION

**Table I.10:** ABAQUS STANDARD - CPE4R - SHEAR - LINEAR GEOMETRY

Integration Point	E11	E22	E12	E Max P	E Min P	S11	S22	S12	S Max P	S Min P	S Mises
1	0	0	0.1	0.05	-0.05	0	0	2143	2143	-2143	3712
Node	RF1	RF2	Magnitude								
1	-1071	-1071	1515								
2	-1071	1071	1515								
3	1071	1071	1515								
4	1071	-1071	1515								
Internal Energy	107.1										

**Table I.11:** ABAQUS STANDARD - CPE4R - SHEAR - NON-LINEAR GEOMETRY

Integration Point	E11	E22	E12	E Max P	E Min P	S11	S22	S12	S Max P	S Min P	S Mises
1	0.002496	-0.002496	0.09983	0.04998	-0.04998	106	-106	2139	2142	-2142	3710
Node	RF1	RF2	Magnitude								
1	-1016	-1022	1441								
2	-1124	1128	1592								
3	1016	1022	1441								
4	1124	-1128	1592								
Internal Energy	107.1										

**Table I.12:** ABAQUS EXPLICIT - CPE4R - SHEAR - LINEAR GEOMETRY

Integration Point	E11	E22	E12	E Max P	E Min P	S11	S22	S12	S Max P	S Min P	S Mises
1	0	0	0.1	0.05	-0.05	0	0	2143	2143	-2143	3712
Node	RF1	RF2	Magnitude								
1	-1071	-1071	1515								
2	-1071	1071	1515								
3	1071	1071	1515								
4	1071	-1071	1515								
Internal Energy	107.1										

**Table I.13:** ABAQUS EXPLICIT - CPE4R - SHEAR - NON-LINEAR GEOMETRY

Integration Point	E11	E22	E12	E Max P	E Min P	S11	S22	S12	S Max P	S Min P	S Mises
1	0.002496	-0.002496	0.09983	0.04998	-0.04998	106.9	-106.9	2139	2142	-2142	3710
Node	RF1	RF2	Magnitude								
1	-1016	-1022	1441								
2	-1123	1128	1592								
3	1016	1022	1441								
4	1123	-1128	1592								
Internal Energy	107.1										

**Table I.14:** FE CODE - QUAD 1 INTEGRATION POINT - SHEAR - LINEAR GEOMETRY

Integration Point	E11	E22	E12	E Max P	E Min P	S11	S22	S12	S Max P	S Min P	S Mises
1	0	0	0.1	0.05	-0.05	0	0	2143	2143	-2143	3712
Node	RF1	RF2	Magnitude								
1	-1071	-1071	1515								
2	-1071	1071	1515								
3	1072	1071	1515								
4	1072	-1071	1515								
Internal Energy	107.1										

APPENDIX I: FINITE ELEMENT CODE VALIDATION

**Table I.15:** FE CODE - QUAD 1 INTEGRATION POINT - SHEAR - NON-LINEAR GEOMETRY

Integration Point	E11	E22	E12	E Max P	E Min P	S11	S22	S12	S Max P	S Min P	S Mises
1	0.002496	-0.002496	0.09983	-0.04998	0.04998	107	-107	2139	-2142	2142	3710
Node	RF1	RF2	Magnitude								
1	-1016	-1022	1441								
2	-1123	1128	1592								
3	1016	1022	1441								
4	1123	-1128	1592								
Internal Energy	107.1										

APPENDIX I: FINITE ELEMENT CODE VALIDATION

**Table I.16:** ABAQUS STANDARD - CPE4 - TENSION - LINEAR GEOMETRY

Integration Point	E11	E22	E12	E Max P	E Min P	S11	S22	S12	S Max P	S Min P	S Mises
1	0	0.1	0	0.1	0	8571	1.286e+004	0	1.286e+004	8571	4286
2	0	0.1	0	0.1	0	8571	1.286e+004	0	1.286e+004	8571	4286
3	0	0.1	0	0.1	0	8571	1.286e+004	0	1.286e+004	8571	4286
4	0	0.1	0	0.1	0	8571	1.286e+004	0	1.286e+004	8571	4286
Node	RF1	RF2	Magnitude								
1	-4286	-6429	7726								
2	4286	-6429	7726								
3	4286	6429	7726								
4	-4286	6429	7726								
Internal Energy	642.9										

**Table I.17:** ABAQUS STANDARD - CPE4 - TENSION - NON-LINEAR GEOMETRY

Integration Point	E11	E22	E12	E Max P	E Min P	S11	S22	S12	S Max P	S Min P	S Mises
1	0	0.09531	0	0.09531	0	8169	1.225e+004	0	1.225e+004	8169	4085
2	0	0.09531	0	0.09531	0	8169	1.225e+004	0	1.225e+004	8169	4085
3	0	0.09531	0	0.09531	0	8169	1.225e+004	0	1.225e+004	8169	4085
4	0	0.09531	0	0.09531	0	8169	1.225e+004	0	1.225e+004	8169	4085
Node	RF1	RF2	Magnitude								
1	-4493	-6127	7598								
2	4493	-6127	7598								
3	4493	6127	7598								
4	-4493	6127	7598								
Internal Energy	642.4										

**Table I.18:** FE CODE - QUAD 4 INTEGRATION POINTS - TENSION - LINEAR GEOMETRY

Integration Point	E11	E22	E12	E Max P	E Min P	S11	S22	S12	S Max P	S Min P	S Mises
1	0	0.1	0	0.1	0	8571	1.286e+004	0	1.286e+004	8571	1.134e+004
2	0	0.1	0	0.1	0	8571	1.286e+004	0	1.286e+004	8571	1.134e+004
3	0	0.1	0	0.1	0	8571	1.286e+004	0	1.286e+004	8571	1.134e+004
4	0	0.1	0	0.1	0	8571	1.286e+004	0	1.286e+004	8571	1.134e+004
Node	RF1	RF2	Magnitude								
1	-4286	-6429	7726								
2	4286	-6429	7726								
3	4286	6429	7726								
4	-4286	6429	7726								
Internal Energy	642.9										

APPENDIX I: FINITE ELEMENT CODE VALIDATION

**Table I.19:** FE CODE - QUAD 4 INTEGRATION POINTS - TENSION - NON-LINEAR GEOMETRY

Integration Point	E11	E22	E12	E Max P	E Min P	S11	S22	S12	S Max P	S Min P	S Mises
1	0	0.09531	0	0.09531	0	8169	1.225e+004	0	1.225e+004	8169	1.081e+004
2	0	0.09531	0	0.09531	0	8169	1.225e+004	0	1.225e+004	8169	1.081e+004
3	0	0.09531	0	0.09531	0	8169	1.225e+004	0	1.225e+004	8169	1.081e+004
4	0	0.09531	0	0.09531	0	8169	1.225e+004	0	1.225e+004	8169	1.081e+004
Node	RF1	RF2	Magnitude								
1	-4493	-6127	7598								
2	4493	-6127	7598								
3	4493	6127	7598								
4	-4493	6127	7598								
Internal Energy	622.4										

**Table I.20:** ABAQUS STANDARD - CPE4R - TENSION - LINEAR GEOMETRY

Integration Point	E11	E22	E12	E Max P	E Min P	S11	S22	S12	S Max P	S Min P	S Mises
1	0	0.1	0	0.1	0	8571	1.286e+004	0	1.286e+004	8571	4286
Node	RF1	RF2	Magnitude								
1	-4286	-6429	7726								
2	4286	-6429	7726								
3	4286	6429	7726								
4	-4286	6429	7726								
Internal Energy	642.9										

**Table I.21:** ABAQUS STANDARD - CPE4R - TENSION - NON-LINEAR GEOMETRY

Integration Point	E11	E22	E12	E Max P	E Min P	S11	S22	S12	S Max P	S Min P	S Mises
1	0	0.09531	0	0.09531	0	8169	1.225e+004	0	1.225e+004	8169	4085
Node	RF1	RF2	Magnitude								
1	-4493	-6127	7598								
2	4493	-6127	7598								
3	4493	6127	7598								
4	-4493	6127	7598								
Internal Energy	642.4										

**Table I.22:** ABAQUS EXPLICIT - CPE4R - TENSION - LINEAR GEOMETRY

Integration Point	E11	E22	E12	E Max P	E Min P	S11	S22	S12	S Max P	S Min P	S Mises
1	0	0.1	0	0.1	0	8571	1.286e+004	0	1.286e+004	8571	4286
Node	RF1	RF2	Magnitude								
1	-4286	-6429	7727								
2	4286	-6429	7727								
3	4286	6429	7727								
4	-4286	6429	7727								
Internal Energy	642.9										



APPENDIX I: FINITE ELEMENT CODE VALIDATION

**Table I.23:** ABAQUS EXPLICIT - CPE4R - TENSION - NON-LINEAR GEOMETRY

Integration Point	E11	E22	E12	E Max P	E Min P	S11	S22	S12	S Max P	S Min P	S Mises
1	0	0.09531	0	0.09531	0	8169	1.225e+004	0	1.225e+004	8169	4085
Node	RF1	RF2	Magnitude								
1	-4494	-6128	7599								
2	4494	-6128	7599								
3	4494	6128	7599								
4	-4494	6128	7599								
Internal Energy	622.4										

**Table I.24:** FE CODE - QUAD 1 INTEGRATION POINT - TENSION - LINEAR GEOMETRY

Integration Point	E11	E22	E12	E Max P	E Min P	S11	S22	S12	S Max P	S Min P	S Mises
1	0	0.1	0	0.1	0	8571	1.286e+004	0	1.286e+004	8571	1.134e+004
Node	RF1	RF2	Magnitude								
1	-4286	-6429	7726								
2	4286	-6429	7726								
3	4286	6429	7726								
4	-4286	6429	7726								
Internal Energy	642.9										

**Table I.25:** FE CODE - QUAD 1 INTEGRATION POINT - TENSION - NON-LINEAR GEOMETRY

Integration Point	E11	E22	E12	E Max P	E Min P	S11	S22	S12	S Max P	S Min P	S Mises
1	0	0.09531	0	0.09531	0	8169	1.225e+004	0	1.225e+004	8169	1.081e+004
Node	RF1	RF2	Magnitude								
1	-4493	-6127	7598								
2	4493	-6127	7598								
3	4493	6127	7598								
4	-4493	6127	7598								
Internal Energy	622.5										

APPENDIX I: FINITE ELEMENT CODE VALIDATION

**Table I.26:** FE CODE - QUAD 4 INTEGRATION POINTS - PATCH TEST - LINEAR GEOMETRY

Element-IP	E11	E22	E12	S11	S22	S12
1-1	0.0009375	-0.0003125	0	1	0	0
1-2	0.0009375	-0.0003125	0	1	0	0
1-3	0.0009375	-0.0003125	0	1	0	0
1-4	0.0009375	-0.0003125	0	1	0	0
2-1	0.0009375	-0.0003125	0	1	0	0
2-2	0.0009375	-0.0003125	0	1	0	0
2-3	0.0009375	-0.0003125	0	1	0	0
2-4	0.0009375	-0.0003125	0	1	0	0
3-1	0.0009375	-0.0003125	0	1	0	0
3-2	0.0009375	-0.0003125	0	1	0	0
3-3	0.0009375	-0.0003125	0	1	0	0
3-4	0.0009375	-0.0003125	0	1	0	0
4-1	0.0009375	-0.0003125	0	1	0	0
4-2	0.0009375	-0.0003125	0	1	0	0
4-3	0.0009375	-0.0003125	0	1	0	0
4-4	0.0009375	-0.0003125	0	1	0	0

Node	U1	U2	RF1	RF2
1	0	0	-2.25	0
2	0.00375	0	0	0
3	0.009375	0	0	0
4	0	-0.001406	-5	0
5	0.005156	-0.001719	0	0
6	0.009375	-0.001563	0	0
7	0	-0.003125	-2.75	0
8	0.003938	-0.003125	0	0
9	0.009375	-0.003125	0	0

Internal Energy	0.04688
-----------------	---------

**Table I.27:** FE CODE - QUAD 4 INTEGRATION POINTS - PATCH TEST - NON-LINEAR GEOMETRY

Element-IP	E11	E22	E12	S11	S22	S12
1-1	0.0009378	-0.0003126	0	1	0	0
1-2	0.0009378	-0.0003126	0	1	0	0
1-3	0.0009378	-0.0003126	0	1	0	0
1-4	0.0009378	-0.0003126	0	1	0	0
2-1	0.0009378	-0.0003126	0	1	0	0
2-2	0.0009378	-0.0003126	0	1	0	0
2-3	0.0009378	-0.0003126	0	1	0	0
2-4	0.0009378	-0.0003126	0	1	0	0
3-1	0.0009378	-0.0003126	0	1	0	0
3-2	0.0009378	-0.0003126	0	1	0	0
3-3	0.0009378	-0.0003126	0	1	0	0
3-4	0.0009378	-0.0003126	0	1	0	0
4-1	0.0009378	-0.0003126	0	1	0	0
4-2	0.0009378	-0.0003126	0	1	0	0
4-3	0.0009378	-0.0003126	0	1	0	0
4-4	0.0009378	-0.0003126	0	1	0	0

Node	U1	U2	RF1	RF2
1	0	0	-2.25	0
2	0.003753	0	0	0
3	0.009382	0	0	0
4	0	-0.001406	-5	0
5	0.00516	-0.001719	0	0
6	0.009382	-0.001563	0	0
7	0	-0.003125	-2.75	0
8	0.003941	-0.003125	0	0
9	0.009382	-0.003125	0	0

Internal Energy	0.04693
-----------------	---------

APPENDIX I: FINITE ELEMENT CODE VALIDATION

**Table I.28:** FE CODE - QUAD 1 INTEGRATION POINTS - PATCH TEST - LINEAR GEOMETRY

Element	E11	E22	E12	S11	S22	S12
1	0.0009375	-0.0003125	0	1	0	0
2	0.0009375	-0.0003125	0	1	0	0
3	0.0009375	-0.0003125	0	1	0	0
4	0.0009375	-0.0003125	0	1	0	0

Node	U1	U2	RF1	RF2
1	0	0	-2.25	0
2	0.004178	0.001958	0	0
3	0.008333	9.829e-005	0	0
4	0	0.0001716	-5	0
5	0.004633	-0.001196	0	0
6	0.01027	-0.0001705	0	0
7	0	-0.001963	-2.75	0
8	0.004577	-0.002035	0	0
9	0.008618	-0.002368	0	0

Internal Energy	0.04688
-----------------	---------

**Table I.29:** FE CODE - QUAD 1 INTEGRATION POINTS - PATCH TEST - NON-LINEAR GEOMETRY

Element	E11	E22	E12	S11	S22	S12
1	0.0009378	-0.0003125	0	1	9.013e-005	6.192e-005
2	0.0009378	-0.0003126	0	1	-2.87e-005	-3.098e-005
3	0.0009377	-0.0003125	0	1	3.141e-005	-8.479e-006
4	0.0009378	-0.0003126	0	1	-1.629e-005	4.201e-005

Node	U1	U2	RF1	RF2
1	0	0	-2.25	-0.0003197
2	0.004125	0.001899	0	0
3	0.008479	8.78e-005	0	0
4	0	0.0001616	-5	0
5	0.004706	-0.001264	0	0
6	0.01016	-0.0001544	0	0
7	0	-0.002116	-2.75	0
8	0.004495	-0.00198	0	0
9	0.008724	-0.002466	0	0

Internal Energy	0.04693
-----------------	---------

# APPENDIX I: FINITE ELEMENT CODE VALIDATION

**Table I.30:** ABAQUS STANDARD - CPE3 - SHEAR - NON-LINEAR GEOMETRY

Integration Point	E11	E22	E12	E Max P	E Min P	S11	S22	S12	S Max P	S Min P	S Mises
1	0.002496	-0.002496	0.09983	0.04998	-0.04998	106	-106	2139	2142	-2142	3710
Node	RF1	RF2	Magnitude								
1	53.98	-1075	1076								
2	-1124	1128	1592								
3	1070	-52.99	1071								
Internal Energy	53.53										

**Table I.31:** FE CODE - TRIANGLE 1 INTEGRATION POINT - SHEAR - NON-LINEAR GEOMETRY

Integration Point	E11	E22	E12	E Max P	E Min P	S11	S22	S12	S Max P	S Min P	S Mises
1	0.002496	-0.002496	0.09983	0.04998	-0.04998	107	-107	2139	2142	-2142	3710
Node	RF1	RF2	Magnitude								
1	53.48	-1075	1076								
2	-1123	1128	1592								
3	1070	-53.48	1071								
Internal Energy	53.53										

APPENDIX I: FINITE ELEMENT CODE VALIDATION

**Table I.32:** ABAQUS STANDARD - C3D8 - SHEAR - NON-LINEAR GEOMETRY

Integration Point	E11	E22	E33	E12	E23	E13	S11	S22	S33	S12	S23	S13
1	0.002496	0	-0.002496	0	0	0.09983	106	0	-106	0	0	2139
2	0.002496	0	-0.002496	0	0	0.09983	106	0	-106	0	0	2139
3	0.002496	0	-0.002496	0	0	0.09983	106	0	-106	0	0	2139
4	0.002496	0	-0.002496	0	0	0.09983	106	0	-106	0	0	2139
5	0.002496	0	-0.002496	0	0	0.09983	106	0	-106	0	0	2139
6	0.002496	0	-0.002496	0	0	0.09983	106	0	-106	0	0	2139
7	0.002496	0	-0.002496	0	0	0.09983	106	0	-106	0	0	2139
8	0.002496	0	-0.002496	0	0	0.09983	106	0	-106	0	0	2139

Node	RF1	RF2	RF3
1	-507.8	0	-511
2	-561.8	0	564
3	-561.8	0	564
4	-507.8	0	-511
5	561.8	0	-564
6	507.8	0	511
7	507.8	0	511
8	561.8	0	-564

Internal Energy	107.1
-----------------	-------

**Table I.33:** FE CODE - HEX 8 INTEGRATION POINTS - SHEAR - NON-LINEAR GEOMETRY

Integration Point	E11	E22	E33	E12	E23	E13	S11	S22	S33	S12	S23	S13
1	0.002496	0	-0.002496	0	0	0.09983	107	0	-107	0	0	2139
2	0.002496	0	-0.002496	0	0	0.09983	107	0	-107	0	0	2139
3	0.002496	0	-0.002496	0	0	0.09983	107	0	-107	0	0	2139
4	0.002496	0	-0.002496	0	0	0.09983	107	0	-107	0	0	2139
5	0.002496	0	-0.002496	0	0	0.09983	107	0	-107	0	0	2139
6	0.002496	0	-0.002496	0	0	0.09983	107	0	-107	0	0	2139
7	0.002496	0	-0.002496	0	0	0.09983	107	0	-107	0	0	2139
8	0.002496	0	-0.002496	0	0	0.09983	107	0	-107	0	0	2139

Node	RF1	RF2	RF3
1	-508.1	0	-510.8
2	-561.6	0	564.2
3	-561.6	0	564.2
4	-508.1	0	-510.8
5	561.7	0	-564.2
6	508.2	0	510.8
7	508.2	0	510.8
8	561.7	0	-564.2

Internal Energy	107.1
-----------------	-------

APPENDIX I: FINITE ELEMENT CODE VALIDATION

**Table I.34:** ABAQUS STANDARD - C3D6 - SHEAR - NON-LINEAR GEOMETRY

Integration Point	E11	E22	E33	E12	E23	E13	S11	S22	S33	S12	S23	S13
1	-0.002496	0.002496	0	0.09983	0	0	-106	106	0	2139	0	0
2	-0.002496	0.002496	0	0.09983	0	0	-106	106	0	2139	0	0
Node	RF1	RF2	RF3									
1	-519.8	-329.6	0									
2	555.1	-383.5	0									
3	17.66	-356.6	0									
4	-555.1	383.5	0									
5	519.8	329.6	0									
6	-17.66	356.6	0									
Internal Energy	53.53											

**Table I.35:** FE CODE - WEDGE 2 INTEGRATION POINTS - SHEAR - NON-LINEAR GEOMETRY

Integration Point	E11	E22	E33	E12	E23	E13	S11	S22	S33	S12	S23	S13
1	-0.002496	0.002496	0	0.09983	0	0	-107	107	0	2139	0	0
2	-0.002496	0.002496	0	0.09983	0	0	-107	107	0	2139	0	0
Node	RF1	RF2	RF3									
1	-519.7	-329.8	0									
2	555.3	-383.3	0									
3	17.83	-356.5	0									
4	-555.3	383.4	0									
5	519.7	329.9	0									
6	-17.83	356.6	0									
Internal Energy	53.53											

APPENDIX I: FINITE ELEMENT CODE VALIDATION

**Table I.36:** ABAQUS STANDARD - C3D8 - PATCH TEST - NON-LINEAR GEOMETRY

Element	E11	E22	E33	E12	E23	E13	S11	S22	S33	S12	S23	S13
1	0.001001	-0.0002501	-0.0002501	0	0	0	1	0	0	0	0	0
2	0.001001	-0.0002501	-0.0002501	0	0	0	1	0	0	0	0	0
3	0.001001	-0.0002501	-0.0002501	0	0	0	1	0	0	0	0	0
4	0.001001	-0.0002501	-0.0002501	0	0	0	1	0	0	0	0	0
5	0.001001	-0.0002501	-0.0002501	0	0	0	1	0	0	0	0	0
6	0.001001	-0.0002501	-0.0002501	0	0	0	1	0	0	0	0	0
7	0.001001	-0.0002501	-0.0002501	0	0	0	1	0	0	0	0	0
8	0.001001	-0.0002501	-0.0002501	0	0	0	1	0	0	0	0	0
Internal Energy	0.5008											

**Table I.37:** FE CODE - HEX 8 INTEGRATION POINTS - PATCH TEST - NON-LINEAR GEOMETRY

Element	E11	E22	E33	E12	E23	E13	S11	S22	S33	S12	S23	S13
1	0.001001	-0.0002501	-0.0002501	0	0	0	1	0	0	0	0	0
2	0.001001	-0.0002501	-0.0002501	0	0	0	1	0	0	0	0	0
3	0.001001	-0.0002501	-0.0002501	0	0	0	1	0	0	0	0	0
4	0.001001	-0.0002501	-0.0002501	0	0	0	1	0	0	0	0	0
5	0.001001	-0.0002501	-0.0002501	0	0	0	1	0	0	0	0	0
6	0.001001	-0.0002501	-0.0002501	0	0	0	1	0	0	0	0	0
7	0.001001	-0.0002501	-0.0002501	0	0	0	1	0	0	0	0	0
8	0.001001	-0.0002501	-0.0002501	0	0	0	1	0	0	0	0	0
Internal Energy	0.5008											

APPENDIX I: FINITE ELEMENT CODE VALIDATION

**Table I.38:** ABAQUS STANDARD - C3D6 - PATCH TEST - NON-LINEAR GEOMETRY

Element	E11	E22	E33	E12	E23	E13	S11	S22	S33	S12	S23	S13
1	0.001001	-0.0002501	-0.0002501	0	0	0	1	0	0	0	0	0
2	0.001001	-0.0002501	-0.0002501	0	0	0	1	0	0	0	0	0
3	0.001001	-0.0002501	-0.0002501	0	0	0	1	0	0	0	0	0
4	0.001001	-0.0002501	-0.0002501	0	0	0	1	0	0	0	0	0
5	0.001001	-0.0002501	-0.0002501	0	0	0	1	0	0	0	0	0
6	0.001001	-0.0002501	-0.0002501	0	0	0	1	0	0	0	0	0
7	0.001001	-0.0002501	-0.0002501	0	0	0	1	0	0	0	0	0
8	0.001001	-0.0002501	-0.0002501	0	0	0	1	0	0	0	0	0
9	0.001001	-0.0002501	-0.0002501	0	0	0	1	0	0	0	0	0
10	0.001001	-0.0002501	-0.0002501	0	0	0	1	0	0	0	0	0
11	0.001001	-0.0002501	-0.0002501	0	0	0	1	0	0	0	0	0
12	0.001001	-0.0002501	-0.0002501	0	0	0	1	0	0	0	0	0
13	0.001001	-0.0002501	-0.0002501	0	0	0	1	0	0	0	0	0
14	0.001001	-0.0002501	-0.0002501	0	0	0	1	0	0	0	0	0
15	0.001001	-0.0002501	-0.0002501	0	0	0	1	0	0	0	0	0
16	0.001001	-0.0002501	-0.0002501	0	0	0	1	0	0	0	0	0
Internal Energy	0.5008											

**Table I.39:** FE CODE - WEDGE 2 INTEGRATION POINTS - PATCH TEST - NON-LINEAR GEOMETRY

Element	E11	E22	E33	E12	E23	E13	S11	S22	S33	S12	S23	S13
1	0.001001	-0.0002501	-0.0002501	0	0	0	1	0	0	0	0	0
2	0.001001	-0.0002501	-0.0002501	0	0	0	1	0	0	0	0	0
3	0.001001	-0.0002501	-0.0002501	0	0	0	1	0	0	0	0	0
4	0.001001	-0.0002501	-0.0002501	0	0	0	1	0	0	0	0	0
5	0.001001	-0.0002501	-0.0002501	0	0	0	1	0	0	0	0	0
6	0.001001	-0.0002501	-0.0002501	0	0	0	1	0	0	0	0	0
7	0.001001	-0.0002501	-0.0002501	0	0	0	1	0	0	0	0	0
8	0.001001	-0.0002501	-0.0002501	0	0	0	1	0	0	0	0	0
9	0.001001	-0.0002501	-0.0002501	0	0	0	1	0	0	0	0	0
10	0.001001	-0.0002501	-0.0002501	0	0	0	1	0	0	0	0	0
11	0.001001	-0.0002501	-0.0002501	0	0	0	1	0	0	0	0	0
12	0.001001	-0.0002501	-0.0002501	0	0	0	1	0	0	0	0	0
13	0.001001	-0.0002501	-0.0002501	0	0	0	1	0	0	0	0	0
14	0.001001	-0.0002501	-0.0002501	0	0	0	1	0	0	0	0	0
15	0.001001	-0.0002501	-0.0002501	0	0	0	1	0	0	0	0	0
16	0.001001	-0.0002501	-0.0002501	0	0	0	1	0	0	0	0	0
Internal Energy	0.5008											



APPENDIX I: FINITE ELEMENT CODE VALIDATION

**Table I.40:** ABAQUS STANDARD - C3D8 - SHEAR - NON-LINEAR GEOMETRY - ANISOTROPIC - 100 ITERATIONS

Integration Point	E11	E22	E33	E12	E23	E13	S11	S22	S33	S12	S23	S13
1	-0.002496	0.002496	0	0.09983	0	0	151	-14.72	0	8.312	0	0
2	-0.002496	0.002496	0	0.09983	0	0	151	-14.72	0	8.312	0	0
3	-0.002496	0.002496	0	0.09983	0	0	151	-14.72	0	8.312	0	0
4	-0.002496	0.002496	0	0.09983	0	0	151	-14.72	0	8.312	0	0
5	-0.002496	0.002496	0	0.09983	0	0	151	-14.72	0	8.312	0	0
6	-0.002496	0.002496	0	0.09983	0	0	151	-14.72	0	8.312	0	0
7	-0.002496	0.002496	0	0.09983	0	0	151	-14.72	0	8.312	0	0
8	-0.002496	0.002496	0	0.09983	0	0	151	-14.72	0	8.312	0	0

Node	RF1	RF2	RF3
1	-36.04	1.81	0
2	-39.44	-5.966	0
3	-39.44	-5.966	0
4	-36.04	1.81	0
5	39.44	5.966	0
6	36.04	-1.81	0
7	36.04	-1.81	0
8	39.44	5.966	0

Internal Energy	0.21
-----------------	------

**Table I.41:** ABAQUS STANDARD - C3D8 - SHEAR - NON-LINEAR GEOMETRY - ANISOTROPIC - 1000 ITERATIONS

Integration Point	E11	E22	E33	E12	E23	E13	S11	S22	S33	S12	S23	S13
1	-0.002496	0.002496	0	0.09983	0	0	149.6	-14.59	0	8.238	0	0
2	-0.002496	0.002496	0	0.09983	0	0	149.6	-14.59	0	8.238	0	0
3	-0.002496	0.002496	0	0.09983	0	0	149.6	-14.59	0	8.238	0	0
4	-0.002496	0.002496	0	0.09983	0	0	149.6	-14.59	0	8.238	0	0
5	-0.002496	0.002496	0	0.09983	0	0	149.6	-14.59	0	8.238	0	0
6	-0.002496	0.002496	0	0.09983	0	0	149.6	-14.59	0	8.238	0	0
7	-0.002496	0.002496	0	0.09983	0	0	149.6	-14.59	0	8.238	0	0
8	-0.002496	0.002496	0	0.09983	0	0	149.6	-14.59	0	8.238	0	0

Node	RF1	RF2	RF3
1	-35.72	1.794	0
2	-39.08	-5.913	0
3	-39.08	-5.913	0
4	-35.72	1.794	0
5	39.08	5.913	0
6	35.72	-1.794	0
7	35.72	-1.794	0
8	39.08	5.913	0

Internal Energy	0.2063
-----------------	--------

APPENDIX I: FINITE ELEMENT CODE VALIDATION

**Table I.42:** FE CODE - HEX 8 INTEGRATION POINTS - SHEAR - NON-LINEAR GEOMETRY - ANISOTROPIC

Integration Point	E11	E22	E33	E12	E23	E13	S11	S22	S33	S12	S23	S13
1	-0.002496	0.002496	0	0.09983	0	0	149.3	-14.56	0	8.216	0	0
2	-0.002496	0.002496	0	0.09983	0	0	149.3	-14.56	0	8.216	0	0
3	-0.002496	0.002496	0	0.09983	0	0	149.3	-14.56	0	8.216	0	0
4	-0.002496	0.002496	0	0.09983	0	0	149.3	-14.56	0	8.216	0	0
5	-0.002496	0.002496	0	0.09983	0	0	149.3	-14.56	0	8.216	0	0
6	-0.002496	0.002496	0	0.09983	0	0	149.3	-14.56	0	8.216	0	0
7	-0.002496	0.002496	0	0.09983	0	0	149.3	-14.56	0	8.216	0	0
8	-0.002496	0.002496	0	0.09983	0	0	149.3	-14.56	0	8.216	0	0
Node	RF1	RF2	RF3									
1	-35.66	1.793	0									
2	-39.01	-5.9	0									
3	-39.01	-5.9	0									
4	-35.66	1.793	0									
5	39.01	6.025	0									
6	35.66	-1.668	0									
7	35.66	-1.668	0									
8	39.01	6.025	0									
Internal Energy	0.2056											

# Quadtree

A quadtree is a tree data structure which can be used to partition a two-dimensional space. In the context of this thesis it is used to optimise the contact algorithm. For large models it can be very computationally intensive to perform intersection tests between all surface triangles against all nodes in the model. The number of point-triangle intersection tests is equal to the number of nodes multiplied by the number of facets in the model. For example, a simple model of a plain weave fabric may contain 2000 nodes and 3000 facets. This results in a total of 6000000 point-triangle intersection tests for every iteration. By partitioning space with a quadtree it is possible to cut down the number of intersection tests considerably. The quadtree is generated as follows:

Given a number of nodes randomly placed in 2D space a square bounding box is created that completely encompasses all of the nodes (Figure J.1).

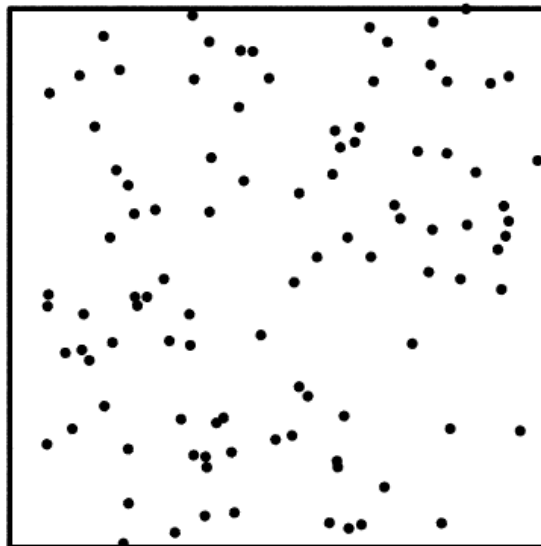


**Figure J.1:** Unit cell containing randomly distributed nodes

The bounding box is then divided into four equal sized child boxes labelled *A*, *B*, *C* and *D* (Figure J.2). Box *A* keeps a list of all nodes contained within itself, similarly boxes *B*, *C*, *D* each keep a list of all nodes contained within themselves. This is illustrated by the colour coding in the figure.

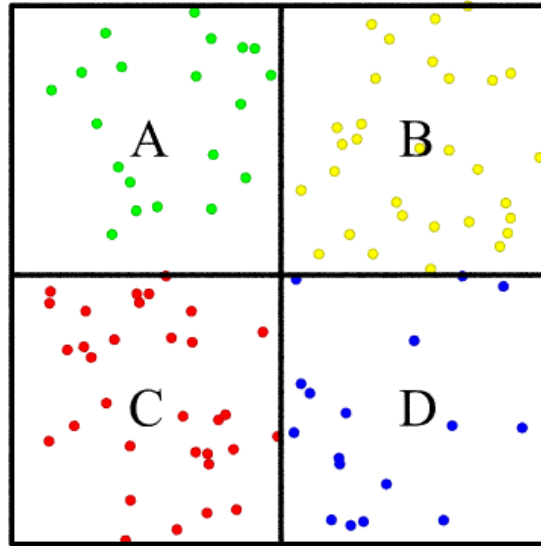


**Figure J.2:** Unit cell divided into four equal sized child boxes

Box *A* can be further subdivided into four equal sized child boxes labelled *a*, *b*, *c* and *d* (Figure J.3). Again each of the child boxes *a*, *b*, *c* and *d* keeps a list of the nodes contained within themselves. This is accomplished by iterating over the nodes contained within the parent box *A*, sorting the nodes into the appropriate child box *a*, *b*, *c* or *d*. Note that it is not necessary to iterate over all the nodes since the child boxes will never contain nodes that are not contained within the parent box thus providing a significant increase in speed which is of course the point of the exercise.

Boxes *B*, *C* and *D* can be subdivided in a similar fashion and of course children of the subdivided boxes can be further subdivided and so on. A criterion must be used to determine when a box should no longer be subdivided. One solution is to limit the number of subdivisions to a fixed number resulting in a homogeneous grid, another solution is to only subdivide a box if it contains more than a certain number of nodes. The method actually implemented is a combination of the two, subdivisions stop when either of these criterion are met.

Once the quadtree has been built, it can be used to find nodes quickly within the vicinity of a given point. Suppose the nodes within the vicinity of the point illustrated in red in Figure J.4 are to be found. The nodes illustrated in green are the nodes that are in the

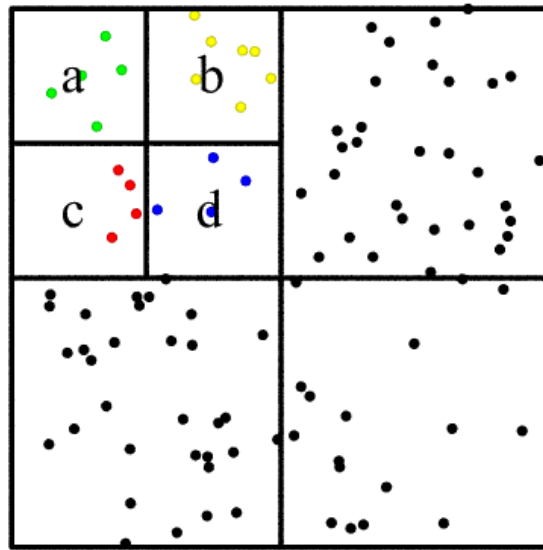


Figure J.3: Unit cell top left box subdivided further

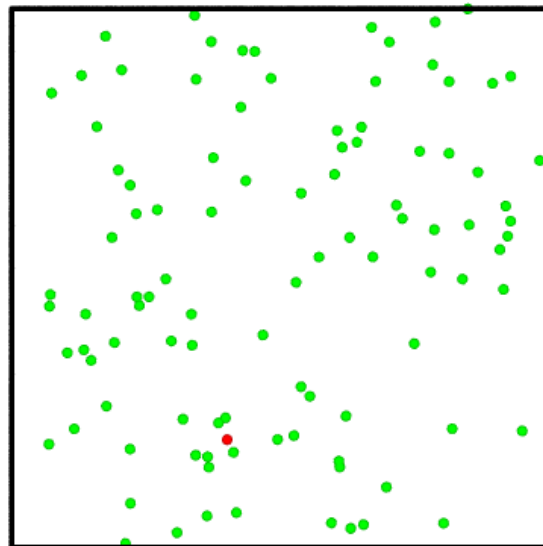


Figure J.4: Parent quadtree

vicinity of the red point. Initially this includes all the nodes. It can be observed that the red point lies within the lower left hand side of the bounding box. The quadtree can be accessed to obtain a list of points within the lower left hand side of the bounding box, thus reducing the number of nodes within the vicinity by a factor of 4 on average if the nodes are randomly distributed (Figure J.5).

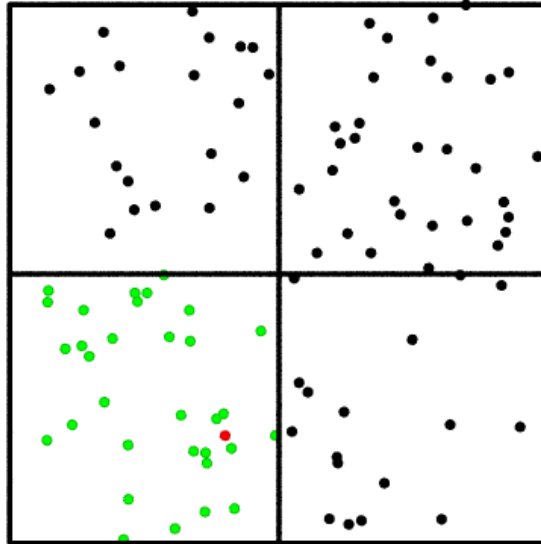


Figure J.5: 1st level subdivision

The red point now lies within the lower right hand side of the child box, reducing the number of nodes within the vicinity by a further factor of 4 (Figure J.6). The total reduction of nodes found within the vicinity of the red point is a factor of 16 in just 2 steps.

Continuing this process in an iterative manner until the quadtree no longer has any child boxes the number of nodes found within the vicinity can be greatly reduced (Figure J.7).

This is a very efficient way to find nodes close to the specified point of interest. However in the case of the contact algorithm, it is necessary to perform intersection detection between points and triangles. If all the nodes are sorted into a quadtree as described above, the nodes within the vicinity of a triangle can be found. However the location of a triangle cannot be expressed by a single point. A triangle may lie over several quadtree boxes. The worse case scenario where the triangle lies over all four quadtree boxes is shown in Figure J.8.

Each of the four boxes can be subdivided and combined to obtain a list of nodes within the vicinity of the triangle J.9.

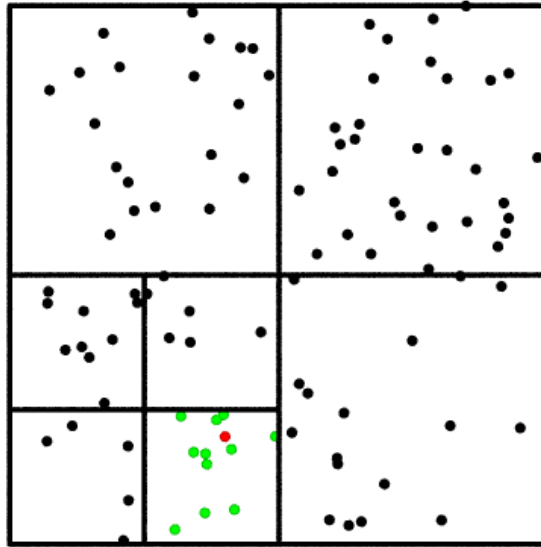


Figure J.6: 2nd level subdivision

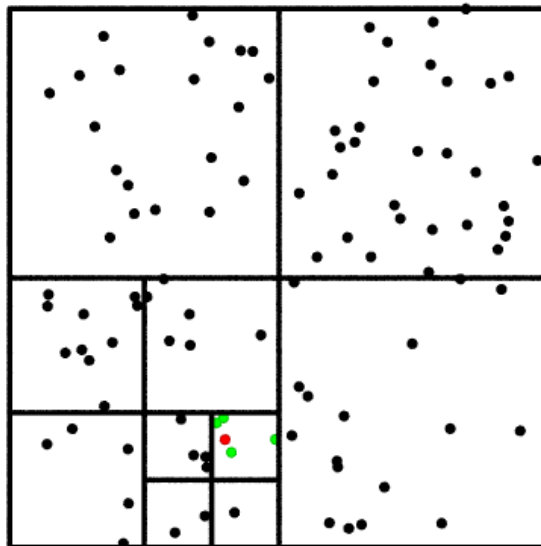


Figure J.7: 3rd level subdivision

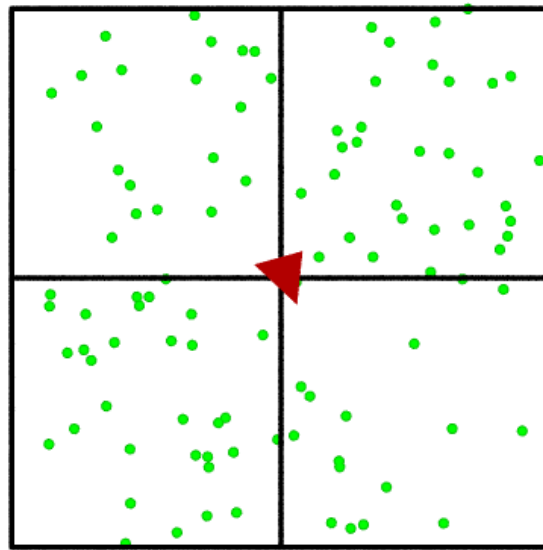


Figure J.8: Triangle used to index quadtree level 1

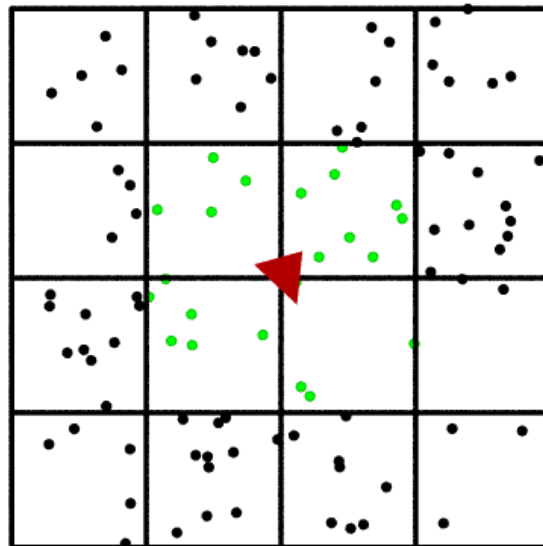


Figure J.9: Triangle used to index quadtree level 2



The subdivision continues rejecting the nodes contained within the quadtree boxes that do not intersect with the triangle J.10.

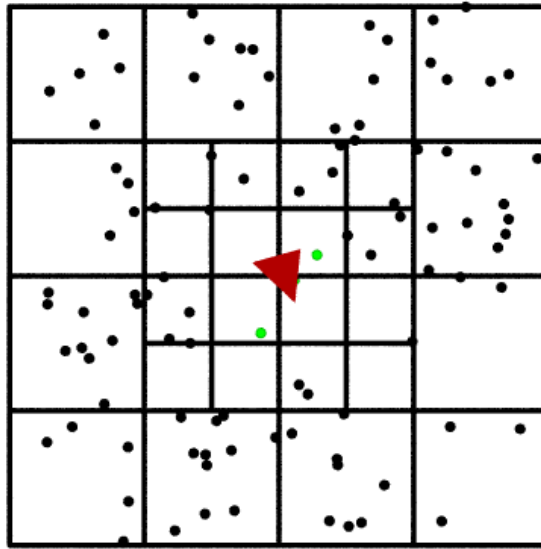


Figure J.10: Triangle used to index quadtree level 3

An alternative is to place the triangles in the quadtree rather than the nodes. The node position is then used to obtain the triangles within the vicinity of the node rather than the other way round.

The quadtree construction is complicated due to the fact that the triangles can overlap between bounding boxes. The triangle must be added to all boxes with which it intersects. Thus the triangles may be contained within several same-level quadtree boxes. From J.11, triangles belonging to the bottom left box are illustrated in red, top left in green, bottom right in blue and top right in black. Triangles belonging to several boxes are illustrated as the combination of these colours.

The subdivision limits must be chosen with care. If subdivision continues until the number of triangles found within a box is less than a certain number the process may never end. Since when the subdivision box gets to be approximately equal to the size of the triangle, further subdivisions may result in the triangle being placed in all four of its child boxes.

Once the quadtree has been built, triangles in the vicinity of a given point can efficiently be obtained in the same manner as was illustrated for the nodes (Figure J.12).

This technique is applied to the model of a cotton plain weave where the surface is defined by triangles. The first quadtree subdivision step for the model is shown in Figure J.13.

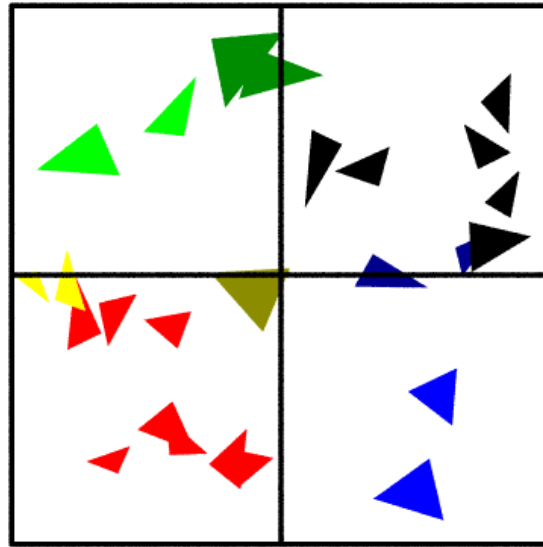


Figure J.11: Triangles partitioned into a quadtree

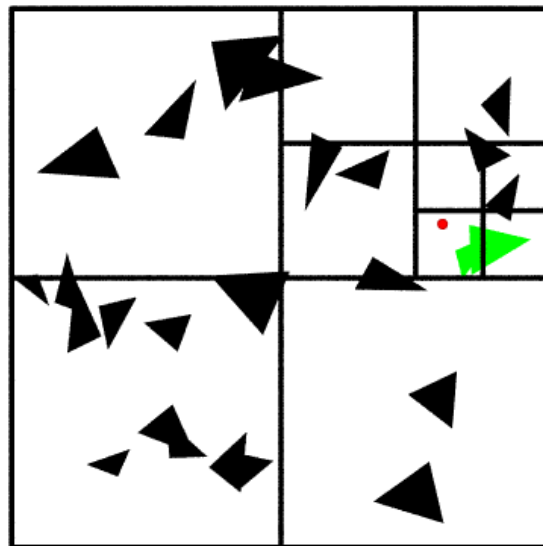
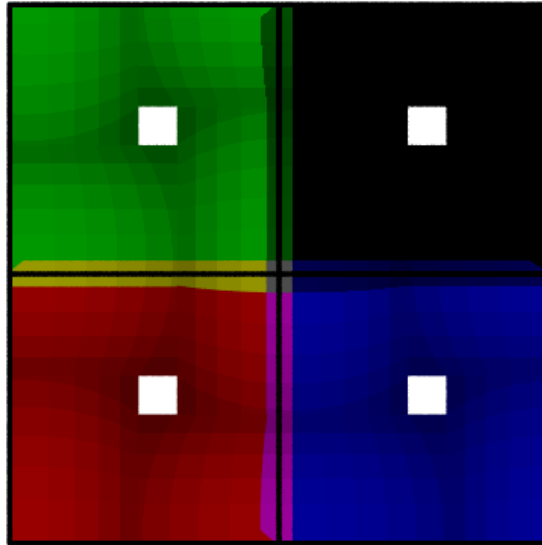
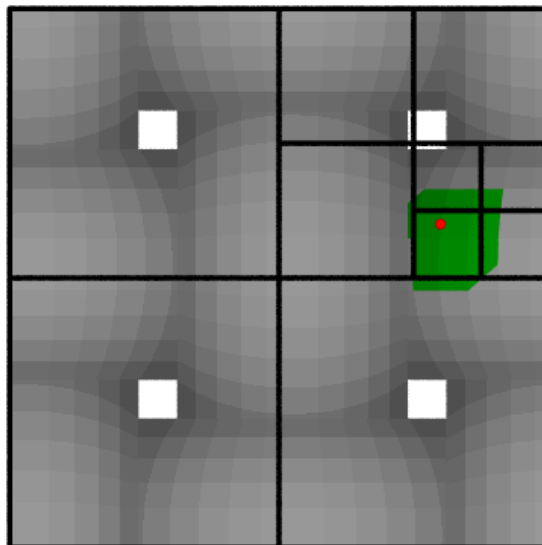


Figure J.12: Triangles in 3rd level subdivision



**Figure J.13:** Cotton weave partitioned into a quadtree

Further subdivisions are performed as described previously. Then the quadtree is used to obtain a list of triangles in the vicinity of the specified point illustrated in red (Figure J.14).



**Figure J.14:** Cotton weave triangles in 3<sup>rd</sup> level subdivision

In order to determine contact between a node and a triangle, it is only necessary to iterate over the triangles shown in green rather than all of the triangles within the model. With the use of a quadtree, the time taken to perform the contact algorithm is  $O(n)$  as opposed to  $O(n^2)$ , where  $n$  is the number of nodes and triangles.

## Predicted fabric compaction graphs

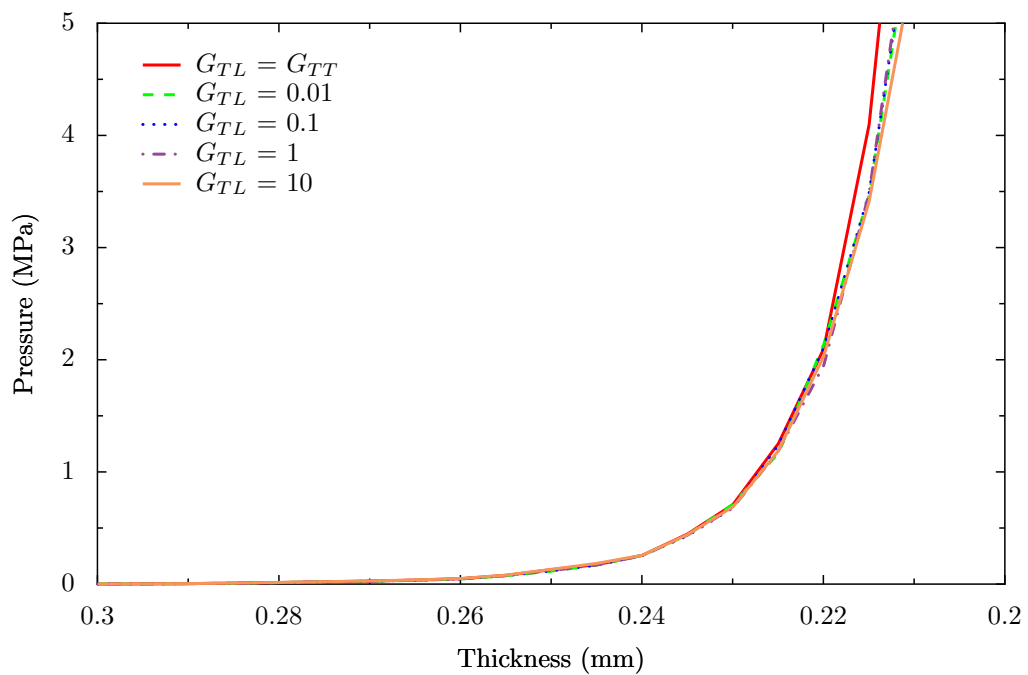


**Figure K.1:** Pressure vs thickness for different values of  $G_{TL}$

Figure K.1 shows the compaction results of the Chomarat 150TB fabric with different values of transverse longitudinal shear modulus  $G_{TL}$  to illustrate that the value of  $G_{TL}$  has little effect on the compaction pressure.

Figure K.2 shows the compaction results of the Chomarat 150TB fabric with different values of damping. Increasing the damping reduces the fluctuations in pressure. However if the damping is too high it affects the results as can be seen by the graph. A damping value of 100 was found to smooth out the fluctuations without significantly affecting the results.

Figure K.3 shows the compaction results of the Chomarat 150TB fabric for different

APPENDIX K: PREDICTED FABRIC COMPACTION GRAPHS

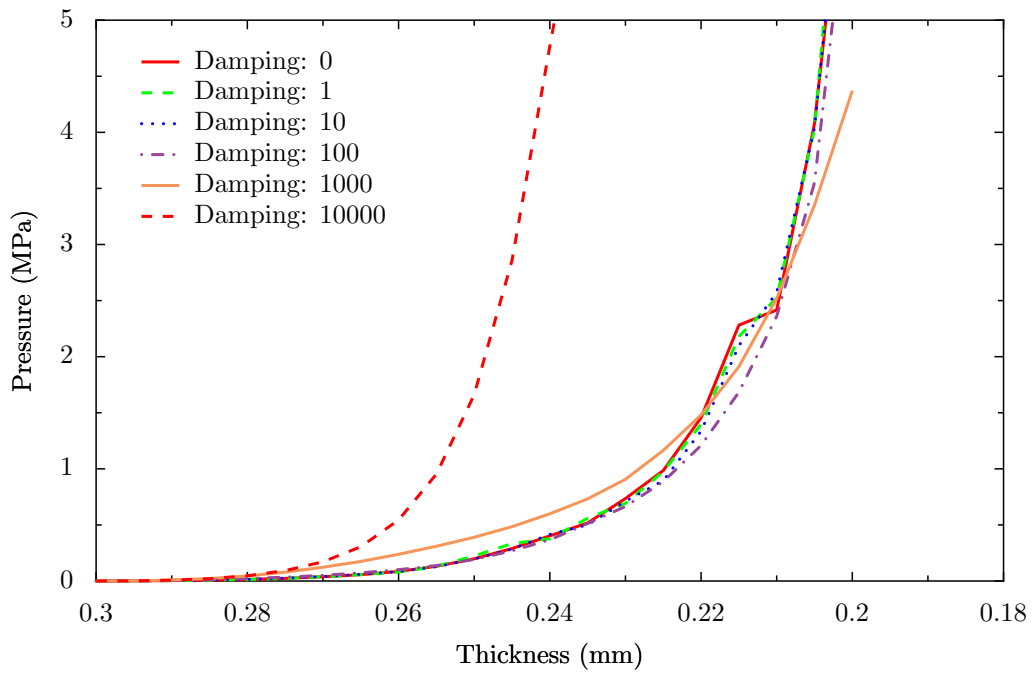


Figure K.2: Pressure vs thickness for different values of damping

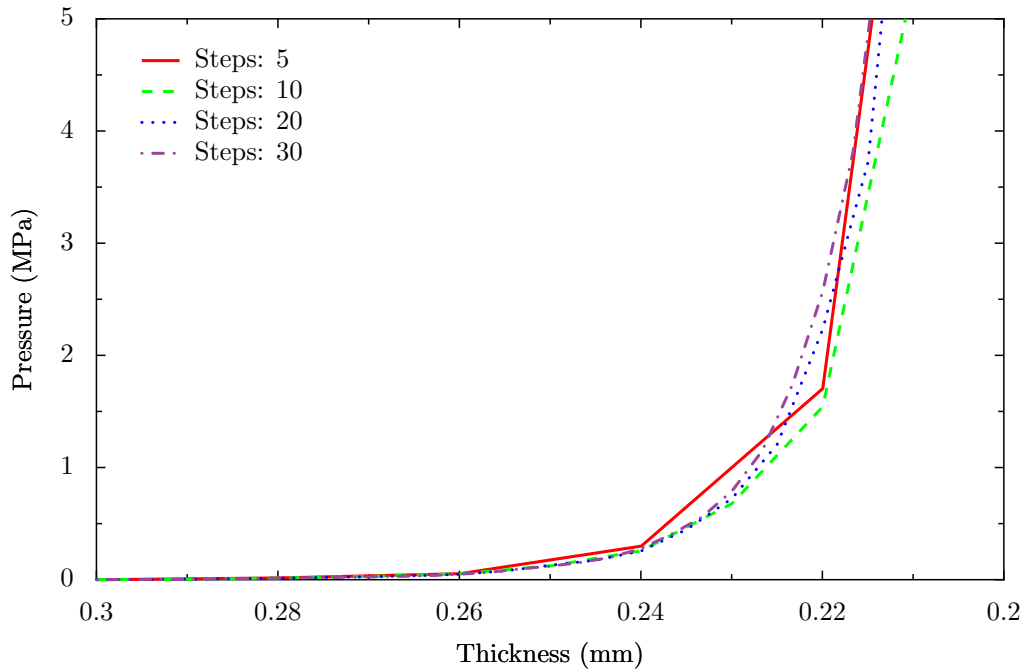
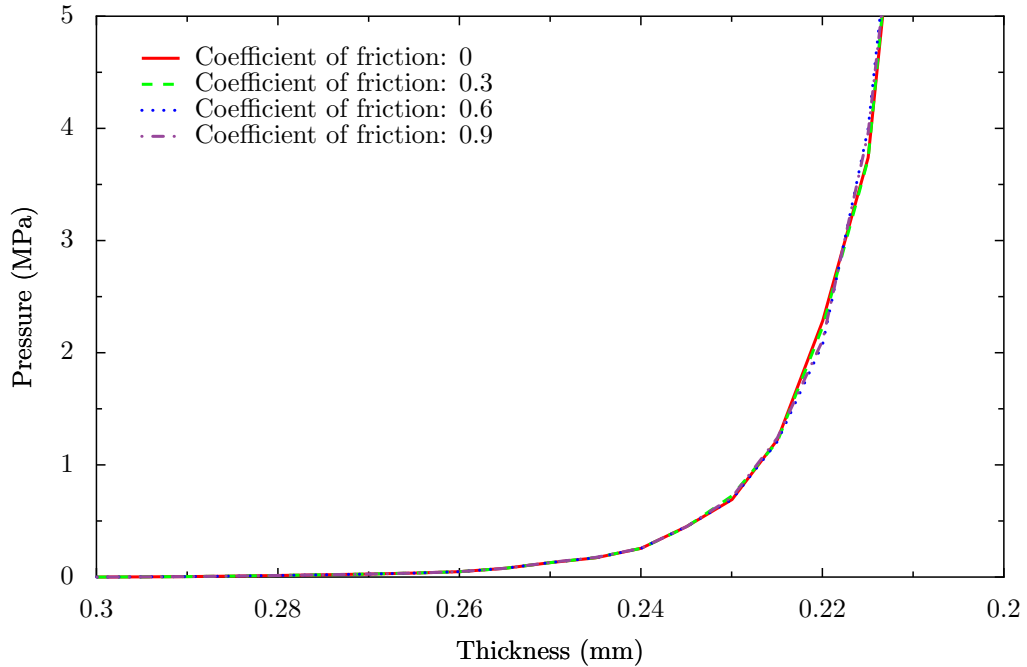


Figure K.3: Pressure vs thickness for different numbers of steps

numbers of steps. Using a low number of steps means less sample points are obtained and hence the pressure vs thickness curve looks jagged. Increasing the number of steps increases the smoothness of the curve. Apart from that, the results are largely unaffected.



**Figure K.4:** Pressure vs thickness for different coefficients of friction

Figure K.4 shows the compaction results of the Chomarat 150TB fabric for different coefficients of friction between yarns. It can be seen that the coefficient of friction has very little effect on the results. This is to be expected since very little inter-yarn sliding is expected during compaction.

Figure K.5 shows the compaction results of the Chomarat 150TB fabric for different contact of stiffnesses. It can be seen that above a contact stiffness of 100000 the results converge, thus this is a suitable contact stiffness to use.

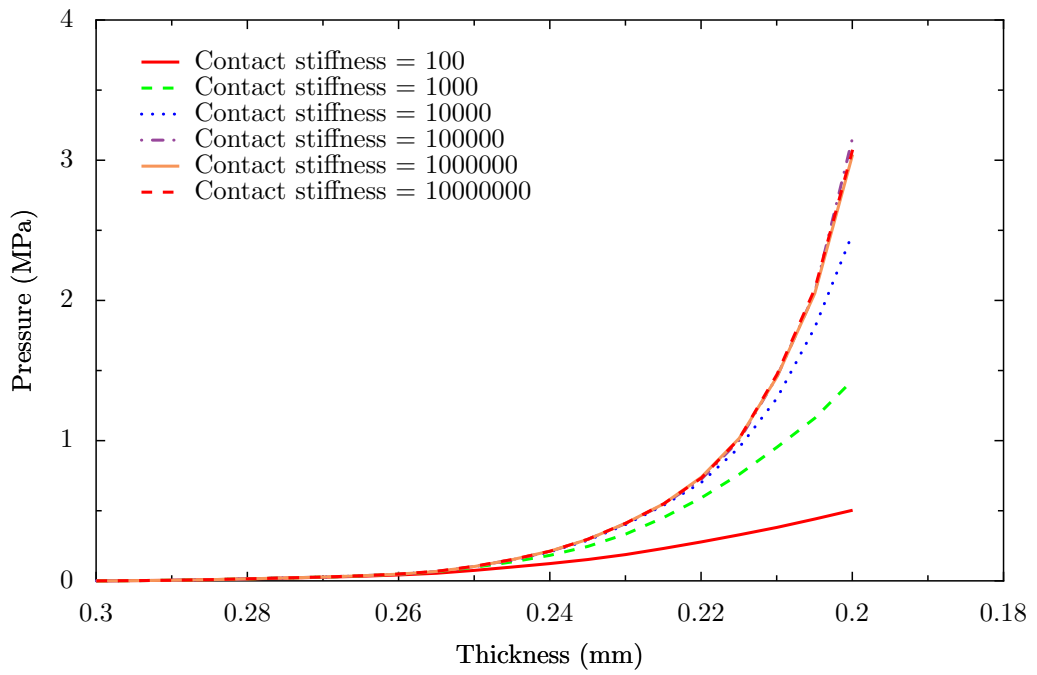


**Figure K.5:** Pressure vs thickness for different contact stiffnesses